Tybaud Goyetche
PhD Thesis
Barcelona - 2021

SEAWATER INTRUSION, TRANSITION ZONE DYNAMICS AND REACTIVE MIXING

Example of Argentona Coastal alluvial aquifer

Universitat Politècnica de Catalunya

Ph.D. Thesis

Seawater Intrusion, transition zone dynamics and reactive mixing – Example of Argentona coastal alluvial aquifer

Author:

Tybaud Goyetche

Advisors:

Prof. Jesus Carrera Ramirez

Dr. habil. Linda Luquot

Tutor :

Prof. Maarten Saaltink

Hydrogeology Group (GHS)

Institute of Environmental Assessment and Water Research (IDAEA, CSIC)

Department of Civil and Environmental Engineering (DECA), Universitat Politècnica de Catalunya (UPC)

June, 2021

Barcelona, Spain

Dedication

To my parents,

my grand-parents,

and my brother.

Without their endless support,

this could not have been possible.

This thesis was funded by the PhD fellowship (BES-2017-080028) from the FPI Program by the Spanish Ministry of Economy, Industry and Competitiveness. Financial support was also provided by "MEDISTRAES" project (Spanish government MICINN grants CGL2013-48869- C2-1-R/2-R and CGL2016-77122-C2-1-R/2R).

Acknowledgments

It will be very difficult for me to thank everyone because it is thanks to the help of many people that I was able to complete this thesis.

Firstly, I would like to acknowledge my advisors:

- To my advisor Jesus Carrera, for giving me the opportunity to join his team and for the support during my Ph.D study and related research.
- À ma co-directrice de thèse Linda Luquot, pour m'avoir donné cette opportunité de thèse à l'étranger, pour son encadrement tout au long de cette thèse et m'avoir fait partager ses brillantes intuitions. Qu'elle soit aussi remerciée pour sa gentillesse, sa disponibilité permanente et pour les nombreux encouragements qu'elle m'a prodiguée.

Es imposible para mí olvidar a Maria Pool por su inestimable ayuda con sus perspicaces comentarios y ánimos.

En tercero lugar, quiero agradecer a toda la gente con la que he podido compartir esta experiencia. Tanto la gente del Proyecto MEDISTRAES como del Grupo de Hidrología Subterránea (GHS). Especialmente la gente del CSIC y del despacho 1434 aunque sea el único que quede de esta oficina de cuando llegue. Han sido un gran soporte, con un buen ambiente y unos grandes compañeros de trabajo, de cervezas o de viajes, con quien esta experiencia no hubiera sido igual.

También quiero agradecer a todos los grandes amigos que he conocido fuera del trabajo que me han acompañado durante este tiempo.

J'aimerai également remercier mes amis du groupe des «Caledo» sans qui cette expérience n'aurait pas été la même, ils sont aussi une grande partie de cette thèse.

Et pour finir j'aimerai remercier ma grande famille : mes parents, mon frère, mes grands-parents, mes oncles et cousins qui ont fait de moi ce que je suis et sans qui je ne pourrai avoir réalisé cette thèse. Merci pour leur soutien et surtout de m'avoir supporté dans tout ce que j'ai entrepris.

Abstract

Freshwater quality and availability in coastal areas are affected by seawater intrusion into coastal aquifers. While coastal water quality and coastal ecosystems can be significantly affected by pollutants discharged into the sea.

In this thesis we investigate: (i) the use of sea level periodic fluctuations (e.g. tides) to characterize coastal aquifers hydrodynamic parameters; (ii) the chemical reactions that occur in the mixing zone between freshwater and seawater; and (iii) the impact of high-frequency fluctuations (e.g. storms) on the mixing zone and chemical reactions. Thus, the Argentona experimental site allowed us to apply and validate the investigated methods.

The results show that thanks to the tidal method we have been able to clarify the technique and make its application easier. In addition, we make one of the first applications to a real aquifer where we detail the entire process from the acquisition and filtering of head data to finally obtain the hydrodynamic parameters by numerical modeling. This allowed refining the conceptual model and observing the pronounced impact of aquitard on the propagation of inland tidal fluctuations.

In addition, we have investigated the chemical reactions that occur by the mixing between freshwater and saltwater. The results show that coastal aquifers are a fairly complex system with many chemical reactions. We observe the predominance of cationic exchange reactions, but also quite a few redox reactions using organic matter as electron donors and molecules such as dissolved oxygen, nitrates, iron, or manganese oxides as electron acceptors. We have observed that quite a few reactions associated with the rocks that form the reservoir also occur. But we go beyond identifying them, we present a method to quantify these reactions, which allows us to observe the spatial distribution of the reactions. Furthermore, by quantifying them, it is possible to estimate the chemical composition of the water that is discharged into the sea. As a result, nutrients discharge to the sea can be estimated through the quantification of their degradation.

Finally, we investigated the impact of an intense rain event over a coastal aquifer and its mixing zone. We acknowledge a freshwater displacement occurs in the direction of the sea caused by the aquifer recharge. But we also observed how the interface is pushed inland during the recovery. These unique conditions can have a significant impact on the annual nutrients balance released to the sea. In fact, by moving the interface, the chemical conditions are modified and a significant impact on the chemical reactions is observed.

Resumen

La calidad y la disponibilidad del agua dulce en las zonas costeras está afectada por la intrusión marina en los acuíferos costeros. Del mismo modo, la calidad de las aguas costeras y los ecosistemas costeros pueden ser afectados significativamente por la descarga de agua subterráneaal mar.

En esta tesis investigamos: (i) el uso de las fluctuaciones periódicas del nivel del mar (como las mareas) para caracterizar los parámetros hidrodinámicos de los acuíferos costeros; (ii) las reacciones químicas que ocurren en la zona de mezcla entre el agua dulce y el agua salada; y (iii) el impacto de las fluctuaciones temporales de alta frecuencia (por ejemplo las tormentas) sobre la zona de mezcla y las reacciones químicas que ocurren en el acuifero. Los metodos estudiados han sido aplicados y validados en el campo experimental de Argentona.

Consideramos el acoplamiento hidromecanico sobre la respuesta del acuifero a las fluctuaciones de las mareas. El método de las mareas se aplica por primera vez a un acuífero real donde detallamos todo el proceso desde la adquisición y el filtrado de datos a la obtención de los parámetros hidrodinámicos por modelación numérica. Esto permitió refinar el modelo conceptual y observar el impacto pronunciado de las capas poca permeables sobre la propagación de las fluctuaciones de mareas hacia tierra dentro.

Además, hemos investigado sobre las reacciones químicas que ocurren a lo largo de la mezcla entre el agua dulce y el agua salada. El estudio se realiza utilizando el analisis de mezcla acaplado a una herramienta de mezcla reactiva. Los resultados muestran que los acuíferos costeros son unos sistemas bastante complejos con muchas reacciones químicas. Observamos una preponderancia de las reacciones de intercambio catiónico, pero también bastantes reacciones redox usando la materia orgánica como donador de electrones y las moléculas tipo el oxígeno disueltos, los nitratos, los óxidos de hierro o de manganeso como aceptor de electrones. Hemos observado que también ocurren bastantes reacciones asociadas a las rocas que forman el reservorio. Pero vamos más allá de identificarlas, presentamos un método para cuantificar esas reacciones lo que nos permite observar la distribución espacial de las reacciones. Además, al cuantificarlas se puede

estimar la composición química del agua que se descarga al mar, y saber cuántos nutrientes se degradan por reacciones en el acuífero y cuantos llegaran al mar.

Por último, investigamos el impacto de un evento de lluvia intensa sobre un acuífero costero y su zona de mezcla. Reconocemos que ocurre un desplazamiento de agua dulce en la dirección del mar causado por la recarga del acuífero. Pero también observamos cómo se empuja la interfaz tierra adentro durante la fase de recuperación. Estas condiciones únicas pueden tener un impacto significativo en el balance anual de nutrientes que se liberan al mar. De hecho, al mover la interfaz, se modifican las condiciones químicas y se observa un impacto significativo en las reacciones químicas.

Resumé

La qualité de l'eau et sa disponibilité dans les zones côtières sont affectées par l'intrusion marine dans les aquifères côtiers. De même, la qualité des eaux côtières et les écosystèmes côtiers peuvent être considérablement affectés par les polluants rejetés dans la mer.

Les travaux de cette thèse étudient : (i) l'utilisation des fluctuations périodiques du niveau de la mer (par exemple les marées) pour caractériser les paramètres hydrodynamiques des aquifères côtiers ; (ii) les réactions chimiques qui se produisent dans la zone de mélange entre l'eau douce et l'eau salée; et (iii) l'impact des fluctuations temporelles de hautes fréquences (par exemple les tempêtes) sur la zone de mélange et les réactions chimiques. Par conséquent, le site expérimental d'Argentona nous a permis d'appliquer et de valider les méthodes étudiées.

De plus, nous faisons l'une des premières applications à un aquifère réel où nous détaillons l'ensemble du processus depuis l'acquisition et le filtrage des données jusqu'à l'obtention des paramètres hydrodynamiques par modélisation numérique. Cela a permis d'affiner le modèle conceptuel et d'observer l'impact prononcé des couches peu perméables sur la propagation du signal marées dans l'aquifère.

De plus, nous avons étudié les réactions chimiques qui se produisent au cours du mélange entre l'eau douce et l'eau salée. Les résultats montrent que les aquifères côtiers sont des systèmes assez complexes avec de nombreuses réactions chimiques. On observe une prépondérance des réactions d'échange cationique, mais aussi pas mal de réactions redox utilisant la matière organique comme donneur d'électrons et des molécules comme l'oxygène dissous, les nitrates, les oxydes de fer ou de manganèse comme accepteurs d'électrons. Nous avons également observé que de nombreuses réactions associées aux roches qui forment le réservoir se produisent. Mais nous allons au-delà de leur identification, nous présentons une méthode pour quantifier ces réactions, qui nous permet d'observer la distribution spatiale des réactions. De plus, en les quantifiant, il est possible d'estimer la composition chimique de l'eau rejetée dans la mer, et de savoir quelle quantité de nutriments est dégradée par les réactions chimiques dans l'aquifère et donc quelle quantité atteindra la mer.

Enfin, nous étudions l'impact d'un événement de fortes pluies sur un aquifère côtier et sa zone de mélange. Nous reconnaissons qu'un déplacement d'eau douce se produit en direction de la mer causée par la recharge de l'aquifère. Mais au cours de la décrue de la nappe, nous observons comment l'interface s'étend à l'intérieur des terres. Ces conditions uniques peuvent avoir un impact significatif sur le bilan annuel des nutriments rejetés dans la mer. En effet, en déplaçant l'interface, les conditions chimiques sont modifiées et un impact significatif sur les réactions chimiques est observé.

Table of Contents

List of Figures

List of Tables

1 Introduction

1.1 Context

Only 3% of the total water on Earth is available as freshwater resources (USGS). The Gravity Recovery and Climate Experiment (GRACE) satellite from NASA and the German Aerospace Center (DLR) identified the largest groundwater reserves around the globe (Richey et al., 2015). As shown in Figure 1-1, a large majority of these reserves are in contact with seawater. Groundwater is a threatened resource. The water deficit is estimated to be 40% in 2030 (Richard, 2015). It is attributed, on one hand, to climate changes inducing more important droughts, on the other hand, to the increase of groundwater contamination/pollution. Seawater can be one of the groundwater contamination. This contamination can be natural or anthropic.

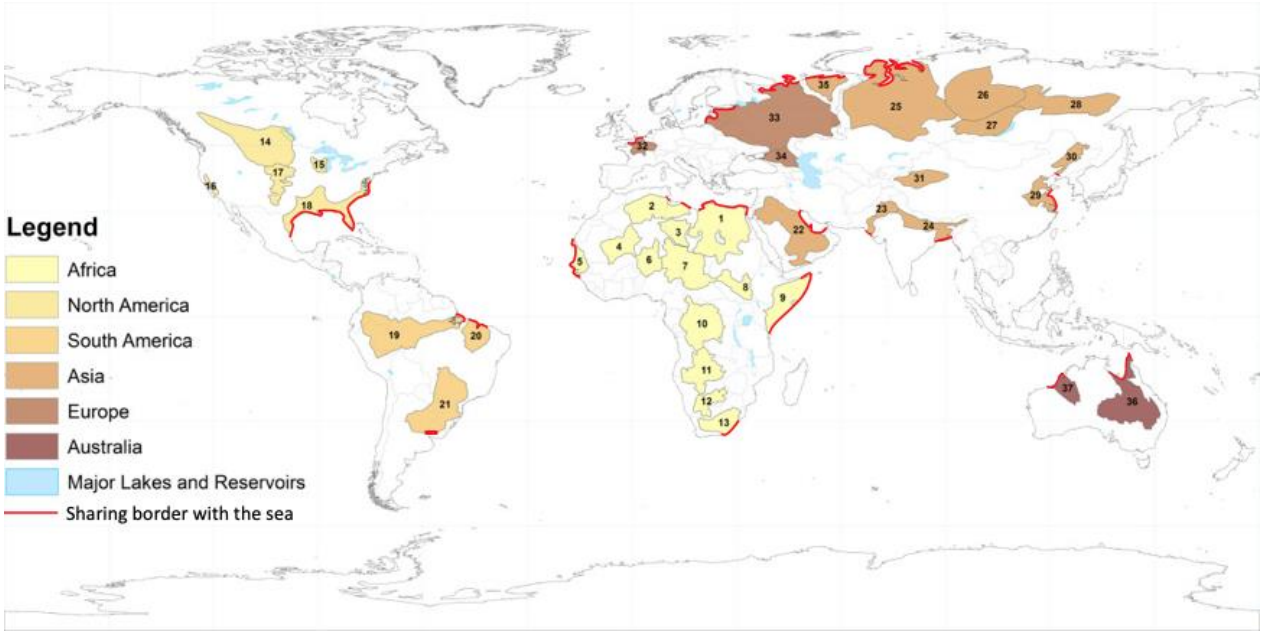

Figure 1-1: World's largest aquifer systems bordered by the sea. Modified from (Richey et al., 2015)

In general, fresh groundwater from coastal aquifers flows to the sea and seawater can enter into the aquifer depending on boundary conditions in the aquifer, whether induced by natural dynamics or by the (over)exploitation of groundwater. This is called the seawater intrusion phenomenon (**Figure 1-2**). The part of a coastal aquifer that is invaded by seawater is commonly known as the saltwater wedge. It is located between the base of the aquifer and a freshwater-saltwater interface (or mixing zone, MZ hereinafter). Usually, the seawater is below the freshwater due to density difference (1025 kg/m3 for seawater and around 1000 kg/m3 for freshwater). The appearance of a saltwater wedge, beyond a natural position of low penetration, is usually a consequence of the overexploitation of the aquifer.

The problem becomes even more complicated when it is viewed from the seaside. The quality of the discharged groundwater or recirculated seawater to the sea is critical for submarine coastal ecosystems. These ecosystems are tributaries of chemical elements, such as essential nutrients for their development, which are naturally poor in seawater. The Submarine Groundwater Discharge (SGD) phenomenon, which also occurs naturally, promotes them. But once again, overexploitation tends to reduce the SGD amounts and its composition is impacted by the activities that take place on the continent. The transport of (reactive) solutes, such as nutrients and pollutants, is important for many environmental processes.

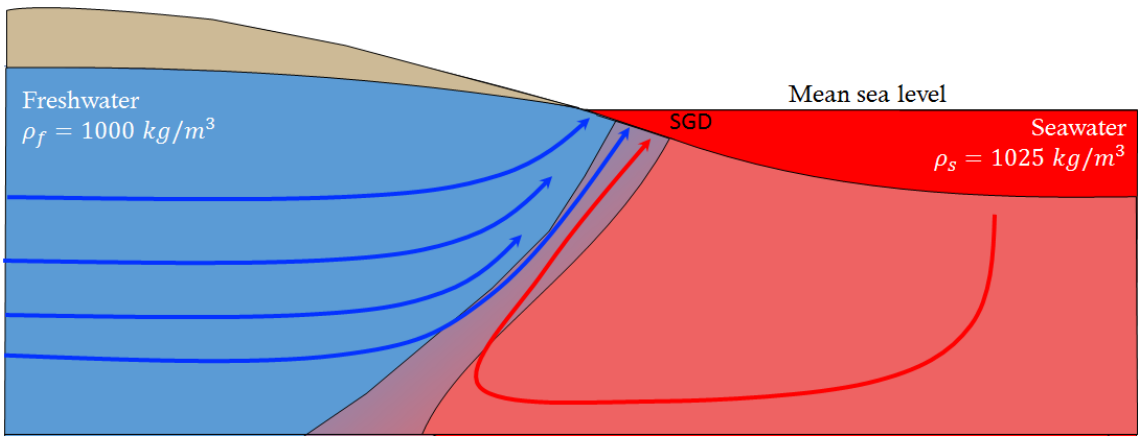

Figure 1-2: Scheme of seawater intrusion and submarine groundwater discharge processes in a coastal aquifer.

Given that two opposite and coupled major phenomena are occurring in coastal aquifers (SWI and SGD), characterizing them remains a challenge. Aquifer characterization has traditionally relied on geological and hydraulic methods, possibly

complemented with tracer tests. These traditional methods can be expensive and have some limitations. Moreover, some of these techniques are intrusive and sometimes damaging the aquifer, favoring the salinization process (e.g. repeated pumping). Non-invasive methods such as geophysical techniques have been revealed to be quite accurate for salinity monitoring (de Franco et al., 2009; Ogilvy et al., 2009; Sherif et al., 2006). Also, the monitoring of groundwater response to sea-level fluctuations can be considered as an aquifer scale hydraulic test. We know that the amplitude of head fluctuations declines exponentially and the phase shift increases linearly away from the coastline, depending on the hydraulic diffusivity of the aquifer (Carr & Van Der Kamp, 1969). Numerous analytical solutions have been developed for various conditions of connection to the sea (H. Li & Jiao, 2001b; Van Der Kamp, 1972). However, it is emerging that at least a portion of the response is largely hydromechanical (Guarracino et al., 2012; H. Li & Jiao, 2001a, 2002). Yet, these analytical solutions have not been tested in real aquifers. Therefore, aquifer hydraulic parameters determination is the first step before transport models. These last are used to predict SWI and SGD. Indeed, the mixing zone between freshwater and seawater is a place favoring chemical reactions.

A special interest is given to the transport of solutes in coastal aquifers. It is especially relevant because it allows answering the question of where to pump. This is because the intrusion of seawater into the aquifer is one of the main freshwater pollution concerns of coastal regions. The fresh-salt water interface is affected by transport processes with the density-dependent flow. Besides this, SGD is an important source of nutrients and other chemical compounds to the sea. However, SGD sampling remains a challenge and one cannot estimate the discharging water considering only the groundwater composition since several biogeochemical reactions occur in the mixing zone. Reactions occur as a consequence of the interaction between terrestrially-derived groundwater, recirculated seawater, and the geological matrix (Moore, 1999). As a result, these areas are key hotspots that control the discharge of nutrients and other chemical compounds into the sea, a key factor for many coastal ecosystems. Unfortunately, solute transport is complex, because it is very sensitive to the natural heterogeneity of the geological media. In the case of coastal aquifers, it is also sensitive to temporal fluctuations such as recharge, droughts, tides, and wind-driven fluctuations of the sea level. Yet, understanding transport is essential to understand the fate of reacting solutes. One might argue that understanding the biochemical system is sufficient to understand

reactions. This may be true in well-mixed (batch) systems. It is not in aquifers, where mixing is extremely slow and never complete.

1.2 Objectives

This thesis is part of the second stage of the national project Mixing and dispersion in the transport of energy and solutes (MEDISTREAS) mainly managed by the Barcelona Hydrogeology Group (GHS) formed by the Institute of Environmental Assessment and Water Research (IDAEA) of the Spanish National Research Council (CSIC) and the Polytechnic University of Catalonia (UPC). This project follows MEDISTRAES 1 whose objectives were the construction of the Argentona experimental site to study seawater intrusion and the submarine groundwater discharge in an alluvial aquifer. A full description and characterization of the aquifer, based on the four pillars of hydrogeology: geology, geophysics, hydraulics, and hydrochemistry have been developed during the first stage of these projects (Martínez-Pérez et al., in press a). The main conclusion of this first project part is that geology is more complicated than expected. A low permeability layer (i.e. silts) was identified during this first phase of the project at around 12 m, maybe limiting intrusion, discharge, or mixing effect. Moreover, it appears that many chemical reactions take place in the identified mixing zone located between 14 m and 16 m.

So, the aim of this thesis is to understand the effect of complex geology, over the hydraulic response to the sea-level fluctuations and its impact on the mixing processes within the aquifer. The Argentona coastal aquifer was used to illustrate the methods we investigated to contribute to the understanding and characterization of coastal aquifers.

1.3 Thesis outlines

This thesis is divided into 6 chapters in which all the chapters are written in such a way that they can be read separately. Those chapters are organized as scientific papers that are in preparation for submission to international journals. For this reason, the description of the Argentona experimental site may seem repetitive to the reader. The thesis proceeds as follows:

Chapter 2 focuses on the tidal method. Yet few studies apply the tidal method to real aquifers. The questions addressed in this chapter are: (1) How to treat the phreatic surface of the unconfined aquifers; (2) When the mechanical effect must be taken into

account; and (3) What happens when the aquifer system has a complex geometry. To this end, numerical simulations have been performed taking into account different aquifer geometry, the phreatic surface and the mechanical effect generated by the load/unload over the sea bottom.

Chapter 3 presents the application to a real case of the tidal method from the data acquisition to the hydraulic parameter determination. Moreover, a detailed data filtering procedure is presented in order to separate the tidal signal from head fluctuations. In this chapter, we take into account the recommendations made in Chapter 2. The application is illustrated, using Argentona experimental site as an example.

Chapter 4 proposes a coupled form of the End-Member Mixing Analysis (EMMA), the calculation of the mixing ratios (MIX), and the quantification of chemical reactions. We denote it as "EMMA-reactive". Yet the mixing between freshwater and seawater is described as highly reactive (chemically) but the chemical reactions have not been quantified. Furthermore, the direct sampling of submarine groundwater discharge remains a challenge. Thus, we propose a methodology able to identify the chemical processes occurring in the mixing zone and quantify them. In this work, we aim at finding an estimation of SGD composition.

Chapter 5 presents the monitoring of the mixing zone response and its impact on geochemical processes during a fast freshwater inflow event. In this work, different techniques from geophysics and hydrogeology were applied. Also, the EMMA-reactive (presented in Chapter 4) is applied to evaluate the effect of the mixing zone dynamic over chemical reactions.

Chapter 6 summarizes the general conclusions and perspectives of the thesis.

In **Appendix** the ongoing work and other works enrollment can be found.

2

Hydromechanical characterization of tide-induced head fluctuations in coastal aquifers: the role of delayed yield and minor permeable layers

2.1 Abstract

Tidal analysis is an aquifer scale method and a low-cost alternative to pumping tests for determining aquifer hydraulic parameters without groundwater extraction. Aquifer head fluctuations in response to tidal fluctuations can be analyzed using many analytical solutions. Yet, they are rarely applied in the field. Besides this, most analytical solutions are based on a conceptual model that usually consists of an unconfined aquifer and a confined aquifer separated by an aquitard, where hydraulic head fluctuations in the unconfined aquifer part are commonly neglected. Additionally, the confined aquifer short response time to sea-level fluctuations cannot rely on the hydraulic connection of the confined aquifer through the aquitard. As a consequence, the application of the analytical solutions to real cases leads to an overestimation of the hydraulic diffusivity. In this study, we investigate through different numerical simulations the fluctuations of the phreatic surface by considering the delayed yield. Numerical results demonstrate that the mechanical effect generated by the load over the bottom of the sea due to sea-level fluctuations is a key factor when determining hydraulic aquifer parameters. We also demonstrate that for multilayer systems head fluctuations in the different aquifer layers can create interferences and consequently higher attenuation of the tidal signal leading to overestimating the inferred hydraulic diffusivity. Our results provide guidance on how to properly reproduce tidal responses in coastal aquifers.

2.2 Introduction

As global population soars, economic activities cause significant demand of freshwater resources and coastal aquifers overpumping worldwide, which leads to seawater intrusion (SWI) with major social and economic consequences. Controlling SWI requires detailed characterization of the aquifer and its connection to the sea, which is challenging and costly. Therefore, in coastal areas, accurate aquifer characterization is essential to design sustainable management schemes and to control or limit the propagation of the seawater wedge (Werner et al., 2013). The tidal method is a low-cost option for large-scale aquifer characterization.

Tidal tests consist of analyzing the aquifer response to sea-level fluctuations. Tides have been studied by humanity for centuries. They are generated by the movement of celestial bodies around the Earth, with the Moon as the most important element, causing the rise and fall of sea level. Sea level (h_s) fluctuations can be approximated as a sum of harmonics. The response of a linear system to a harmonic stress will also be a harmonic. Therefore, the aquifer response to every harmonic component of tides will be described by (1) the amplitude damping (A/A_0, ratio of the amplitude observed in the well (A) to the sea level fluctuation amplitude (A_0)); and (2) the time-shift (t_s).

Jacob (1950) and Ferris (1952) (JF hereinafter) computed analytically the aquifer response to a harmonic fluctuation of the sea-level by considering a homogeneous, isotropic, and confined aquifer with an infinite inland extent and a vertically connection with the sea at the coastline. They prescribed head at the coast ($x = 0$) as a harmonic function with a tidal amplitude (A_0, $[L]$) and a tidal period ($\tau = 2\pi/\omega$, $[T]$, where ω $[T^{-1}]$ is the frequency). They found that the response in a well located at a distance x $[L]$ from the coastline is $h\,(x,t) = A_0 e^{-x/L_c}\sin(\omega t + x/L_c)$, where the characteristic length is $L_c = \sqrt{T\tau/\pi S}$ (**Figure 1-1**). That is, the tidal amplitude decreases exponentially with distance whereas the time-shift increases linearly in the aquifer. Therefore, we can obtain L_c from either from the dampening of the amplitude ($ln(A/A_0) = x/L_c$) or the time-shift ($t_s = \omega\, x/L_c$). Knowing L_c, one can obtain $D_h = T/S$ as:

$$D_{h_A} = -\frac{x^2\,\pi}{\tau\left(ln\left(A/A_0\right)\right)^2} \tag{2-1}$$

$$D_{h_S} = \frac{x^2\,\tau}{4\pi\,t_s^2} \tag{2-2}$$

where D_{h_A} is the hydraulic diffusivity obtained from the amplitude dampening and D_{h_S} is the one obtained from the time-shift. The simplicity of the method (set sensors in coastal wells and the sea to monitor fluctuations) makes it very appealing. A key issue in coastal aquifer management is where to pump and how much can be pumped. Tidal tests yield aquifer hydraulic diffusivity (D_h), which is a good indicator of connectivity (Knudby & Carrera, 2006). Slooten et al. (2010) showed that tidal response inland is most sensitive to hydraulic conductivity near the shore. Therefore, by performing this analysis at many observation wells, one can infer which areas are well connected to the sea (i.e., those with high diffusivity). In fact, tidal response data coupled with pump test have been used to derive spatially varying maps of transmissivity (Alcolea et al., 2007; Alcolea et al., 2009). This is relevant in coastal aquifers because it is needed to avoid pumping in boreholes well connected to the sea. Ideally, D_{h_A} and D_{h_S}should be identical. In practice, they are not, which may explain why it has been applied on few occasions (Jiao & Tang, 1999; K.-F. Liu, 1996; Nielsen, 1990; Van Der Kamp, 1972; P. Zhou et al., 2016).

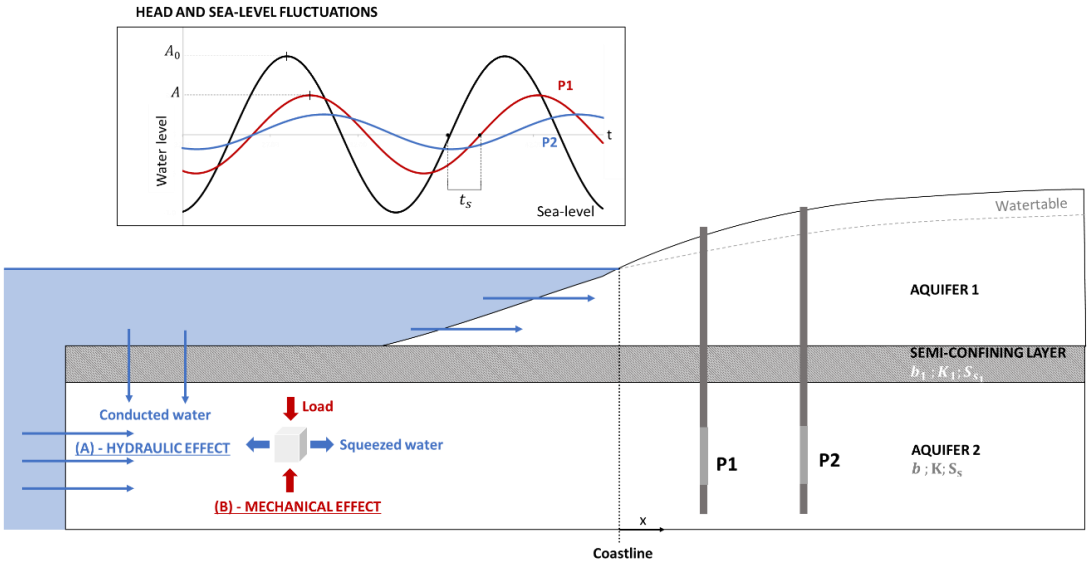

Figure 2-1: Factors affecting coastal aquifers level in response to seawater level fluctuations. The aquifer response is damped ($A < A_0$) and shifted (t_s) with respect to sea level. Hydraulic effect (Blue thin arrows) and Mechanical effect (thick arrows)

The disparity between JF's predictions and observations suggests that their assumptions may not be appropriate. This has prompted the derivation of numerous analytical solutions for more complex and realistic aquifer configurations such as confined aquifers connected to the sea (Guo et al., 2010; Guomin & Chongxi, 1991; Van Der Kamp, 1972), coastal leaky confined aquifers (Chuang & Yeh, 2008; Jeng et al., 2002; Jiao & Tang, 1999; H. Li & Jiao, 2001b, 2002) coastal aquifers with sloping beaches (H. Li et al., 2008; Teo et al., 2003) and leaky confined aquifers that extend below the sea with an effect of the elastic storage or mechanical effect over the aquitard (Geng et al., 2009; G. Li et al., 2008; H. Li & Jiao, 2001a, 2003a, 2003b; H. Li et al., 2007). These latter solutions are integrated and generalized by Guarracino et al. (2012) (ME hereinafter). Mechanical effects add a further complication to the interpretation of the aquifer response to sea-level fluctuations. A rise in sea level can be viewed as an increase in the load exerted by the sea on the seafloor. According to Terzaghi's (Terzaghi, 1954) theory, this load is initially absorbed by the water as an increase in water pressure. The overpressure is slowly dissipated as water flows away (inland in coastal aquifers) and the load is taken up by the solid skeleton (increase in effective stress), whose porosity is reduced. Acknowledging the mechanical effect has led to a large number of analytical solutions.

The essential feature of these solutions is that (1) the amplitude at the coast is about one half of that in the sea (Van Der Kamp, 1972) and (2) the time shift can be significantly proportional to the time derivative of the sea level, which is largest one quarter of the period before the harmonic maximum (Guarracino et al., 2012; G. Li et al., 2008). Accounting for the mechanical effect is not particularly difficult, but it represents an additional complication. Therefore, it is natural to wonder under which conditions should this effect be accounted for.

Another feature of equations (1) and (2) is that large damping and time-shift should be observed in unconfined aquifers where D_h is small (large storage coefficient, S [-]). However, significant head responses to tides have been observed several kilometers inland in shallow unconfined coastal aquifers, such as in Spain (Llobregat delta, internal communication), in Hong Kong (Jiao & Li, 2004; Merritt, 2004). We attribute these observations to the slow mobilization of the storage. The storage coefficient of unconfined aquifers consists of two components: an elastic component associated with

compression of the aquifer ($S_s b$) and a specific yield (S_y) component associated with pore dewatering. Meinzer (1932) himself pointed "appreciable drainage may occur during a period of several weeks", while discussing of field estimation of S_y (see Dietrich et al. (2018) and Lv et al. (2021)). But the issue was not formalized until it became necessary for the interpretation of pumping wells, when it was labeled "delayed yield" (Boulton, 1954, 1963; Bouwer & Rice, 1978; Neuman, 1972). Delayed yield implies only a fraction of the full storage coefficient (small S) is actually mobilized during a tide period so that the unconfined aquifer reacts as if D_h was larger than in reality. Yet, none of the solutions described above acknowledge delayed yield in tidal response, which we conjecture may be important.

In light of the above considerations, the first relevant question when using the tidal method is how to treat the phreatic surface of the unconfined aquifers. A complementary key question is when the mechanical effect must be taken into account. The study is aimed at addressing these questions to give quantitative guidance on the relation tide-aquifer-head and aquifer characterization in coastal aquifers. To this end, we perform numerical simulations considering the hydro-mechanical effect generated by tidal fluctuations. Our results give new insight into the tidal method and contribute to its application in complex coastal systems.

2.3 Methods

2.3.1 Tidal method generalities

2.3.1.1 Governing equations

Sea level fluctuations cause heads to fluctuate in coastal aquifers hydraulically connected to the sea (**Figure 2-1A**). Also, aquifer head respond to the loading effect of sea level fluctuations on the seafloor. According to Terzaghi's (Terzaghi, 1954) theory, an increase in loading is initially reflected as an increase in water pressure, and rapidly dissipated as water flows away (water is squeezed, **Figure 2-1B**). The mechanical effect can be included in the flow equation as a sink/source term (f) proportional to the time derivative of the total stress (Bear, 1972). For tidal fluctuations, the induced mechanical

effect is represented by a sink/source term proportional to the seawater level (h_s). In this case, fluid mass conservation is given by:

$$S_s \frac{\partial h}{\partial t} = \nabla(\mathrm{K}\,\nabla\,\mathrm{h}) + f \tag{2-3}$$

$$f = S_s L_e \frac{dh_s}{dt} \tag{2-4}$$

where S_s is specific storage [L^{-1}]; h is aquifer head [L] and the source/sink term f only on the offshore part ($x > 0$, $f = 0$), L_e [-] the tidal loading efficiency defined by (Van der Kamp & Gale, 1983) to describe the formation pressure change caused by a distributed change of pressure at the bottom of the sea (Eq.5), defined by:

$$L_e = \frac{\alpha}{\alpha + \phi\beta} \tag{2-5}$$

where α is the (oedometric) compressibility of the aquifer skeleton, β is the compressibility of the pore water in the confined aquifer and ϕ porosity [-]. Since coastal sediments are usually young, they are a lot more compressible than water (i.e. $\alpha \gg \beta$). Therefore, we will assume $L_e = 1$ (see G. Li et al. (2008) and H. Li et al. (2007) for a collection of values). Following Guarracino et al. (2012) analytical solution, the tidal signal observed in the confined aquifer (h) can be expressed as the sum of three different components: (i) h_h the direct hydraulic connection where the aquifer opens the sea (horizontal blue arrows at the left of **Figure 2-1**), (ii) $h_{h1}$the hydraulic component caused by the indirect connection through the aquitard (vertical blue arrows in **Figure 2-1**), and (iii) h_m the mechanical component induced by tidal loading (the red arrows in **Figure 2-1** compress the aquifer and squeeze water away, thick blue arrows). Guarracino et al. (2012) analyze them in detail. The three components are illustrated in **Figure 2-2** for a specific case considering an aquitard with the following parameters: aquitard thickness (b_1) of 5 m, hydraulic conductivity (K_1) of 0.01 m/d, and a specific storage (S_{s_1}) of $5 \cdot 10^{-4}$ 1/m and a confined aquifer with the following parameters: aquifer thickness (b) of 18 m, hydraulic conductivity (K) of 10 m/d and specific storage (S_s) of $5 \cdot 10^{-5}$ 1/m at the coastline (x = 0 m). Note that, for this example, h_m displays the most resemblance to h whereas the leakage through the aquitard (h_{h1}) is small. However, real-world applications

of the Guarracino et al. (2012) analytical solution remains complex and non-trivial. Therefore, to simplify the procedure, in this study we use the principle of superposition over numerical simulations and consider only two hydraulic components of the head response: (1) the hydraulic component (considering $h_h$and h_{h1} together) and (2) the mechanical contribution. To this end, we adopt a flow model (described in section 2.2) which includes periodic elastic compressions and expansions of the aquitard and the confined aquifer, similar to that of Guarracino et al. (2012) (**Figure 2-3**).

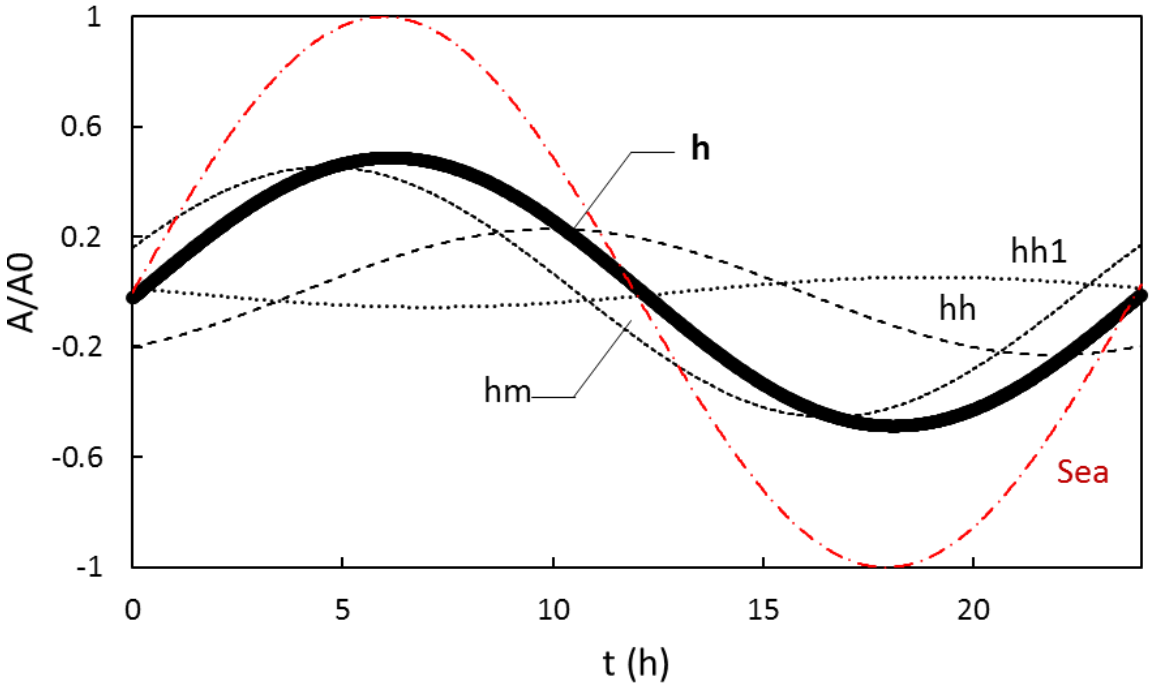

Figure 2-2: The aquifer response (h, thick black line) to sea tides (red dashed line) consists of the superposition of (1) h_h hydraulic connection at the open offshore boundary; (2) h_{h1} hydraulic connection across the aquitard; and (3) h_m hydro-mechanical response. Note that h_m reaches its maximum before sea level.

2.3.1.2 Phreatic surface and delayed yield

The phreatic surface boundary condition (**Figure 2-3**) is described by the following equation:

$$S_y \frac{\partial h}{\partial t}\Big|_{z=h} = -K_z \frac{\partial h}{\partial z} \tag{2-6}$$

Generally neglected in analytical solutions, the unconfined aquifer phreatic surface also fluctuates with tides even far from the coast just like a confined aquifer. This

kind of observation has been largely documented for hydraulic tests (Batu, 1998; Boulton, 1954, 1963; Neuman, 1972). It explains the delayed watertable response of unconfined aquifers during a pumping test. Three drawdown phases are observed: (1) Drawdown similar to a confined aquifer (Theis curve with small S) explained by wellbore and the elastic storage, then (2) it reaches a pseudo steady-state (Hantush like) and finally (3) water table decline again (Theis curve with large S). From (3) the specific yield (S_y) can be derived after a long pumping test. In the case of tidal oscillations, phase (1) is observed because it represents instantaneous mobilization of storage, but whether phases (2) and (3) are mobilized depends on the tide period relative to the time it takes to mobilize the delayed yield. The net result is that the unconfined aquifer acts like a semi-confined. So, if not all the part of the storage is mobilized instantaneously, Eq. 2-6 becomes Eq. 2-7.

$$\begin{cases} S_{y0}\dfrac{\partial h}{\partial t} + \displaystyle\sum_{L=1}^{N} S_{y_i}\frac{\partial h_i}{\partial t} = -K_z\frac{\partial h}{\partial z} & \text{(2-7a)} \\ S_{y_i}\dfrac{dh_i}{dt} = C_i(h - h_i) & \text{(2-7b)} \end{cases}$$

where S_{y0} is the instantaneous specific yield and the immobile (or slowly yield) zones are characterized by their specific yield (S_{y_i}) and conductance (C_i). Their characteristic time is $1/\alpha_i$ with $\alpha_i = C_i/S_{yi}$. To simplify the analysis, we neglect S_{y0} and consider N=1 so that $S_y = \sum_{i=0}^{N} S_{yi}$ (Boulton, 1963). We solve the system of equation 2-7 assuming $h = A_0 \sin \omega t$. Then, equation 2-7b reads:

$$\frac{dh_f}{dt} = \alpha A_x \sin \omega t - \alpha h_f \quad \text{(2-8)}$$

It is easy to check that the long-term, solution to this equation is:

$$h_f = \mathrm{A_{Sy}} \sin(\omega t - \varphi_{Sy}) \quad \text{(2-9)}$$

where $\mathrm{A_{Sy}} = A_x(\alpha/\sqrt{\alpha^2+\omega^2})$, $\varphi_{Sy} = \cos^{-1}(\alpha/\sqrt{\alpha^2+\omega^2}) = \sin^{-1}(\omega/\sqrt{\alpha^2+\omega^2})$. This solution points out that h_f behaves, both in terms of dampening and time-shift, as if the fraction of specific yield actually mobilized is $\alpha/\sqrt{\alpha^2+\omega^2}$. If $\alpha \gg \omega$ (i.e. fast response), then, $\varphi_{Sy} \approx 0$, $A_{Sy} = A_x$, and the full specific yield is mobilized (i.e., the aquifer behaves as if it was unconfined). The opposite occurs if $\alpha \ll \omega$, then $A_{Sy} \approx 0$,

the aquifer behave as if it was confined. Finally, if $\alpha \sim \omega$, the aquifer behaves as if it had an intermediate storage coefficient:

$$S_{Dy} = S_0 + S_y \frac{\alpha}{\sqrt{\alpha^2 + \omega^2}} \quad (2\text{-}10)$$

Another, simple approximation to the delayed yield effect can be obtained by observing that, Eq.2-3 and 2-4 with BC's (Eq.2-7) is a linear system subject to a harmonic fluctuation forcing term. Therefore, any output will also be a harmonic fluctuation with a damped amplitude and a time-shift. To generalize Ferris solution ($h\,(x,t) = A_0 e^{-x/L_c} \sin(\omega t + x/L_c)$) we need to acknowledge that both the amplitude and the time-shift will damp, depending on x. We have fitted S to reproduce the additional damping, and found that a solution can be obtained by adopting

$$S_{Dy} = S_s \cdot b + S_y (1 - e^{-\frac{a\tau}{t_{c_z}}}) \quad (2\text{-}11)$$

where b is the aquifer thickness [L], $t_{c_z} = 1/\alpha$, is the vertical characteristic time and a = 0.25, obtained from sensitivity analysis.

2.3.2 Numerical methodology

In this section, the numerical methodology is presented. Several sets of simulations were carried out to properly define aquifer characterization in coastal aquifers from the tidal method. First, we consider a fully homogeneous confined aquifer similar to the JF conceptual model. Additionally, more complex geometries have been considered in order to (i) simulate properly delayed yield effects and (ii) include layered configurations commonly found in sedimentary systems.

2.3.2.1 Numerical model setup

An idealized coastal aquifer represented by a 2D vertical section extended 750 m offshore and 250 m onshore is considered in this study. The model domain was discretized into 15.643 triangular elements, refined near the coast and the aquitard portions. We simulate constant density water flow because density variations do not affect fluctuations. Ataie-Ashtiani et al. (2001) and Slooten et al. (2010) showed that tidal response inland is most sensitive to hydraulic conductivity near the shore. The following boundary conditions were adopted (**Figure 2-3**). A Cauchy-type boundary condition was imposed at the inland boundary (considered infinite in the analytical solution) in order to minimize

boundary effects. Thus, the inflow/outflow, $Q = \alpha\ (h - H_{ext})\ [L^3.T^{-1}]$, depends on the difference between the calculated head ($h, [L]$) and the reference imposed head at the boundary ($H_{ext}, [L]$), and the leakage coefficient ($\alpha, [\mathrm{L}^2/\mathrm{T}]$). Two different boundaries represent the seaward boundary where the tidal fluctuation of the sea level is assumed to be sinusoidal and simulated with a Dirichlet boundary condition $h_S(t) = A_0 \sin(\omega t)$, with A_0 the amplitude and ω the tidal angular velocity $[T^{-1}]$. In the submerged portion, the mechanical effect was applied through the source and sink terms included as a recharge (f term in Eq.3). Models were run imposing tidal oscillations until the dynamic quasi-steady-state was reached.

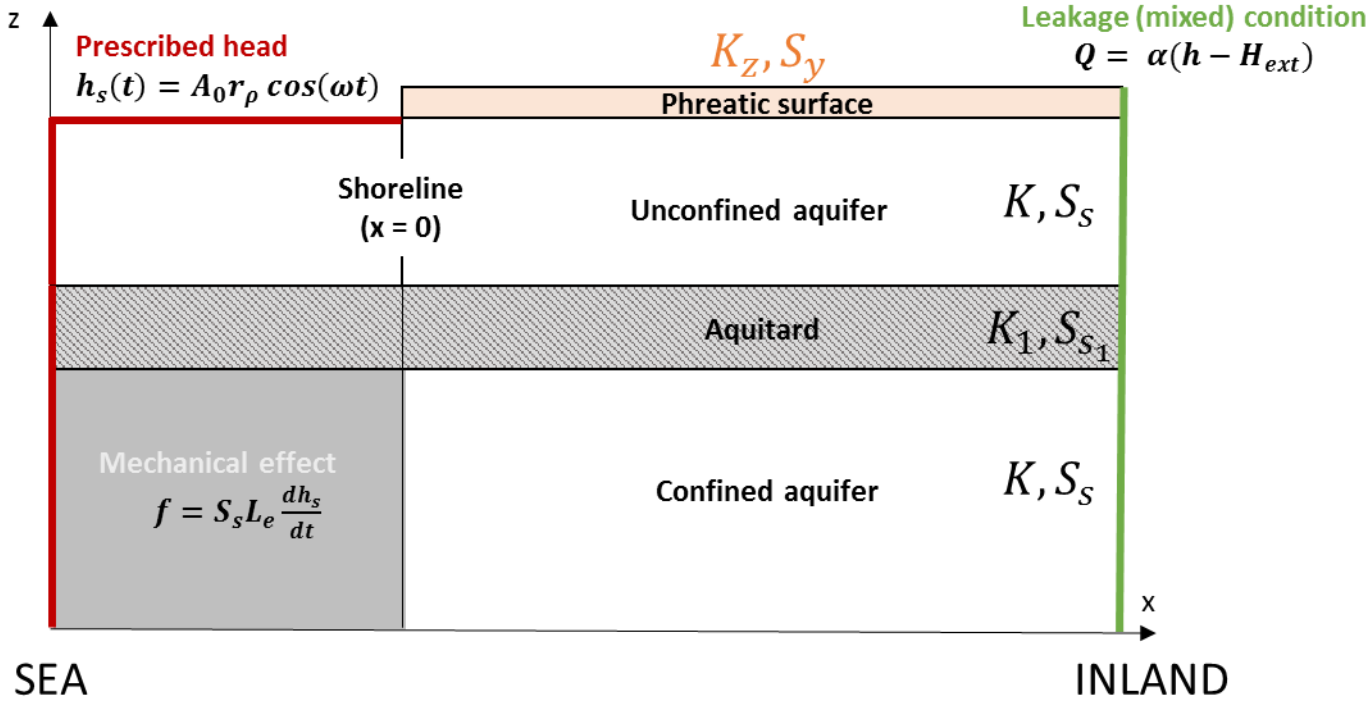

Figure 2-3: Conceptual model modified from Guarracino et al. (2012) indicating the boundary conditions applied for numerical simulations. Prescribed head is indicated by the red line, the gray rectangle indicates the mechanical boundary condition, the orange rectangle indicates the phreatic surface boundary condition, the inland boundary condition appears in green.

Table.1 summarizes the parameters used for all numerical simulations. In the following, we describe the different configurations considered.

Table 2-1: Parameters used in the base case simulation

Parameter	Value	Description
L_x (m)	1000	Domain x length
L_z (m)	35	Domain z thickness
A_0 (m)	1	Tidal amplitude
τ (h)	23.9	Tidal period
K (m/d)	10	Aquifer permeability or hydraulic conductivity
S_s (1/m)	5e-5	Aquifer specific storage
K_1 (m/d)	0.01	Aquitard permeability
S_{s1} (1/m)		Aquitard specific storage
H_{ext} (m)	0	Reference external head
α (m^2/d)	0.1	Leakage coefficient inland
D (m)	250	Offshore aquifer extension

2.3.2.2 Phreatic surface

To define the proper treatment of the phreatic aquifer, we analyze different approaches with three configurations: (a) a confined aquifer (**Figure 2-4a**) (Base case), (b) an unconfined aquifer with a free surface (**Figure 2-4b**) and (c) an aquifer with delayed yield (**Figure 2-4c**). The confined aquifer (a) is simulated by setting a no-flow boundary condition at the top of the aquifer. For cases b and c we adopt the approach of Carrera and Neuman (1986), which requires a geometry modification in the inland part of the model including two thin layers at the top with a thickness of 1 m each. In the additional layers the permeability is assumed to be anisotropic ($K_x << K_z$), such that the main component of the flow is vertical. If the hydraulic conductivity of these layers is high, the aquifer behaves as unconfined. Otherwise yield is delayed with $t_{cz} = S_y L_z / K_z$, where L_z = 2 m.

Hydraulic parameters applied to the unconfined (b) and delayed yield (c) cases are presented in **Figure 2-4**. We considered five values for the vertical permeability (K_z) to study the sensitivity of the delayed yield boundary condition directly affecting its characteristic time (t_{c_z}). The following t_{c_z} are tested: 0.1, 1, 10, and 100 days.

2.3.2.3 Aquifers-Aquitard system

A configuration of the aquifers-aquitard system is considered by including one aquitard (b_1= 5 m) between an upper unconfined aquifer (AQ1) and a lower confined aquifer (AQ2) (such as the conceptual models presented in **Figure 2-4 d** to **f**). This conceptual model is similar to the one presented by Guarracino et al. (2012). This aquifer configuration is considered to (i) assess the impact of the AQ1 delayed yield boundary on the AQ2 located below the aquitard and (ii) examine the effectiveness of the mechanical component in AQ2 produced by the loading and unloading over the aquitard. To this end, the aquitard was extended towards the offshore part. Furthermore, the simulation with the phreatic surface as delayed yield (**Figure 2-4**-f) was duplicated without including the mechanical boundary condition by removing the recharge term applied offshore.

2.3.2.4 Multi-Aquifer system

Finally, more realistic simulations are considered with three or more aquifer units separated by semi-permeable layers (**Figure 2-4 g** to **i**). Multilayered aquifers are commonly observed in coastal aquifers due to sequential sedimentation. For these simulations, a vertical permeability of K_z = 0.01 m/d is adopted for the delayed yield boundary, so that the equivalent t_{c_z} is 10 days.

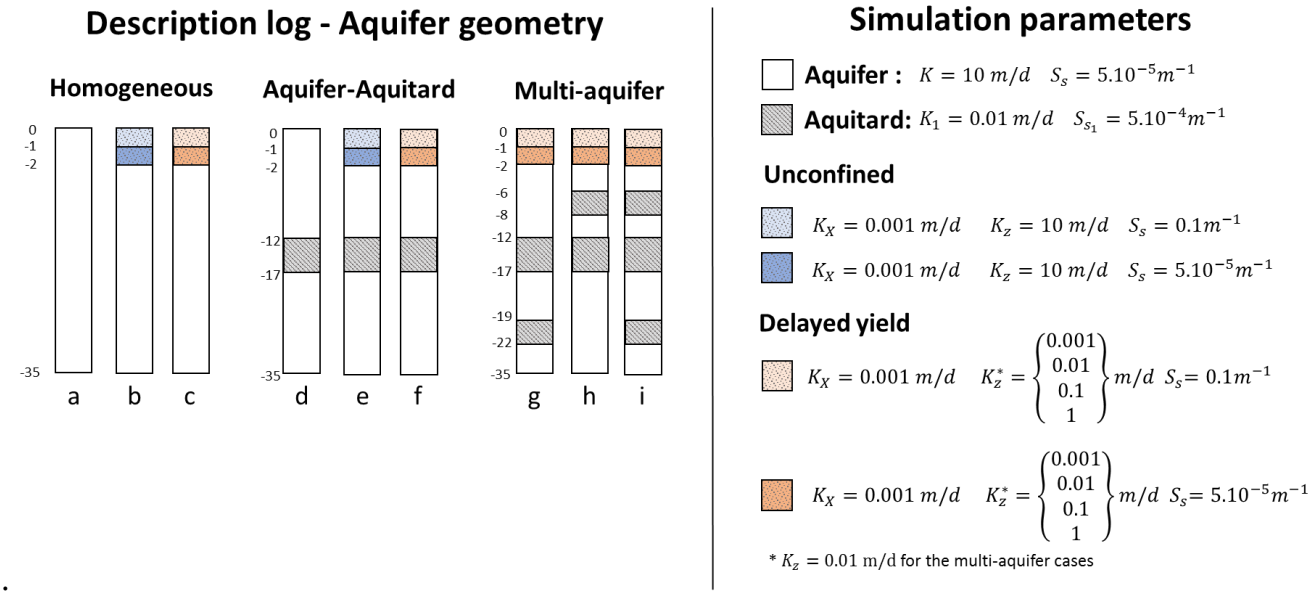

Figure 2-4: Simulations conceptual models (presented in the form of geological logs in inland aquifer part) and simulation parameters, Homogeneous: (a) confined (Base case), (b) unconfined, (c) delayed yield; Aquifers-aquitard system: (d) confined, (e) unconfined, (f) delayed yield; Multi-aquifer system: (g) 2 aquitards with a large unconfined aquifer, (h) 2 aquitards with a large confined aquifer, (i) 3 aquitards

2.4 Results and discussion

2.4.1 Homogeneous aquifer: the role of delayed yield

Figure 2-5 displays the hydraulic diffusivity one would obtain when using amplitude damping (D_{h_A}, Eq. 2-1) or time shift (D_{h_S}, Eq. 2-2). An immediate observation is that aquifer heads are somewhat damped and shifted, even close to the shore due to the depth of the observation point. To illustrate this point, we show in **Figure 2-6** the velocities computed at the tidal maximum for a confined, an unconfined and a delayed yield. Velocities only become horizontal (i.e., according to Dupuit's approximation) in the confined case. In order to address this vertical component of water flux, we substitute x in equations 2-1 and 2-2 by $x_{corr} = \sqrt{x^2 + z^2}$. Note that this correction helps somewhat near the shore, but become irrelevant when it is much larger than z .

The estimated hydraulic diffusivities for the confined case are similar to the true ones (see D_h conf. in **Figure 2-5**), with a small shift in amplitude and in time at the deep observation well. The additional energy dissipation caused by the vertical water flux

causes the estimated D_h to be slightly smaller than the true one. These results confirm those of Todd (1980) and Erskine (1991).

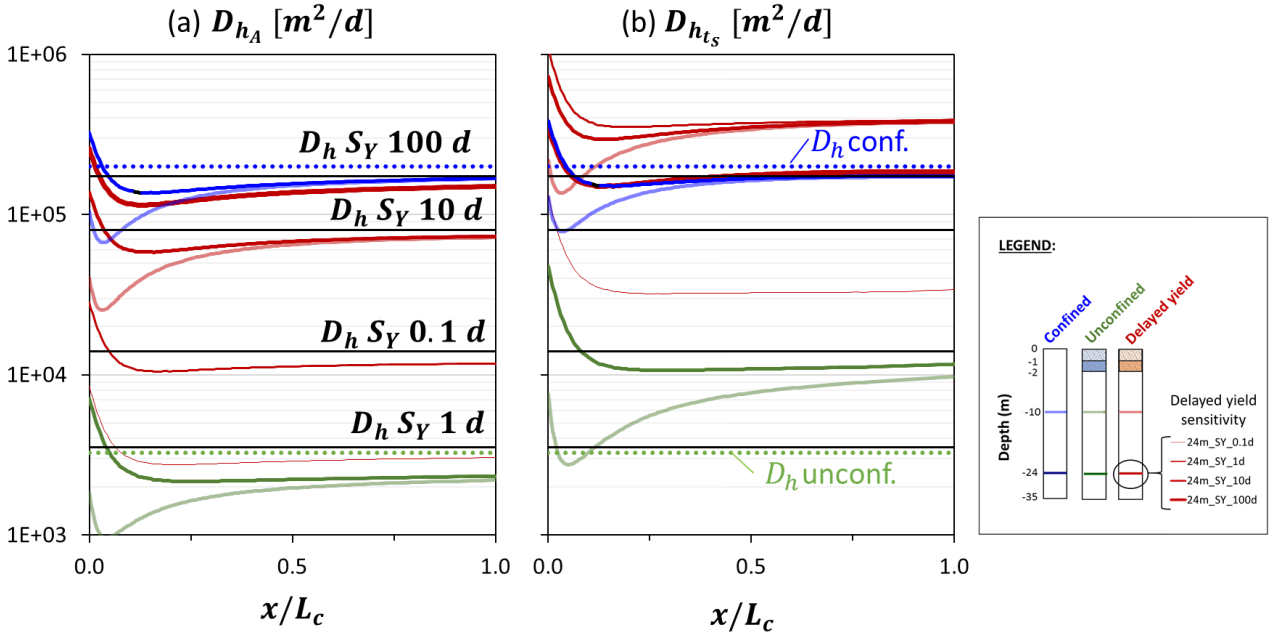

Figure 2-5: Estimated hydraulic diffusivity for a homogeneous aquifer with a confined (blue lines), unconfined (green lines) or a delayed yield (red lines) phreatic surface. (a) Hydraulic diffusivity estimated from amplitude dampening (D_{h_A}). (b) Hydraulic diffusivity estimated from the time-shift ($D_{h_{t_s}}$). They are presented versus dimensionless distance from the coast (x/L_c). The ideal hydraulic diffusivity for a confined aquifer (D_h conf.) is indicated by a blue dotted line and for an unconfined aquifer by a green dotted line (D_h conf.). Light colors represent observations at z = -10 m and dark colors at z = -24 m. Sensitivity of the delayed yield is presented in dark red lines with an increasing line thickness with the t_{c_z} tested values (0.1, 1, 10 and 100 days).

The two other cases (unconfined and delayed yield) are more shifted with respect to D_h conf. in **Figure 2-5**. This shift appears before the coastline. The tidal signal in the unconfined case is rapidly damped. The resulting hydraulic diffusivities are very low. This supports the non-consideration of the unconfined aquifer stated by Jiao and Tang (1999) and G. Li et al. (2008). On the other hand, these results support our conjecture that acknowledging delayed yield is critical to reproduce tidal fluctuations in unconfined aquifers. These results also explain why a tidal response has been observed far inland in unconfined aquifers.

When the delayed yield is included (**Figure 2-5**, $t_{c_z} = 10\ days$), such that the amplitude dampening is lower than in the unconfined case (**Figure 2-5a**), hydraulic diffusivity obtained from the amplitude dampening is similar to the confined case. In terms of time-shift (t_s), delayed yield seems to accelerate the signal propagation, despite traditionally a lower amplitude is reflected by a higher t_s. In fact, including the delayed yield leads to smaller time-shift results compared to the confined case leading to D_h values higher than D_h conf. (**Figure 2-5-b**). This result highlights the lower accuracy of the time-shift with respect to the amplitude.

By increasing the delayed yield vertical characteristic time (t_{c_z}), D_{h_A} and $D_{h_{ts}}$ are closer to D_h conf. and similar to D_h obtained from the confined case. When a small t_{c_z} is applied, the phreatic surface presents an unconfined behavior.

Most analytical solutions neglect changes in the vertical dimension. However, the analysis of head responses at two different depths (z= -10 m and -24 m) shows some vertical differences in the 3 cases. Thus, strong vertical differences in the unconfined case are observed, even at distance from the coast (**Figure 2-5**). These differences are more significant for the time-shift (**Figure 2-5b**).This effect has been described for aquifers placed below a confining layer that is connected to a free surface, designated as "capillary exposed surfaces" (Bear, 1972).

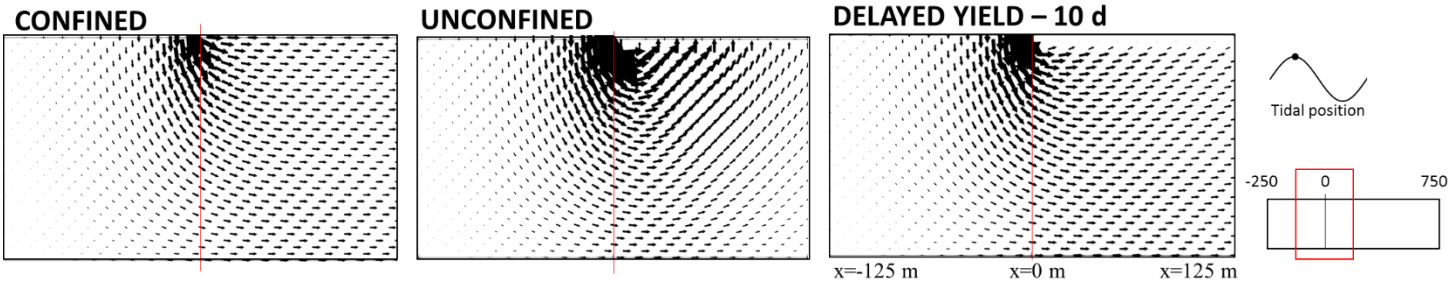

Figure 2-6: Velocity fields for the homogeneous simulations. Note the horizontal and vertical exaggeration are respectively 2 and 4.

2.4.2 Effectiveness of the mechanical component

Hydraulic diffusivity results for the case in which the aquifer is split by one aquitard layer are presented in **Figure 2-7**. These results are complemented with maps of the velocity fields (**Figure 2-8**), and a map of the amplitude damping factor (A/A_0) and the dimensionless time shift (ωts) (**Figure 2-9**).

Hydraulic diffusivities of the upper aquifer derived from 10 m deep (light color in **Figure 2-7**) show amplitude damping smaller than in the homogeneous case, which reflect the reduction of aquifer thickness. Note that the ideal D_h for the confined case (D_h conf. and D_h Sy 10 d in **Figure 2-7**) remains unchanged, but a D_h is underestimated by a factor of 4 for the confined case and 2.5 for the delayed yield case. The unconfined case (light green line in **Figure 2-7**) is more interesting. D_h is slightly underestimated for short distances, but becomes over estimated for distances larger than 0.4 L_c (recall that L_c in **Figure 2-7** is the one corresponding to the confined aquifer, or some 250m, so that $0.4L_c \approx 3L_{c\_unc}$). That is, the distance where D_{h_A} (and also $D_{h_{ts}}$) starts increasing coincides with the distance where the response along the upper aquifer becomes negligible. This suggests that the response observed is the one transferred from the deep aquifer (i.e., interference). Moreover, the break observed in the curve as well as the precision of D_h after this distance cannot be considered since the fluctuations are almost completely attenuated (0.02% of A_0). Numerically it would require a mesh refinement for better accuracy.

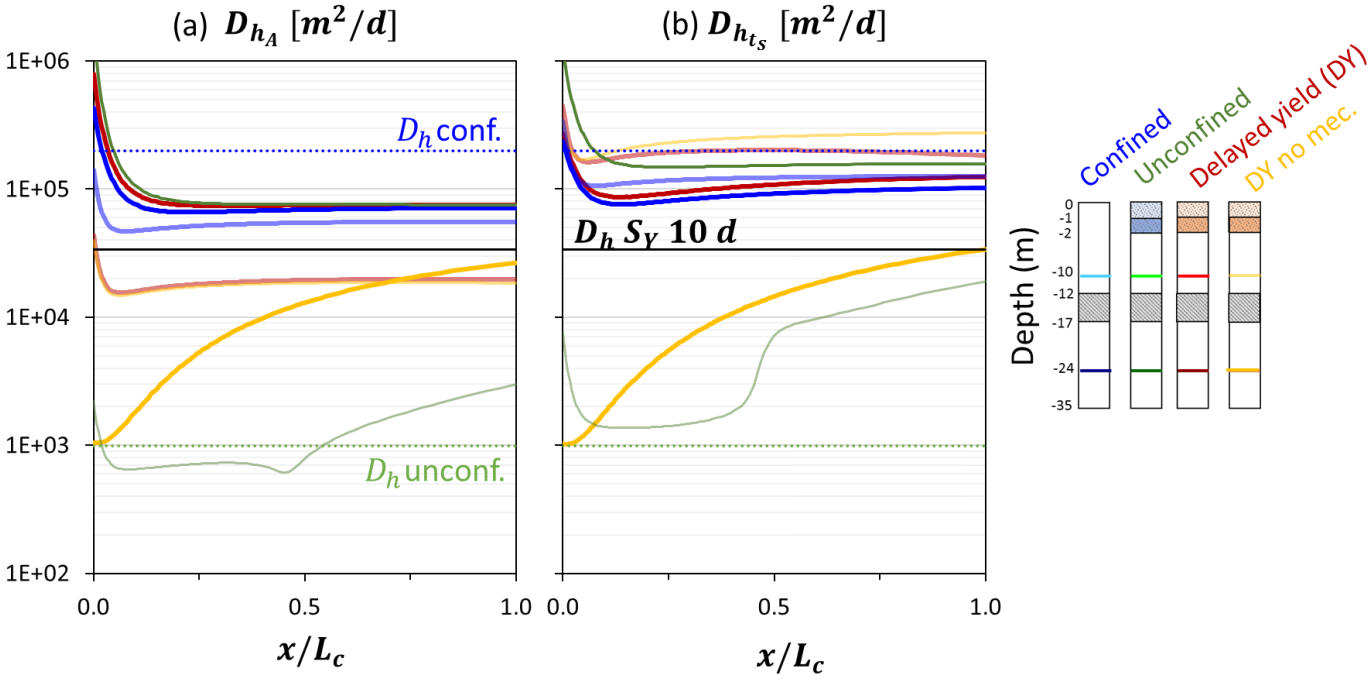

Figure 2-7: Estimated hydraulic diffusivity for an aquifer system with one aquitard dividing two aquifers. Differences results from the phreatic surface: confined (blue lines), unconfined (green lines), and a delayed yield (red lines) phreatic surface. Also, a delayed yield phreatic surface with no mechanical effect is presented (yellow lines). (a) Hydraulic diffusivity estimated from amplitude dampening (D_{h_A}). (b) Hydraulic diffusivity estimated from the time-shift ($D_{h_{t_s}}$). They are presented versus dimensionless distance from the coast (x/L_c). Dotted lines represent the hydraulic diffusivity for a confined aquifer (blue) and for an unconfined aquifer (green). The black line represents the hydraulic diffusivity for the delayed yield for a vertical characteristic time of 10 d. Light colors represent observation at z = -10 m and dark colors at z = -24 m (mostly collapsed at the top of figure near Dh conf.).

The mechanical effect is apparent in the maps of A/A_0, ωt_s and velocities (**Figure 2-9**and **Figure 2-8**). Flux in the deep aquifer is relevant from offshore (distance of the order of L_c) to inland the impact in terms of time shift is moderate, but it is large in terms of amplitude damping. For the parameters of this example, there is a positive time shift at the shore (maximum response slightly delayed with respect to the sea level maximum). Recall that the shift was negative for the parameters of **Figure 2-2**. Also, A/A_0 is slightly smaller than 0.5 at the shore.

An interesting feature of the velocities is that they display a slight vertical downwards component in the offshore portion, just below aquitard, despite the fact that no flux is apparent in the upper aquifer. They also display a slight upwards component

deep inland. In fact, though hardly visible, flow in the aquitard is vertical and away from the center, which shows the squeezing effect.

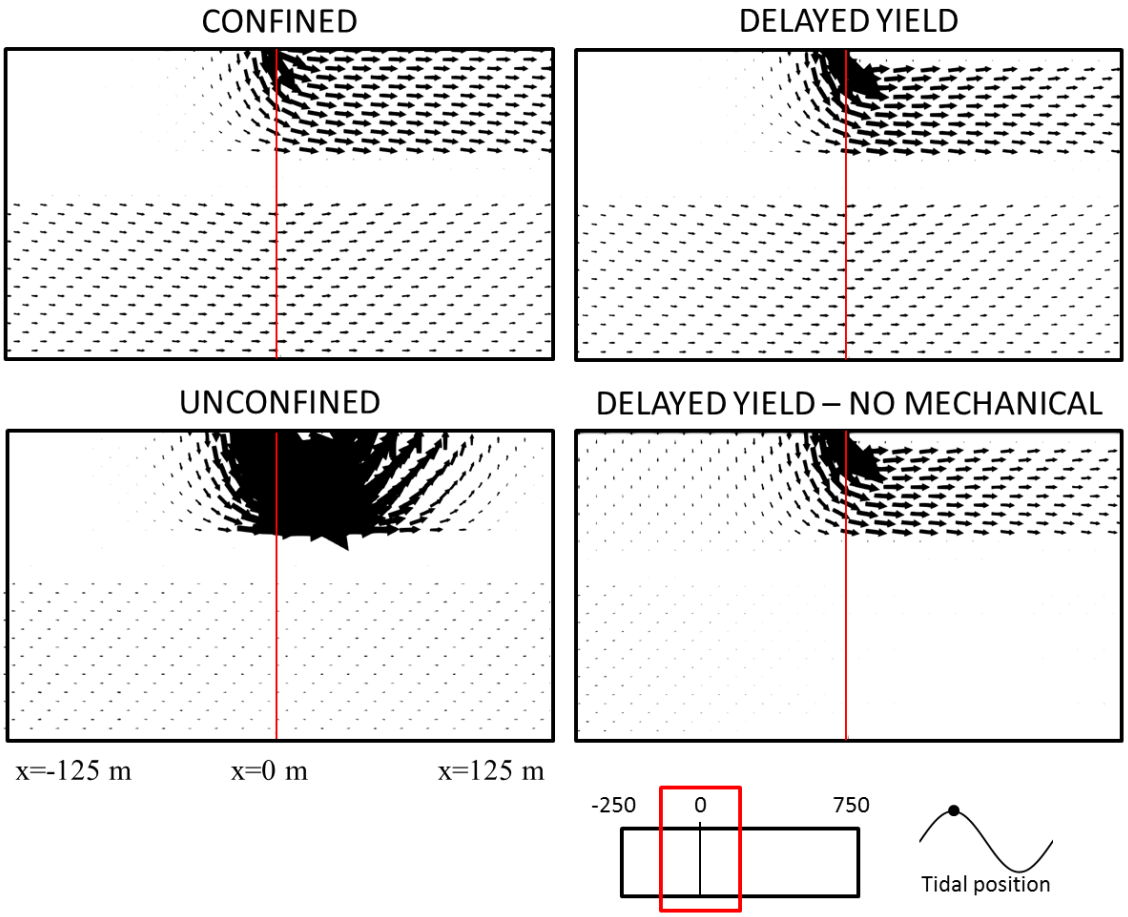

Figure 2-8: Velocity fields for simulations with 1 aquitard. Note the horizontal and vertical exaggeration are respectively 2 and 4.

In spite of the above complexities, estimates of D_h are not quite good. D_{h_A} is some 3 times smaller than the confined aquifer D_h, virtually identical for the three cases (conf., unconf., and delayed yield). This similarity despite the above mentioned aquifer interference, suggests that interference has a moderate effect there the signal is strong. D_{h_s} is closer than D_{h_A} to the time value, but the estimates are more sensitive to the upper aquifer conditions. This implies that interference is more important for time shift than for amplitude damping.

Two additional comments must be made. First, ignoring the mechanical effect does not affect D_{h_A} estimates in the upper aquifer, but they do affect somewhat estimates of $D_{h_{ts}}$. Neglectin the mechanical effect in the deep aquifer is not acceptable.

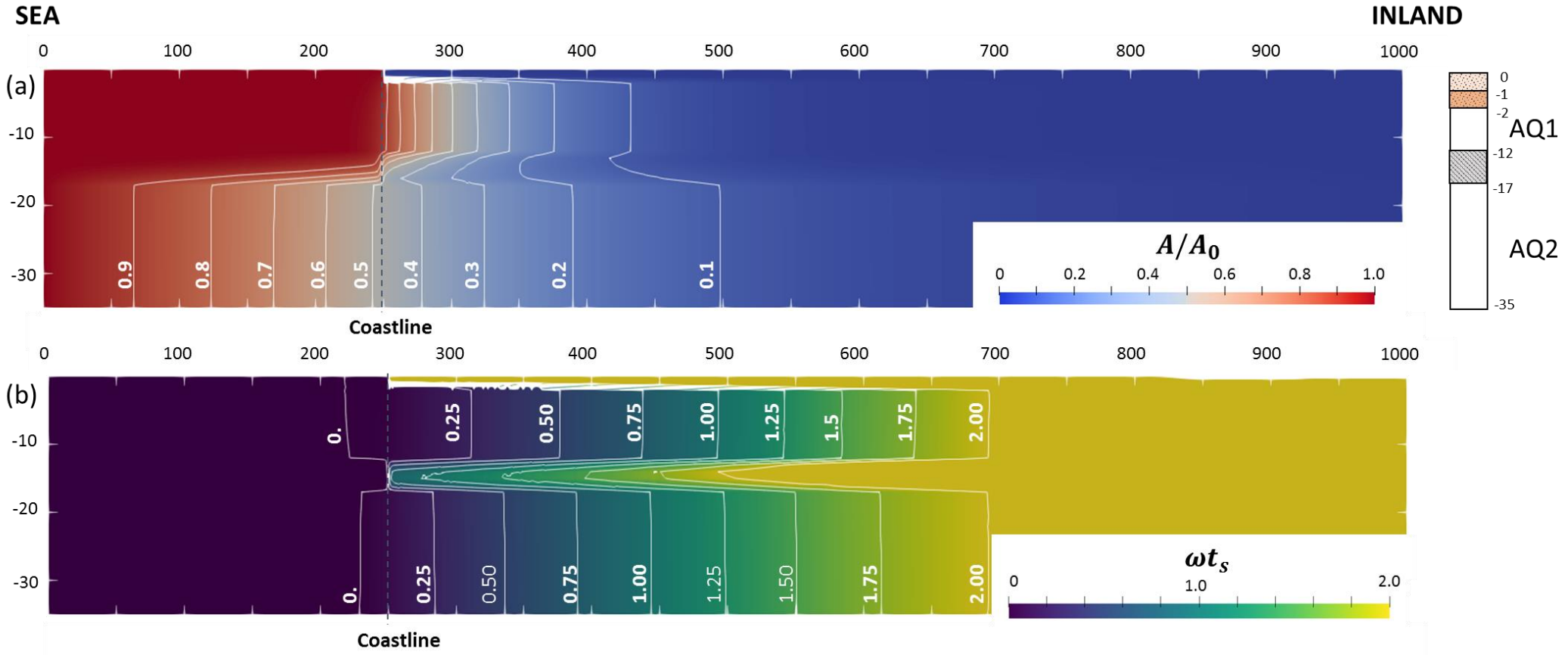

Figure 2-9: Amplitude attenuation (a) and dimensionless time-shift (b) distribution over the domain simulated for an aquifers-aquitard system with delayed yield

2.4.3 **Multilayered aquifer**

Results for the multilayer cases are presented in **Figure 2-10** and complemented with velocity fields in **Figure 2-11**. Results for the shallow aquifers, here represented by : (i) two cases with a 10 m thick aquifer (cases a and b), and (ii) two cases with 1 m thick aquitard dividing these upper aquifer (cases b and d). When we observe at 5 m depth, all the simulations present an underestimation of D_{h_A} with respect to the ideal D_h. which reflects that water flux into/out of aquitards is more significant. From the time-shift, $D_{h_{ts}}$ is overestimated up to 1 order of magnitude. Moreover, we observed differences at high distance between cases with the same shallow aquifer geometry. The only difference in these cases is their deep aquifer geometry, indicating the influence of deeper layers. Observations at 10 m depth presents some D_{h_A} values similar to results of deeper aquifers. This is not the case, in terms of time-shift.

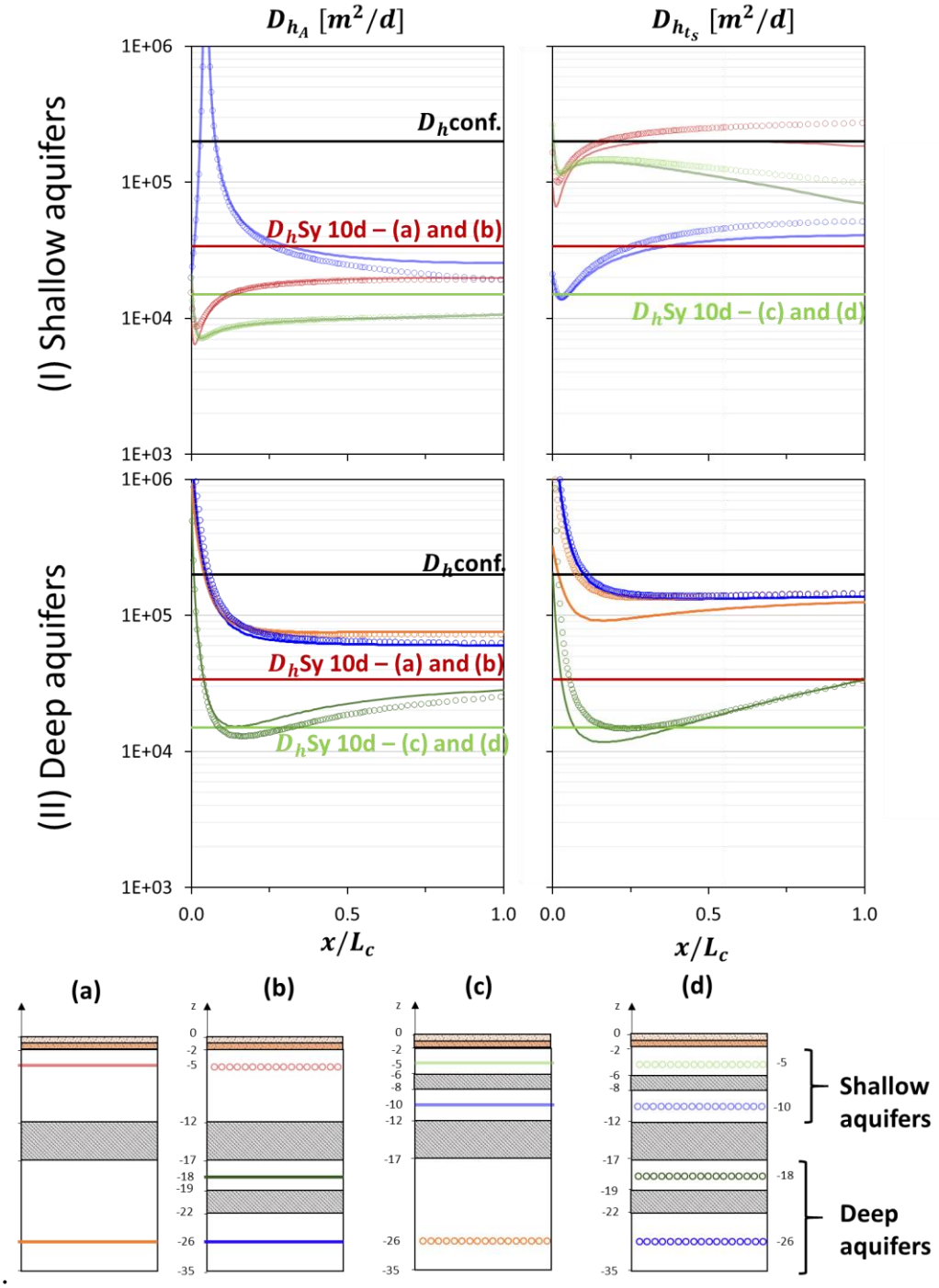

Figure 2-10: Estimated hydraulic diffusivity for multilayered aquifers with 4 different cases (a, b, c, and d). (I) Hydraulic diffusivity estimated at 5 and 10 m. (II) Hydraulic diffusivity estimated at 18 and 26 m depth. They are presented versus dimensionless distance from the coast (x/L_c). We indicate aquifers with similar geometry by a same color with one case with a full line and one case with round unfilled markers. Thus, at -10 m cases a and b are presented in light red and c and d in light green; at -10 m cases c and d are presented in light blue; then at -18 m cases b and d are in dark green and finally at -26 m cases a and c are presented in orange and b and d in dark blue.

In deep aquifers, the considered cases are representing a large confined aquifer (cases a and c) with 18 m of aquifer thickness and a system with a 3 m aquitard diving two aquifers (cases b and d). We observed in deeper layers similar results as previously with value tending to Dh conf. for observation at 26 m depth. These results are reflected in the velocity fields, similar for all cases in the deeper aquifer (**Figure 2-11**). Therefore, the observation at 18 m (cases b and d) are largely underestimating this value. Indicating that fluctuations are rapidly damped, confirmed by their velocity fields.

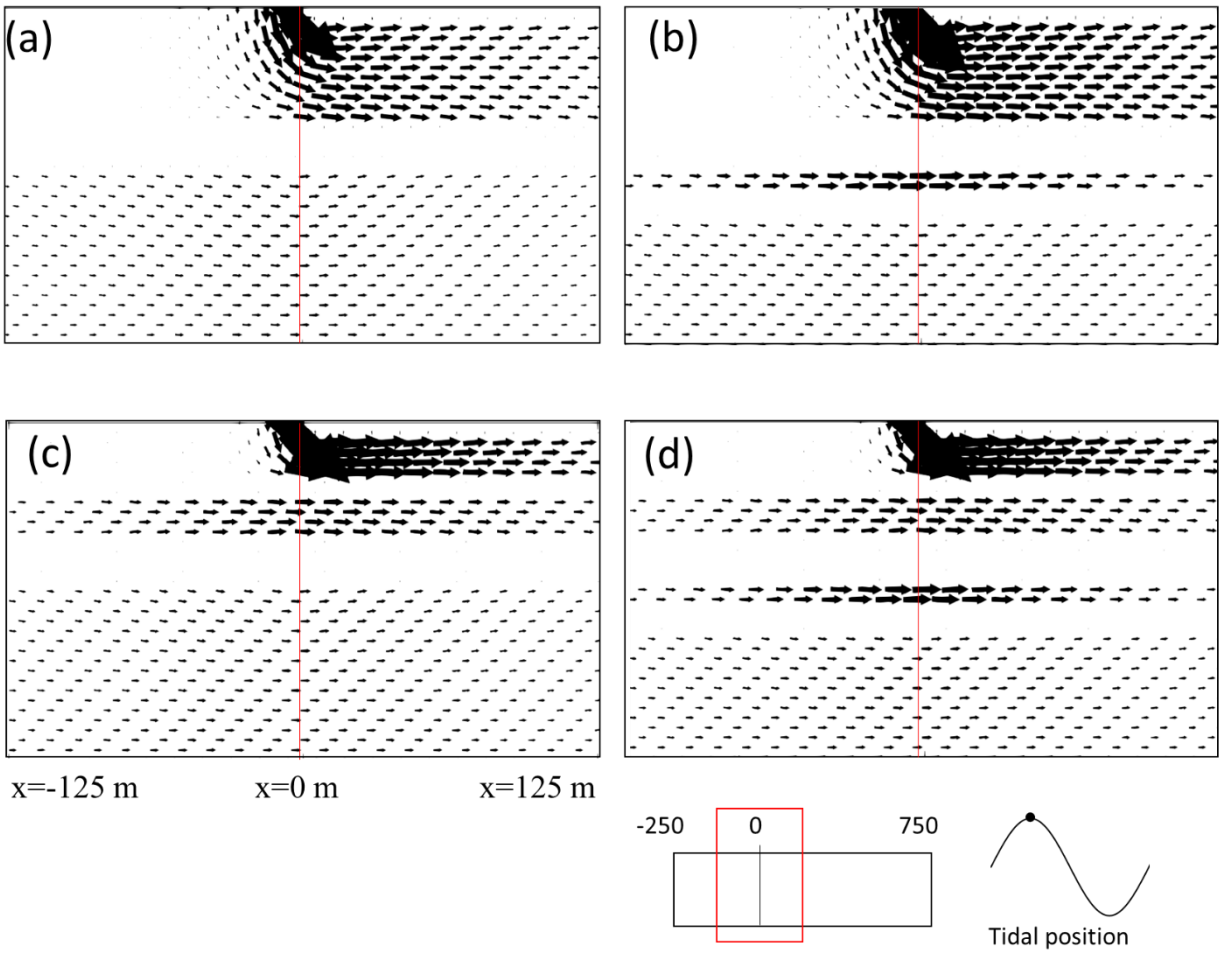

Figure 2-11: Velocity fields for the multilayered aquifers. Note the horizontal and vertical exaggeration are respectively 2 and 4. Letters refers to cases presented in **Figure 2-10**.

2.5 Conclusion

Recent research on tidal methods to characterize the hydrodynamic parameters and connectivity with the sea in coastal aquifers has provided a more complete understanding of the response observed during the tidal cycle. Current findings suggest that various components must be taken into account, such as the hydraulic part of the response combined with the mechanical effect due to load and unload on the submerged portion of the aquifer system. However, various open questions were remaining because of the non-consideration of some part of the system (unconfined aquifer) or due to the vague and weak provisions about the mechanical effect. Consequently, it makes difficult the application of this method to real cases.

In this study, we have systematically analyzed head responses to tidal fluctuations in coastal aquifers. A numerical analysis was performed to define proper aquifer characterization from the tidal method in coastal aquifers. To this end, different aquifer configurations and boundary conditions have been considered. Hydraulic diffusivity results demonstrate that for one simple aquifer, the order of magnitude is well reproduced. The problem lies in the interpretation of the estimated D_h. If the aquifer is unconfined and the modeler assume $T = D_h S$, with $S = S_s b + S_y$, then actual transmissivity can be overestimated by orders of magnitude. This point highligths the need to perform relatively long pumping tests to complement tidal response analysis for robust identification of coastal aquifer parameters.

Furthermore, the mechanical effect must be acknowledged below aquitards, but they should also be acknowledged in open aquifers. Thus, the confined aquifer reacts to tides rapidly and even faster than the superficial aquifer. Moreover, numerical results reveal the presence of interferences between layers in multi-layered systems. So that complexity implies the need of numerical modeling.

This study focused only on simple sinusoidal sea-level fluctuations in coastal aquifers. Further analysis considering real aquifer geometries and real sea-level fluctuations with multiple harmonic constituents signals should be examined in future investigations.

3

Using the tidal method for conceptual model identification and hydraulic characterization at the Argentona site

3.1 Abstract

Tidal response analysis in coastal aquifers represents a unique low-cost aquifer scale test to determine hydraulic diffusivity, and connectivity to the sea. Yet, the method is not as widely used as it deserves mainly because it barely behaves according to traditional simplified analytical models. To illustrate the complexities of tidal response interpretation, we use the analytical and numerical methods to observed tidal responses at a Mediterranean coastal aquifer (Argentona experimental site, Barcelona, Spain (Martínez-Pérez et al., in press a)From a harmonic analysis over a two-month period, we identified the main tidal constituents and quantified their amplitude and phase shift (delay between the tidal fluctuation and the well response) at the sea and observation wells. We found that hydraulic diffusivities estimated from amplitude attenuation are more than one order of magnitude smaller than those derived from the phase shift, linked to the assumption of a homogeneous aquifer, and because only the hydraulic effect is considered. In order to take into account aquifer system heterogeneity, some other analytical solutions were developed but still few applications to real cases have been performed due to their degree of complexity. So, this study is the first application of the tidal method to a real aquifer. We reproduced our aquifer system by numerical simulation considering a multilayered aquifer system with homogeneous aquifer portions where two different effects are considered: (i) the hydraulic connection between the differentiated aquifer layers and the sea, and (ii) the mechanical effect generated by the compression of the undersea aquifer portion affected by tidal fluctuations. A stratified configuration with different aquifer layers and aquitards and including mechanical effects is required to reproduce properly the head response observed in the wells, particularly for the phase shift calculation. Furthermore, after calibrating the main constituents separately we observe that a decrease in the tidal period leads to higher diffusivity estimates, highlighted a scale effect. Our numerical results demonstrate that mechanical effects play a drastic effect in aquifer response to tidal oscillations, even in shallow thin aquifers, and must be accounted for proper characterization and estimation of hydraulic parameters in coastal aquifers. Also, this approach allows to refine the studied site conceptual model and calibrate its hydraulic parameters for further studies.

3.2 Introduction

The increasing demographic pressure on coastal areas affects groundwater resources located in these zones due to their overexploitation. As a consequence, aquifer salinization through seawater intrusion (SWI) is accentuated (Bear, 1999; Werner et al., 2013). SWI is known as a natural phenomenon where seawater is found below fresh groundwater due to density differences at the meet-up of the two water bodies in coastal aquifers. Furthermore, pumping in coastal aquifers also leads to a reduction of the water fluxes discharging to the sea by submarine groundwater discharge (SGD, Rufí-Salís et al. (2019)). Also, with the transport of pollutants and a large amount of nutrients, groundwater quality decreases too, disturbing coastal ecosystems. Large advances have been made to investigate processes accruing in coastal aquifers, but despite 50 years of research, many challenges remain around seawater intrusion (Werner et al., 2013). As a passive and low-cost technique, the tidal method is a good approach to characterize them and specifically the connectivity with the sea in order to manage the impact of saltwater wedge expansion inland.

The tidal method consists of analyzing groundwater head fluctuations in a well as a response to sea level oscillations. The analysis and comparison of both signals, enables sea-aquifer connection characterization, together with aquifer hydraulic parameters estimation. Jacob (1950) and Ferris (1952) developed an analytical solution for tidal fluctuations in a confined homogeneous aquifer connected with the sea at the coastline. This solution is widely applied in the literature to obtain hydraulic diffusivity (D_h). The method usually yields different results depending on whether one calculates D_h from the amplitude attenuation or from the time shift. Moreover, this analytical solution can lead to D_h overestimation for observations below an aquitard because it neglects the mechanical effects generated by loading and unloading over the aquitard. Consequently, further developments have been done considering an infinite or finite extension of the confined aquifer below the sea (Guomin & Chongxi, 1991; H. Li & Jiao, 2001a; Van Der Kamp, 1972), while others contemplate leakage through the aquitard overlaying the confined aquifer (H. Li & Jiao, 2001b; Wang et al., 2014), and more recently, the loading or mechanical effect generated over the aquitard at the sea bottom (Guarracino et al., 2012; G. Li et al., 2008). Most of the cases consider a conceptual model limited to an unconfined

aquifer (where usually groundwater fluctuations are neglected with respect to the ones observed in the confined aquifer, see details in Jiao and Tang (1999) and G. Li et al. (2008), an aquitard or semi-confining layer over a confined layer (Geng et al., 2009; Guarracino et al., 2012; G. Li et al., 2008; H. Li & Jiao, 2001a, 2003a, 2003b; H. Li et al., 2007) and, only a few recent studies consider multi-confined aquifers (Ratner-Narovlansky et al., 2020).

Practical application of the tidal method remains infrequent, despite the importance of coastal aquifers and the fact that the test is easy to perform. A number of applications have been reported in the scientific literature (Carr & Van Der Kamp, 1969; Comte et al., 2017; Guo et al., 2010; Guomin & Chongxi, 1991; Jardani et al., 2012; Jiao & Tang, 1999; M. G. Trefry & Bekele, 2004; P. Zhou et al., 2016; X. Zhou, 2008; Zhuang et al., 2017). But applications by practicing hydrologists remain scarce. Tidal tests are not part of the "bag of tools" of hydrogeologists.

Several reasons contribute to explain the paucity of real applications. First, tides may be complex depending on site location. Second, tides may consist of numerous harmonics plus wind-driven sea-level fluctuations while analytical solutions typically consist of one harmonic. While the effect of several harmonics can be handled directly by superposition, proper management of tidal data remains a challenge. Fourier analysis would be the method of choice, but it requires long records. Long records are hard to obtain unless the site is close to a harbor because, in own experience, conventional sea-level sensors only last until the next storm.

3.3 Material and methods

3.3.1 Field site and data acquisition

We carried the study at the Argentona experimental site (NE Spain, Mediterranean coast), located at the downstream end of the Argentona ephemeral Stream (Folch et al., 2020; Martínez-Pérez et al., in press a). It is Holocene alluvial deposits organized in several semi-horizontal layers underlined by the upper part of the granitic weathering front (**Figure 3-1**). The aquifer structure is made of various sandy aquifer layers interspersed by semi-confining silts and sandy silt layers (see details in Martínez-Pérez et al. (in press a)). Small scale measurements on samples and short hydraulic tests performed

in the field show a permeability range from 0.5 to more than 20 m/d (Del Val et al., in press; Martínez-Pérez et al., in press a). Head is monitored (Diver® by Schlumberger Water Services) up to 100 m inland in 16 boreholes, distributed in nests of 3 boreholes open at different depths (see screened intervals in **Figure 3-1c**). In addition, a data logger has been deployed in the sea to monitor sea-level fluctuations of 30 m offshore.

Data were recorded during 2 months in the absence of rainfall, so recharge is negligible. The monitoring period extends from June 1st to July 24th of 2017 and was performed at a 5-minute sampling intervals. During the monitoring period, we covered a complete lunar cycle, with two full moons that took place on the 09th of June and July respectively.

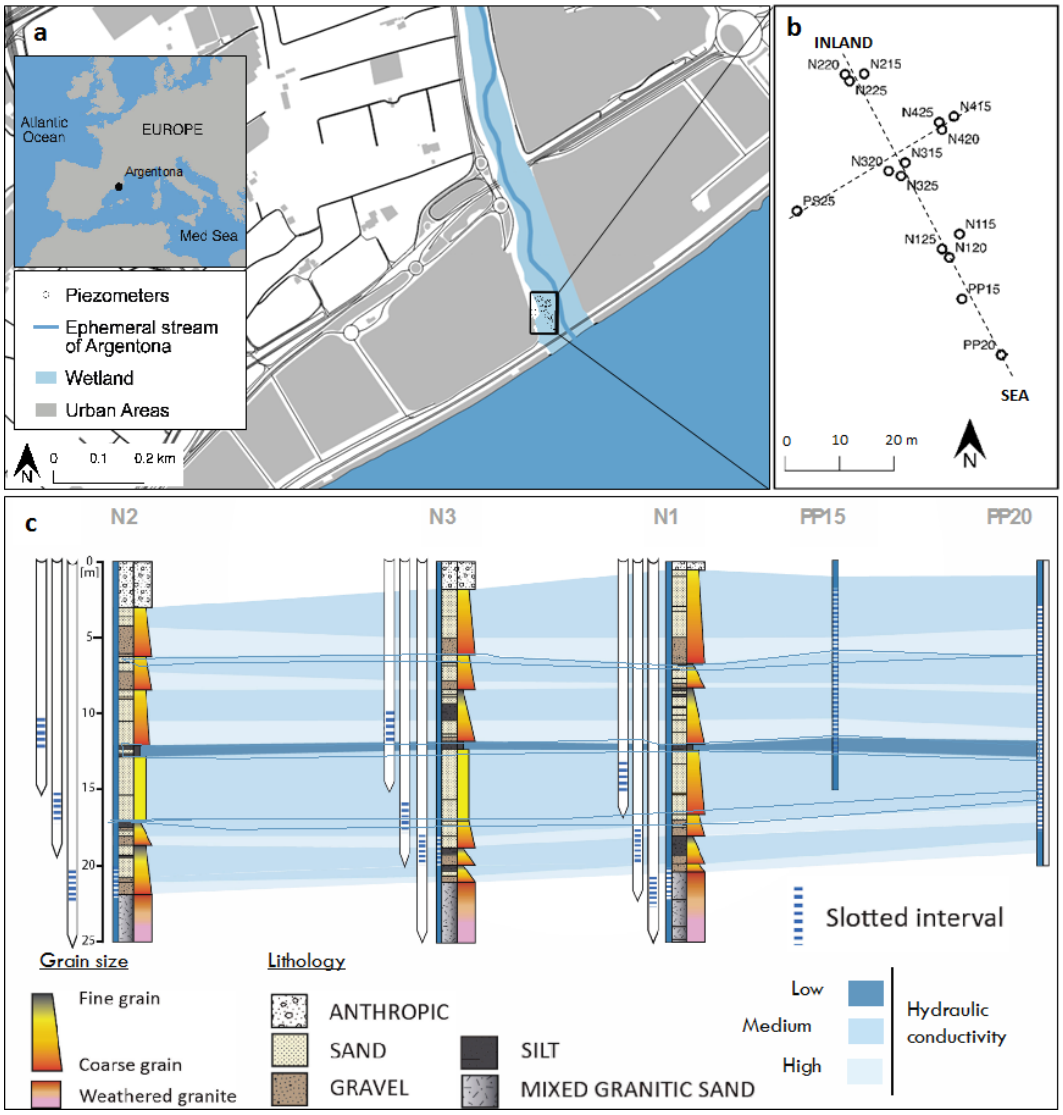

Figure 3-1: Experimental site of Argentona: (a) location, (b) borehole distribution, and (c) aquifer system (Modified from Martínez-Pérez et al. (in press a) and Diego-Feliu et al. (2021))

3.3.2 Data filtering

Data filtering is needed in order to: (i) remove the noise using a low pass filter; (ii) identify the main harmonics constituting the tidal signal, and (iii) obtain the amplitude and phase shift from the filtered signal for each identified tidal constituent. Barometric pressure variations have been compensated to water level data beforehand to data processing so that atmospheric tidal loading is not considered.

3.3.2.1 Step one: low and high pass filters (Godin, 1972) to remove noise and trend

The low pass filter described by Godin (1972) is largely known as a filter to remove diurnal, semidiurnal, and shorter-period components from a signal (Emery & Thomson, 2001). Conversely, it can be used to eliminate any non-tidal influence in groundwater head records and in the sea. Other filtering methods based on the Fourier transform are frequently used in signal processing. However, despite its powerful analysis, its effectiveness has a downside, as its transformation depends on two parameters: the signal sampling frequency and the total signal length. Therefore, the number of points in the transform defines the frequency spectrum resolution; the longer the signal, the better the resolution frequency.

In the tidal method, we are interested in the harmonics with periods (τ) identified within the frequency spectrum. Even if most of the frequencies out of interest are previously removed during the calculation of inverse Fourier transformation, non-relevant information can remain or an unexpected phase shift can appear in the data. Consequently, in this study, we decide to use the Godin filter.

Godin's filter works as the summation of the n consecutive data points defined as An. Their average is A_n/n. This averaged value represents the center of the interval of n data points. The low pass filter consists of repeating three moving averages, written as $A_n^2 A_{n+1}/[n^2(n+1)]$. For tides, we are interested in avoiding high-frequencies (τ < 1 h) and low-frequencies (τ > 24 h). To do so, we first remove high-frequencies, which can be written as $A_{12}^2 A_{13}/[12^2 \times 13]$ for data monitored every 5 min. To do so, we need two successive moving averages over n = 12 data points per hour, followed by one over $n+1$ = 13, to pass the data to an hourly average. The time series is made hourly by keeping every twelfth data point. Then, low-frequency fluctuations are isolated by the same

approach applying it over 24 hours $A_{24}^2 A_{25}/[24^2 \times 25]$. Again, two consecutive moving averages are needed over n = 24 followed by one with $n + 1$ = 25 data points. The result is a smoothed dataset (trend) an isolated noise and a clean tidal signal (**Figure 3-2**). However, the main drawback of this filter is the non-isolation of the different tidal components, while analytical solutions only require one component.

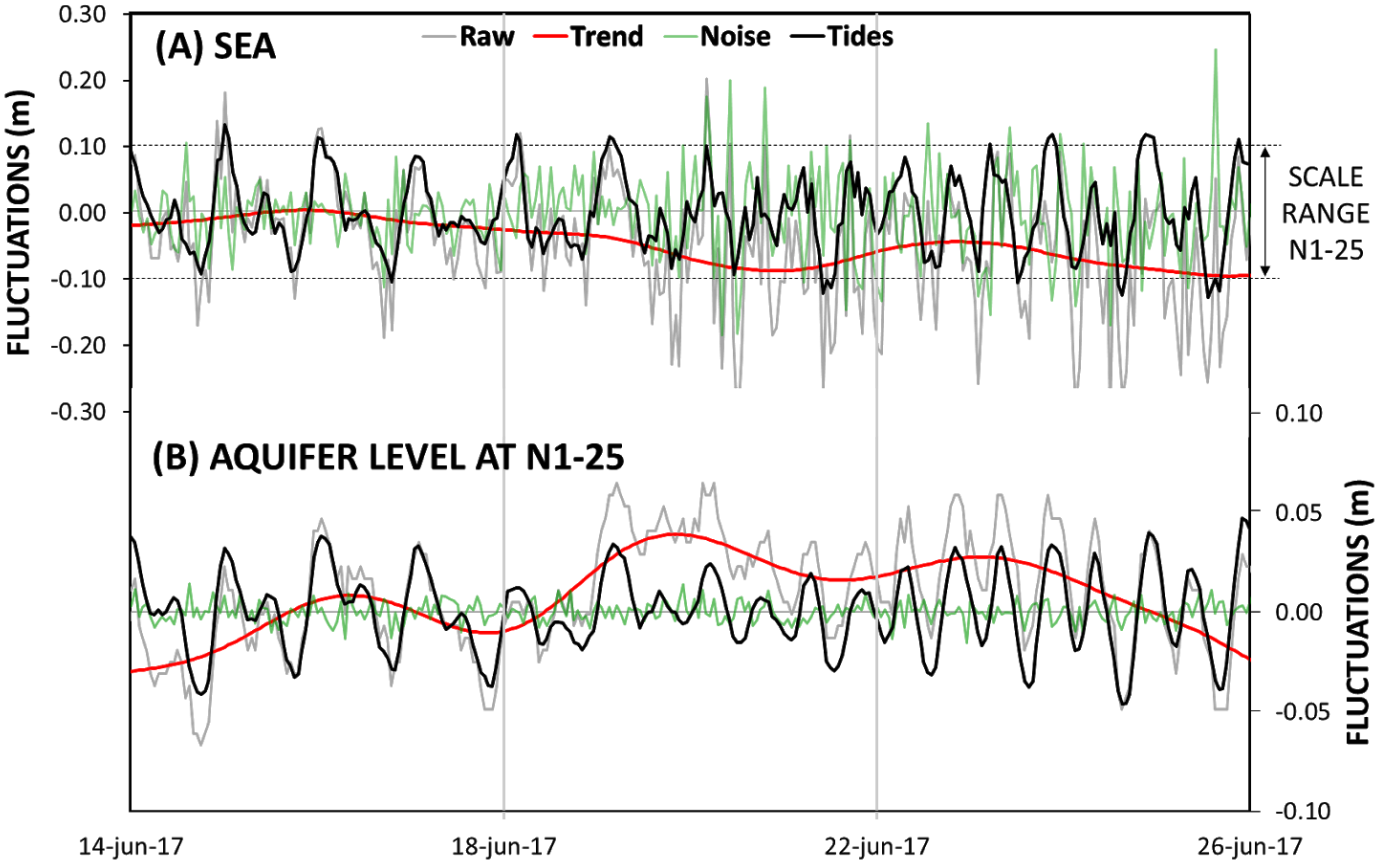

Figure 3-2: Signal decomposition of two noisy time series: (A) Sea and (B) N1-25. The raw measurements (gray) can be viewed as the sum of a trend (red), the actual tidal signal (black) resulting from step 1, and the noise (green) after removing the tidal signal. Note that the scale between the sea fluctuations and the aquifer level at borehole N1-25 is reduced by one-third, which will be relevant for further steps.

3.3.2.2 Step two: Harmonics identification

After filtering, the tidal signal is divided into harmonic constituents using a spectral analysis. The Fast Fourier Transform (FFT) is widely used for this purpose, as it allows to decompose a sequence of values into components of different frequencies (**Figure 3-3A**). We used the fft function from R-project (https://www.r-project.org). The

tidal constituents identified in the field are O_1, K_1, N_2, M_2, S_2-K_2, and M_4 (**Table 1**). The fact that they coincide with those listed by Arabelos et al. (2011) and de Toro et al. (1994)for the Mediterranean Sea confirms the validity of our analysis.

Table 3-1 : Identified tidal components with its corresponding amplitude in the sea at Argentona experimental site.

Tidal constituents	Period (h)	A_0 (cm)
Lunar diurnal (O_1)	25.82	1.55
Lunar diurnal (K_1)	23.90	3.81
Larger lunar elliptic semidiurnal (N_2)	12.66	1.15
Principal lunar semidiurnal (M_2)	12.41	5.04
Principal solar semidiurnal (S_2-K_2)	11.95	1.20
Shallow water overtides of principal lunar (M_4)	6.20	0.5

3.3.2.3 Step three: Calibration of amplitude and phase shift for each tidal component

After removing noise and identifying tidal harmonics, the tidal parameters (amplitude and time-shift) can be obtained. To this end, we express each time series as a sum of P tidal components, previously identified from harmonic analysis (identified in step two, Table 1, P = 6). The coefficients in this sum are estimated by least squares:

$$S = 1/n \sum_{i=0}^{n} \left[h_i - \sum_{j=1}^{P} \left(a_j \cos \omega_j t_i + b_j \sin \omega_j t_i \right) \right]^2 \quad (3\text{-}1)$$

Minimizing S with respect to a_j and b_j, allows us to obtain the amplitude (A_j) and the time-shift (t_{sj}) of each component as:

$$A_j = \sqrt{(a_j^2 + b_j^2)} \quad (3\text{-}2)$$

$$t_{sj} = \text{atan}\left(b_j / a_j\right) \tag{3-3}$$

The calibrated A_j and t_{sj} with their associated errors for each observation point can be found in Appendix B. Calibrated fluctuations summing the 6 main tidal harmonics in the sea and in the boreholes are presented in **Figure 3-3B** and the isolated components fluctuations in **Figure 3-3C**.

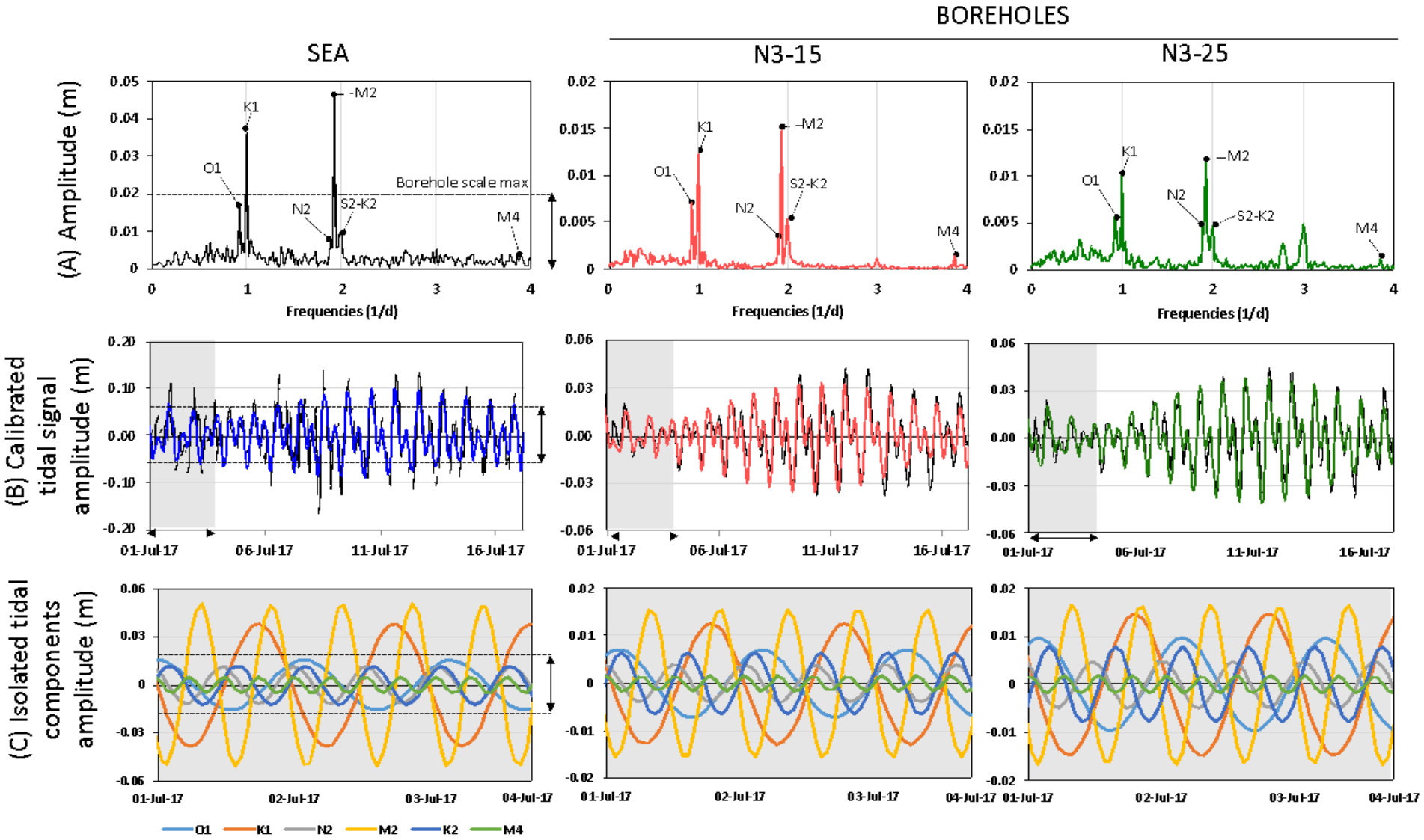

Figure 3-3: (A) Frequency spectrum obtained with identified tidal components; (B) Calibrated signal by least square method with 6 main tidal components; and (C) Isolated tidal components for 3 selected observation points: Sea, N3-15, and N3-25.

3.3.3 Application of the analytical solution (Ferris)

The analytical solutions of Jacob (1950) and Ferris (1952) describes head fluctuations of a homogeneous aquifer directly connected with the sea at the coast as:

$$h(x,t) = A_0 e^{-x/L_c} \sin\left(\frac{2\pi}{\tau}t - \frac{x}{L_c}\right) \quad (3\text{-}4)$$

where $h(t)$ is the aquifer head at a distance x $[L]$ from the coast at time t $[T]$, $A_0[L]$ is the tidal amplitude, and the characteristic length is defined as $L_c[L] = \sqrt{\tau T/\pi S}$, with τ $[T]$ being the period of the tidal oscillation, T $[L^2/T]$ is transmissivity and $S[-]$ is storage coefficient. Hydraulic diffusivity ($D_h = T/S$) can be derived from the amplitude (A) or the phase shift (t_s) measured at a distance x from the coast.

$$D_{h_A} = -\frac{x^2\,\pi}{\tau\left(ln\left(\frac{A}{A_0}\right)\right)^2} \quad (3\text{-}5)$$

$$D_{h_{t_s}} = \frac{x^2\,\tau}{4\pi\,t_s^2} \quad (3\text{-}6)$$

The D_h values obtained from the amplitude and from time-shift differ from one to two orders of magnitude. Moreover, the latter presents a large dispersion. This inconsistency is regularly reported in the literature (Drogue et al., 1984; Erskine, 1991; Michael G. Trefry & Johnston, 1998). It is clear that the assumptions of Jacob (1950) and Ferris (1952) are rarely met in practice. Still, a number of trends can be observed. First, the value of D_h should be around 10 m^2/d (K~10 m/d and S_s~ $10^{-4}m^{-1}$). The values of D_h derived from the time-shift are too high, while those from amplitude are too small. These observations suggest a hydromechanical response. The maximum loading rate occurs $\tau/4$ ahead of the tidal maximum, which causes a very small time-shift, possibly negative depending on the aquitard properties (Guarracino et al., 2012). Therefore, hydromechanical response explains why $Dh_{t_s}$is too large. The loading is distributed during half a period, which causes the amplitude of the mechanical response at the coast to be only half of those at the sea (Van Der Kamp, 1972). As a result, the mechanically driven amplitudes are much smaller than those at the sea, and the corresponding D_h too small, but increasing away from the shore (see Chapter 2 -).

We also observe that each tidal component (here M_2 and K_1, in **Figure 3-4**) gives different hydraulic diffusivity values, with a decreasing trend with the period length.

Perhaps the most useful conclusion from this work was that all piezometers displayed a marked mechanical response. This was unexpected because the shallowest piezometers were assumed to be representative of an unconfined aquifer. This observation forced us to re-examine on initial geological interpretation. The re-analysis of the cores and gamma logs showed the presence of two silt layers that had gone unnoticed at first (those a 7 and 17 mbsl, **Figure 3-1**). The fact that these layers were relatively thin implied that hydraulic interference between the aquifer layers should be expected, which would make analytical interpretation very hard and requires numerical modeling.

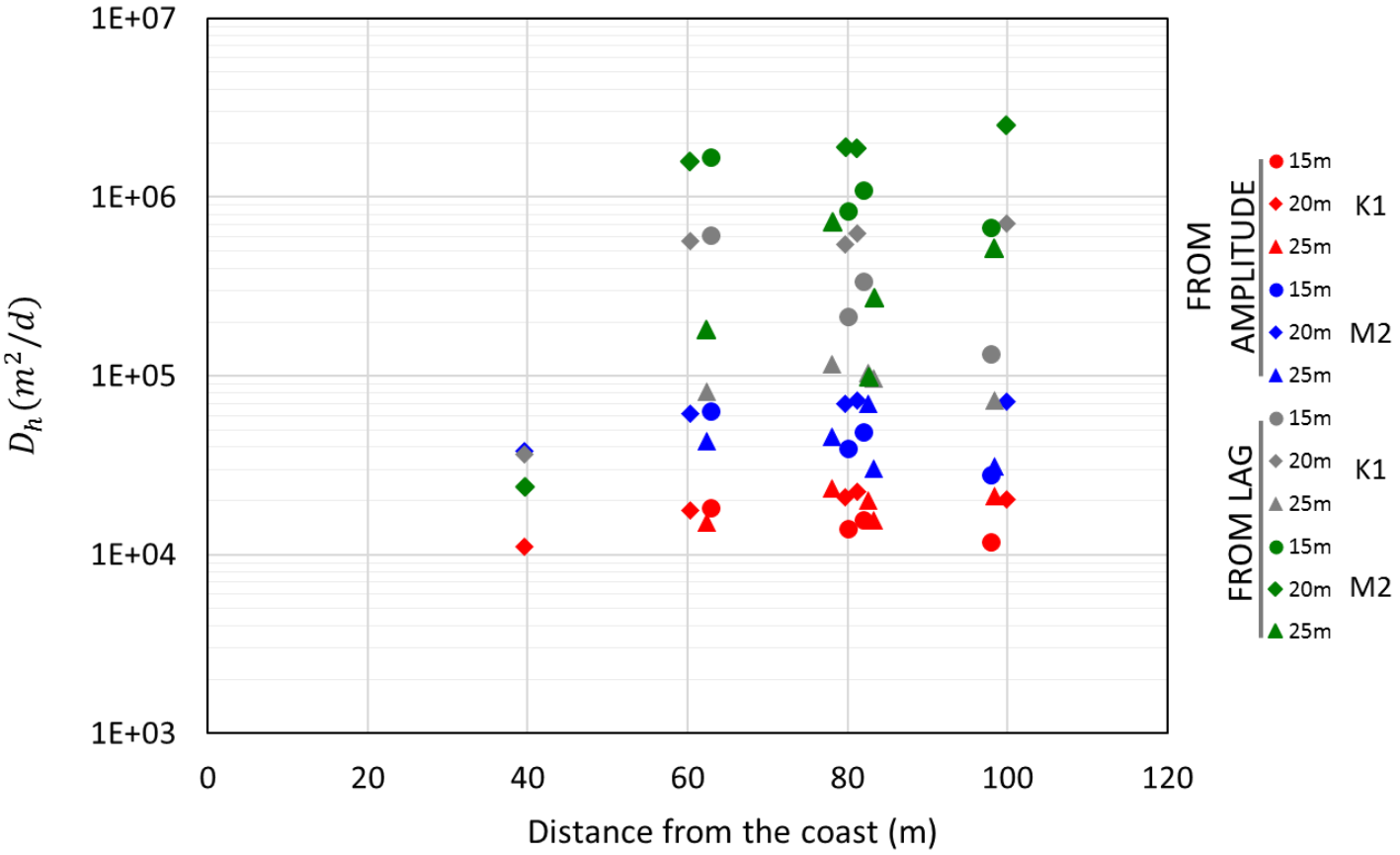

Figure 3-4: Hydraulic diffusivity obtained at every piezometer from the amplitude and the time-shift of the K_1 (diurnal) and M_2 (semidiurnal) tidal harmonics, using Eq. 3-5 and 3-6 from Jacob (1950) and Ferris (1952) analytical solution

3.3.4 Numerical model

3.3.4.1 Model setup and conceptual model

To reproduce the tidal fluctuations observed in the field, we built a pseudo-steady-state model using the TRANSIN code (Medina et al., 2004; Medina & Carrera, 1996). We used a two-dimensional vertical section with a lateral extension (L_x) of 1 km. The considered domain is formed by 750 m of the inland aquifer and 250 m of a submerged portion of the aquifer. The aquifer thickness (L_z = 35 m) is constant up to the aquifer basement (weathered granite, considered impervious).

The complex geology characterized by the alternation of various permeable and semi-permeable layers (**Figure 3-1c**), makes it difficult to reproduce it numerically. In particular, the consideration of all the thin layers implies higher degrees of freedom that will impact the following calibration process. We divided the domain into 9 permeability zones to reproduce the geological sequence of Figure 1: 4 aquifers (AQF-1 to 4, **Figure 3-5**), 3 aquitards (AQT-1 to 3, **Figure 3-5**), and two layers to model delayed yield as described in Chapter 2 - . Specific storage coefficient was taken as $S_{AQF} = 5 \cdot 10^{-5}$ m^{-1} for the aquifer units and $S_{AQF} = 5 \cdot 10^{-4}$ m^{-1} for aquitards. The permeability of each layer was calibrated, assuming an initial value at $K_{AQF} = 10$ m/d for aquifers and $K_{AQF} = 0.01$ m/d for aquitards.

We generated a finite element mesh with 8050 nodes arranged in 15643 triangular and irregular elements (**Figure 3-5**). The grid was refined in the areas of greatest interest such as near the coastline and in the boreholes locations. Note that there are no observation points in AQF-1, so we expect a higher estimation error in this layer.

3.3.4.2 Boundary conditions and mechanical effect

As described by Guarracino et al. (2012), aquifer level fluctuations result from the superposition of two different effects: (1) hydraulic response due to sea-aquifer connection at the aquifer edge and across the aquitard; and (2) mechanical, response to tidal loading and unloading over the sea bed. The hydraulic effect was represented by a prescribed head to be equal to sea level, $h_s(t)$, at the right edge and top of the submerged

part of the aquifer (Red transects in **Figure 3-5**). The mechanical component in the submerged part was simulated by a recharge term $R = S_s L_e \, dh_s/dt$ (Alcaraz et al., 2021).

These types of representations have been adopted for sea level fluctuations during model calibration:

1)Simulate each tidal component j separately (j =1 to 6, with 1 for M_4, 2 for $S_2 + K_2$, 3 for M_2, 4 for N_2, 5 for K_1 and 6 for O_1). Therefore, sea level is given by:

$$h_s(t) = A_0 \sin(\omega t) \tag{3-7}$$

2)Add up the 6 identified tidal components together:

$$h_s(t) = \sum_{j=1}^{P} \left(A_{0_j} \sin(\omega_j t_i) \right) \tag{3-8}$$

(3) Simulate directly the measured sea level after removing noise with the low pass filter results ("Tides" in **Figure 3-2**, called "full signal" hereinafter).

With respect to the inland boundary condition, due to the possible propagation of the mechanical effect far from the coast, we applied a leakage BC ($Q = \alpha\,(h - H_{ext}), [L^3.T^{-1}]$) to reduce the calculation time and keep the model dimensions reasonable. This BC simulates an inflow or outflow, depending on the aquifer head. So, we fixed the head outside of the model ($H_{ext} = 0\,m, [L]$) and the leakage coefficient ($\alpha = 0.01\,m^2/d, [L^2/T]$).

3.3.4.3 Calibration process

The calibration of permeability against head values is done through transient inverse modeling. It consists of obtaining the optimum set of parameters by minimizing an objective function (F, Eq.3-9) depending on the computed head (h), the measured head (h^*), and the weight attributed to the parameters to estimate head at observation points (W) (Medina & Carrera, 2003). We avoided fully penetrating boreholes, due to possible interferences between aquifer levels inside the well. Also, we assumed that head residuals are heteroscedastic, with a standard deviation equal to 5% of h_{max} for all the observation points, except for piezometer PP-18, in which we applied 10% of h_{max} because we have less confidence.

$$F = (h - h^*)^t W (h - h^*) \quad (3\text{-}9)$$

This calibration process was repeated for each of the identified 6 tidal harmonics previously (M_4, S_2-K_2, M_2, N_2, K_1 and O_1). Then, we calibrated permeabilities for the sum of harmonics and for the full signal.

The application of this procedure requires some time discretization adjustments since Δt depends on the tidal period simulated, and the time step must be as small as the sinusoidal period. However, to ensure numerical performance and reduce CPU time, we used two time-steps. First, a broad time step (Δt_1) until we reach steady-state (which also constitutes the warm-up period) and then a reduced time-step.

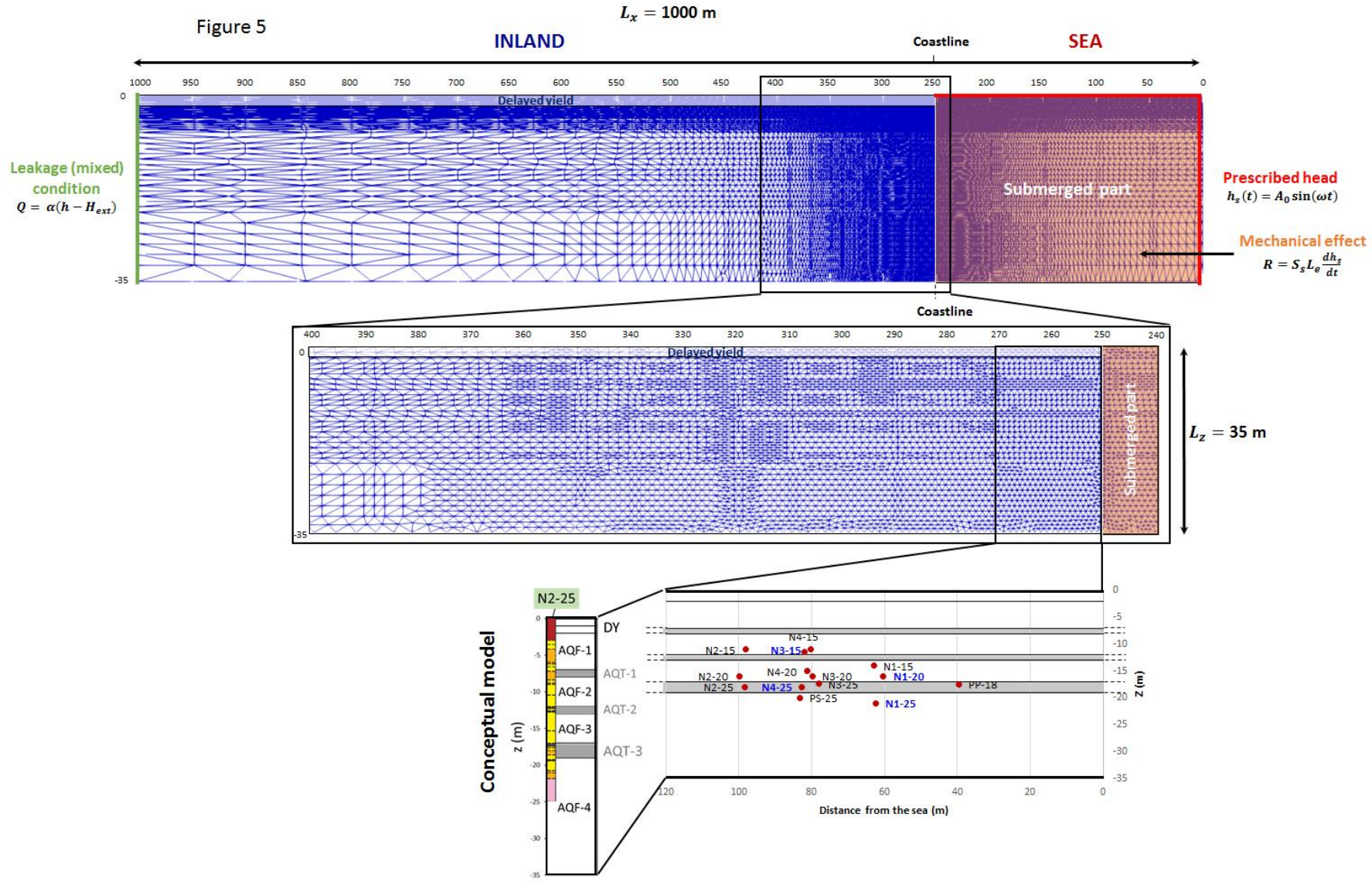

Figure 3-5: Geometry, boundary conditions and mesh used in the two-dimensional numerical model. The boundary conditions are shown in red for the hydraulic effect, in orange for the mechanical effect and in green for the inland boundary condition.

3.4 Results and discussion

3.4.1 Tidal components identified parameters

Important information about the aquifer can be obtained directly during data processing. We observed that the low pass filter performed with Godin (1972) was more efficient than the Fourier method. This can be explained by the fact that Fourier requires larger time series, such as one year. However, this last is useful to identify tidal components. Indeed, the spectral analysis using the Fourier transform has identified 6 tidal components of which two are the main components (K_1 and M_2). Nevertheless, the Fourier transform constraints are still a limitation as it decomposes the signal into frequencies that depend on the input signal length as observed on the tidal components S_2 and K_2 which appear in the same peak in the frequency spectrum (Fig. 3-A) while they are different components with a respective period of 12 h and 11.97 h.

Then, we observed an attenuation of 50% in the amplitudes (even in observations <100 m from the coast). Considering an unconfined aquifer, the signal would dissipate towards inland due to its large storage coefficient and tidal fluctuations would be negligible. If we only consider the hydraulic effect, the amplitude dampening would be greater (reduced up to ¾) as it depends on the distance (D) at which the aquifer is connected with the sea (here D = 250 m, Internal communication). This far connection with the sea would suggest that the dampening is due to low permeability, but results from field tests indicate the opposite (Del Val et al., 2021; Folch et al., 2020; Martínez-Pérez et al., in press a), especially in AQF-3. These observations question the unconfined behavior attributed to the Argentona alluvial aquifer especially as Guarracino et al. (2012) shown that an amplitude dampening of 0.5 in a confined aquifer is due to a mechanical effect and not influenced by hydraulic effect. This suggests that the Argentona aquifer should be considered confined.

Finally, another argument indicates that our aquifer is not homogeneous, and should be defined as a multi aquifer system: the amplitude dampening and the time-shift increase distribution is quite dispersed. Theoretically, if the aquifer was homogeneous, all the boreholes would be following an exponential decay for the amplitude dampening and a linear increase for the time-shift. In Argentona case, non-unique relation has been

observed. In fact, at least 3 lines (representing each boreholes level: 15, 20, and 25) have been estimated. This also clearly indicates that a classical conceptual model (aquifer-aquitard-aquifer) is not a good option either for the Argentona site. As in this configuration, all the points located in the upper aquifer should follow the same amplitude damping curves and time-shift increase. This same behavior would be observed for the lower aquifer but on different curves.

With this approach, we conclude that the Argentona site is not following the classical aquifer-aquitard-aquifer model. The amplitude dumpling clearly indicates a mechanical effect and demonstrates that Argentona should be considered as a confined aquifer and more specifically a multi-layer confined aquifer. Finally, this proves the importance of starting from a detailed aquifer geological characterization, because even small heterogeneities have a strong impact on tidal fluctuations monitored in the aquifer. However, special attention must be paid to the degree of freedom given to permeability calibrations.

3.4.2 **Calibration results**

Field estimations made with pumping tests or measurements performed on cores can provide information on hydraulic conductivity. Nevertheless, the scale (Sanchez-Vila et al., 2006) and time (Meier et al., 1999) dependence induce a hard and mostly wrong extrapolation to the aquifer scale. In this sense, tides represent a good alternative to characterize aquifer hydraulic parameters to avoid the spatial and temporal limitations of other methods. Moreover, as tides are composed of different components with different periods, they can be used to characterize aquifers at different scales (e.g. the characteristic length (L_c) for the period (τ)). Indeed, short period tidal components will give information on boreholes connectivity located close to the sea, while large period tidal components will promote connectivity at a large scale.

Figure 3-6 displays the comparison of model outputs with field measurements for 4 selected observation points located at different levels. Each of them presents results for 2 tidal harmonics (K_1 and M_2). Also, results for two tidal signal multi harmonics are presented: the sum of harmonics (corresponding to the 6 identified tidal harmonics) and the full tidal signal (corresponding to “tides” in **Figure 3-2**).

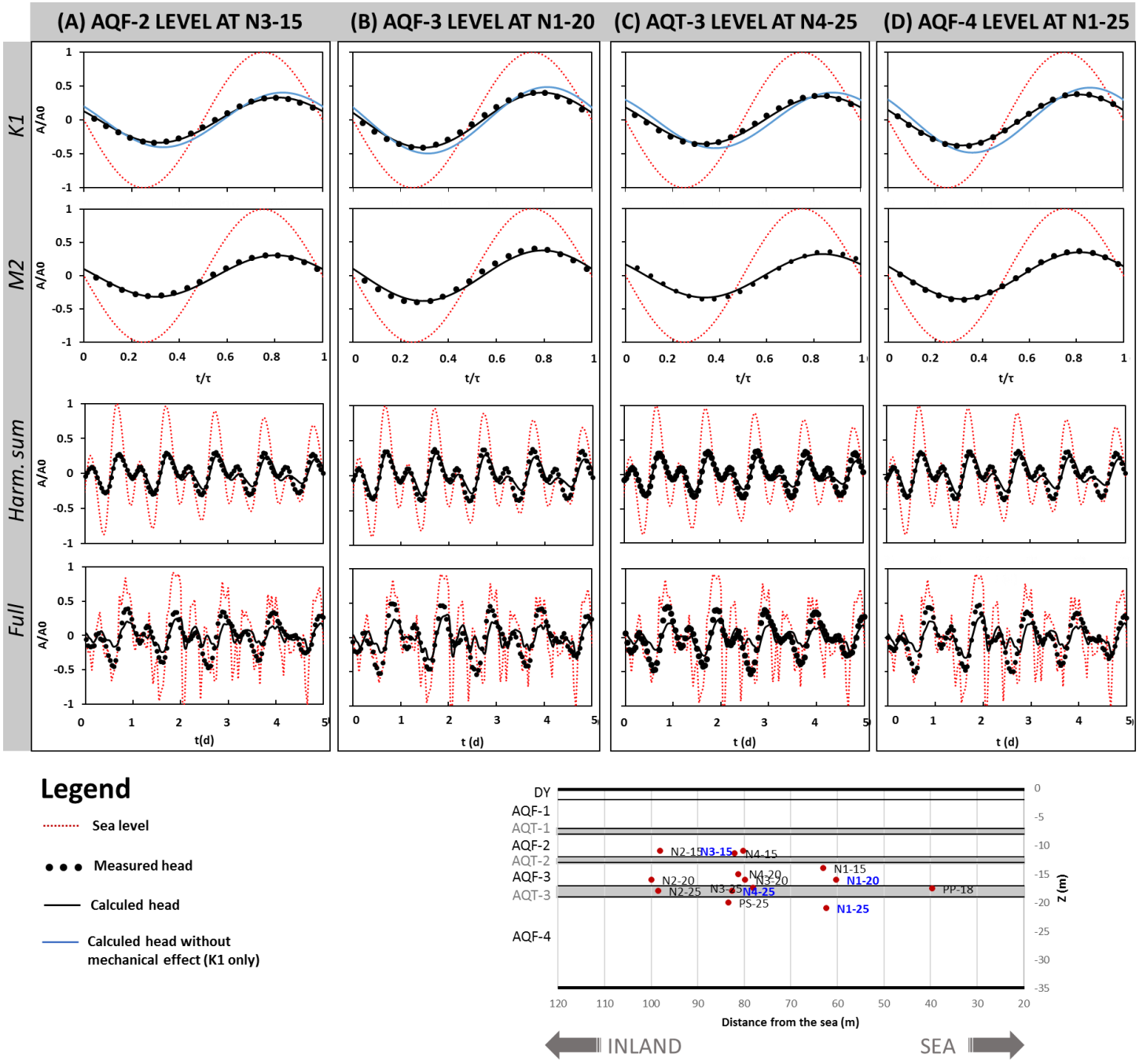

Figure 3-6: Calculated and measured heads at 4 selected observation points (N3-15 located in AQF-2, N1-20 located in AQF-3, N4-25 located in AQT-3, N1-25 located in AQF-4) for 2 tidal harmonics (K_1, M_2) (two top rows), the sum of harmonics (third row)and the full tidal signal(bottom row). Black lines represent calculated heads from the numerical model, black dots depict the measured head data used for calibration, red dotted lines represent the sea-level, and gray lines the calculated head with only hydraulic effect using K_1 tidal harmonic.

Calibrated permeability values (K) for each of the 6 tidal harmonics are presented in **Figure 3-7**. M_4 is the tidal harmonic identified with the shortest period at Argentona experimental site (6.2 h) and a very small amplitude compared to the other tidal harmonic. Calibrated M_4 K values are high for aquitards, which indicates that this component is not properly representing these layers. We suggest that this is related to the small L_c caused by low harmonic τ, as aquifer layers are rather well identified (Martínez-Pérez et al., in press a) and have been proven to have an impact using other components. Therefore, M_4 results have to be taken with caution, since M_4 has a very small amplitude compared to the other tidal harmonic (**Table 3-1**).

Calibrated permeabilities obtained with other components such as S_2-K_2 are quite high (i.e., $K_{AQF-3} = 593.66$ m/d). As mentioned before, S_2 and K_2 represent two different harmonics, very close in the frequency spectrum and with a similar period (τ = 12 h and τ =11.97 h), which complicates the distinction. So, high permeabilities obtained with these components could be a consequence of the filtering phase, as the data length is short, and therefore FFT is unable to discretize S_2 from K_2 in the harmonic analysis.

For M_2 (τ = 12.41 h) and K_1 (τ = 23.9 h) components (which are the main harmonic components identified at the sea observation point), K calibrated values are quite similar and respect the conceptual model with the alternation of aquitards and aquifers.

The intermediate component N2 (τ = 12.66 h) also gives K values that are in good agreement with the M_2 and K_1 calculated values. However, for the AQF-3 K, calibrated values were higher with respect to the other estimations.

Finally, we observe that transmissivity in permeable layers (AQF-2, AQF-3, AQF-4) increases when the period decreases. This behavior reveals a scale effect. Indeed, the more the period associated to a large characteristic length is long, the more the distance cover from the coast is long. For AQF-1 presents a higher variation of permeability values that tend to yield lower permeability values during the inversion process. This is directly linked to the lack of observation points.

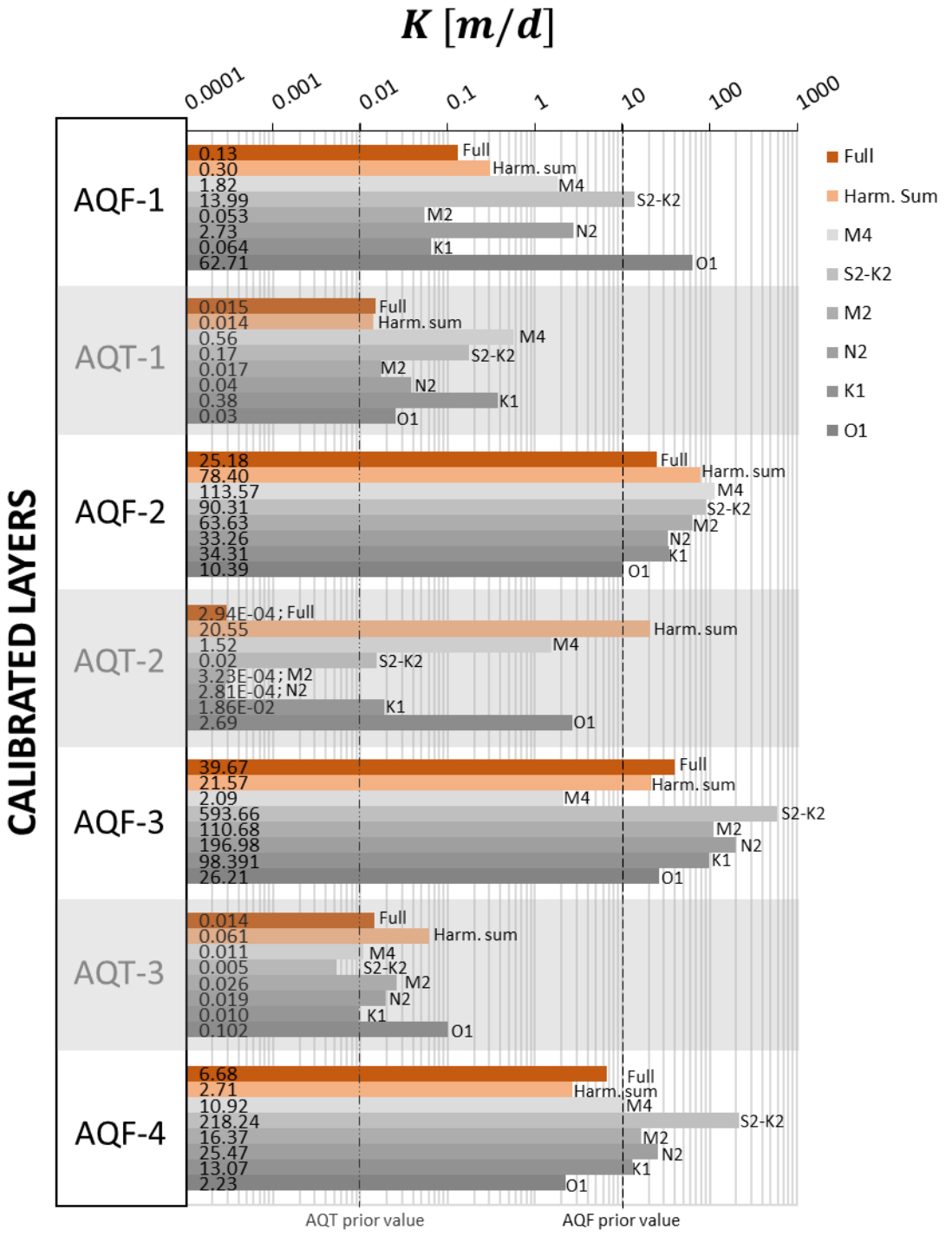

Figure 3-7: Calibrated transmissivity values in each aquifer (AQF) and aquitard (AQT) layers for the defined conceptual model.

3.4.3 Should we separate the tidal component for calibration?

The complete signal calibration was performed in order to assess whether the separation of tidal harmonics in the parameter estimation is valid and whether it agrees well with the results obtained. We then compared it to the calibrated sum of the 6 tidal harmonics identified in **Figure 3-3**A. When we compare the measured and calibrated heads using both methods (full tides signal and harmonic sum), the numerical model reproduces the measured head fluctuations (see **Figure 3-6**), except for a few peaks. However, when a unique tidal component is simulated, these features are correctly displayed. In the full tidal signal case, the sea-level signal is much more complex than the one observed in the aquifer, which indicates that the aquifer is acting as a filter for the sea noise. Indeed, the removed noise is drastically lower in the wells than in the sea (**Figure 3-2**). For permeabilities estimation, the results obtained using both methods are quite different (**Figure 3-7**). Full signal values are fairly close to the K average obtained from the separated harmonics calibrations, whereas the harmonic sum overestimates the AQT-2 permeability, ignoring the conceptual model (see **Figure 3-5**).

So, even if it is easier to calibrate permeability using the full signal, avoiding the entire filtering process, the calibration results clearly indicate that the conceptual model is better captured with the separated component. So, a special caution has to be taken with head reproduction using the full tidal signal.

3.4.4 Effectiveness of the mechanical component

After calibrating the aquifer, including both hydraulic and mechanical effects (generated by the loading over the seabed induced by sea-level fluctuations), we test the mechanical component insertion and evaluate the role of the hydraulic connection between the aquifer and the sea in the tidal method. To do so, we made the same calibration for the K_1 tides considering only the hydraulic effects, which implies an offshore connection to the sea and through semi-confining layers. Results show that the calculated head is delayed with respect to the measured head (**Figure 3-6**) as observed in Chapter 2 - . Using only the hydraulic effect, the numerical model is actually unable to further accelerate the response to match the observations for all the observation points (see objective function discrepancies for both types of simulations $F_{Hydraulic\_K1} =$ 691200,

F_{K1} = 85670). We conclude that the mechanical effect is important even in cases where low permeability layers are thin (< 2 m thick).

3.5 Summary

The non-intrusive and low-cost tidal method is not widely used to characterize coastal aquifers. A detailed procedure is described here and applied at the Argentona experimental site, where data loggers are installed to measure head fluctuations both in boreholes and at the open sea. This fully detailed study demonstrated the complexity of using tidal methods to real cases:

(1) Existing analytical solutions cannot be readily applied because they fail to represent the complexity of real systems. Using simplified solutions causes hydraulic diffusivity estimations from the amplitude or from the time-shift yields different values. Despite this, tidal information is rich and can be exploited by a numerical model.

(2) The mechanical effect may be essential to reproduce measured heads, even for the case of shallow alluvial aquifers. In our case, we were expecting an unconfined aquifer connected to the sea with some less permeable layers, but results show that even thin low k layers may suffice to cause a significant mechanical response.

(3) Sea-level fluctuations are complex due to the multiple tidal harmonics, which makes the method difficult to apply. The tidal response scale depends on the tidal period through L_c, proportional to$\sqrt{2}$. The multiplicity of harmonics causes the response to be multiscale while this multiplicity complicates interpretation (especially when non-harmonic wind-driven fluctuations are considered), it also increases the information.

4) The full information is contained in the full signal, which can be most directly interpreted through modeling. Still, a separate analysis of each harmonic facilitates conceptual model development. It was this analysis that convinced us that the initial geological model was not adequate and forced us to revise it.

This study provides for other coastal aquifers a detailed filtering process to other coastal aquifers focused on removing any non-tidal signal and obtain tidal parameters at observation points (amplitude and time-shift for each tidal harmonic), giving preliminary information about the aquifer complexity, response, and connection with the sea. Aquifer hydraulic conductivity estimations using numerical modeling gave good results, with nice fitting between head measurements, and are also consistent with the defined conceptual model.

4

Identification and quantification of chemical reactions in a coastal aquifer to evaluate submarine groundwater discharge composition

4.1 Graphical abstract

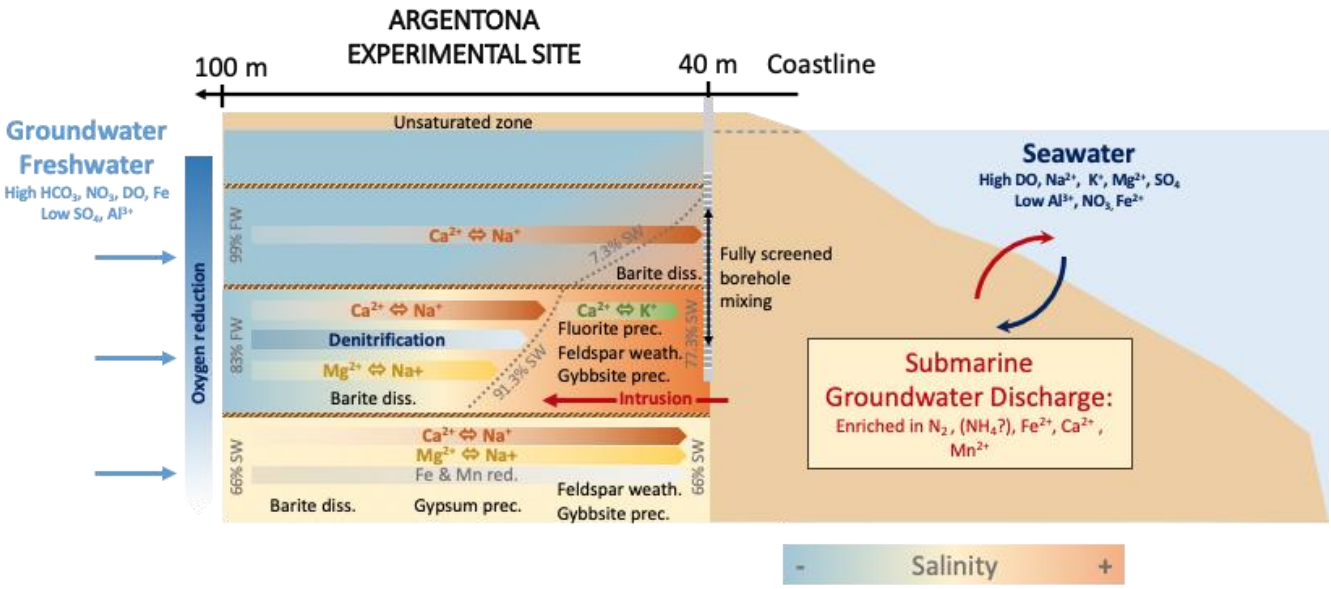

4.2 Abstract

In coastal aquifers, two main processes, in opposite directions, are usually observed: Seawater intrusion and Submarine groundwater discharge (SGD). The meeting of these two waters forms a mixing zone where specific chemical reactions can occur. Characterizing and above all quantifying these reactions are essential to predict the aquifer water quality but also the submarine groundwater discharge composition. Indeed, sampling SGD is a key challenge and thus its composition is usually unknown or estimated mixing freshwater and seawater composition. A full and detailed description of a statistical method based on principal component analysis to identify the end-members of a sample is presented. The use of the EMMA (End Member Mixing Analysis) coupled with a reactive-mix procedure allows to identify the end-members and their spatial proportion in the Argentona coastal aquifer located in the North of Barcelona. We quantified the extent of the reactions and their spatial distribution of the different chemical processes occurring in this coastal aquifer. The most important reaction is cation exchange, especially between Ca and Na. We also highlight the important role of coastal aquifers in the reduction of groundwater organic matter. And we finally estimate the submarine groundwater discharge composition taking into account all the identified reactions.

4.3 Introduction

Population density in coastal areas is some three times higher than the global average density (Small & Nicholls, 2003). The impact of high population on freshwater demand is very strong. One of its consequences is the intensification of seawater intrusion (SWI) (Alfarrah & Walraevens, 2018). SWI is a natural process enhanced in coastal aquifers where there is a significant extraction of freshwater (FW). At the same time, coastal aquifers discharge continental water towards the sea through Submarine Groundwater Discharge (SGD). Some authors argue that the quantified volumes of (Saline + Fresh) SGD are many times greater than the river discharge (Taniguchi et al., 2019). SGD carries high solute and nutrients concentrations into the sea (Slomp & Van Cappellen, 2004). Those chemical elements may be important and/or harmful to submarine ecosystems (Luijendijk et al., 2020), which makes coastal aquifers hydrochemistry fundamental.

The hydrochemistry of coastal aquifers depends not only on the nature of the different types of groundwater (end-members) that mix in these areas but also on their ensuing interactions and reactions with the solid phases. Numerous studies indicate the occurrence of chemical reactions in coastal aquifers including ion exchange, redox reactions related to some biodegradation, mineral dissolution, and precipitation. Wigley and Plummer (1976) and Hanshaw and Back (1980) observed that the mixing between freshwater (FW) and seawater (SW), both in equilibrium with calcite, may tend to dissolve calcite, thus favoring coastal karst formation (Back et al., 1986; Fratesi, 2013). The fact that dissolution has been reported with only 2% of SW (Magaritz et al., 1980), together with the fact that transport dynamics favor dissolution on the freshwater side of the mixing zone (Rezaei et al., 2005), not only explain karst development features, but also highlight the high reactivity (high surface area) of porous media when compared to the sea.

Cation exchange, driven by the invasion of SW, is frequently reported as a leading geochemical process. A significant deviation of cations (increases in calcium and decreases in sodium, magnesium, and potassium) is usually observed (Appelo & Willemsen, 1987; Giménez-Forcada, 2010; Gomis-Yagües et al., 2000; Martínez & Bocanegra, 2002; Pulido-Leboeuf, 2004). Russak et al. (2016) studied the effect of

seawater intrusion and freshening cycles on other minor cations Li^+, B^-, Mn^{2+} and Ba^{2+} using field data and column experiments. Cation exchange, together with the dissolution of some minerals, can promote the precipitation of others. This is the case for Dolomite and, especially, gypsum. In fact, a depletion in sulphate concentrations is observed in a majority of works (Andersen et al., 2005; A. P. Barker et al., 1998; Custodio, 1992; Gomis-Yagües et al., 2000). Sulphate reduction, which has also been proposed, requires anoxic conditions and significant amounts of electron donors, which may be caused by organic deposits or from FW contamination. In fact, iron and manganese reduction has been described in the mixing zone where microbial iron reduction has been proposed to account for most of the anaerobic degradation of natural organic matter (Snyder et al., 2004).

These biogeochemical reactions explain that the composition of submarine groundwater discharge differs from the one predicted by simple mixing of FW and SW. They also explain that saline water returning to the sea due to sea-aquifer exchange may be quite different from sea-water, which may help understanding sea chemical balances. For example, calcium balance had traditionally missed an important input (Milliman, 1993; Wilkinson & Algeo, 1989). Actually, the SGD calcium input is estimated between 40 and 120% of the fluvial inflow (Sawyer et al., 2016). Most research on SGD chemistry focuses on nutrients, which control primary production (Grzelak et al., 2018; Y. Liu et al., 2021; Valiela et al., 1990). It has been found that commercial fish, aquaculture and lobster yields are positively correlated with terrestrial nutrients discharged into coastal waters (Peng et al., 2021; Sutcliffe Jr, 1972). Nutrients, which are essential elements for photosynthetic organisms, may become harmful for submarine ecosystems and lead to algal blooms when in excess (Anderson et al., 2002; Chen et al., 2020; Luo & Jiao, 2016). Attention to major ions cycles (Cl^-, SO_4^{2-}, Na^+, K^+, Mg^{2+}, Ca^{2+}, and HCO_3^-) has been relatively less. Yet, they can exert a significant control on the chemical forcing in coastal areas and stimulate primary production (Kłostowska et al., 2020; Y. Liu et al., 2017; Santos et al., 2008).

Chemical reactions in coastal aquifers are numerous and can be interdependent. This makes coastal aquifer hydrochemistry difficult to explain. Hydro-chemical studies in coastal aquifers are usually qualitative: describe groundwater composition and conjecture the reactions that may lead to measured concentrations. We suggest that

quantifying such potential reactions is useful to confirm or discard conceptual models, strengthen the analysis and help to build numerical models. Quantification is traditionally achieved through models, which also help to assess the response of the system to changing conditions. But reactive transport models are conceptually difficult, because of difficulties of transport and density dependent modelling, and practically complex, because they require a large amount of data and long observation time-series. To simplify the numerical model implementation, it is mandatory to identify the most important reactions.

A preliminary approximation to chemistry can be achieved using mixing models. These are based on writing the concentration of species i in sample j (C_{ij}) as (Christophersen et al., 1990; Hassen et al., 2018; Jurado et al., 2015) :

$$C_{ij} = \sum_{e} \lambda_{ej} C_{ei} \tag{4-1}$$

where C_{ei} is the concentration of species i in end-membereand λ_{ej} is the proportion of end-member e in sample j. λ_{ej} must satisfy the following constraints:

$$0 \leq \lambda_{ej} \leq 1 \tag{4-2}$$

$$\sum_{e} \lambda_{ej} = 1 \tag{4-3}$$

Mixing ratios can be obtained from the samples and end-members concentrations using these equations. The solution is trivial in the frequent case where only two end-members (FW and SW) are present. In this case, the fraction of seawater in sample j (λ_{SWj}) can be calculated from Cl^- concentration (Appelo & Postma, 2005):

$$\lambda_{SWj} = \frac{C_{Cl,j} - C_{Cl,FW}}{C_{Cl,SW} - C_{Cl,FW}} \tag{4-4}$$

The large difference between Cl^- concentrations or similar salinity indicators, such as electrical conductivity, in FW and SW makes Eq. 4-4 quite robust and, thus, widely used. Still, attention must be paid to measurement errors, which can be identified if other species are used for the calculation of mixing ratios. For example, Shin et al. (2020) report some underestimations using Br ions compared with Cl ions. Therefore, the chemical element chosen to calculate λ_{SWj} may be important. Conservative chemical elements such as stable isotopes, or metals are used as SWI and/or SGD tracers (Long & Valder, 2011;

Nakaya et al., 2007). Other tracers (i.e. Sr and Ra isotopes) provide accurate mixing ratios but require specific sampling protocols and additional costs to regular monitoring campaigns. Moreover, the use of these tools can be hindered when the mixing between end-members is not clear or when they are not identified (C. Kendall & Caldwell, 1998).

Identification of end-members is a conceptual problem (i.e., a hydrologist should be able to identify them from the conceptual understanding of the system). But, identification is greatly aided by End Member Mixing Analysis (EMMA, Christophersen et al. (1990); Hooper (2003); Hooper et al. (1990); Vázquez-Suñé et al. (2010)). EMMA is a powerful statistical method based on principal component analysis (PCA) that aims at explaining the great majority of a data set by reducing the dimensions of the problem by grouping correlated variables. To do so, eigenvalues are calculated and then projected into a low-dimensional space (2 or 3) by selecting the eigenvectors explaining most of the variability. End-members should encircle all the other projected observation points, which together with conceptual understanding helps in their identification. Once the end-members have been identified, the quantification of the end-member percentage of mixing within each sample can be done. EMMA is an adequate technique, but cannot be directly applied to species that undergo some reaction. Therefore, a fairly widespread EMMA rule is to keep only the conservative species in the analysis (P. Li et al., 2016; Tubau et al., 2014), which is a limiting factor when many reactions occur and affect most species. This is particularly the case when the two mixing solutions are not in equilibrium with the host sediments such as in coastal aquifers.

Including reactions in mixing calculations has been addressed by several researchers. Tubau et al. (2014) and Jurado et al. (2015) considered reactions as end-members by adding, for every reaction, an artificial end-member with the species participating in the reaction. Unfortunately, this approach does not properly represent mixing in the aquifer since the calculated mixing ratios do not add up to one (Eq. 4-3) and the identification of actual reactions remains unclear. Pelizardi et al. (2017) present a methodology to formalize mixing ratio calculations, which can be rewritten as:

$$C_{ij} = \sum_{e} \lambda_{ej} C_{ei} + \sum_{e} S_{ir}^{t} R_{rj} \qquad (4\text{-}5)$$

where S_{ir} is the stoichiometric coefficient of species i in reaction r and R_{rj} is the reaction extent of reaction r in sample j.That is, R_{rj} should be understood as the amount (expressed as moles or equivalents per liter) of reaction r reactants that go to products to explain the concentrations of sample j. The method consists of several steps: (i) use the EMMA to identify the species participating in reactions are identified using the EMMA and determine the associated reactions, (ii) define conservative components (u) associated with the reactions identified in the previous step (De Simoni et al., 2005), (iii) repeat the EMMA process with the conservative components for the identification of end-members and (iv) calculate the mixing ratios in each sample. The method is appealing because it formalizes the gist of hydrology: understanding how water exchanges among compartments and the processes it undergoes (e.g., Davis and DeWiest (1966); Hurrell et al. (2013)). Still, the method does not specify how to quantify the reactions (R_{rj}), and the methodology needs refinements on how to identify the reactions to be applied to real data (Pelizardi et al. (2017) examples are synthetic).

The objective of this work is double. First, we want to refine the reactive EMMA methodology and to apply it to a complex real case (the Argentona site, Martínez-Pérez et al. (in press a)). Second, we want to identify and quantify hydrochemical processes at this coastal site to understand the chemistry of SGD.

4.4 Materials and methods

4.4.1 Study site, sampling, and analytical techniques

We use chemical data from the well-instrumented Argentona Experimental Site located 30 km north of Barcelona (Spain), at the mouth of the Argentona ephemeral stream (**Figure 4-1**). This site is characterized by a dynamic SWI and SGD yielding to the formation of an active mixing zone (Martínez-Pérez et al., in press a). The site is characterized by a Mediterranean climate with dry summers and mild, wet winters. Rainfall (some 600 mm/year) concentrates mainly in heavy rain events during autumn and spring that controls the Argentona stream flow and the alluvial aquifer recharge. The site aims at monitoring seawater intrusion dynamics at different depths thanks to 15 wells. 12 of these boreholes are nested 3 by 3 and have a 2 m screened interval at 3 different depths (15, 20, and 25 m). They are labeled Nx-15, Nx-20, and Nx-25 where x is the nest

number (1 to 4). 3 other solitary boreholes complete the experimental site: PS-25 with a 2 m screened zone at 25 m depth and 2 fully screened boreholes of respectively 15 and 20 m depth (PP-15 and PP-20). The site is 100 m long inland from the coastline and 30 m wide.

The aquifer system is formed by alluvial deposits with an alternation of gravel, sands, and silty layers over a weathered granitic substratum. Mineralogy composition was measured through XRD at different depths and indicates a majority of silicates as Quartz (13–37%, SiO_2), Microcline (10–34%, $KAlSi_3O_8$), Albite (21–46%, NaAl Si_3O_8) and Fe rich Mg-hornblende (3–7%). Some clay minerals, such as Illite, are also observed with a fairly wide range depending on the depth (3–38%) (see details in Martínez-Pérez et al. (in press a)). The anthropogenic impact in the watershed is quite significant with urban, agricultural, and industrial areas that can have an impact on groundwater quality (Rufí-Salís et al., 2019). Both the geological background and human activities in the watershed may foster reactions associated with the above minerals such as silicate alterations, cation exchange with clays, and some organic matter degradation.

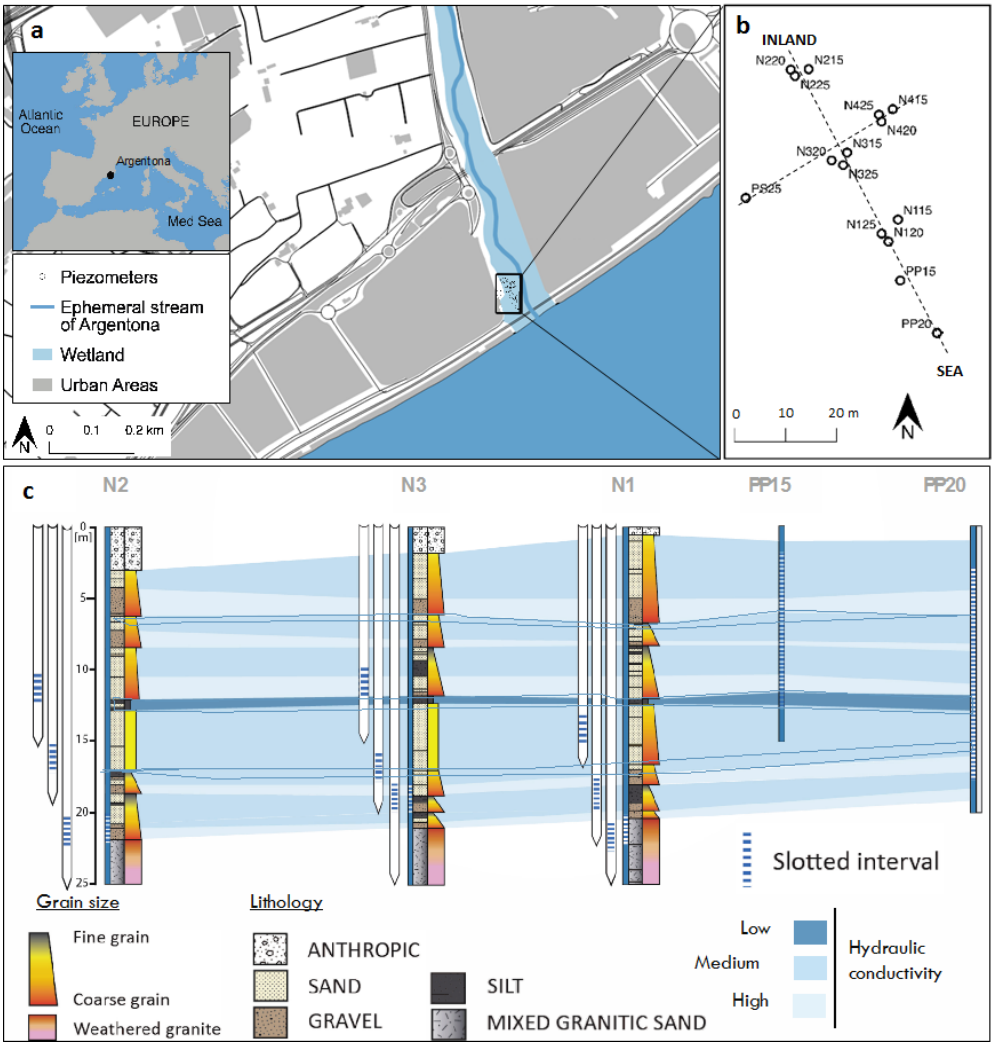

Figure 4-1: Experimental site of Argentona: (a) location, (b) borehole distribution, and (c) aquifer system (Modified from Martínez-Pérez et al. (in press a) and Diego-Feliu et al. (2021))

Water sampling campaigns have been performed using submersible pumps (Gigant Submersible Pumps, Van Walt). Purging duration was determined by pumping at least three times the volume of the piezometer. Groundwater samples were then collected following a strict protocol and stored in pre-sanitized bottles. Sampling bottles had been washed with diluted HNO_3 acid and rinsed with distilled water in the laboratory. Then in the field, each bottle was rinsed three times with groundwater before sampling and every other precaution was taken (use of gloves, handling one sample at a time, cleaning of utensils between taking each sample,…) to avoid any possible contamination. Electrical conductivity (EC), pH, temperature, Eh, and dissolved oxygen are measured on-site with a YSI multiparameter meter, previously calibrated with standard solutions. These measurements are made through a flow cell to directly pass groundwater across

sensors to avoid contact with ambient air and prevent degasification or mineral precipitation. Alkalinity (as HCO_3^-) was analyzed manually by chemical evaluation with sulfuric acid, accounting for the pH of the sample.

Table 4-1 summarizes the considered chemical species for this study, the analytical method, and the laboratory of analysis. The water samples used for this study were collected during the field campaign performed in January 2016 (presented in Martínez-Pérez et al. (in press a)). Please see Appendix C for the full chemical dataset.

As the selected site is a coastal aquifer affected by SWI and SGD, the expected end-members for the mixing zone are a freshwater end-member representing the global aquifer water (SGD) and seawater end-member (for the SWI part). As a representation of such end-members, we considered a well located on the Argentona watershed upper part for the freshwater (F1) and seawater (SW) from the nearby coast. To constrain all the possible water inflows in the Argentona site and to be sure to not exclude any potential end-members, we also sampled the ephemeral stream during a rainfall event (STREAM) and the wastewater treatment plant bypass (SEWAGE) near the experimental site.

Table 4-1 : Chemical species considered, analysis method, and laboratories of analysis.

Chemical species	Symbol	Analysis Method	Laboratory
Chloride	Cl^-	Ion Chromatography (IC)	Catalan Institute for Water Research (ICRA)
Sulphate	SO_4^{2-}		
Nitrate	NO_3^-		
Calcium (Ca)	Ca^{2+}	Inductively Coupled Plasma – Mass Spectrometry (ICP-MS)	Institute of Environmental Assessment and Water Studies (IDAEA)
Sodium (Na)	Na^+		
Magnesium (Mg)	Mg^{2+}		
Potassium (K)	K^+		
Manganese (Mn)	Mn^{2+}		
Iron (Fe)	Fe^{2+}		
Fluorine (F)	F^-		
Silicon (Si)	Si^{4+}		
Barium (Ba)	Ba^{2+}		
Bromine (Br)	Br^-		
Aluminium (Al)	Al^{3+}		
Lithium (Li)	Li^+		
$\delta^{18}O$ and δD	$\delta^{18}O$ and δD		University of Barcelona (UB).
Alkalinity (as HCO_3^-)	HCO_3^-	Titration-based	Field measurement
Electrical conductivity	EC	YSI multiparameter meter	Field measurement
Dissolved Oxygen	O_2	YSI multiparameter meter	Field measurement

4.4.2 Identification and quantification of chemical reactions

We propose a three step procedure for the Identification and quantification of chemical reactions using reactive mixing calculations:

(1) Reactive EMMA for identification of reactions and end-members
(2) Mixing calculations
(3) Quantification of chemical reactions

These steps are detailed below.

4.4.2.1 Step 1: Reactive EMMA for identification of reactions and end-members

Interpretation and representation of hydrogeochemical data may be complex because of the large number of compounds and their time evolution. To simplify the

analysis, the whole chemical data set is presented as a concentration matrix (X) ($n_s \times n$, where n_s is the number of chemical species and n is the number of samples). We used the application of EMMA-MIX (Carrera et al., 2004) to select end-members, evaluate the mixing ratios between different end-members and quantify the reactions occurring in the coastal aquifer of Argentona.

The identification of chemical reactions and end-members follows an iterative process, summarized in **Figure 4-2**:

Preliminary analysis: EMMA is applied to the original matrix X resulting from raw concentration data.

Step a: Propose candidate reactions: this is done by (1) conceptual analysis (some reactions, e.g., cation exchange may be expected to occur), (2) identification of species possibly participating in reactions by checking departures from expected conservative mixing behaviour. For example, the eigenvector associated to FW-SW mixing typically display contributions of $1/\sqrt{n_s}$ for all conservative species except those affected by chemical reactions, which tend to display a reduced contribution. Another typical example is the case of eigenvectors without clear end-members, but involving few species, which might come from a reaction (e.g., an eigenvector with large contributions to Ca^{2+} and SO_4^{2-} can be indicative of gypsum dissolution-precipitation).

Step b: **Build the stoichiometric matrix of the proposed reactions**. This matrix includes the species and the stoichiometric coefficient associated with the reactions.

Step c: Derive components (i.e., combinations of species that remain unchanged by the proposed reactions). This involves (1) computing the components matrix U ($n_s - n_r \times n_s$) from the stoichiometric matrix (see details in Pelizardi et al. (2017) and Molins et al. (2004)), and (2) multiply the vector of concentrations of all species in each sample by the components matrix. This implies obtaining a new data matrix, $X_u = U \cdot X$. In practice, this reduced data matrix results from eliminating the species involved in the reactions and replacing them with the corresponding components u, while keeping the species that do not participate in any reaction.

Step d: Conservative EMMA analysis: EMMA is repeated using X_u. In case new reactions are identified, the procedure is repeated until a significant percentage of the variance (say, more than 90%) can be explained by a few eigenvectors and the data projections are encircled by conceptually reasonable end-members.

In our analysis, described in detail in section 4.5.1, we identified 12 potential reactions in agreement with the geological context and human activities around the experimental site affecting our system:

$Ca^{2+} + SO_4^{2-} + 2H_2O \Leftrightarrow CaSO_4.2H_2O(s)$	Gypsum precipitation	(R_1)
$Na^+ + 0.5X_2Ca \Leftrightarrow 0.5Ca^{2+} + XNa$	Na – Ca Cation exchange	(R_2)
$K^+ + 0.5X_2Ca \Leftrightarrow 0.5Ca^{2+} + XK$	K – Ca Cation exchange	(R_3)
$Mg^{2+} + X_2Ca \Leftrightarrow Mg^{2+} + X_2Mg$	Mg – Ca Cation exchange	(R_4)
$CH_2O + O_2 \rightarrow HCO_3^- + H^+$	Aerobic respiration	(R_5)
$CH_2O + 0.8NO_3^- \rightarrow 0.4N_2 + HCO_3^- + 0.2H^+ + 0.4H_2O$	Denitrification	(R_6)
$2\,CH_2O + 4MnO_2 + 6H^+ \rightarrow 2HCO_3^- + 4Mn^{2+} + 4H_2O$	Manganese reduction	(R_7)
$CH_2O + 4FeO(OH) + 7H^+ \rightarrow HCO_3^- + 4Fe^{2+} + 6H_2O$	Iron reduction	(R_8)
$Ca^{2+} + 2F^- \Leftrightarrow CaF_2$	Fluorite precipitation.	(R_9)
$Ba^{2+} + SO_4^{2-} \Leftrightarrow BaSO_4$	Barite precipitation	(R_{10})
$KAlSi_3O_8 \rightarrow 3\,Si^{4+} + K^+ + Al^{3+}$	Feldspar weathering	(R_{11})
$Al^{3+} + 3H_2O \Leftrightarrow Al(OH)_3 + 3H^+$	Gibbsite precipitation.	(R_{12})

The 2 conservative components resulting from these reactions are :

$u_1 = [Ca^{2+}] - [SO_4^{2-}] + 0.5[Na^+] + 0.5[K^+] + [Mg^{2+}] - 0.5[F^-] + [Ba^{2+}] + 1/6[Si^{4+}]$ (1)

$u_2 = [HCO_3^-] + [DO] + 1.25[NO_3^-] + 0.5[Mn^{2+}] + 0.25[Fe^{2+}]$ (2)

where u_1 corresponds to the reactions associated with cation exchange and minerals dissolution-precipitation affecting $[Ca^{2+}]$ while u_2 is associated with $[HCO_3^-]$ and redox reactions in the fluid phase. So, X_u is the matrix $(n_s \times n)$ containing the two above components and the remaining species not participating in reactions ($[\delta^{18}O]$, $[\delta D]$, $[EC]$, $[Br^-]$, $[Li^+]$ and $[Cl^-]$).

4.4.2.2 Step 2 : Mixing calculations

Once the end-members for each sample are identified using EMMA, mixing ratios can be calculated using the MIX code (Carrera et al., 2004). A feature of this code is that it acknowledges that the uncertainty of end-member compositions may be larger than that of the actual samples. In essence, it is assumed that the measured concentrations, C_{mij}, of species in sample j results from conservative mixing of n_e end-members (Eq. 4-1) plus a

measurement error and that the measured concentrations of end-members, C_{mei}, also contain errors. That is,

$$C_{mij} = \sum_{e=1}^{n_e} \lambda_{ej} C_{ei} + \varepsilon_{mij} \qquad i = 1, n_s; j = 1, n_m \tag{4-6a}$$

$$C_{mei} = C_{ei} + \varepsilon_{ei} \qquad i = 1, n_s; e = 1, n_m \tag{4-6b}$$

where ε_{mij} and ε_{ei} are the measurement errors of concentrations of mixtures (samples) and end-members, respectively. Mixing rations, λ_{ej}, and end-member concentrations, C_{ei}, are obtained by minimizing the objective function:

$$F_{obj} = \sum_{i=1}^{n_s} \sum_{j=1}^{n_m} \left(\frac{\varepsilon_{mij}}{\sigma_{ij}} \right)^2 + \sum_{i=1}^{n_s} \sum_{e=1}^{n_e} \left(\frac{\varepsilon_{ei}}{\sigma_{ei}} \right)^2 \tag{4-7}$$

where σ_{ij} and σ_{ei} are the standard deviations of $\varepsilon_{mij}$and ε_{ei} respectively. These are the only data that needs to be specified, in addition to actual measurements, to run MIX. Here we have assigned by default a standard deviation of 0.1 times the measured concentration ($\sigma_{ij} = 0.1 C_{ij}$), except for very small concentrations ($C_{mij} < 0.1\sigma_{si}$, where σ_{si} is the standard deviation of species i in all measurements), in which case σ_{ij} = $0.01\sigma_{si}$. The same criterion was initially applied to end-members. Variances can be adjusted to broaden or restrict the concentration calculations. To this end, it is convenient to verify the deviation of both end member and sample concentrations from the raw data to ensure that the projections of calculated end-members over the selected eigenvectors using EMMA (**Figure 4-2**e) encircle the samples. Otherwise, σ_{ei} can be adjusted so that the concentrations of the end-members do not deviate too much from conceptual expectations and the distribution is preserved.3

In our case, we had to adjust σ_{ei} for the F1 sample for Cl^- and u_1. The initial values are respectively: 7.210 mmol/L ± 51.98 mmol/L and 1.881 mmol/L ± 528.59 mmol/L.

4.4.2.3 Quantification of chemical reactions

Once the end-member e proportions in sample j (λ_{ej}, Eq. 4-1) are calculated, we can quantify the extent of reactions in the sample j (R_j) occurring in the model (Step 3,

Figure 4-2) for Equation 4-4. Taking advantage that we have built the stoichiometric matrices in such way that considering conservative mixing, the deviation from the measured concentration of specie i ($C_{i_{Meas.}}$) from the conservative mixing concentrations of specie i ($C_{i_{Cons.}}$) can be defined as the reaction extent R_j (Eq. 4-5).

$$R_j = \left[C_{i_{Cons.}}\right] - [C_{i_{Meas.}}] \tag{4-8}$$

where $\left[C_{i_{Cons.}}\right]$ Is calculated using λ_{ej} according to Eq. 4-1, as if there were no reactions (conservative mixing).

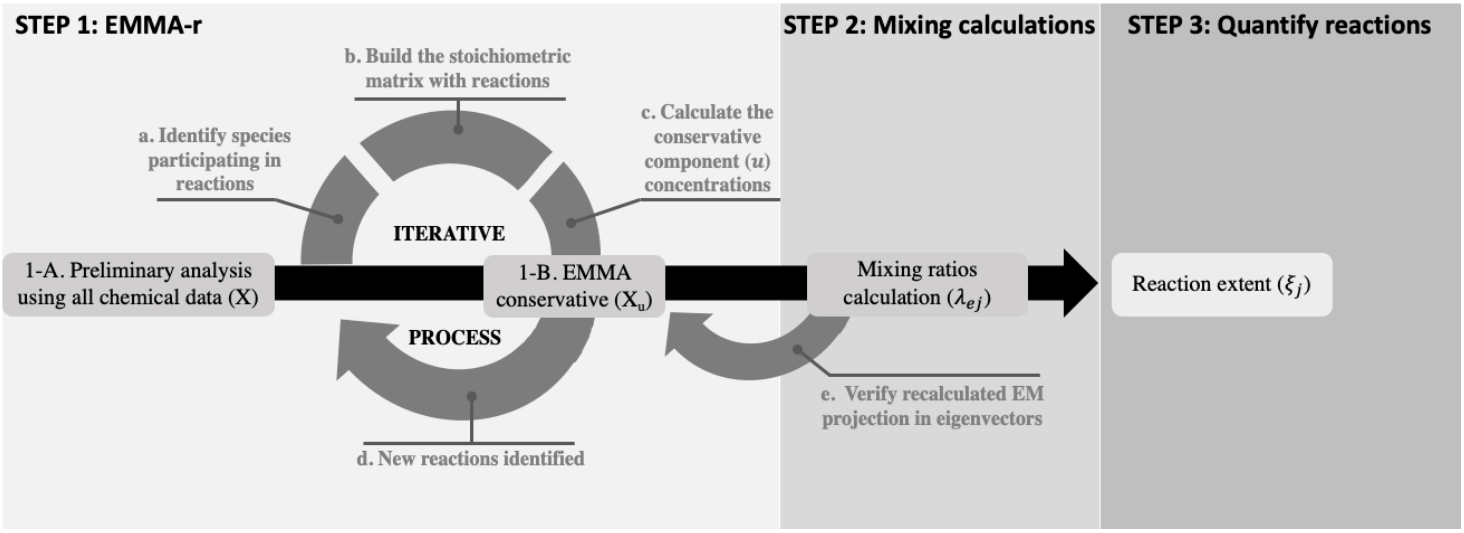

Figure 4-2: EMMA reactive flow chart for the end-member identification and chemical reactions quantification

4.5 Results and discussion

4.5.1 Step 1: Chemical reactions for end-member identification

In this section, we detail how we obtained our chemical reaction system applying the EMMA. In the beginning, the analysis considers all the chemical species (presented in **Table 4-1**) to later narrow down a first set of chemical species implied in chemical reactions. Then, an iterative process begins until a maximum of the variance is explained by the least number of eigenvectors. Moreover, end-members must represent the edges of a plane that involves the chemical composition of our system. **Table 4-2** presents the parameters for each iteration and the results of the variance explained by EG1 and EG2.

Table 4-2 : Parameters varying in each iteration to identify chemical reactions using EMMA. Where n_r is the number of reactions considered, R_n the reaction identifier, n_s is the number of species considered, n_u is the number of conservative components, $\sqrt{1/(n_s+n_u)}$ is the theoretical contribution of each species, if all species and components were equally weighted, and n_e is the number of potential end-members identified.

Iteration number	0	1	2	3	4
$\boldsymbol{n_r}$	0	4	8	11	12
$\mathbf{R_n}$	-	R_1 to R_4	R_5 to R_8	R_9 to R_{11}	R_{12}
$\boldsymbol{n_s}$	20	15	10	6	6
$\boldsymbol{n_u}$	-	1	2	3	2
$\boldsymbol{\sqrt{1/(n_s+n_u)}}$	0.22	0.25	0.29	0.33	0.35
$\boldsymbol{n_e}$	>4	4	4	3	2
EG1 contribution (%)	67.47	62.87	73.03	87.12	96.73
EG2 contribution (%)	11.53	13.96	11.50	10.43	2.10

Iteration 0 or preliminary analysis starts by applying the EMMA the raw chemical data without reactions (i.e., 20 x 18 matrix, both n_r and n_u are set to zero in **Table 4-2**). The two first eigenvectors explain 79% of the variance (EG1 and EG2 relative contributions are presented in **Table 4-2**). As presented in **Figure 4-3**a, the EG1 direction represents the mixing between a freshwater end-member (FW) and the saline end-member (SW). However, at the same time, we observe that many chemical species are affected by other processes than mixing. That is, their contribution is not equal to the theoretical contribution of each species and components ($\sqrt{1/(n_s+n_u)}$) if all were equally weighted (the values are shown in **Table 4-2** and indicated in **Figure 4-3**, top row). Moreover, results show that more than two end-members are needed to explain a significant portion of the data variability ($n_e > 4$, see **Figure 4-3**c). The results from the first iteration (Iteration 0) require chemical reactions to interpret groundwater hydrochemistry.

To acknowledge reactions, in the first reactive EMMA (EMMA-reactive hereinafter) iteration (Iteration 1), we included cation exchange reactions (R_2 to R_4, Na^+, $K^+$and Mg^{2+} with Ca^{2+}) as they represent the main type of reaction occurring in non-karstic coastal aquifers (Russak & Sivan, 2010). We also included gypsum precipitation (R_1) because it is frequently observed and because groundwater composition at the

Argentona experimental site presents a large excess in Ca^{2+} (Martínez-Pérez et al., in press a). Results from the preliminary analysis (Iteration 0) do not indicate that Na^{+}, K^{+}, Mg^{2+}, $SO_4^{2-}$and Ca^{2+}(species indicated by a square in **Figure 4-3**a) are affected by chemical reactions. Despite this, we have decided to include R_1 to R_4 in iteration 1 to highlight the importance of the conceptual model and the robustness of EMMA, allowing us to analyze and discuss the validity of chemical reactions.

Reacting species are eliminated from the data matrix X during EMMA-reactive iterations. Instead, conservative components (i.e. combinations of reactive species that remain unaffected by reactions) are added to X. In iteration 1, the conservative component resulting from cation exchange and gypsum precipitation is: $u_1 = Ca^{2+} - SO_4^{2-} + 0.5Na^{+} + 0.5K^{+} + Mg^{2+}$(see Appendix D1.1). Results of iteration 1 demonstrate two things: (i) The variance explained by the two first eigenvectors is reduced to 76.8%, with a reduction of the EG1 relative contribution (see the difference with iteration 0 in **Table 4-2**); and (ii) We are still not able to identify end-members (**Figure 4-3**f). This lack of improvement reflects that we were not following the EMMA recommendations (i.e. reduced contribution to the eigenvector representing mixing) when considering chemical reactions. In our case, it would have been better to consider other reactions first and possibly add R_1 to R_4 in a later iteration. Consequently, as suggested by EMMA, we added reactions affecting DO, NO_3^-, Mn^{2+}, and Fe^{2+}in the following iteration (indicated in **Figure 4-3**d). Note that all these species are relevant to redox reactions.

In the second iteration, we added 4 more chemical reactions (R_5 to R_8) representing redox reactions. These 4 supplementary reactions make the chemical system more complex with 8 chemical reactions ($n_r = 8$, **Table 4-2**) that lead to a second conservative component ($u_2 = HCO_3^- + DO + 1.25NO_3^- + 0.5Mn^{2+} + 0.25Fe^{2+}$) besides u_1, obtained from the previous iteration (see Appendix D1.2). With two eigenvectors we were able to explain up to 84.5% of the variance. This represents an increase of 5.53% more of the variance explained during iteration 0. Nevertheless, it remains difficult to identify the end-members (**Figure 4-3**i). New reactions are suggested by EG1, affecting the following chemical species: Al^{3+}, F^-, Ba^{2+}, and Si^{4+}(see **Figure 4-3**g). Given the nature of these chemical species and analyzed mineral composition, the missing reactions would be related to mineral dissolution-precipitation reactions. By adding 3 supplementary

chemical reactions (R_9 to R_{11}) a third conservative component can be obtained such that $u_3 = Al^{3+} + 1/3\ Si^{4+}$(see Appendix D1.3). u_3 represents the weathering of the granitic minerals present in the Argentona aquifer. Furthermore, for stoichiometric equilibrium, the conservatives components u_1 now read as follows: $u_1 = Ca^{2+} - SO_4^{2-} + 0.5Na^+ + 0.5K^+ + Mg^{2+} - 0.5F^- + Ba^{2+} + 1/6Si^{4+}$ and u_2 is unchanged.

The iterative process is repeated for a third time. According to this chemical system with 11 chemical reactions ($n_r = 11$), we explain 97.6% with 2 eigenvectors. This iteration gives better results than all the previous ones (+18.55% compared to iteration 0, **Table 4-2**). However, end-members identification remains unclear since it would be necessary to include 3 end-members to explain the data (F1, SW, and N1-25 as suggested in **Figure 4-3**l). The presence of 3 end-members in a case of seawater intrusion is not unusual and has been described in several cases of study in the literature (Chatton et al., 2016; Eissa, 2018; Kim et al., 2017; Sivan et al., 2005; Wicks & Herman, 1996). We see that EG2 is mainly controlled by u_3 which corresponds to the granitic weathering. The fact is that if R_{11}, takes place, for each mole of weathered feldspar, 3 moles of Si^{4+} and 1 mole of Al^{3+} should be added to the solution. But Al^{3+} is unstable in solution at pH > 5, which suggests that some secondary processes of precipitation should be happening.

For this reason, we repeated a 4th and last iteration by adding one last chemical reaction (R_{12}), corresponding to the Gibbsite precipitation (see Appendix D1.4). This reaction removes the Al^{3+} from the solution.

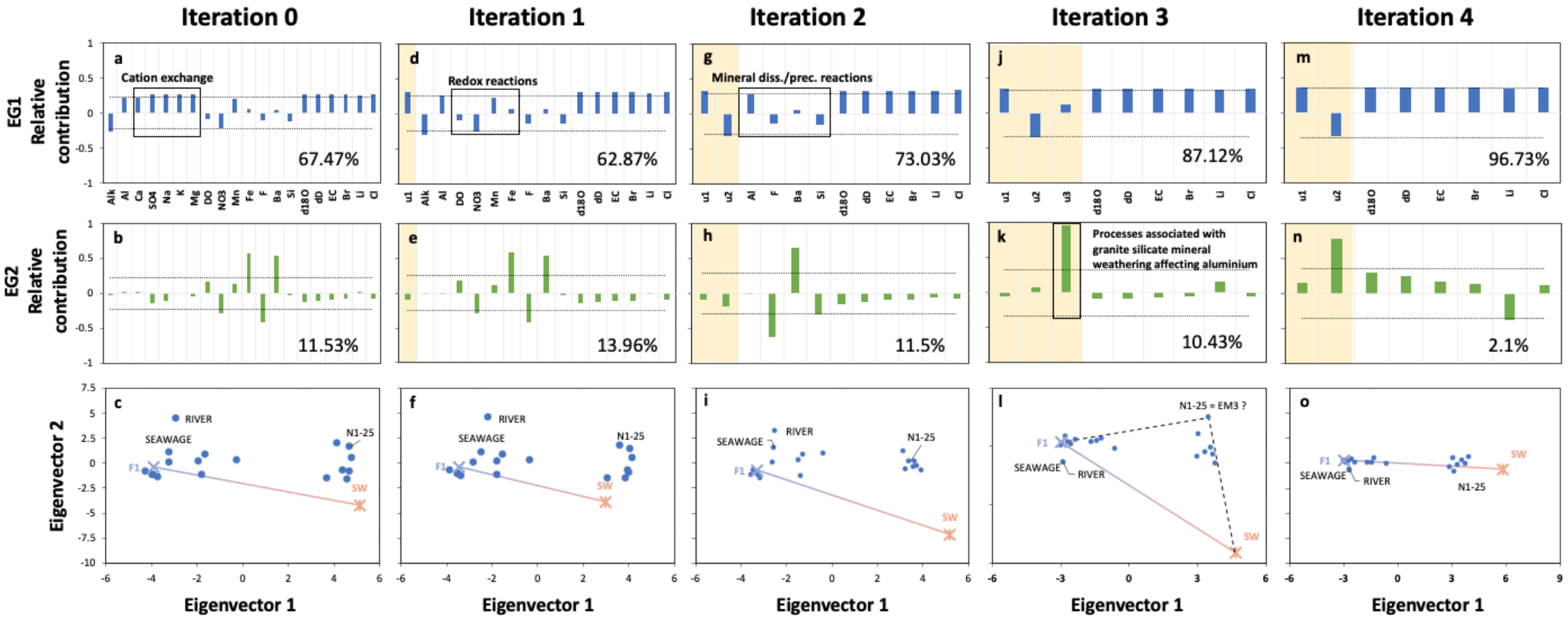

Figure 4-3: Results of the EMMA iterative process for the identification of chemical reactions and end-members. Columns represent the iterations from left to right, going from 0 to 4, with the increasing number of reactions included in the chemical system. (1) species relative contribution to Eigenvector 1; (2) species relative contribution to Eigenvector 2 and (3) EMMA projection of concentration data defined by eigenvectors 1 and 2. Yellow vertical bands represent the number of conservative components involved in each iteration process.

The 4th EMMA-reactive iteration further improves results, with 98.83% of the variance explained by the first 2 eigenvectors. But the greatest improvement is seen in Eigenvector 1 (EG1, **Figure 4-3**m), which explains almost 97%. Furthermore, we observe that almost all the species contribute equally with a relative weight of 0.35 ($\approx \sqrt{1/(n_s + n_u)}$), except u_2 which is anticorrelated (-0.35). As we indicated before, the EG1 direction is controlled by the mixing between freshwater and seawater. Accordingly, the u_2 anticorrelation with EG1 is quite consistent since the chemical species constituting u_2 (HCO_3^-, DO, NO_3^-, Mn^{2+}, Fe^{2+}, F^-) are representative of the freshwater and are poor in seawater with respect to other species. Moreover, in this last iteration, the relative contribution of Eigenvector 2 is reduced to 2% (see the reduction from iteration 0 to 4 in **Table 4-2**). EG2 is characterized mainly by the conservative component u_2 with a relative weight of 0.79. We consider the relative contribution of the rest of the species irrelevant since EG2 represents only 2% of the variance. From these results, the end-members are identifiable in the projection of sampling points using the first two eigenvectors. We observe an alignment of the points in the mixing line between F1 and SW (**Figure 4-3**o).

4.5.2 Step 2: Mixing ratios and recalculated end members

Based on the iteration process we chose the model with 2 end-members (Iteration 4, **Table 4-2**) for our data set. End-members exact composition is recalculated using the MIX code (Carrera et al., 2004) together with mixing ratios for each sample (Step 3, **Figure 4-2**). **Table 4-3**, presents the recalculated composition of end-members. Recalculated end-members are indicated by a subscript letter "r".

For $F1_r$, the code tends to reduce all concentrations, more specifically for Li, Br, u_1, and EC. Changes are respectively: -100% (irrelevant concentration $1.44.10^{-6}$ mmol/L), -63%, -61%, -31%. As EG1 direction is represented by the salinity, recalculated concentrations for $F1_r$ will tend to be much less than seawater (as mentioned in section 4.5.1). This way, both $F1_r$ and SW_r encircle all the other samples in the projection of EG1 and EG2 (not presented here as it overlays with the initial end-members). In the same way, to bring F1 closer to wells Nx-15 in EG1 and EG2 projections, a slight increase in $\delta^{18}O$ and δD with respectively 3.6% and 2.4%.

While for SW_r, the most impacted concentrations are Li and u_2. The code tends to lower them respectively by 58% and 48%. Furthermore, the EC rises from 53.00 mS/cm to 56.89 mS/cm.

Of course, bear in mind that to recalculate the end-members, the MIX code takes into account the variance indicated by the user. As mentioned before, as we were quite in agreement with the end-members initial position, we had to reduce the degree of freedom for two species in F1: u_2 and Cl^-. So that the code does not change too much the concentrations. In the case of more unknown end-members, this variance can be increased to assess the composition of their end-members following the approach of Carrera et al. (2004).

Table 4-3 : Mix calculation chemical composition of the end-members. Units expressed in mmol/L for chemical species and conservative components (u_1 and u_2) and mS/cm for EC.

	u_1	u_2	$\delta^{18}O$	δD	EC	Br	Li	Cl
Input end-members composition								
F1	6.972	7.210	-6.143	-37.527	0.980	0.011	0	1.881
SW	289.085	2.423	0.700	7.500	53.000	0.898	0.028	612.162
Output end-members composition								
$F1_r$	2.738	7.088	-5.92	-36.64	0.672	0.004	0	1.655
SW_r	287.983	1.262	0.684	6.627	56.894	0.883	0.012	552.43

We then calculated the proportion of each end-member in the observation wells using the MIX-recalculated end-members composition. (**Table 4-4**). Results are described, with respect to the distance to the coast, according to three different groups representing the 3 depths (A: 15 m, B: 20 m, and C: 25 m). To simplify the interpretation, fully open boreholes (indicated by ** in **Table 4-4**) have been grouped also by depth: PP15 is described with the 15 m boreholes group (Group A), while PP20 (which is sampled at two depths: 10 m PP20-A and 15 m PP20-B) is associated to the 20 m borehole group (Group B) and 25 m group (Group C), respectively. Furthermore, as the N1-20 slotted interval is deeper than other 20 m boreholes, we include its description with the 25 m borehole group.

The observed general trend is a decrease of the $F1_r$ amount from inland to the coast to the advantage of seawater (**Table 4-4**). The same can be observed with depth.

Table 4-4 : Calculated % of F1r in Argentona experimental site. Calculated using different methods.* indicates wells located on the transect parallel to the coastline, ** indicates fully open wells.

		% $F1_r$ in samples			
Group	**Wells**	**EC**	**Cl**	**H_2O Isotopes**	**Mix code**
A	N2-15	99.7	99.9	98.6	99.7
	*N4-15	99.4	99.6	98.5	99.6
	N3-15	98.8	99.1	93.9	97.4
	N1-15	96.1	96.6	89.0	93.7
	**PP15	93.9	95.0	90.2	92.7
B	N2-20	80.6	83.4	84.4	88.2
	*N4-20	63.2	68.2	75.4	78.3
	N3-20	76.7	80.2	82.4	85.9
	**PP20-A	72.7	76.8	75.2	77.8
C	N2-25	26.5	30.0	34.1	33.3
	*PS-25	13.1	20.7	25.9	24.5
	*N4-25	11.0	18.1	19.8	18.3
	N3-25	12.1	19.5	19.8	18.4
	N1-25	25.2	30.3	34.3	34.9
	N1-20	4.2	14.2	9.2	8.7
	**PP20-B	15.4	23.9	23.7	22.7

Group A results present a large $F1_r$ ratio (>90%). These boreholes are the shallowest, thus located in the freshwater part of the aquifer. The percentage of $F1_r$ decreases from inland to the coast (recall **Figure 4-1** for the locations), decreasing from 99.7% $F1_r$ at N2-15 to 92.7% $F1_r$ at PP15.

Group B includes most intermediate depth boreholes. The percentages of $F1_r$ end-members are still important (between 90% and 77%) with a reduction towards the coast (N2-20 88.2% of $F1_r$ and PP20-A 77.8%). We observed a different amount of SW_r in two boreholes located at the same distance to the coast (N4-20 and N320). SW_r values were higher in the borehole closer to the stream (N4-20), located in the transect parallel to the coast. This difference between the two boreholes could be explained by lateral heterogeneities not considered in this study since it is focused mainly on the axis perpendicular to the coast.

Finally, SW_r is dominating in Group C, with % $F1_r$ <35%. The highest SW_r ratio (91.3% SW_r) for N1-20, corresponds to the intermediate depth of the aquifer and at around 60 m from the coast. This area coincides with the location on a highly permeable layer which confers an important connection with the sea (Folch et al. (2020); Martínez-Pérez et al. (in press a); Palacios et al. (2020) and in Chapter 3 -). Furthermore, in Group C, we observe that the deeper monitored part of the aquifer (N2-25 and N1-25, 33.3% and 34.9% $F1_r$ respectively) contains more FW than the deepest part of the group (8.7%, 18.4%, 18.3%, and 24.5% $F1_r$ for N1-20, N3-25, N4-25, and PS25, respectively). We attribute this feature to their deeper location and

thus a different lithological context (weathered granite) observed by Martínez-Pérez et al. (in press a) at these boreholes. Moreover, the PP20 mixing ratios do not reflect groundwater composition derived from mixing within the aquifer, since vertical flow inside the borehole causes the elevation of the mixing zone at this specific sampling point. This effect was observed by various studies in boreholes fully screened: Church and Granato (1996); Hutchins and Acree (2000); Shalev et al. (2009) and Poulsen et al. (2019).

The contribution to the objective function (F_{Ojb}) obtained by the MIX code after the end-members recalculation are presented for each water sample (18), end-member (2), and chemical species (8) in **Table 4-3**. Note the large contributions of samples from boreholes N1-15 (18%), N3-15 (14%).

N1-15 has its screened interval (from 12.5 to 14.5 m) deeper than other boreholes belonging to the same group (Group A, Nx-15, from ~10 to 12 m). However, N1-15 is shallower than boreholes from Group B (Nx-20, from 15 to 17 m). Also, it is located just below a silt layer, identified at 12 m by Martínez-Pérez et al. (in press a). This silt layer could represent a hydraulic barrier, which would affect mixing zone dynamics. Despite this, N1-15 presents 93.7% of $F1_r$ and a small SWr ratio that is reflecting a low penetration of the saltwater wedge at this sampling hydrologic conditions.

For N3-15, MIX calculations pointed out an analytical error. $\delta^{18}O$ measured concentration is higher (-5.475 ‰) than the calculated concentration (-5.745 ‰). This calculated value is similar to another groundwater sampling campaign (-5.84 ‰), carried out one month later in the same well and with the same hydrological conditions. $\delta^{18}O$ is the chemical species with the highest contribution to the objective function and represents 35% of F_{Ojb} (**Table 4-5**). The rest of the species have a low contribution to the objective function. The large contributions of stable isotopes to the objective function concentrate in the shallowest (freshest) samples, which suggests that the high variability of stable isotopes in rainfall may not be well represented by a single freshwater end member.

Table 4-5 : End-members and observation wells contribution to the objective function by species. Colored data bars are used to highlight the range of values. A longer bar represents a higher value.

		u1	u2	d18O	dD	EC	Br	Li	Cl	Total	Contribution to Fobj (%)
Normalized difference of end-members											
F1 vs F1r		-0.01	-0.08	-0.39	-0.14	-0.01	-0.02	-0.04	-0.01	-0.70	11.67
SW vs SWr		-0.12	0.00	0.00	-0.01	0.00	0.00	-0.16	-0.01	-0.29	4.87
Normalized difference of observation wells											
SEWAGE		0	0	0	0	0	0	0	0	0	0.00
RIVER		0	0	0	0	0	0	0	0	0	0.00
	N2-15	-0.001	-0.003	-0.001	-0.125	-0.01	-0.013	-0.011	0	-0.164	2.74
	***N4-15**	0	-0.005	-0.013	-0.14	-0.016	-0.015	-0.073	0	-0.263	4.39
A	**N3-15**	0	-0.045	-0.575	-0.012	-0.039	-0.064	-0.008	-0.077	-0.82	13.69
	N1-15	-0.001	-0.097	-0.487	-0.149	-0.087	-0.076	-0.002	-0.187	-1.086	18.13
	****PP15**	-0.001	-0.02	-0.125	0	-0.012	-0.007	-0.002	-0.042	-0.21	3.51
	N2-20	-0.006	-0.052	-0.195	-0.076	-0.058	-0.051	-0.009	-0.064	-0.511	8.53
	***N4-20**	-0.023	-0.056	-0.1	-0.037	-0.065	-0.053	-0.002	-0.073	-0.409	6.83
B	**N3-20**	-0.01	-0.062	-0.1	-0.051	-0.059	-0.047	-0.055	-0.063	-0.446	7.44
	****PP20-A**	-0.001	-0.004	-0.018	-0.019	-0.009	-0.003	-0.14	-0.009	-0.203	3.39
	N2-25	-0.033	-0.005	-0.002	-0.007	0	-0.002	-0.049	-0.01	-0.109	1.82
	***PS-25**	-0.071	0	-0.009	-0.019	-0.002	-0.002	-0.001	-0.01	-0.114	1.90
	***N4-25**	-0.001	0	-0.006	-0.007	0	0	-0.026	-0.005	-0.045	0.75
C	**N3-25**	-0.028	0	-0.006	-0.006	0	0	-0.019	-0.004	-0.063	1.05
	N1-25	-0.222	-0.005	-0.053	-0.023	-0.002	-0.003	-0.117	-0.012	-0.436	7.28
	N1-20	-0.064	0	0	-0.009	0	-0.001	-0.009	-0.001	-0.085	1.42
	****PP20-B**	-0.028	0	-0.002	-0.002	0	0	0	-0.003	-0.036	0.60
Total		-0.619	-0.429	-2.081	-0.832	-0.373	-0.358	-0.726	-0.57	-5.991	
Contribution to Fobj (%)		10.33	7.16	34.74	13.89	6.23	5.98	12.12	9.51		

4.5.3 Step 3: Quantification of chemical reactions

Bearing in mind that the calculated concentrations are conservative concentrations, the extent of chemical reactions (R_{rj}, Eq. 4-5) can be quantified by calculating the deviation between the measured and the calculated concentrations. The spatial distribution of R_{rj} expressed in mEq/L is presented in **Figure 4-4** with positive (in red) and negative (in blue) values indicating the reaction direction, while wheat color represents weak or no reaction. As a reference, **Figure 4-4** displays the measured groundwater electrical conductivity to identify the SWI distribution in the aquifer.

Cation exchange reactions represent the most important type of reactions in the Argentona experimental site. Specifically, R_2 presents the highest extent of chemical reactions (R, up to 60 mEq/L). This implies that a lot of Ca^{2+} is desorbed to leave free sites to Na^{+}. This reaction is occurring throughout the aquifer. However, the extent of cation exchange (Na-Ca) is small in the inland and shallow part of the aquifer, where the fraction of SW is small. Note, however, that highest Na^{+}sorption does not occur at the most saline sample, but at the deepest part of the aquifer, in the seawater intrusion front. R_3 displays lower extent values, and a maximum of 6 mEq/L of K^{+} is exchanged with Ca^{2+}. This reaction is occurring principally in the salty part of the aquifer (> 45 mS/cm). The last cation exchange reaction considered is Mg – Ca exchange (R_4). For this reaction, the two directions of the reactions are observed, with some Mg^{2+}sorption ($R > 0$) up to 5.5 mEq/L and a strong desorption ($R < 0$) up to 30 mEq/L. Changes in magnesium concentration can only be explained by sorption/desorption reactions as the only Mg-rich mineral at the site, is a Mg-rich-hornblende identified as trace and could not explain up to 30 mEq/L excess of Mg^{2+} by dissolution processes. Strong magnesium desorption is somewhat unexpected as $[Mg^{2+}]$ is already very high in seawater. Mg^{2+}desorption occurs in the deep and middle aquifer portion in the inland part. At this same level, we observe the highest Na^{+}sorption values. Accordingly, we attribute the desorption of $Mg^{2+}$to the exchange with Na^{+}.In fact, salty samples often display more magnesium than would be expected from seawater (Kouzana et al., 2009; Mahlknecht et al., 2017; Shin et al., 2020). The release of chemical elements can be directly correlated with the ionic strength of the solution and the selectivity of a material for certain cations. Jiao and Post (2019) defined the selectivity sequence as $Na^{+} > K^{+} > Mg^{2+} > Ca^{2+}$, which coincides with

the cation exchange sequence observed in Argentona. Na^+ sorption in the front of the SWI, followed by the K^+ in the salty part and the desorption of the Mg^{2+} a posteriori.

The release of calcium promotes the precipitation of gypsum, R_1 presents positive values. We observe that FW boreholes exhibit values close to 0 mEq/L of gypsum precipitation. The large quantity of Ca^{2+} released during SW penetration, together with the high SO_4^{2-}in seawater (2907 mg/L) promotes the precipitation of gypsum. In this way, the area where gypsum will precipitate the most will be the area where Ca2+ is released. This is confirmed by the gradient observed in the deepest boreholes from inland to the coast, with more gypsum precipitation in the inland part. This is in good agreement with Gomis-Yagües et al. (2000) that demonstrated the possibility of gypsum precipitation during seawater intrusion in the intrusion front. Sulfate concentration reduction can also be attributed to sulfato-reduction reaction as mentioned by Canfield (2001).

For the discussion of redox reaction amounts, it is important to recall that Figure 4-4 should not be interpreted as a map of the place where reactions take place, of the amount needed elsewhere. The values associated to aerobic respiration reflect that SW is initially fully oxygenated as it is in equilibrium with the atmosphere while freshwater dissolved oxygen is reduced due to aerobic reactions in the aquifer. We measured low DO in deep boreholes such as PS25 and N4-25 imply that aerobic respiration (R_5, Figure 4-4) has occurred, but probably not there. Instead, we consider more logical to expect aerobic respiration to occur near the seafloor where organic matter concentration is expected from dead marine biota.

Denitrification is also occurring as R > 0 (R_6, Figure 4-4). The reaction is mainly localized in the middle and deep part of the aquifer section (Nx-20 and Nx-25 level). Unlike R_5, where oxygen comes from the sea, nitrate in R_6 comes from FW, which explains why denitrification is most apparent in the mixing zone. Mn reduction (R_7) and Fe reduction (R_8) display similar patterns, with small reaction extents. Here, negative values indicate that Mn^{2+} and Fe^{2+} are released to groundwater. This occurs only in the deepest part of the aquifer, where O_2 is absent. Elsewhere, Mn and Fe are oxidized. However, it appears that N3-25 stands out from other boreholes located at the same depth. It forms a localized zone with reducing conditions. This effect was observed by various studies (Brown et al., 1999; Chapelle & Lovley, 1992). Redox reactions have been extensively studied in aquifers (McMahon et al., 2011; Rosecrans et al., 2017) and it is well known that they appear in a very precise order. They are

controlled by the availability of dissolved oxygen as the first electron acceptor proceeding from highest to lowest energy yield, as we observe it here DO > NO_3 > Fe > Mn.

Finally, R_9 to R_{10} are dissolution-precipitation processes or weathering of minerals. Fluorite dissolution-precipitation is driven by the Calcium released by cation exchange. Therefore, it is virtually absent in the FW portion and highest where calcium is highest. Both R_{10} and R_{11}, display negative values which indicate mineral dissolution. Barite dissolution (R_{10}) is very low (max 0.0046 mEq/L) and does not show a specific pattern. In the freshwater part of the aquifer, *R* presents higher values (boreholes N2-15, N3-15, and N4-15). Feldspar weathering (R_{11}) is following the SWI shape with more alteration near the coast and increasing with depth (up to 1 mEq/L). Note that, at depth, the granite is also less weathered and willing to further alteration. As a consequence of feldspar alteration, Al tends to precipitate in the same areas and in these pH conditions (pH>5, which destabilizes aluminum). We quantify Al precipitation as gibbsite precipitation (R_{12}) which is consistent with pH variability. Still, some clay precipitation might also act as an Al sink.

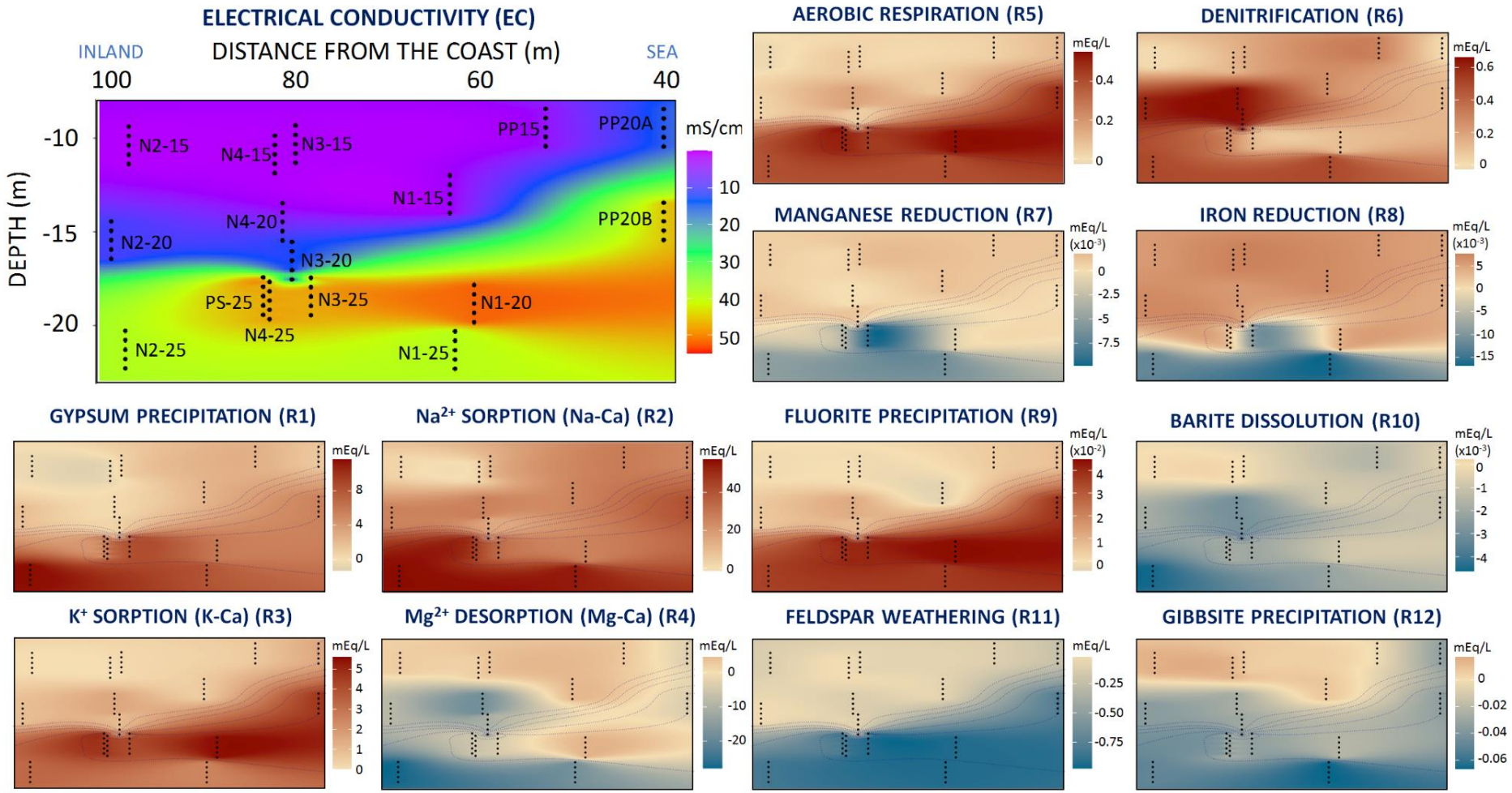

Figure 4-4: Chemical reaction amounts at the site samples. Note that the maps do not represent where the reactions take place, but the amount (mEq/L) needed to explain the observed concentrations. EC is displayed in the upper left as a SWI reference and dotted lines represent EC contours (15, 20, 25, 35, 45 mS/cm) in other subfigures.

4.5.4 Two end-members vs Three end-members accuracy

As presented in Section 4.5.1, the EMMA was suggesting to consider 3 end-members (**Figure 4-3**l) to explain 97.55% of the variance. **Figure 4-5** presents a comparison between the reaction extent using 2 end-members (as presented in **Figure 4-4**) and 3 end-members (F1, SW, and N1-25, **Figure 4-3**l). We observe that, in most of the cases, the reaction extent is much reduced with respect to the case with 2 end-members. We attribute it to mixing. The code tends to add/remove the chemical elements that should come from the reactions by adjusting the 3rd end-member as the sum of the proportion of end-members (λ_{ej}) must be one (Eq. 4-3). Thus, lead to an average of 49% less gypsum precipitation (**Figure 4-5**a) and fluorite precipitation (**Figure 4-5**i) since calcium desorption (R_2 to R_4, **Figure 4-5**b, c, d) is reduced by an average of 31%. This is related to the 3rd end-member composition (recalculated based on N1-25 concentrations), which contributes with more Mg and less Na than seawater, therefore no competition between Na and Mg for exchange sites occurs, avoiding Mg desorption as it was occurring with 2 end-members (**Figure 4-5**d). The reductions of dissolved oxygen (**Figure 4-5**e) and denitrification (**Figure 4-5**f) are much lower (46% and 30% less) since the code tends to dilute oxygen and nitrate concentrations in samples by adding a 3rd end-member with lower concentrations of the same elements. So that the concentration reduction is made by dilution instead of being caused by redox reactions. We observe that using 3 end-members can lead to the opposite reaction as for R_6 where negative R values are observed. With 2 end-members, Mn and Fe reduction (R_7 and R_8) were only affecting the deepest wells, and to a lesser extent Mn reduction was occurring at intermediate depths (Nx-20). However, if we consider three end-members, this manganese reduction is not observed and both Mn and Fe reduction are lower (40 and 50% less respectively). In the same way, barite dissolution and feldspar weathering are reduced by 37% and 57% respectively since the chemical compounds such as SO4, Ba, Si, and Al are modified by mixing processes with the third end-member. In conclusion, adding a third end-member minimizes the occurrence of chemical reactions. It compensates the difference between the conservative mixing line and sampled points by diluting with the composition of the third end-member. So, we consider that the 2 end-members model is the best option for our conceptual model.

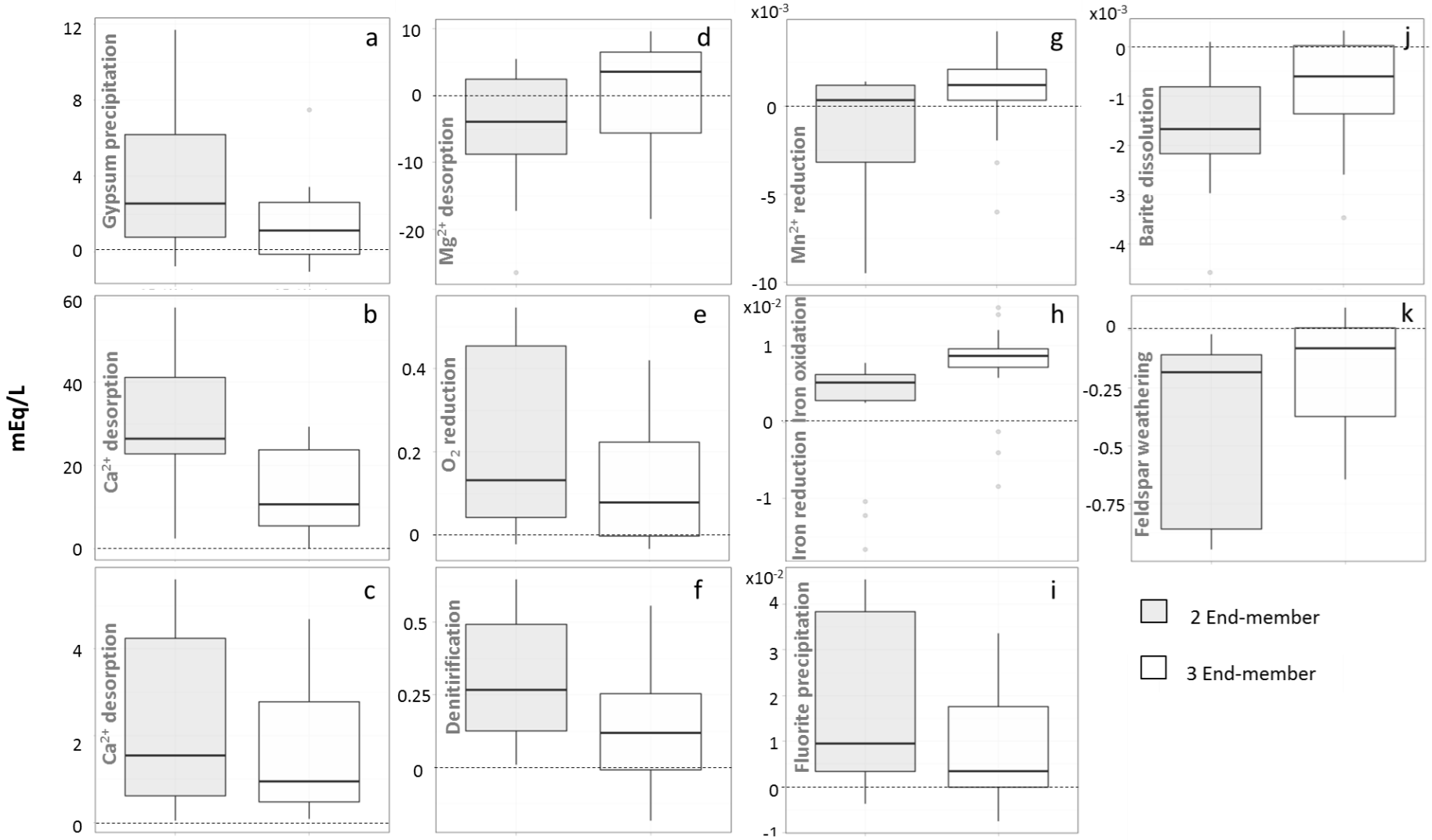

Figure 4-5: Comparison of reactions extent considering 2 end-members (gray) and 3 end-members (white)

4.5.5 Implication for SGD

SGD's contribution to the assessment of biogeochemical cycles at the sea is rarely considered, mostly due to the lack of chemical data (Duque et al., 2020). Indeed, SGD samplings are difficult. In a karstic context, the submarine springs are easily identifiable due to the high flow at the spring location (Fleury et al., 2007). However, chemical sampling remains difficult and requires significant technical resources. In the case of coastal aquifers where the groundwater discharge is slow and diffused through sediments, the spatio-temporal fluctuations of the discharge further complicate its sampling. Therefore, dissolved substances and diffuse pollution are delivered into the coastal zone through SGD via submarine springs and seeps (B. Burnett, 1999; W. C. Burnett, 1996; W. C. Burnett et al., 2001; Monastersky, 1996). Our method could address the limitation due to sampling constraints since we can determine SGD composition by quantifying the chemical reactions occurring in the aquifer linked to the mixing between FW and SW.

For example, as mentioned previously, the simple mixing of end-members cannot explain the Ca^{2+} concentrations sampled in coastal aquifers since much more calcium is measured (**Figure 4-6**). At the Argentona experimental site, measured Ca^{2+} concentrations can reach 10 times the concentration measured in seawater. We attributed this concentration to desorption processes (i.e. cation exchange), coupled with some gypsum and fluoride precipitation limiting Ca^{2+} concentration increase. We estimated that the ratio of Ca^{2+} desorption-precipitation decreases from inland to the sea in groups B and C, with an average of 8% ±4% and 19% ±8% respectively. The remaining calcium will reach the sea through submarine groundwater discharge. Ca^{2+} concentrations in the sea are very high (~ 400 mg / L) and the oversaturation in calcite and other carbonate minerals means that the availability of Ca^{2+} is not a limiting element for the biological activity where foraminifera, coccoliths, and corals being the main carbonate organisms in the oceans (Morse & Berner, 1995). Gattuso et al. (1998) demonstrated that coral calcification increases nearly 3-fold when aragonite saturation increases from 98% to 390% and that in the future decrease in the saturation level due to anthropogenic release of CO2 into the atmosphere could impact calcification. This reduction would not be due to the availability of calcium but due to the lowered seawater pH, reducing the carbonate ion concentration, and the saturation states of biologically important calcium carbonate minerals (S. Barker & Ridgwell, 2012). Then, the inputs of Ca^{2+} concentrations are not a

risk for submarine ecosystems, since they already have an important availability of dissolved calcium in the sea.

This is not the case for nitrates, N is a limiting element in most oceans (~75%, Bristow et al. (2017)) for photosynthetic organisms (plants or algae). But it is essential for photosynthetic organisms (plants or algae). The nitrogen cycle has been dramatically altered by industrially fixed nitrogen by humans. We have seen that the aquifer plays an important role in the degradation of nitrates, through denitrification. The problem appears when the FW coming from inland has too many nitrates and the denitrification mechanism is not sufficient to eliminate the nitrate overload. The consequences can be serious for underwater ecosystems such as coral reefs or organisms that require oxygen that end up dying asphyxiated by the uncontrolled growth of algae. Actually, no safe level of nitrate has been established for aquatic animals (Scott & Crunkilton, 2000; U. S. Environmental Protection Agency, 1986). The only existing limitation is for seawater culture with a maximum concentration of 20 mg NO3-N / l (Spotte (1979), indicated by a dotted line on **Figure 4-6**b). In the case of Argentona, if there were no reactions and nitrate concentration would be reduced by dilution only, this limit would be exceeded at all the shallow wells (N2-15, N3-15, and N4-15) where there is less than 5% SW. Considering denitrification, only F1 (freshwater end-member) and N2-15 (in the farthest nest from the coast with only 0.3% SW) exceed this limit. Then, we see that nitrates are gradually degraded throughout the mixture within the aquifer (**Figure 4-6**).

Finally, seawater is characterized by low Fe (10–100 µg/L, Armstrong (1957)) because it tends to precipitate under aerobic conditions, so that the river inflow is restricted to iron suspended particles. Yet, iron is an oligoelement that limits primary production in large portions of the ocean. For example, Fe loading from SGD has been shown to stimulate primary production in the South Atlantic Ocean (Windom et al., 2006). However, Fe species in dissolved forms require biochemical oxide-reduction reactions to promote Fe mobility. The highest concentrations were measured in N1-25, N2-25 and N3-25 (0.61, 0.48 and 0.41 mg/L respectively). They correspond to boreholes where we identified the highest iron reduction. All are deep wells where oxygen and nitrates are less available (first electron acceptors). A similar observation appears in a recent study in Indonesia (Rusydi et al., 2021). In the rest of the wells, we observe that the concentrations are much lower than the conservative mixing line. It indicates that it

does not meet the conditions for iron reduction reactions making Fe soluble. To summarize, our findings demonstrate that SGD may be a significant source of iron into the ocean wherever organic matter is available to generate Fe reducing conditions.

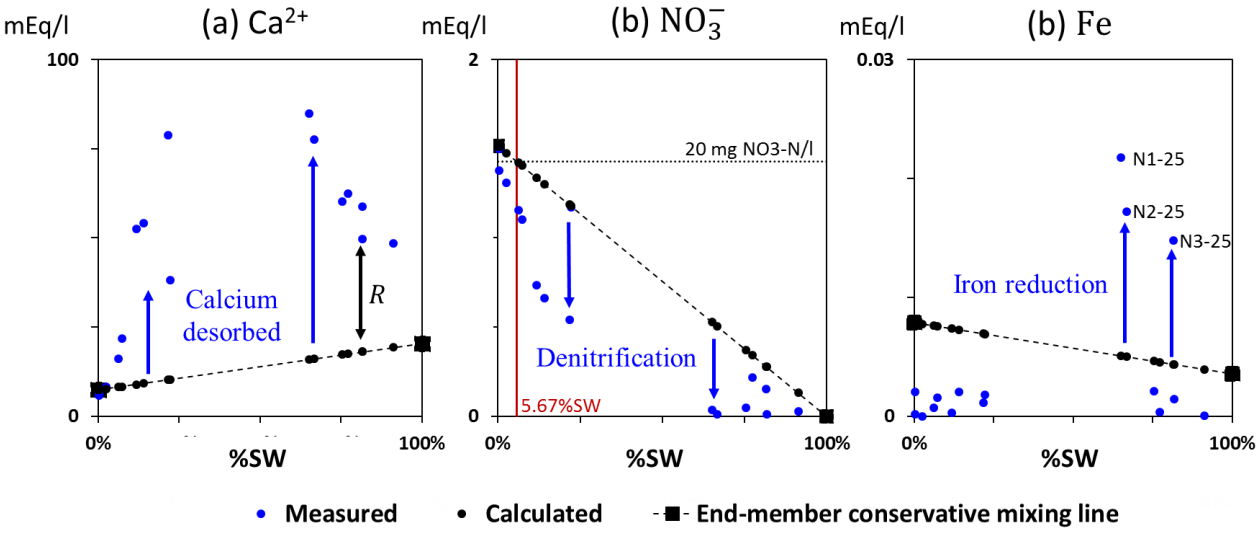

Figure 4-6: Production or loss of key elements (a: Ca^{2+}; b: NO_3; c: Fe) to SGD as a consequence of geochemical reactions induced by mixing between FW and SW

4.6 Conclusion

The End-Member Mixing Analysis (EMMA) associated with the calculation of the mixing ratios is a promising tool to quantify hydrochemical processes occurring in coastal and inland aquifers. In this work, we described a detailed methodology applied to an alluvial coastal aquifer (Argentona experimental site). The presence of chemical reactions in the saline and in the mixing zone between freshwater and seawater has been largely described. This was reflected in the multitude of reactions identified in the analyzed groundwater samples, making the interpretation of groundwater chemical analysis complex. Furthermore, many chemical species, often interdependent, added extra complexity to the interpretation.

As we described in this study, we confirmed the existence of many reactions occurring in a coastal aquifer thanks to the EMMA analysis. Additionally, we obtained a rigorous interpretation of the end-members which was not yet properly assessed and we quantified the extent of the reactions of the different chemical processes occurring in the coastal aquifer. We quantified that the chemical reaction with the highest extent is cation

exchange (up to 60 mEq of Ca^{2+} exchanged with Na^{+}). Calcium is a good example of the interdependence of chemical reactions (involved directly and indirectly in 7 chemical reactions in our system). This indicates that at least 8 species would be removed from the traditional EMMA, following the rule of maintaining only conservative species. We also observed that other reactions such as feldspar weathering and gibbsite precipitation are more specific to the experimental site but they do not detract from being important for the identification of end-members. However, there is limited literature on gibbsite precipitation in coastal aquifers.

Moreover, chemical reaction identification and quantification enable to represent and compare the spatial distribution of the ongoing processes inside the aquifer. An important conclusion is that coastal aquifers play an active role in the reduction of groundwater organic matter. Moreover, by quantifying the reactions in the aquifer we can estimate submarine groundwater discharge composition taking into account that other reactions may occur. So it can be a way to get closer to SGD composition in cases that the SGD sampling may be complex or technically not possible. This way, if the aquifer nutrient quantity is greater than the nutrient degradation reaction extent in the mixing zone, this nutrient will be discharged into the sea and may have consequences for submarine ecosystems.

Regarding the implementation of the code in hydrochemical analysis interpretation, we detected that the use of conservative components instead of reactive chemical species reduces the dimension of the chemical system and removes the dispersion caused by chemical reactions. This led to an increase of the EMMA performance (reaching up to 97% of the variance explained for the Argentona experimental site) whereas considering all-species explains a smaller part of the variance (86%). Moreover, the use of MIX to obtain the mixing ratios between the different end-members identified by EMMA has been proven to be a powerful tool that can be applied in a coupled way to aquifers, of special interest for the case of coastal aquifers. However, measurement analytical errors can be an issue for the major eigenvectors distributions, affecting EMMA analysis accuracy. It is therefore essential to apply a tested methodology to avoid errors in the end-members identification, as we demonstrated here with the discussion between using 2 or 3 end-members. The good news is that analytical errors can be corrected using MIX calculations as the variance can be adjusted. We thus

recommend using EMMA analysis coupled with MIX calculations and support it with analyses of other sampling campaigns.

This easy methodology can be extended and strongly recommended to other aquifers to understand processes and also include it in temporal monitoring (i.e. progradation of carbonate dissolution in karstic systems, trace contaminants discharge/retention and sources).

5

Storm-driven coastal aquifer salinization and submarine groundwater discharge, case of a Mediterranean alluvial aquifer

5.1 Abstract

In coastal aquifers, the fresh-salt water interface dynamics induced by the time variability of recharge affect seawater intrusion (SWI) and submarine groundwater discharge (SGD). The catchments placed in the northwestern coast of the Mediterranean Sea are characterized by heavy rain events in Autumn. Within the coastal aquifers, such events displace the mixing zone, driving back the seawater wedge over a short period. Here, we study the high spatial and temporal frequency response of the mixing zone and its impact on geochemical processes during one such fast freshwater inflow event. We carried the study at the Argentona experimental site (NE Spain), where heads and electrical conductivity are monitored in 16 boreholes along a 100 m straight line perpendicular to the coastline. Water samples were taken over 12 days after the event to monitor changes in aquifer groundwater composition. Furthermore, borehole geophysical methods were applied to perform vertical electrical resistivity tomography and downhole profiles of formation electrical conductivity from electromagnetic induction. Results of this almost 2 weeks-long campaign show (1) different head responses, which helps in confirming the hydrostratigraphic model; (2) changes in salinity, which suggest that dilution occurred rapidly after the event, followed by a recovery towards higher salinity values, which suggest transient response; and (3) biogeochemical changes, which indicate that cation exchange, precipitation-dissolution reactions, and a lower organic matter degradation occurred immediately after the event.

5.2 Introduction

Coastal aquifers play an important role in the water supply of coastal areas (Custodio, 2005). Moreover, they are considered the main nutrient supplier for coastal ecosystems. In the future, the increasing populations will impose a greater food demand promoting intensive farming practices with consequences through nutrients leaching into groundwater resources (Nikolaidis et al., 2008). The pressures may get even worse with the effect of climate change (Sherif & Singh, 1999), which brings more frequent extreme events and longer dry periods (Hoegh-Guldberg et al., 2018; Westra et al., 2014).

In the Mediterranean region, damaging floods are already more and more frequent and with an increasing magnitude (Gaume et al., 2016). These episodes are potentially dangerous due to their duration, extension, and possible virulence. On the Spanish Mediterranean coast, storms usually occur in Autumn and are often associated with heavy/torrential rains and huge waves. This meteorological phenomenon, known as "gota-fria" in Spain, is formed by the descent of a cold and dry air mass from the north pole that meets a hot and humid air mass heading north. This encounter causes rapid condensation and consequently extremely intense rains (Diez et al., 2013). “Gota-fria” events usually last a few hours to one day, until those conditions are over, accumulating precipitation up to 200 mm.

Usually, water quality data are obtained from routine aquifers monitoring at (bi)monthly resolution. These can provide valuable information for the identification and characterization of underpressure sites. Nevertheless, they do not capture the high-frequency dynamics of the system. Problems associated with low-frequency sampling are well documented (Papapetridis & Paleologos, 2011). Moreover, hazard assessment is mainly focused on the surficial hydrologic impacts of storms (Adger et al., 2005) and not on the subterranean processes. Nevertheless, in the last decade, some event-driven sampling campaigns have been performed, particularly with the development of automatic samplers, but mainly applied to surface-water or karst springs (Field, 2021; Horowitz, 2008; Johnes, 2007; Kilroy & Coxon, 2005; Rabiet et al., 2010; Schleppi et al., 2006). Groundwater contamination and recovery after storms are seldom studied and even let alone documented due to the monitoring complexity and cost (Cardenas et al., 2015).

Consequently, few storm events have been studied in coastal aquifers. A particular interest has been given to storm surges since coastal areas not only yield to inland floods caused by rains and rivers. During storm surges, such as tsunamis-like, seawater inundates coastal areas resulting in direct infiltration of saline water at the top of the aquifer leading to significant vertical seawater intrusion (Ataie-Ashtiani et al., 2013; Wilson et al., 2011). The mechanism of vertical salinization appears in several recent studies (Mahmoodzadeh & Karamouz, 2019; Paldor & Michael, 2021; J.-A. Yang et al., 2018; J. Yang et al., 2013; J. Yang et al., 2015; Yin et al., 2016; Yu et al., 2020). The low elevation along the Mediterranean coastline classifies the aquifers as risky areas to storm surges (Androulidakis et al., 2015). The consequences (anthropic, economic, social, and environmental) on the ground are known to be potentially serious but they can be relevant and not directly visible in the underground. Storm surges can thus salinize groundwater drinking aquifers, affecting potable water resources. Quantifying aquifer salinization due to storm surges is complex as storm surges are very punctual during extreme events and appear on short time scales. Moreover, the impacts on the aquifer (changes in head and salinity) can persist and damage water quality (Paldor & Michael, 2021). Several studies highlight the importance of intense monitoring in coastal aquifers to acquire more data in different hydrogeological conditions (Ketabchi et al., 2016; Werner et al., 2013). Geophysical (time-lapse) measurements are quite accurate in coastal aquifers to monitor seawater intrusion and also storm surges (de Franco et al., 2009; Huizer et al., 2017; Ogilvy et al., 2009; Sherif et al., 2006). Additionally, geophysical data can be helpful for groundwater model validation (Beaujean et al., 2014; Nguyen et al., 2009). However, even if they can give us a proxy of the groundwater salinity, these tools do not inform us about the quality of the water resource, its composition, and its geochemical evolution.

The main objective of this paper is to study the implications of a storm event over coastal aquifers dynamics. We especially focused our study on the increase in groundwater level and water quality variations. To do so, we use a combination of geophysical and chemical techniques together with geochemical modelling tools (End-members mixing analysis with chemical reaction quantification: EMMA-Reactive, presented in Chapter 4 -) in dynamic conditions to follow the displacement of the mixing zone and its consequences over the chemical reactions occurring in the aquifer. This approach allows us to predict submarine groundwater discharge composition and the potential effect on the local coastal ecosystem. The

developed methodology, coupling direct field monitoring and numerical modeling, is essential for local governmental institutions management and non-governmental organizations.

5.3 Material and Methods

5.3.1 Site description and well instrumentation

The consequence of an intense rainfall event in a coastal aquifer has been monitored on the Argentona experimental site (site presented by Martínez-Pérez et al. (in press a), **Figure 5-1**a). This site is located 30 km north of Barcelona on the Maresme Coast. It is characterized by a Mediterranean climate with dry summers and mild, wet winters. It is situated at the mouth of the ephemeral stream of Argentona. The streamflow, and so the alluvial aquifer recharge, are controlled by precipitations mainly concentrated in heavy rain events during the Autumn. The average precipitation is approximately 600 mm/year. With an area of 77.86 km^2, the catchment of the Argentona stream is fairly small. Its length is only 20.02 km and makes it the largest stream of the Maresme Coast (Cisteró & Camarós, 2014). As a consequence of its reduced dimensions, the Argentona stream has a low time of concentration (time needed for water to flow from the furthest point to the watershed outlet, Haan et al. (1994).

The experimental site is well equipped and several previous studies have been published (on geology description (Martínez-Pérez et al., in press a), geophysical equipment (Folch et al., 2020), fiber-optic distributed temperature sensing (Del Val et al., 2021), cross-hole electrical resistivity tomography (Palacios et al., 2020), radium and radon isotopes (Cerdà-Domènech et al., 2017; Diego-Feliu et al., 2021). It is composed of 17 wells drilled through alluvial sediments deposited from the stream (**Figure 5-1**b). 12 of the wells are grouped in nests. In each nest, there are 3 wells with different depths: 15, 20, and 25 m and are open over 2 m. These wells are identified as follows: Nx where x ranges from 1 to 4 followed by the depth (i.e . N1-15 indicates the 15 m well of nest 1). There are also 2 single wells (PS-25 and PP18), and 2 additional fully open wells (PP15 and PP20). Finally, the Argentona experimental site presents a 30 m deep well (MH) located between N3 and PS-25 (**Figure 5-1**c).

The geology of the site described by Martínez-Pérez et al. (in press a) presents an alternation of silty and sandy layers. They are typical materials of fluvial deposits where the stream strong energy mobilizes thick and more permeable material and the lower energies thin material with low permeability. The latter seems to have an importance in the hydrodynamics

of the aquifer (see details in Chapter 3 -) and consequences over the intrusion (Palacios et al., 2020).

All wells are equipped with data loggers that measure pressure and temperature at 15 min time steps. Also, data loggers in 20 m and 25 m depth boreholes register groundwater electrical conductivity (EC_w) every 15 min. The Nx-25, PP15, and PP20 are equipped with 36 electrodes along depth that allow performing Cross Hole Electrical Resistivity Tomography (CHERT) measurements as described by Palacios et al. (2020). Also, electrodes along depth allow downhole electrical resistivity logs measurements. The MH well is equipped with the Subsurface Monitoring Device (SMD) from the french imaGeau company. It is a fully automated system for log-type measurements of ground electrical conductivity that allows continuous monitoring of the aquifer properties.

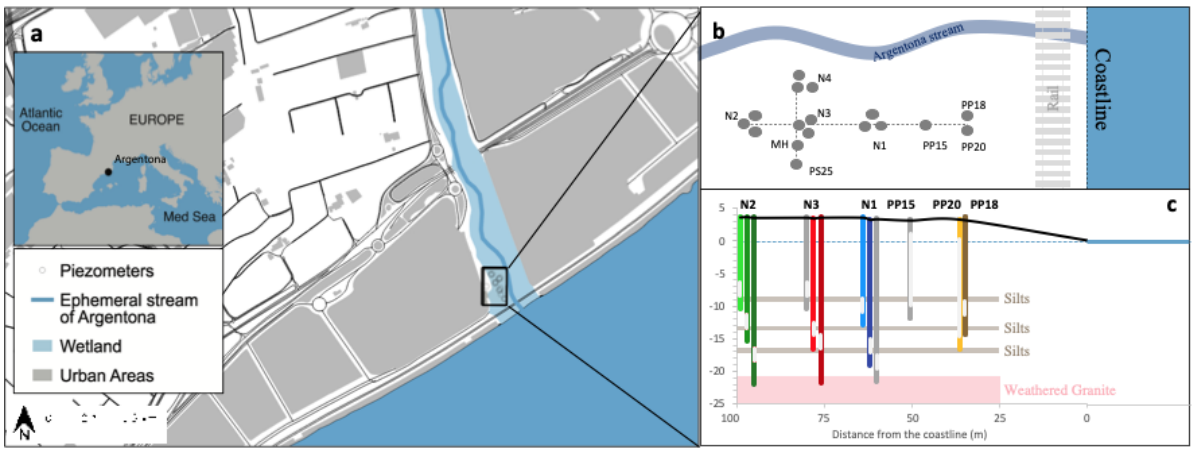

Figure 5-1: (a) Site location; (b) boreholes distribution; (c) cross-section of the transverse towards the sea (Modified from Martínez-Pérez et al. (in press a)).

5.3.2 **Data acquisition**

Heavy rainfall events are not easily predictable in advance. This strongly makes the monitoring complicated. So, to be prepared, special attention to the weather forecast is necessary. In the study area, some heavy rainfall events usually happen during the autumn. 50% of rainfall events above 50 mm/day are concentrated in the period between August 15 and September 30. So, we expected that during this period, at least one intense event could occur. Before this period, all the material and measurement equipment maintenance had been done and the transverse towards the coast (transect perpendicular to the coast) of the Argentona experimental site was chosen to monitor the coastal aquifer (**Figure 5-2**).

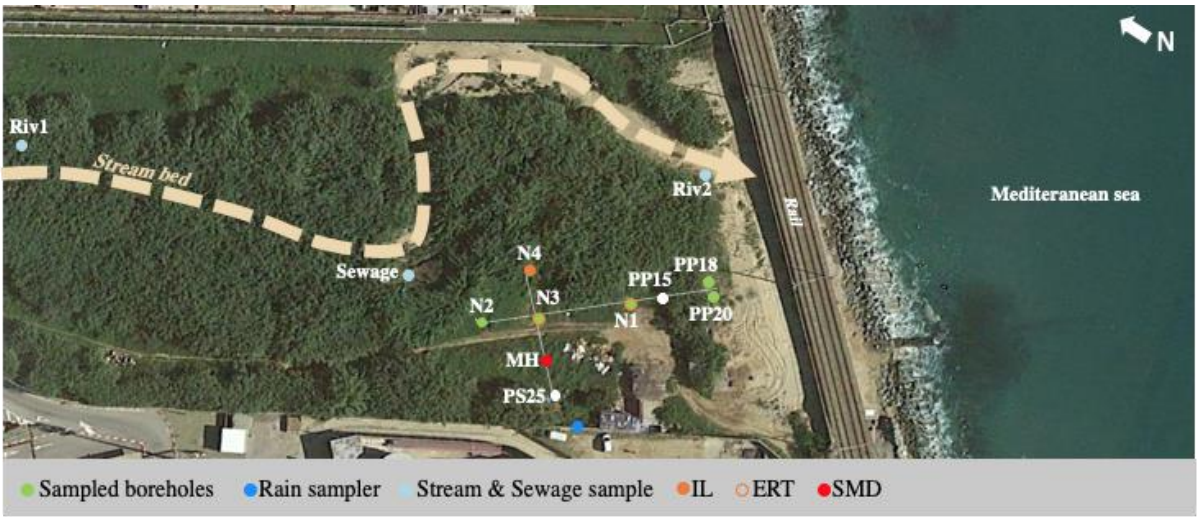

Figure 5-2: Spatial distribution of the boreholes and their specific measurements with groundwater, rain, stream and sewage sampling points and boreholes with geophysical measurements.

The time interval of the data sets considered in this document goes from October 16 to October 31, 2017. This period includes all the data related to the "gota fria" that affected the Maresme coast on October 19, 2017, with a total precipitation of 74.5 mm. The rainfall data has been provided by the Cabrils meteorological station (5 km southwest from the site), from the Catalan meteorological service (METEOCAT, 2017).

During this period, a series of different measurements have been acquired. The hydrostatic pressure data measured with data-loggers were converted to head water levels considering atmospheric pressure data recorded by a data logger installed on-site. Head water levels were filtered using the Godin method as described in Chapter 3 - . Sealevel and wave height data were collected from the closest tide gauge, located at Barcelona Port (Puertos del estado, 2017).

Both water and rock electrical conductivity were measured depending on the techniques: (i) manual measurement during hydrochemical sampling and (ii) data-loggers measurements for groundwater electrical conductivity; (iii) geophysical tools for formation electrical conductivity (EC_b): electromagnetic Induction logging (IL), subsurface monitoring device (SMD), and Vertical Electrical Resistivity Tomography (ERT). Sampling and geophysical tools location are presented in **Figure 5-2**. The associated temporal and spatial resolutions of the different measurements are presented in **Table 5-1**. The ERT was measured in the transverse towards the sea in boreholes N3-25 and N1-25 from Oct-19 to Oct-23 in log mode since acquisition time is shorter than CHERT. The acquisition was performed using a

vertical Werner configuration with a measurement device: Syscal Pro 10-channels. To evaluate the changes in aquifer formation electrical conductivity, we use an ERT baseline from Sept-28 presented in Palacios et al. (2020). Finally, downhole electromagnetic Induction logging was carried out in one borehole (N4-20) with measurements only during the daytime on Oct-16, Oct-17, Oct-19, and Oct-20. Due to interferences with the borehole metallic cap, measurements start 5 m below the surface. The first measurement performed on Oct-16 is defined as the baseline. For technical issues, measurements stopped at the end of Oct-20. Note that ERT and SMD measurements are not intrusive as they are permanently installed in the PVC casing of the boreholes. IL is an intrusive technique, since the probe is deployed inside the PVC casing, so we cannot perform it into a well where groundwater samples will be taken. IL measurements cannot also be deployed into Nx-25 boreholes as the metal electrodes of the ERT interfere with the IL acquisition. Using geophysical methods, we can monitor the electrical conductivity of the formation EC_b which is linked to the electrical conductivity of water (EC_W), the formation factor (F), and a surface conduction term (C_s) through Archie's law equation: $EC_b = EC_W/F + C_s$ (Archie, 1942; Waxman & Smits, 1968). So, during the rainfall event, changes in EC_b imply changes in EC_W since F and C_s can be considered constant. Consequently, EC_b can be used as an indirect measurement of EC_w (Lesmes & Friedman, 2005; Purvance & Andricevic, 2000).

Table 5-1 : Monitoring methods temporal and spatial resolution for mixing zone dynamic

Technique		**Temporal resolution (Δt)**	**Spatial resolution (Δx and Δz)**
(i) Manual measurements	Groundwater sample electrical conductivity	6 sampling days	**Transect perp. to the sea** Middle of the screened interval
(ii) Data-logger measurements		15 min	**Transect perp. to the sea** **Nx-20, Nx-25, PP18:** 1 data-logger per screen interval **PP20:** 2 data-loggers (10 m and 15 m depth)
(iii) Geophysical tools	Electrical Resistivity Tomography (ERT)	30 min	**N3-25 and N1-25** 0.7 m x 25 m
	Electromagnetic Induction Logging (IL)	15 min	**N4-20** 0.1 m x 20 m
	Subsurface Monitoring Device (SMD)	15 min	**BH** 0.3 m x 20 m

The hydrochemical baseline of the aquifer was established for all the boreholes before the rainfall event (Oct-16). Then, during the rainfall event (R: Oct-19) and throughout the rainfall event following days: Oct-20 (R + 1 day and R + 1.5), Oct-21 (R + 2 and R + 2.5), Oct-24 (R + 5), and Oct-31 (R + 12) groundwater was sampled only in boreholes located in the transverse towards the coast (**Figure 5-2**). Groundwater sampling protocol is described in detail in Chapter 4 - : (i) borehole stagnant water is purged by removing 3 times the borehole water volume; (ii) groundwater parameters (i.e. Temperature, pH, eH, and Dissolved Oxygen) are measured through a flow cell; and (iii) samples are analyzed following the laboratory techniques indicated in Chapter 4 - .

Chemical analyses are then used as input values in the EMMA-reactive model. We use the Mix code (Carrera et al., 2004) following the iterative process described in Chapter 4 - . The EMMA-reactive is applied to the full data set (Analyzed samples: 78, Analyzed chemical species: 20) to quantify the chemical reactions identified during the EMMA iteration process in Chapter 4 - . To do so, the calculation is based on a stoichiometric and component matrix leading to conservative components representing chemical reactions (as defined by Pelizardi et al. (2017)). Once the conservative components are obtained, the EMMA can be recalculated using conservative concentrations, and mixing ratios are obtained avoiding the EMMA limitations (i.e. removing species involved in a chemical reaction). In this study, we add the rainfall composition (RW, see sampling location on **Figure 5-2**) as an end-member to the previously identified ones (F1 and SW, see Chapter 4 -) in order to include the recharge effect induced by the storm. A detailed description of the EMMA-reactive can be found in Chapter 4 - . The reaction extent in sample j (R_j) is then calculated from the difference between the conservative concentration and the measured concentration (as presented in Chapter 4 -). However, to compare with results from the previous Chapter, R_j are divided by their freshwater end-member(s) ratio (%FW). As in this Chapter, we consider 3 end-members the %FW is the sum %F1 and %RW.

5.4 Results & Discussion

5.4.1 Rainfall event and analysis of the groundwater-level response

On October 19th, 2017, a rainfall event accumulated 74.9 mm of precipitation. The total amount of rainfall is concentrated in a short period, with 3 main events (**Figure 5-3**). The 3rd event is the most important, with 20.2 mm registered in only 30 min at the Cabrils station Radar images (**Figure 5-3**) identified that the rainfall is coming from the Mediterranean sea heading north. This rainfall event is typical of the aforementioned "Gota-Fria" Mediterranean episode.

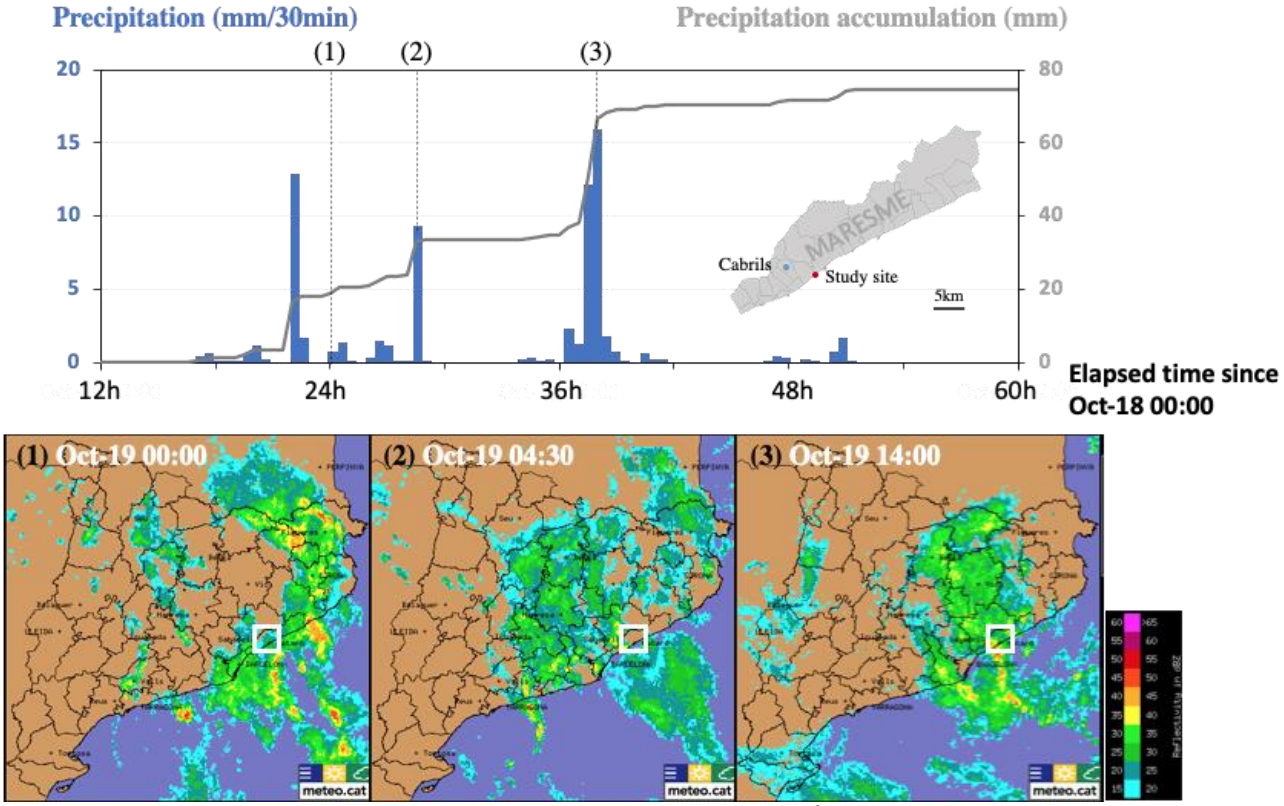

Figure 5-3: Precipitations during the rainfall event of October 19th of 2017. Top: Recorded precipitation in the Cabril station (5 km from the experimental site). Bottom: Oct-19, 2017 rainfall event and radar images from Meteo.cat . The experimental site is located by the square.

With such a great precipitation intensity, the ephemeral streams of the Maresme coast are flooded (**Figure 5-4**a). As an ephemeral stream, the Argentona stream is not part of the hydrometric network. Therefore, the flood discharge value (Q) can be estimated from the precipitations and the return period between 2.33 and 1000 years (Agència Catalana de l'Aigua, 2001) (**Figure 5-4**b). We estimated a stream discharge of 21.49 m3/s from the 74.5 mm

precipitation. As the experimental site is in the stream bed, we know that it was flooded during the rainfall event. The Catalan Water Agency estimated a time of concentration between 2.6 and 5.7 h for the Argentona stream. At the experimental site, we observed a streamflow event lasting 2 to 3 hours. The stream started to flow at 3:26 p.m. and intensified until 4:47 p.m., when we decided to evacuate the site because of the intense flooding at the site (water level increased ~ 30 cm at N4, the closest nest to the stream). At 6:35 p.m. water stopped flowing through the stream. The peak of the rain was recorded at 2:00 p.m., so we estimated a response time of the stream between 1h30 and 2h. Note that during the flood, well N4-20 remained open since the geophysical probe was inside the PVC casing making records with the electromagnetic induction tool (IL). This borehole was therefore instantly filled by the stream floodwater.

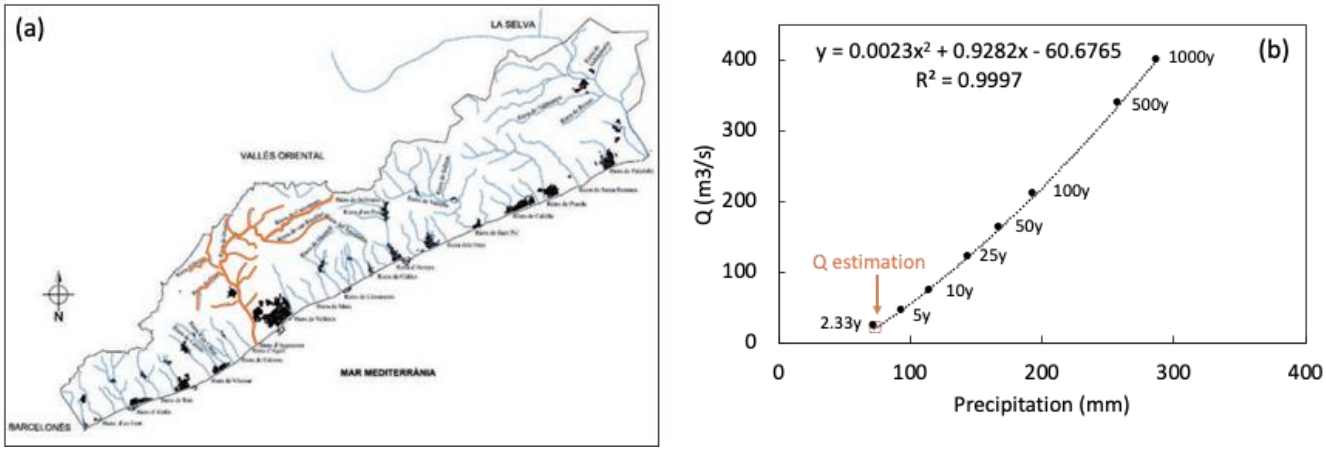

Figure 5-4: Flooding in the Argentona ephemeral stream. (a) Maresme ephemeral streams, Argentona stream is indicated in orange (Source: Cisteró and Camarós (2014); (b) Return period for Argentona discharge estimation

The results of groundwater level monitoring are reported in **Figure 5-5**a and b. The hydraulic head is affected in all wells by the storm. We observe a rise of the aquifer level up to almost 40 cm. The aquifer reaction time is much slower than the stream, and the peak is observed between 18 and 42 h later depending on the observation depth. In the shallow wells, a high amplitude (>25 cm) and a short response time (<30 h) is observed while a low amplitude (<15 cm) and long response time (>42 h) is noticed in deeper wells. This different response could be interpreted as recharge from the surface, since the shallowest aquifer levels will be the first to respond. Moreover, the geological structure of the aquifer is characterized by localized silt layers that isolate the deepest aquifer sections.

This leads us to question the impact of the stream on the aquifer, and their interconnection. Actually, from the observations, the stream flooding does not seem to be the cause of groundwater flooding since the aquifer level has an average level of 3 m below the surface. Furthermore, the short flood extension in the stream demonstrates that runoff controls the streamflow with little infiltration during intensive rain. This is very characteristic of the Maresme streams, where most of the rain is transported by runoff towards the sea with a short transit time due to the steep slope and the small catchment size.

The coastal aquifers' head on the sea boundary is imposed by the sea and its fluctuations. But the impact of the sea-level fluctuations dissipates moving inland. So, it is difficult to distinguish which part of the aquifer level rise can be attributed to the rainwater infiltration and the rise observed in the sea (**Figure 5-5**c). Before the storm, a reduction of almost 10 cm of the water table is observed. In this specific case, we attribute the reduction to the sea level decline, where a reduction was measured the days before the rainfall. Also, the sea-level rise could create a load over the seabed favouring a faster reaction of the boreholes located below the silts layers. In Chapter 3 - , we discuss this kind of observed behavior in the deepest boreholes during tidal fluctuations. The loading effect cannot be considered here as the response in the deepest borehole happens later.

Moreover, during the storm event, the rise in sea level is coupled with high waves reaching an average of 2 m in height and maximum values of almost 3 m. As a consequence, low lands of the Maresme coast can be threatened by storm surges. Furthermore, at the site Palacios et al. (2020) observed in CHERT panels salinization during another storm event. For the studied event, coastal flooding was observed at least in the first 10 m from the shore, perhaps it reached the closest borehole (PP20 at 40 m from the coastline) or the lowest borehole (PP15, 2.66 m amsl). Some additional data should be necessary to confirm it.

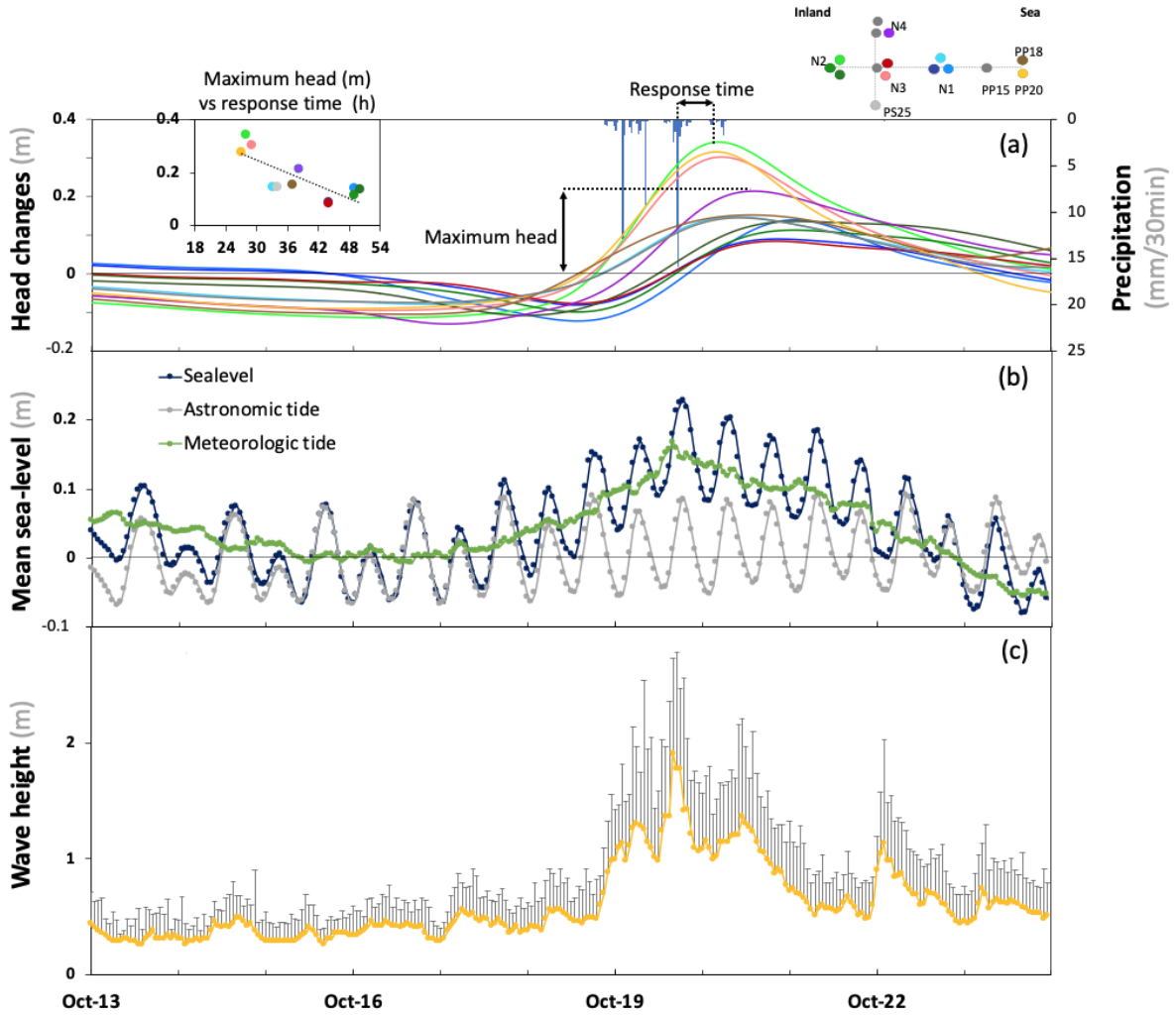

Figure 5-5: Aquifer head affected by the recharge from the rainfall and the sea-level fluctuations during the event. (a) Groundwater level measured in Argentona Experimental site during the rainfall event. Box present: Aquifer maximum head and response time; (b) Mean sea-level measured and (c) Mean wave height at the closest tide-gauge (Barcelona Port). Error bar in (c) represents waves maximum.

5.4.2 **Mixing zone movement**

Figure 5-6 presents the electrical conductivity (EC_W) changes in N3 during groundwater sampling. We observe different behavior according to the three observation depths (N3-15, N3-20, N3-25). In the upper part of the aquifer (15 m), we observe a freshening. After the rain, groundwater EC_W is reduced by 15% and remains at the same value until the last sampling. At intermediate depths (20 m), groundwater becomes saline just after the rain, increasing by 10% the baseline value. This rise is not continuous because we observe a small reduction of the EC_W in samples 4 (22/10) and 5 (24/10). In the deeper part of the aquifer, EC_W

is reduced by 10% in the post-rain sampling. This decrease in EC_W is followed by salinization, with an increase of 5% more saline than the baseline performed 15 days after the baseline.

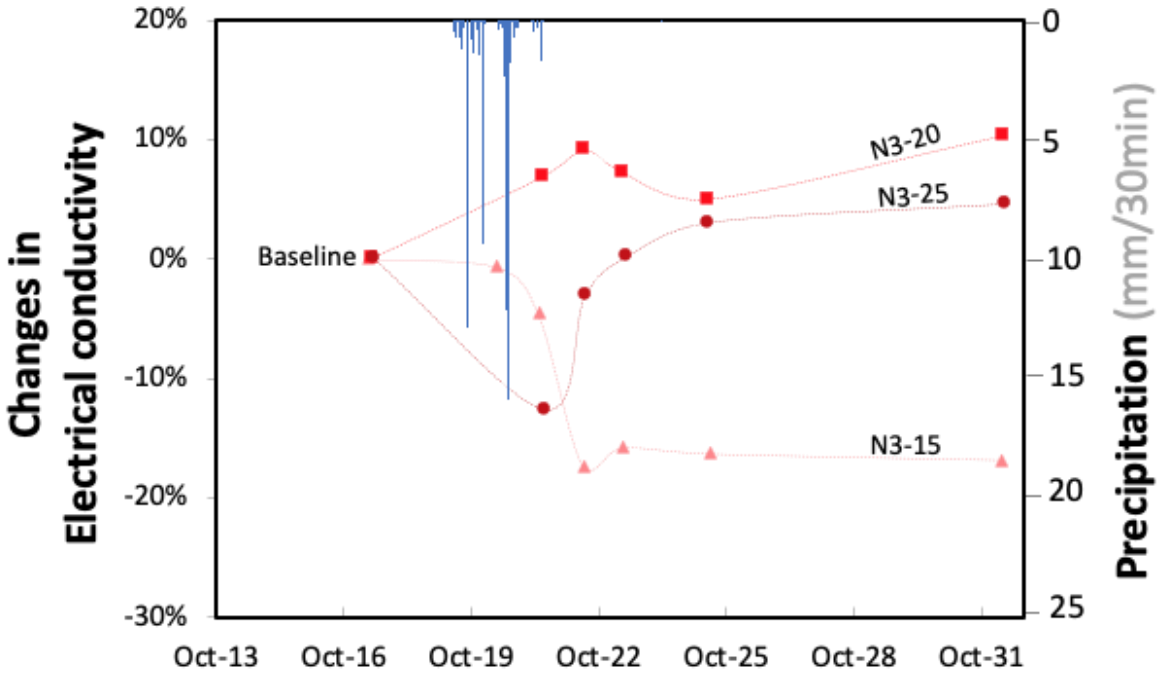

Figure 5-6: Freshening and salinization during the rainfall event. Water electrical conductivity measurements (in red) for N3 boreholes and storm precipitation values in blue.

During this rainfall event, data loggers monitored groundwater electrical conductivity evolution within the wells. As presented in **Figure 5-7**a, the obtained measurements dropped during each water sampling. Furthermore, we observed that immersion and/or removal of the pump also introduces a measurement error. The biggest problem comes from the pumping itself as we first purged the borehole before sampling. This procedure induces a temporal mixing of waters in the pumping zone, implying time for the water in the well to return to an equilibrium state (**Figure 5-7**b). This re-equilibrium time will depend on the sampling frequency and on the permeabilities of the different aquifer layers adjacent to the sampling points. In general, the more widely distributed in time the sampling will be, the less the series of continuous measurements will be impacted.

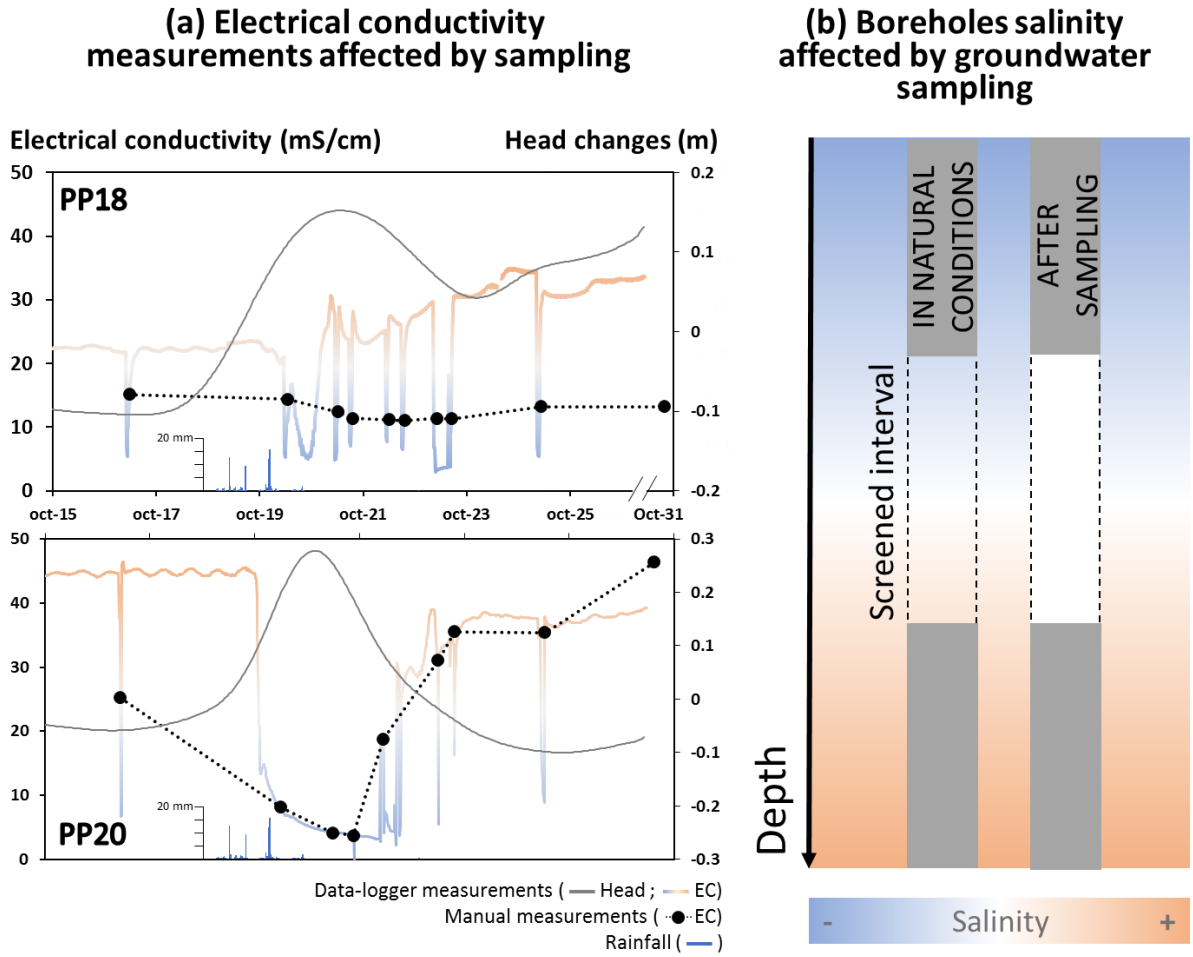

Figure 5-7: The effect of sampling in boreholes. (a) Continuous Electrical conductivity measurements affected by sampling; (b) Explanation of salinity variations induced by groundwater sampling.

Results for the 3 geophysical techniques (SMD, ERT, and IL) applied in 4 boreholes (N3-25, MH, N4-20, and N1-25) are presented in **Figure 5-8**. During the baseline, the first 14 m of each borehole reflects freshwater. Then, a clear transition is observed from 14 m to 17 m with increasing conductivity values. Except for N4-20, since the borehole was not deep enough to register the full transition zone. In the other boreholes, the maximum conductivity values are reached between 16 and 17 m depth. Beyond this depth, a decrease in salinity is observed. This decrease was already observed by Palacios et al. (2020) and Martínez-Pérez et al. (in press a). We explain these lower salinities values in depth by silts layers that could create a physical barrier. Indeed, during the rain event, the main changes are observed in the transition zone (between 16 and 17 m). It corresponds to the most dynamic part of the aquifer (Nx-20 boreholes). In this area, the high salinity zone is thinner at N3-25, while it is pushed down in N1-25. In N3-25 it seems that the level located between 17.5 and 18 m was freshened and then

salinized. This effect was already observed thanks to the punctual water conductivity measurements (**Figure 5-6**). N4-20 appears to be freshened with an important movement of the mixing zone followed by a recovery. As the borehole was open during the flood with the IL tool inside, the borehole was immediately filled with the floodwater.

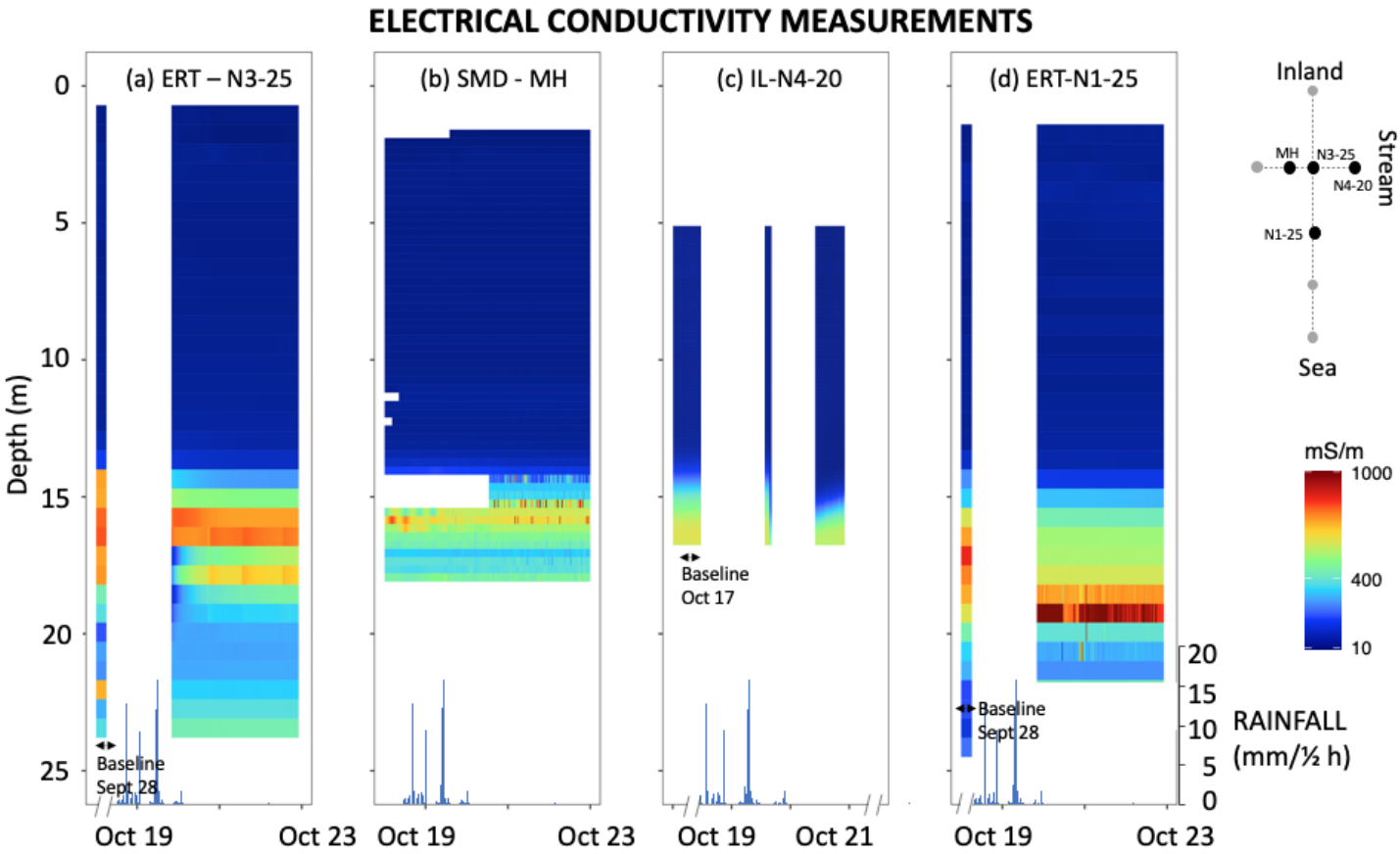

Figure 5-8: Timelapse obtained from geophysical measurements. EC_b measured in boreholes N3-25, MH, N4-20, and N1-25.

5.4.3 **Mixing ratios evolution**

End Member Mixing Analysis (EMMA) projection of groundwater samples (see chemical dataset in Appendix E) on the first 2 eigenvectors, explaining 98.5% of sample variances (**Figure 5-9**). EG1 represents the mix between freshwater end-member (F1) and seawater end-member (SW), whereas EG2 represents the conservative components u_2 (redox chemical reactions). In this projection, we can observe the temporal evolution of groundwater chemistry. This evolution is particularly marked for the fully screened borehole PP20-B. We observed that before the rainfall, its composition is projected near the F1 end-member and moves closer to the SW after the rainfall event. These changes are mainly observed on the main

eigenvector EG1. In this study, the contribution of EG2 is minimal and was added only to highlight the relevance of rainfall composition (RW).

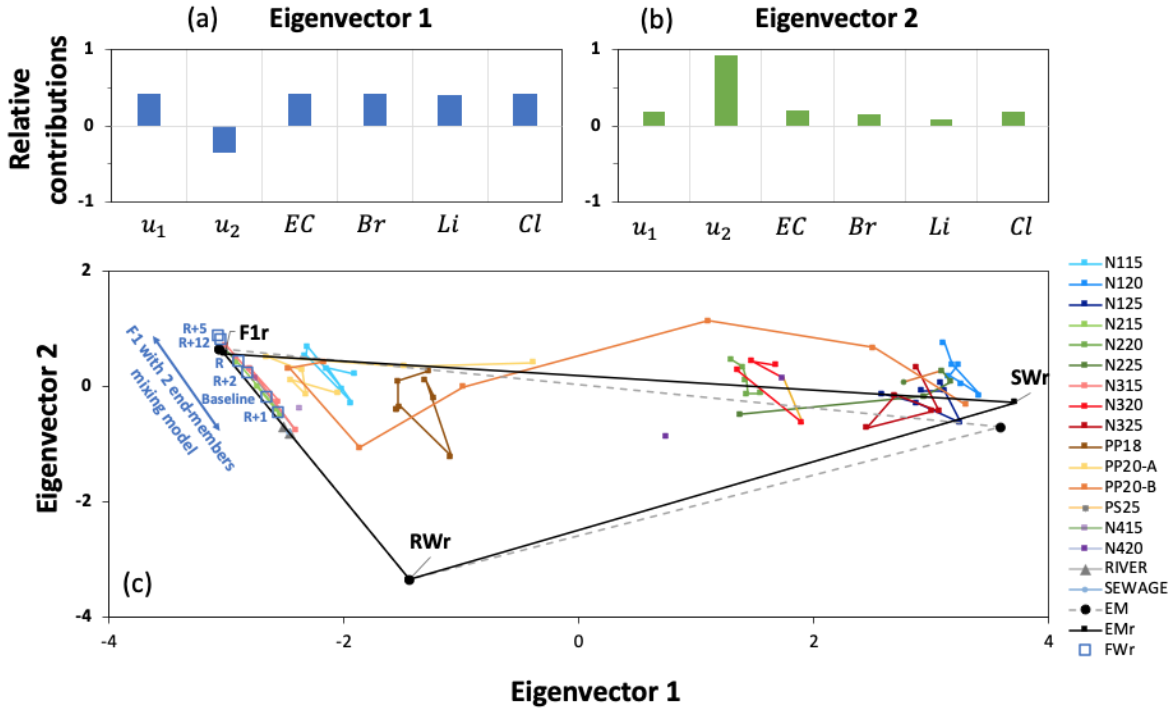

Figure 5-9: EMMA results for the identification of end-members and end-members composition. (a) Relative contributions to eigenvector 1; (b) Relative contributions to eigenvector 2; (c) Groundwater samples projection over EG1 and EG2. F1 samples in blue represent the evolution for each sampling date (Baseline, R, R+1, R+2, R+5 and R+12) without taking into account rainwater (RW) during Mix calculation. Recalculated end-members are encircled by black lines.

Following the method presented in Carrera et al. (2004), we determined the end-members composition with respect to our data set. We started from the end-members identified by the EMMA in a previous study, where 2 end-members were considered: F1 and SW (see details in Chapter 4 -). As presented in **Figure 5-9**c, when the rainwater is not taken into account during the MIX, we observe that the F1 end-member evolves towards the rain direction at each sampling date. So, we choose to include the rain (RW) as a third end-member.

The recalculated end-members are indicated with an undersigned "r" in **Figure 5-9**c. From the recalculated end-member composition, we can calculate the mixing ratios for each sample using the MIX code (Carrera et al., 2004). The results of the mixing ratios (**Figure 5-10**) applied to the baseline sampling are consistent with those presented in Chapter 4 - since they are from the same aquifer. Before the rain of October 2017, the aquifer is more affected

by SWI than in January 2016, since the rainfall event baseline is at the end of summer 2017. There is an important seasonal effect in this aquifer and in summer, the aquifer tends to become more saline due to the pumping increase in the area and recharge decrease (dry summer). We see that the intrusion wedge extends inland, affecting the Nx-20 and Nx-25 levels. This increase in salinity is observed in the mixing ratios.

Only little changes are observed in the upper part of the aquifer, as they have already small SW percentages. The main changes are observed in middle and deep levels, with a salinization effect. We know from different previous studies that these levels are the most connected to the sea (Folch et al., 2020; Palacios et al., 2020). Larger %SW changes are observed in PP20-B, with a freshening of the borehole during the event. Then, the borehole is salinized to reach again some high values after the storm, similar to January 2016. We attributed these large changes in mixing ratios to borehole mixing since PP20 is fully screened. This effect was already observed and discussed in Chapter 4 - for the same borehole in steady-state conditions.

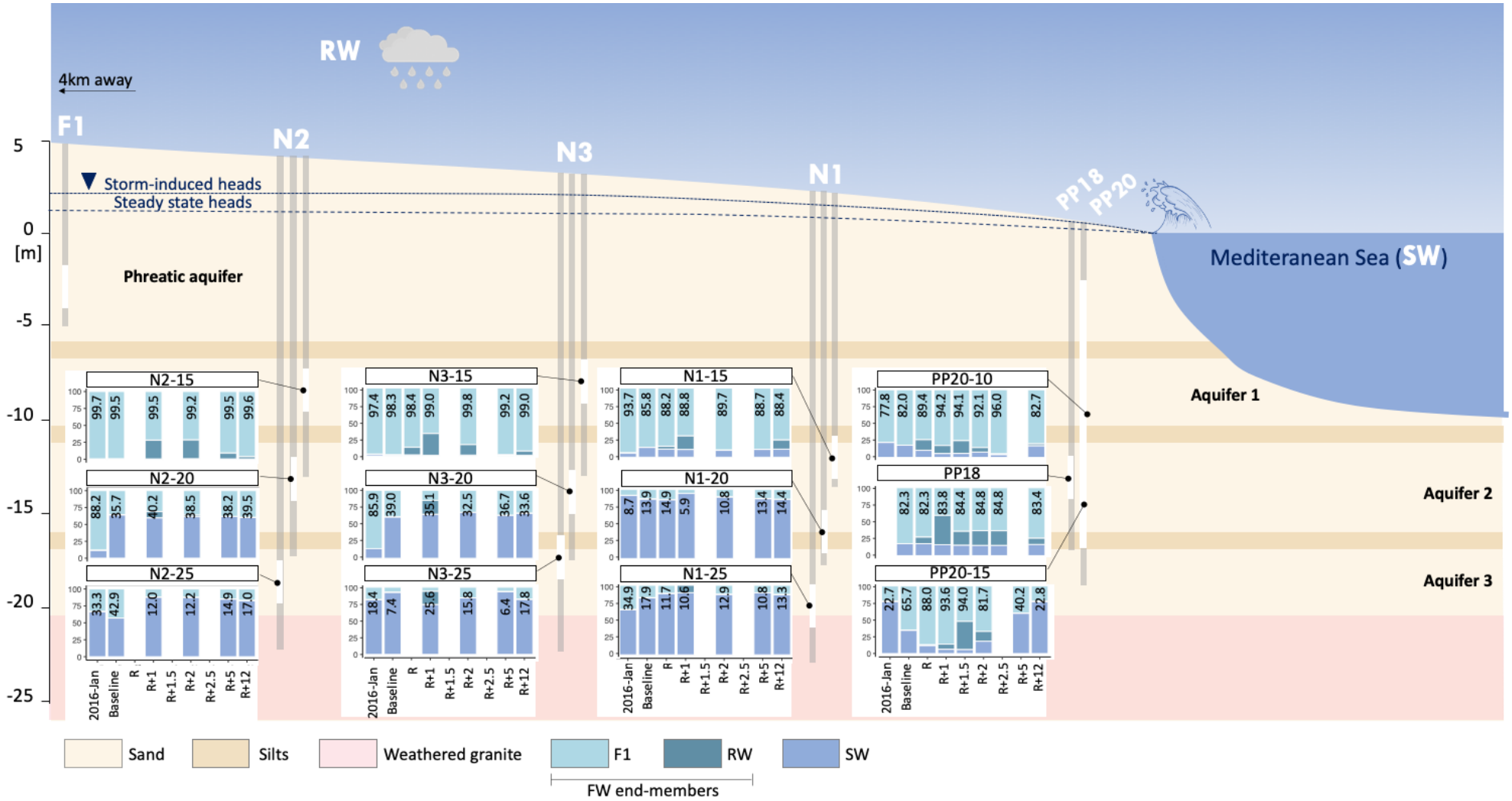

Figure 5-10: Temporal evolution of the mixing ratios in the wells at different depths from inland to the coast. Values are indicating %FW which is here the sum of %F1 and %RW. Horizontal direction not to scale.

5.4.4 Chemical reactions and impact on SGD

In this section, results are not presented for all boreholes, see Appendix F for all boreholes results. In Chapter 4 - , we indicated that cation exchange processes are important at the Argentona experimental site. We especially discussed Ca^{2+} desorption followed by gypsum precipitation. At the baseline, we observed the same processes but with greater reaction extents (**Figure 5-11a**). Also, a higher degree of salinization is observed indicating that seawater intrusion occurs mainly in summer. During the rain event, shallow wells maintain small reaction extent values since little variations of %SW are obtained. In deeper wells (the most dynamic part of the mixing zone), salinization is observed during the storm (%SW increase). During the displacement of freshwater by seawater, groundwater is enriched in Ca^{2+} and depleted in Na^{+}. At the same time, precipitation of gypsum and fluorite is induced progressively (**Figure 5-11b** and **c**). Then, once the salinization stops and the %SW starts reducing, the cation exchange reaction extent drops until reaching values close to 0. This drop was also observed in column experiments during salinization and freshening cycles (Beekman; Giménez-Forcada, 2014; Gomis-Yagües et al., 1997). A small freshening is observed in well N1-20 (well that presents the highest EC measured at the site). This freshening induces the desorption of Na^{+}, enriching the groundwater in this element.

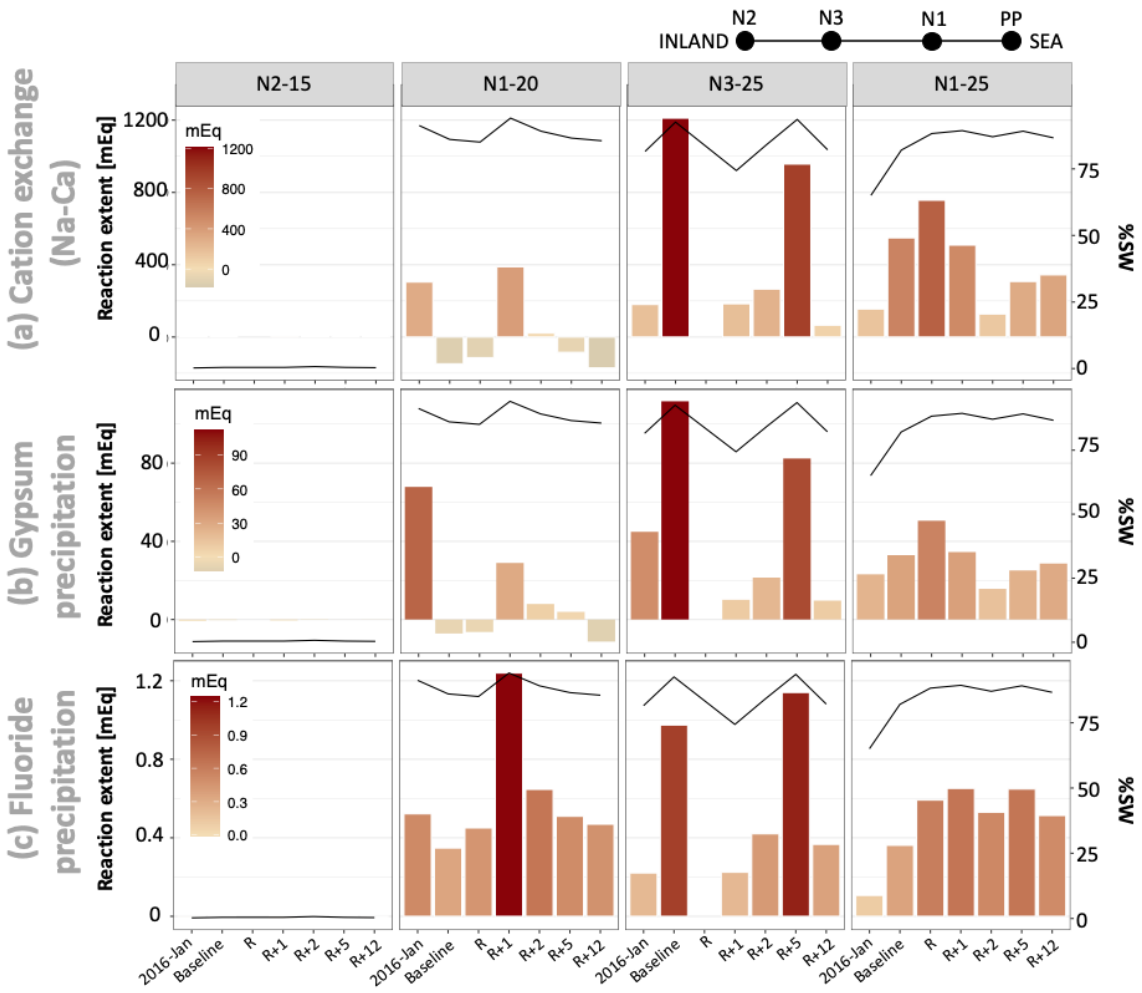

Figure 5-11: Calcium desorption (a), and Gypsum (b) and Fluorite (c) precipitation during salinization induced by the rainfall event for wells N2-15 (as control sampling point), N1-20, N3-25 and N1-25. The black line represents the %SW.

In the aquifer, redox reactions were also identified and discussed in Chapter 4 - . The organic matter is degraded through aerobic and anaerobic respiration of bacteria using different chemical substances as electron acceptor (i.e. O_2, NO_3, FeO(OH), and MnO_2). During the rainfall event, aerobic respiration is present in deep boreholes (Nx-25) where salinization happens (**Figure 5-12**a). As dissolved oxygen is high in seawater, the salinization event enhances aerobic respiration in deep boreholes. As a consequence, anaerobic respiration is reduced (**Figure 5-12**b and c). We observe a drop in iron and manganese concentrations after the rainfall event. These drops are directly correlated with a lower reaction extent. This phenomena occur independently of the low Fe and Mn reduction observed in January 2016 and during the baseline in deep wells (specifically in N2-25 and N3-25). Therefore, 5 days after the rainfall (R+5) we can assess that aerobic

respiration is lower, and the system changes to the anaerobic state, with an increase in Fe and Mn reduction. Iron reduction and manganese reduction in N3-25 are high, as already observed in the previous study. It seems that a localized zone with reducing conditions exists around N3-25, extending to N2-25 punctually (e.g. intrusion moving inland).

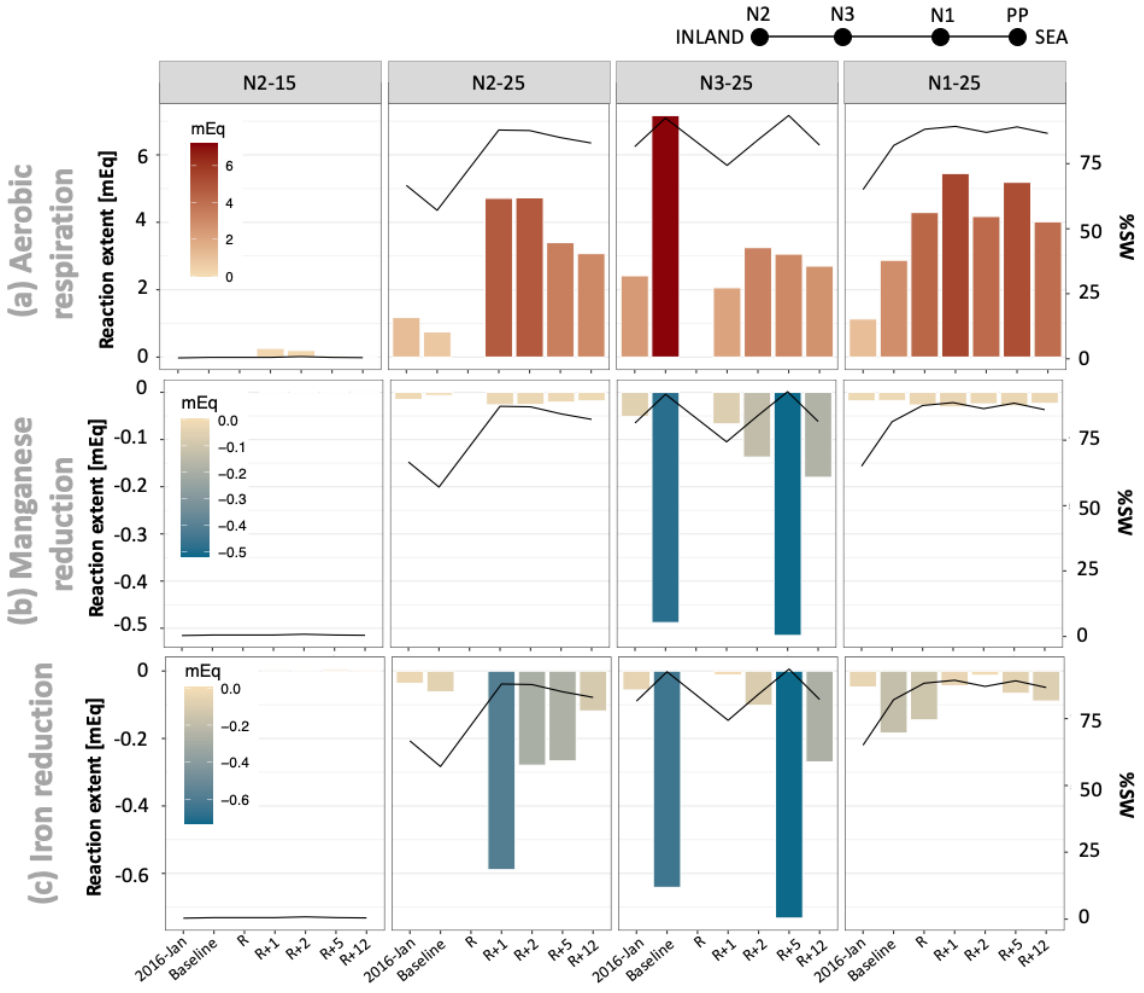

Figure 5-12: Increase in organic matter degradation during salinization event in N2-15 (as a control sample), N2-25, N3-25, and N1-25. The black line represents the %SW.

Nitrate values in the aquifer are higher during the baseline acquisition than in the winter 2016 campaign, revealing a seasonal contamination (**Figure 5-13**). As observed by Martínez-Pérez et al. (in press a), nitrate concentrations are higher in shallow boreholes (>1 mM) than in deep boreholes (<0.1 mM). In the previous chapter, we highlighted that denitrification reactions occur principally in the deeper part of the aquifer. For this case, the nitrate becomes the electron acceptor for organic matter degradation, as dissolved is low. At shallow depths (Nx-15), NO_3 concentrations tend to decrease during the rainfall event (**Figure 5-13**i-a). We cannot attribute this reduction to dilution processes by the

rainfall since measured concentrations are higher than conservative mixing concentrations (**Figure 5-13**i-b). These higher concentrations measured are indicating nitrate mobilization during the rainfall event that could reach the sea. High nitrate concentration in SGD can favour algal development as already observed and discussed by Hu et al. (2006) who linked Florida's red tides (an algal bloom) to SGD caused by heavy rainfall. In deep boreholes, nitrate concentrations are much lower than the conserving mixing indicating some denitrification processes (**Figure 5-13**ii-b). During the rainfall event some increases in nitrate concentration are observed at R+1. These increasing concentration periods correspond to a reduction of the denitrification reactions (**Figure 5-13**ii-a). We associate these reductions to the salinization process that adds dissolved oxygen at depth promoting aerobic respiration instead of anaerobic. After a few days, the system comes back progressively to an anaerobic state and high denitrification rates are observed. The same effect was observed with Mn and Fe reduction.

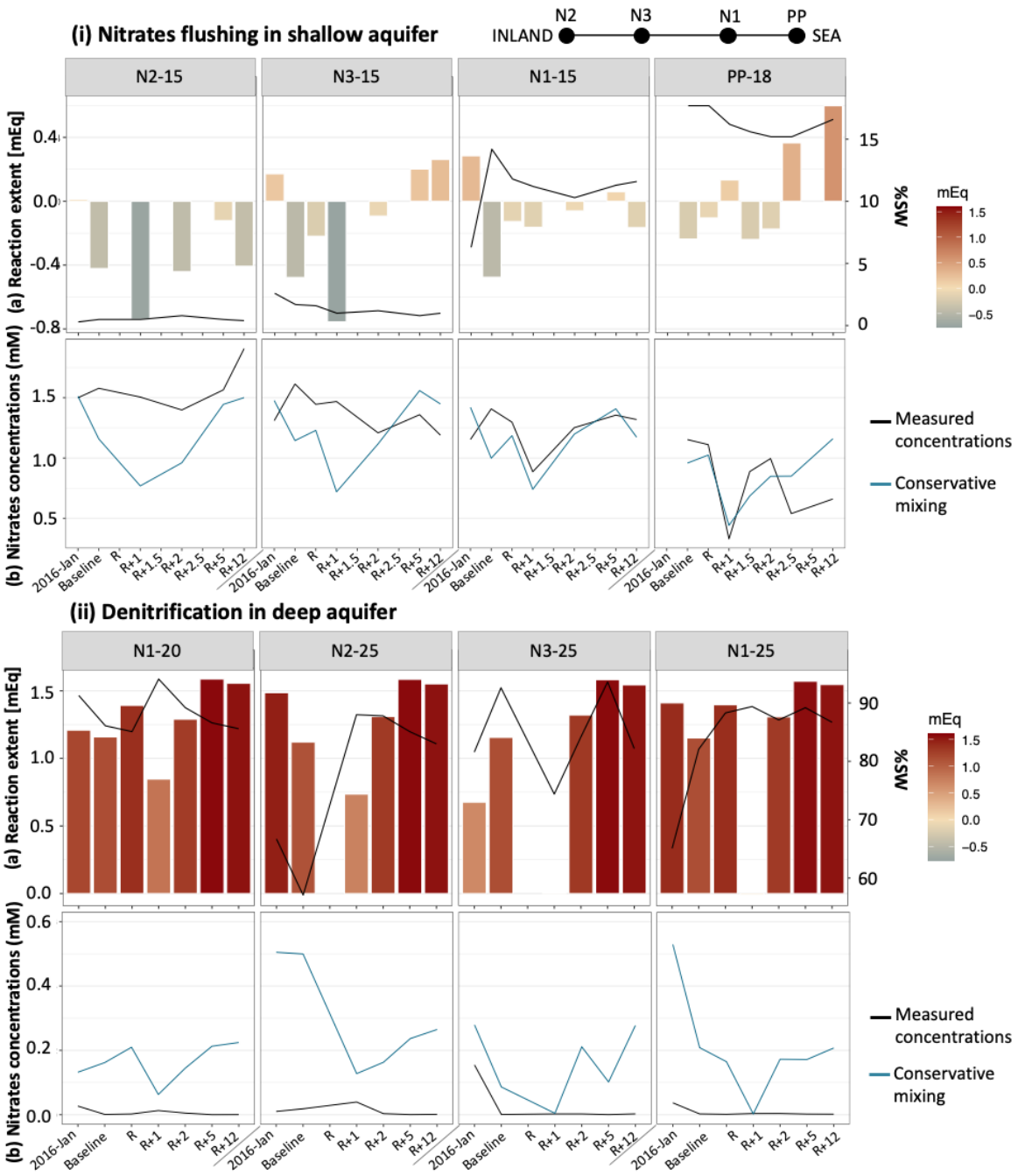

Figure 5-13: (i) Nitrate flushing in the shallow aquifer (N2-15, N3-15, N1-15 and PP18) and (ii) a reduction of the denitrification in the deep aquifer during the rainfall (N1-20, N2-25, N3-25, N1-25).

Finally, we observe that feldspar weathering, barite precipitation, and gibbsite precipitation are much higher at the rainfall event baseline than in January 2016. They have similar trends: the 3 reactions tend to be more important during salinization and present lower occurrences during freshening (results for these reactions and for other boreholes are presented in Appendix F).

5.5 Conclusions

This research study demonstrates that samplings focused on hydrological events or campaigns allow obtaining very rare and relevant data and have demonstrated the importance of high-resolution monitoring. We further show that short-term events affect chemical reactions. Even that the use of data-loggers coupled with sampling campaigns may be incompatible for proper monitoring purposes. Nevertheless, geophysical techniques arose as precise tools to track the dynamics of the mixing zone. From this, we can conclude that:

Before the rainfall event, although the trend of the mixing ratios is maintained with respect to previous studies, the aquifer is quite salinized, since the aquifer comes from the summer season characterized to be quite dry. Also, we observed that before the rain the sea level is much lower, which induces a drawdown in aquifer heads.

During the rainfall event, the recharge from inland develops freshening of the aquifer due to migration of the freshwater-saltwater interface seaward. This freshening reduces chemical reactions and the reversed cation exchange process happens. Also, the entrance of dissolved oxygen in the anoxic part allows aerobic respiration instead of previously anaerobic respiration of the bacterial population.

After the rainfall event, the interface recovery is characterized by a seawater intrusion (migration of the freshwater-saltwater interface inland) which appears to be much faster and stronger than the freshening event, particularly in the deeper aquifer portion. Even if the deepest levels are below several silt layers, salinization affects these levels during the rain event. This observation confirms the good connection of the aquifer with the sea, which is reflected in the chemical reactions. Chemical reactions are reduced or reversed during the freshening but the stronger salinization increases the system reactivity.

In the long-term, if heavy events become more frequent, at contrary to what would be expected, salinization could be the principal drawback. So that the aquifer would remain saltier with consequences over the groundwater resources availability. This could be accentuated with other processes not considered here (i.e. coast erosion, sea-level rise, etc.). This study opens the door to future works, especially considering numerical

modelling in order to understand the salinization processes during heavy rainfall events. Coupled with reactive transport codes, these numerical models could increase the spatial resolution and understanding of processes occurring at larger catchment scales. Moreover, such an approach can provide information on SGD quality and potential risks on sea ecosystems.

7

General conclusions and perspectives

This chapter is a summary of the main contributions of this thesis and some trials on future works.

In the first part of the thesis, we investigated an “ideal” but not used technique to characterize coastal aquifers: the tidal method. This method consists of evaluating the hydraulic diffusivity from head responses to tidal fluctuations in coastal aquifers. Even though many analytical solutions exist, the technique is not so much applied to real cases. We investigated it, testing a simplified procedure and we performed a numerical analysis through different aquifer configurations and boundary conditions.

The results demonstrated that the phreatic surface plays an important role in the inland propagation of sea fluctuations in an unconfined aquifer. Thus, we highlighted that in unconfined aquifers with tidal fluctuations far from the coast, the delayed yield must be considered. Moreover, fluctuations are damped rapidly moving inland. Furthermore, we established that in deep aquifers located below low permeable layers, a mechanical effect is generated by the load and unload over the seabed. Thus, the induced aquifer fluctuation is observed far from the coast with a small amplitude reduction and time shift in respect of tides. Lastly, for realistic cases, we demonstrated interferences between aquifer levels in multilayered systems. All these inconsistencies, not detailed in previous studies lead to overestimations of hydraulic diffusivity and contribute to the non-application of the method.

In the second part of this thesis, we made the first application of the tidal method to an experimental site located in a coastal area (Argentona). Following the procedure presented in the previous part, we used a numerical model to calibrate the hydraulic conductivity using head data from the Argentona experimental site. One limitation for analytical solutions application is that they consider only one tidal harmonic. In this part of the thesis, we also describe a detailed procedure for the identification and isolation of the tidal signal from noisy measurements. Results showed that in the case of Argentona, and probably many others, analytical solutions cannot be applied because they fail to represent the complexity of real systems. Furthermore, we were expecting an unconfined aquifer connected to the sea but results showed that even thin low permeable layers can cause a significant mechanical response. Comparing the isolated tidal signal and the full signal calibrations, we observed that the full signal includes important information. Therefore, the isolated tidal components allow us to refine the conceptual model.

In the third part of this thesis, we focused on coastal aquifer hydrochemistry. A full and detailed description of a statistical method based on principal component analysis to identify the end-members of a mixed water sample is presented. The use of the EMMA (End Member Mixing Analysis) coupled with a reactive-mix procedure allows to (i) identify the end-members and their spatial proportion; and (ii) determine and quantify the chemical reactions occurring in the Argentona coastal aquifer. Results showed the extent of the reactions and their spatial distribution of the different chemical processes occurring in this coastal aquifer. The most important reaction is cation exchange, especially between Ca and Na. We also highlighted the important role of coastal aquifers in the reduction of groundwater organic matter. And we finally estimated the submarine groundwater discharge composition taking into account all the identified reactions.

In the last chapter, we monitored the effect of a heavy rainfall event over a coastal aquifer. Such non-periodic events displace the mixing zone to a greater magnitude than usual (e.g. movement induced by tides). We carried out the study at the Argentona experimental site, where heads, electrical conductivity (water + rocks), and groundwater chemistry were monitored. The EMMA-reactive method allowed us to investigate the chemical reactions and their temporal and spatial evolution.

Results of this almost 2 weeks-long campaign show (1) different head responses, which helps in confirming the hydrostratigraphic model; (2) changes in salinity, which suggest that dilution occurred rapidly after the event, followed by a recovery towards higher salinity values, which suggest transient response; and (3) biogeochemical changes, which indicate that cation exchange, precipitation-dissolution reactions, and a lower organic matter degradation occurred immediately after the event.

To summarize, in this thesis, after highlighting the importance of mechanical effect on coastal aquifers imposed by low permeable layer, we described a geochemical procedure allowing the determination of the different chemical reactions occurring in the aquifer as a consequence of the mixing of fresh and seawater. This method allows the prediction of the submarine groundwater discharged composition, rarely sampled and known.

Finally, the full procedure presented here gives us the conceptual model and the key reactions that are needed for the further and final step of a complete reservoir description and prediction through a 2/3D reactive transport numerical model.

APPENDIX A

Ongoing work and other tasks enrollment

1.1. Density variable model

The work presented in this Appendix is the result of a shared research task with Palacios A. (Ph.D. Student in charge of the hydrogeophysical monitoring and inversion at the Argentona experimental site).

1.1.1. Conceptual model

From the first stratigraphic interpretation of the Argentona site, we created a conceptual model consisting of two aquifers separated by a silt layer (**Figure A- 1**). However, once we did the time-lapse CHERT experiment interpretation we observed several SWI wedges (Martínez-Pérez et al., in press b; Palacios et al., 2020) . An upper seawater wedge was observed above 7 m depth, then a second between 7 and 12 m, a third one was observed between 12 and 17 m, and finally below 17 m, elevation at which we observed an inversion in the formation electrical conductivity, from conductive to resistive. This change in the electrical conductivity was linked to a decrease in water salinity, observed in the water samples of piezometer N1-25, and to a decrease in bulk electrical conductivity, confirmed by the induction logs, which can be associated with a change from alluvial sediments to weathered granite. For fresher water to be trapped below these seawater wedges, geological barriers had to be present at an elevation of 7, 12, and 17 m below the surface.

Also, the tidal method required low permeability layers in order to generate the mechanical effect induced by tides over the seabed. This information was contrasted with the centimeter-scale core description made at the Argentona site and it was found that clay and silt layers as thin as a few centimeters were present at these depths in several piezometers. The fact that very thin silt layers can control the flow and the salt distribution in a 100-meter scale site was discussed in a work by Folch et al. (2020) and in Chapter 3 - . After all these revisions, the site conceptual model has eight units: a free water-table layer, three aquifers, three aquitards, and a weathered granite layer which impervious nature is still unknown.

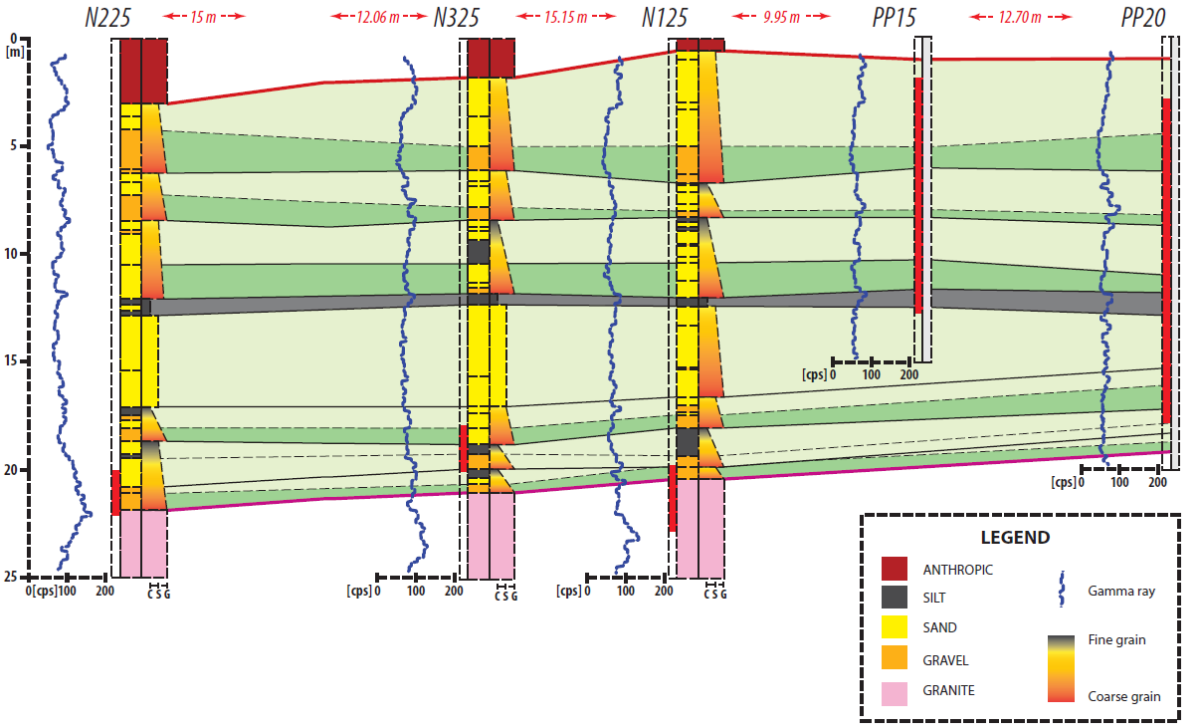

Figure A- 1 Geological cross-correlation of the Argentona experimental site from Martínez-Pérez et al. (in press a).

From the experiments we have understood the main hydrological processes occurring at our study area which affect its hydrological and geophysical response:

- **Rainfall** fluctuations at several time scales. Heavy daily rainfalls cause the Argentona ephemeral stream to discharge in a flash-flood manner, and lead to recharge events that are highly concentrated in time. Seasonal fluctuations cause the advance and retreat of the seawater wedge and are reflected in the head responses, in the water salinity measurements, and in the time-lapse CHERT. Droughts, in the years-scale,

also affect the study site. The one registered since 2015 caused an overall salinization of the study area in the two years of monitoring.

- **Storm surges** affect the beach area, from the coastline until approximately piezometer PP15. Surges were registered with the time-lapse CHERT experiment when the wave height increased. The bulk electrical conductivity images showed the saltwater infiltration from the top of the soil until the first lithological barrier.

- The **water table** at the site is found at roughly 3-meters depth. A delayed response of the phreatic surface was observed by previous studies (Goyetche et al., in prep).

- **Agricultural, commercial and industrial use** of the surroundings controls the flow of water below the ground from the nearest mountains towards the sea. This water flow was monitored through a piezometer located 400 meters away from the site, at which we were able to measure the diminishing trend of the water table in the two years of monitoring, another hint for the salinization of the site.

- **Head** small scale fluctuations are related to sea-level fluctuations.

- **Fresh groundwater flows** through the deepest layer of the study area and it remains trapped below **the** seawater wedge, as it has been evidenced by water samples from piezometer N1-25 and from bulk electrical conductivity measurements.

1.1.2. Density-dependent flow and transport model

The Argentona alluvial aquifer is simulated by a two-dimensional model. The discretization of the mesh is shown in **Figure A- 2**. Delayed yield is simulated through the assignment of a high storage coefficient to the first layer of the model covering all the area above 0 m.a.s.l., as described in Chapter 2 - . The top boundary from the coastline (x=0m) to the right boundary, and the vertical right boundary, represent the transient seawater level boundary with a salt concentration of 38 g/L. The flow of freshwater coming from the inland regional system towards the sea enters the model from the left boundary, from 0 m.a.s.l until -45 m.a.s.l, with a salt concentration of 0.22 g/L. Precipitation is represented in the model as a prescribed flow boundary condition directly at z = 0 m.a.s.l to avoid the delay of the first layer. The effect of storm surges is modelled as a surface recharge over the area from the top of the

model until -5 m.a.s.l and from the coastline until piezometer PP15 with a salt concentration of 30 g/L. The base of the model is considered as a no-flow boundary.

The freshwater top recharge was computed using a soil-water balance program which uses precipitation and temperature data to estimate the potential evapotranspiration and the real evapotranspiration. The program computes the effective precipitation and, by subtracting the surface runoff, can yield the amount of water that actually infiltrates the subsurface. Fresh groundwater flow was estimated by calibrating a water balance in a box model. The estimated freshwater top recharge from the soil-water balance is what enters the box, and the outflow from the box is what enters the Argentona site model. The calibration of the box model was done with respect to the head measurements from the piezometer 400 meters uphill.

For the sea-side boundary, the daily time-series from "Puertos del Estado" website was used, specifically the data from Barcelona Port located 30 km at the south of the Argentona site. For the same website, we used simulated wave height data and set a threshold to 2.5 m of wave height as a minimum for a surge to take place (Puertos del estado, 2017).

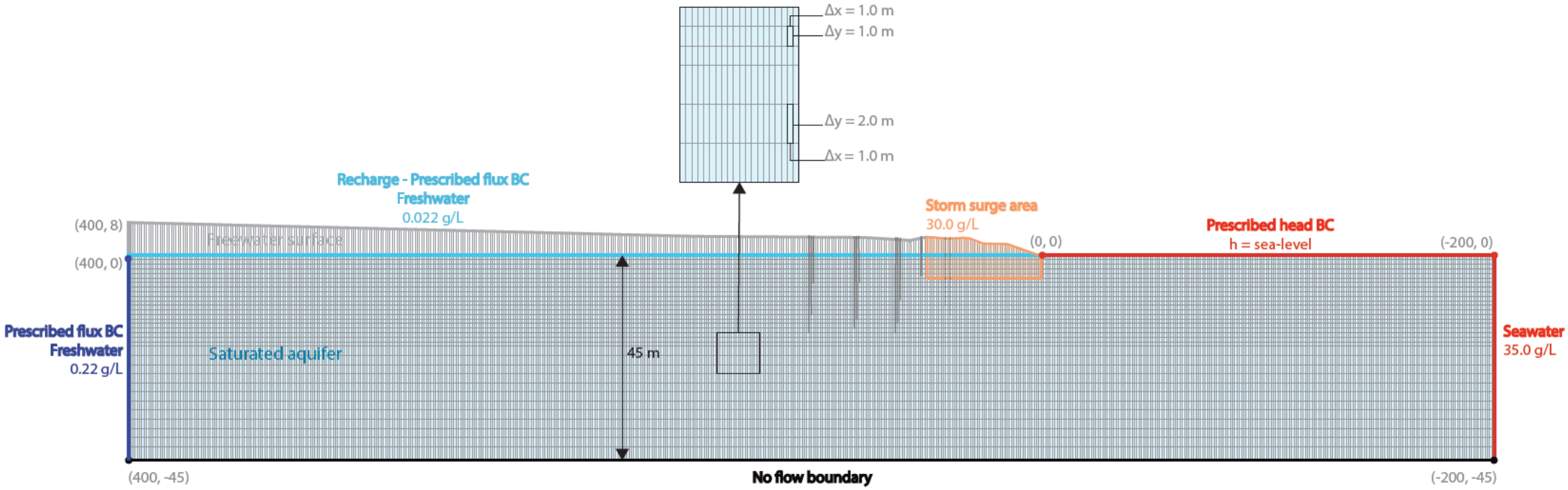

Figure A- 2 Model geometry, boundary conditions, and mesh discretization Red line represent the sea boundary, dark blue line the inland boundary, light blue line the recharge boundary condition and in the area where storm-surges boundary condition is included.

The simulation time includes three periods: a first 200-years pseudo-state-state period; a second four-and-a-half-year transient period, from 2011 to mid-2015, with a regular time step of 30 days; and a third two-and-a-half-year transient period with a regular time step of 1 day, representing the monitoring period in Argentona from 2015 until 2017. This third period was divided in two for calibration purposes: a first one-year period, from mid-May 2015 until July 2016 for the calibration of the model, and a one year and a half period for validation, from July 2016 until the end of 2017.

The parameters included in the numerical model to solve the flow and transport equation in variable density conditions are presented in Table A-1. Hydraulic conductivity values are from the calibration using the tidal method (Chapter 3). The density-dependent groundwater flow and solute transport code SEAWAT (Langevin et al., 2008) was used to perform the simulations.

Table A- 1 Parameters included in flow and transport numerical model

Parameter	Hydrological Unit	Initial Value
Hydraulic Conductivity [m/d]	Free water-table	1.00E-03
	Aquifer 1	5
	Aquitard 1	0.01
	Aquifer 2	25
	Aquitard 2	0.01
	Aquifer 3	40
	Aquitard 3	1.00E-04
	Weathered granitic basement	7
Storage Coefficient	Free water-table	1.00E-01
	Aquifer 1	1.00E-05
	Aquitard 1	1.00E-04
	Aquifer 2	1.00E-05
	Aquitard 2	1.00E-04
	Aquifer 3	1.00E-05
	Aquitard 3	1.00E-04

	Weathered granitic basement	1.00E-05
Porosity	All	0.1
Molecular Diffusion	All	1.00E-08
Longitudinal / Transverse Dispersivity	All	1.0 / 0.1
Fresh Groundwater Flow Multipliers	Aquifer 1	1
	Aquifer 2	1
	Aquifer 3	1
	Weathered granitic basement	1
Top Freshwater Recharge Multiplier		4
Top Saltwater Flow Multiplier		1

1.1.3. Preliminary results

The simulated groundwater salinity results are presented in **Figure A- 3**, using the hydraulic conductivity resulting from the application of the tidal method. The results validate the values obtained with the tidal method and supporting its robustness. Then, we encourage to use it for the initial characterization of coastal aquifers.

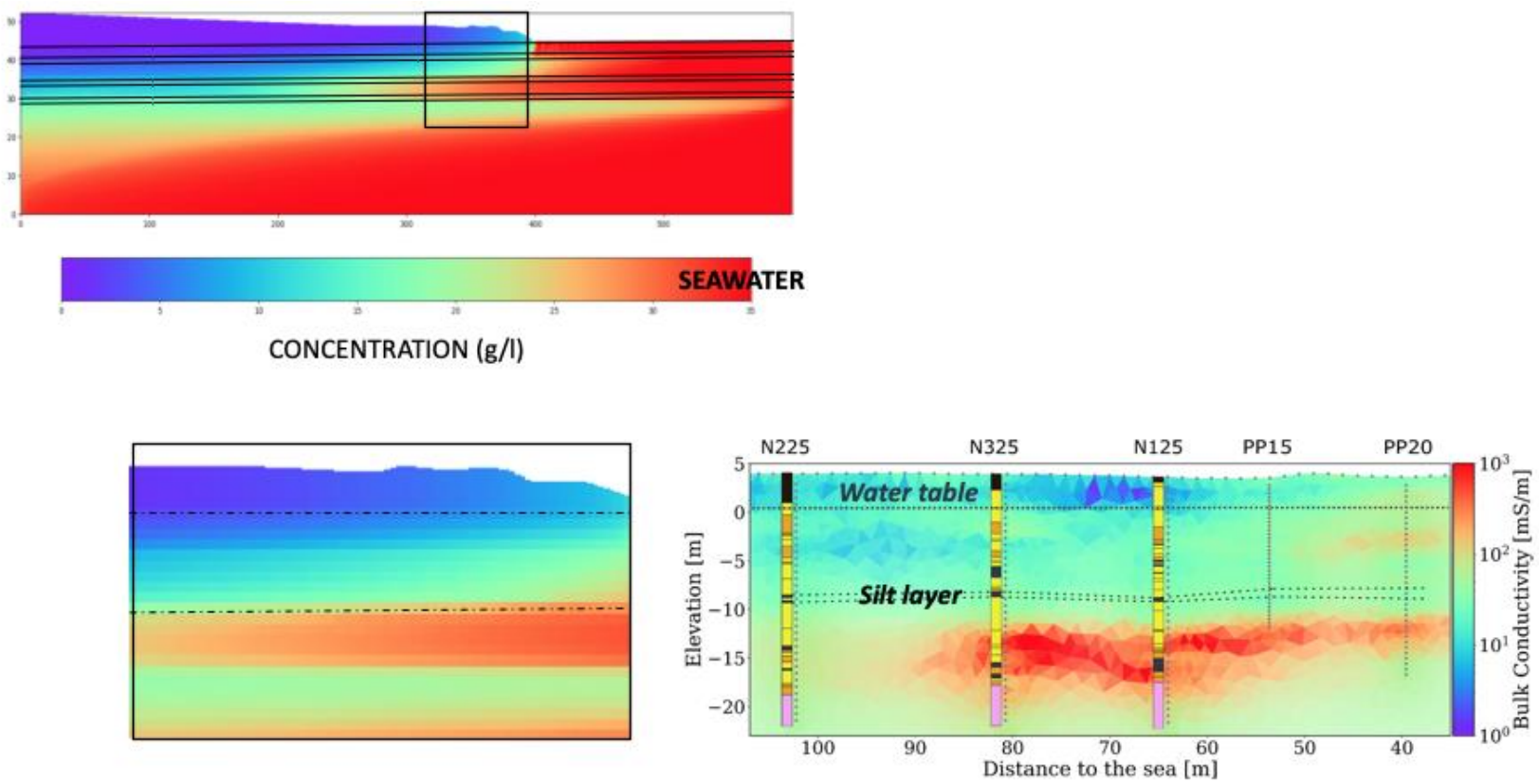

Figure A- 3 Simulated groundwater salinity and CHERT. Zoom is done over the Argentona experimental site part of the numerical model.

1.1.4. Summary and future works

The above-described flow and transport model with variable density is quite tedious since some freshwater is found below saltier water creating instabilities. The first results are interesting and actually, we are working on the model calibration including in addition to water level and concentrations the geophysical data (not presented here) to adjust the set of parameters. We aim at including reactive transport in future work steps.

1.2. Periodic slug tests

Here we present the early-stage development of a novel approach aiming at characterizing the interconnectivity between boreholes and the aquifer hydraulic parameters. We induce periodic fluctuations simulating successive injections and withdrawals. Advantageously this technique avoids the mobilization or extraction of significant quantities of water and hinders any risk of salinization of the aquifer.

1.2.1. Materil and method

Tested site

The experiment was conducted at the Argentona experimental site. This site is a sandy coastal aquifer located less than 100 m from the sea. It is composed of several wells opened at different depths. The particularity of this site is the presence of silts layers (see cross-section in **Figure A- 4**). The aquifer portions between these layers are thus semi-confined. Several oscillatory slug tests were done to determine the connectivity between the boreholes and the hydraulic parameters of the aquifer.

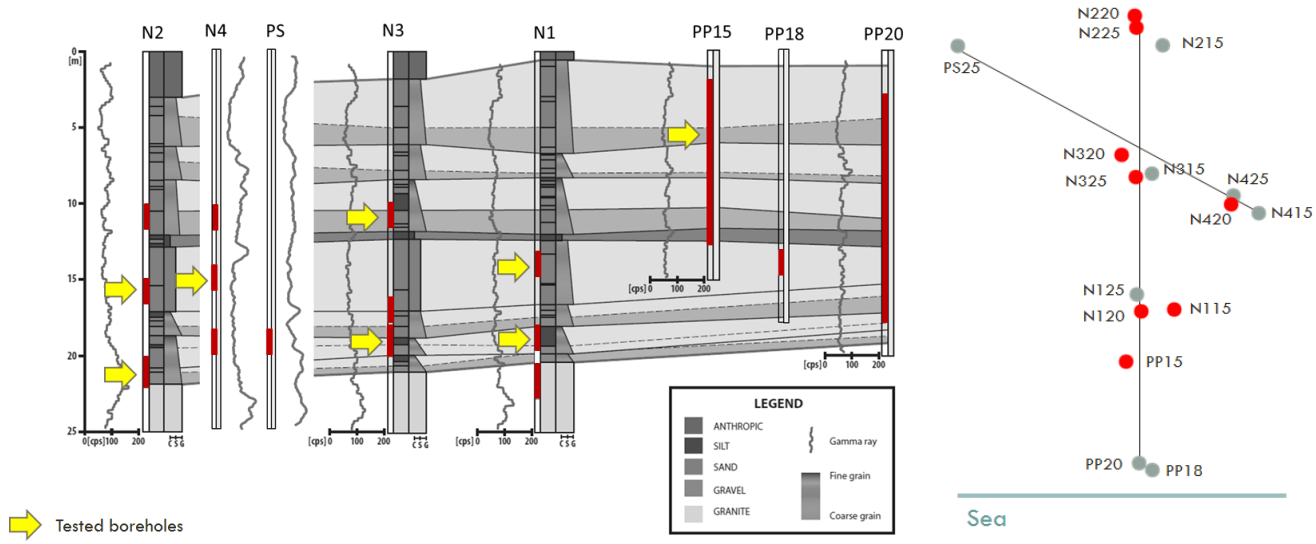

Figure A- 4 Cross-section of the study site perpendicular to the sea. Red intervals show the screened interval for each nest and standalone piezometer (PP15-PP20)). (Martínez-Pérez et al., in press)

Experimental setup

An oscillatory pressure perturbation is created introducing a slug (solid cylinder of l = 3.07 m length and 0.05 m in diameter) in the borehole connected to a motorized winch commanded by a computer from which the amplitude and frequency of oscillation can be programmed (Figure A- 5). A tripod is used to hold the slug and center it inside the borehole. Pressure data-loggers are installed in all the boreholes of the experimental site and registered at a small time interval (t=3 sec). Another data logger is placed at the bottom of the slug to measure its depth in water. Thus, the movement of the cylinder inside the borehole casing causes the rise and drop periodically of the water level, as a sinusoidal signal. The observed signal in other boreholes is the same but with a reduction of the amplitude and a delay with the oscillating borehole.

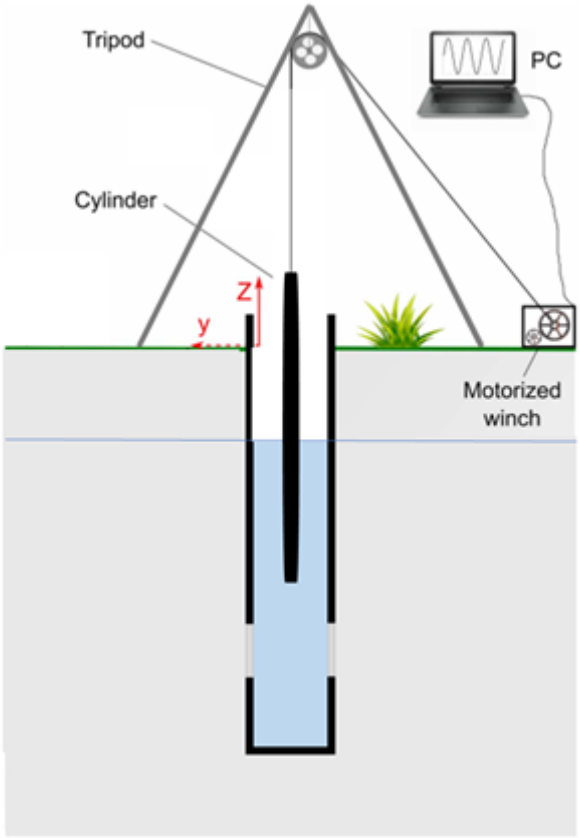

Figure A- 5 Sketch of the experimental setup (Modified from Schuite et al. (2017))

The tested amplitude ranges from 0.9 to 1.4 m starting from the cylinder's middle length so that the slug is not out of the water. Oscillation periods ranging from 40 to 300

sec were applied to the cylinder (Table A- 2). Each test is repeated at least 30 complete periods to reach a pseudo-steady-state so that they last from 1200 sec to 2.5 h.

Table A- 2 Amplitude and period of induced oscillation for each tested borehole. *indicates a long screened borehole.

Tested borehole	Amplitude (m)	Period (sec)
N3-25	1.2 ; 1.4;	40; 60; 90; 120
N3-15	1.4	60; 300
N1-20	1.4	40; 90; 120
N1-15	1.4	40; 60; 300
N2-20	1.4	40; 60; 120
N2-25	0.9; 1.0; 1.4	40; 60; 120
N4-20	1.4	40; 60; 120
PP-15*	1.4	40

1.2.2. Preliminary results

A good aquifer response is observed at the observation boreholes, indicating a good connection with the tested borehole.

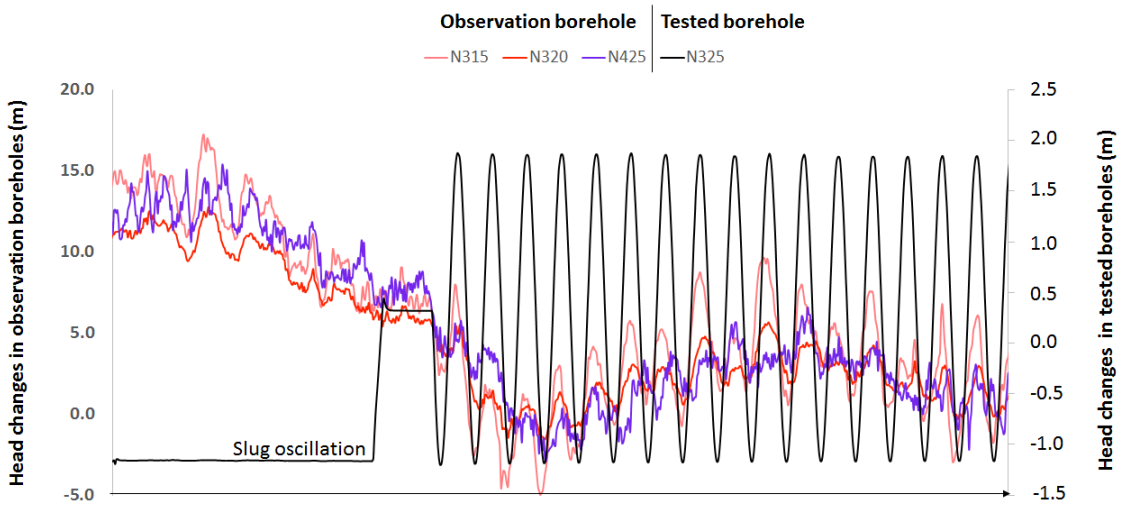

Figure A- 6 Head measurements during one of the oscillatory tests performed at N3-25 and observed at N3-15, N3-20, and N4-25.

1.2.3. Data processing development and reflection

At this high-frequency data-loggers registered a large variety of noise (e.g. waves, tides, or hydromechanical induced by the nearby train line) at the Argentona experimental

site. Moreover, some sinusoidal solicitations with a period of 120 sec were difficult to discriminate from the sea waves of the same period during some of the tests. These noisy data complexify the amplitude and phase shift obtention in observed boreholes. The methodology applied Schuite et al. (2017)is to fit a sine function to the data, of the form:

$$P(t) = P_c \sin\left(\frac{2\pi}{\tau} t + \varphi\right) \quad (0\text{-}1)$$

where $P(t)$ is the measured pressure at time t, P_c is the amplitude, φ is the phase shift and τ is the period of the oscillation. As presented in Figure A- 7, the fit cannot be applied in a direct form to the data.

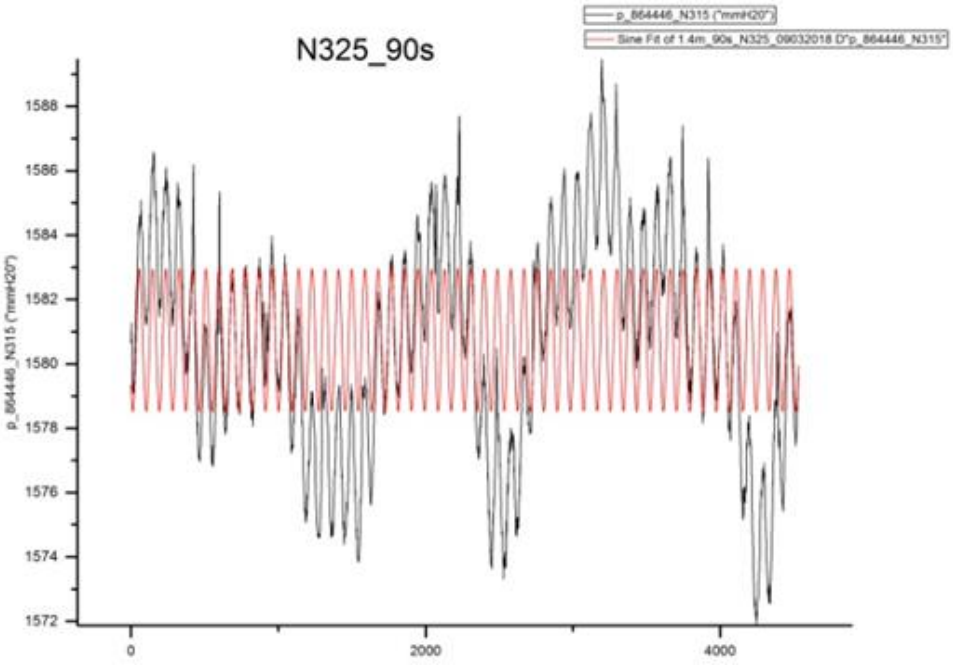

Figure A- 7 Fitted sinus function over data measured in N3-15.

To do so we decompose the signal using an additive model (M. G. Kendall, 1946) as $Y(t)=T(t)+O(t)+e(t)$, where Y is the raw data, T is the trend representing high-frequency fluctuations obtained using a moving average, O is the regular and repetitive signal of a specific period of time. It is obtained by averaging, for each time unit, over all periods. And finally, e represents all irregular oscillations or noise. This last component of the signal is obtained by removing the trend and the repetitive signal from the original data. This method works only over data where the repetitive signal is repeated for many complete periods. Filter results are presented in the Figure below.

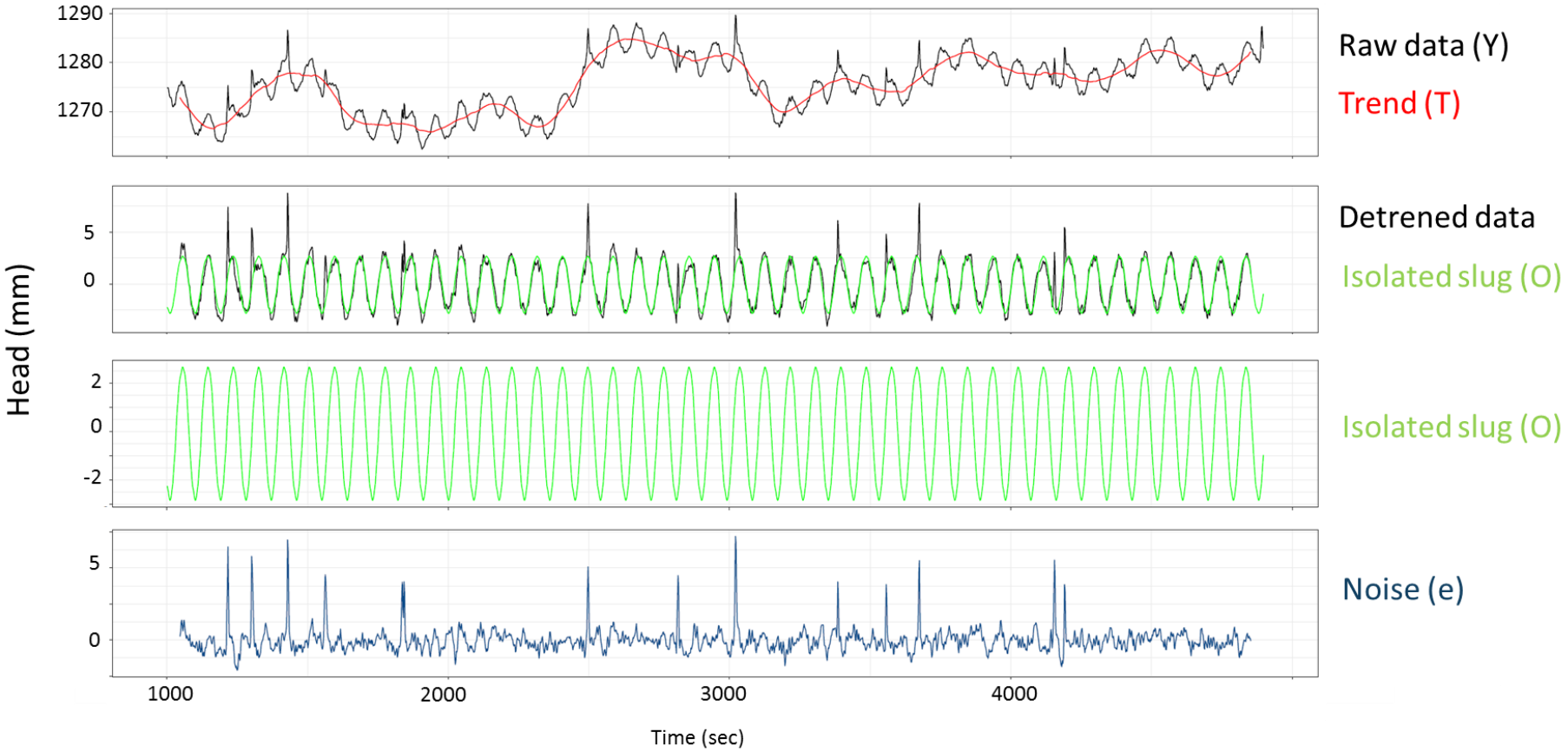

Figure A- 8 Decomposition of the oscillatory signal

1.2.4. Summary and future works

Despite the high permeability of the medium and the important influence of the sea on the water table fluctuation, we detected the oscillatory signal in the observatory wells. However, too important sea waves may highly disturb the signal and avoid the exploitation of the data. Actually, we are working on an analytical solution to interpret these kinds of tests and obtain not only the hydraulic diffusivity D_h, we aim at obtaining the hydraulic permeability (K).

1.3. Contribution to published and in-press scientific articles as co-author

1.3.1. Published scientific articles:

Folch, A., Del Val, L., Luquot, L., Martínez-Pérez, L., Bellmunt, F., Le Lay, H., Rodellas V., Ferrer, N., Palacios A., Fernández, S., Marazuela, M.A., Diego-Feliu, M., Pool M., **Goyetche T.**, ... & Carrera, J. (2020). Combining fiber optic DTS, cross-hole ERT and time-lapse induction logging to characterize and monitor a coastal aquifer. *Journal of Hydrology*, *588*, 125050.

Contribution (CRediT author statement): Investigation, writing (review and editing), visualization

Diego-Feliu, M., Rodellas, V., Saaltink, M. W., Alorda-Kleinglass, A., **Goyetche, T**., Martínez-Pérez, L., ... & Garcia-Orellana, J. (2021). New perspectives on the use of 224Ra/228Ra and 222Rn/226Ra activity ratios in groundwater studies. *Journal of Hydrology*, *596*, 126043.

Contribution: Investigation, writing (review and editing), visualization

1.3.2. In press articles:

Martínez-Pérez, L., Luquot, L., Carrera, J., Marazuela, M.A., **Goyetche, T**., Pool, M., Palacios, A., Bellmunt, F., Ledo, J., Ferrer, N., del Val, L., Pezard, P., García-Orellana, J., Diego-Feliu, M., Rodellas, V., Saaltink, M.W., Vázquez-Suñé, E. & Folch, A. (in press). Multidisciplinary approach to characterize coastal alluvial aquifers affected by seawater intrusion and submarine groundwater discharge.

Contribution: Investigation, writing (review and editing), visualization

Martínez-Pérez, L., Carrera, J., Palacios, A., **Goyetche, T.**, Ledo, J., Pezard, P., Folch, A., Luquot, L. (in press). The role of salinity profiles in the traditional paradigm for seawater intrusion.

Contribution: Investigation, writing (review and editing), visualization

1.4. Conference presentations

2018

Goyetche, T., Diego-Feliu, M., Luquot, L., Garcia-Orellana, J., Rodellas, V., Del Val, L., Martínez-Pérez, L., Palacios, A., Ledo, J., Pezard, P., Folch, A. & Carrera, J. Hydrodynamics and hydrogeochemical changes in the mixing zone of a coastal aquifer during a heavy rain event. EGU General Assembly 2018. Vienna (Austria).

Goyetche, T., Diego-Feliu, M., Luquot, L., Garcia-Orellana, J., Rodellas, V., Del Val, L., Martínez-Pérez, L., Palacios, A., Ledo, J., Pezard, P., Folch, A. & Carrera, J. Effects of a heavy rain event on the hydrodynamical and hydrogeochemical parameters in an alluvial coastal aquifer. 25th Salt Water Intrusion Meeting (SWIM). Gdansk (Poland).

Diego-Feliu, M., Garcia-Orellana, J., Rodellas, V., Alorda, A., Del Val, L., Luquot, L., Martínez-Pérez, L., Pool, M., **Goyetche, T.**, Ledo, J., Pezard, P., Queralt, P., Folch, A., Saaltink, M.W. & Carrera, J. Ra end-member variability in a dynamic subterranean estuary of a microtidal Mediterranean coastal aquifer. 25th Salt Water Intrusion Meeting (SWIM). Gdansk (Poland).

Folch. A, Del Val, L., Luquot, L., Martínez-Pérez, L., Bellmunt, F., Le Lay, H., Rodellas, V., Ferrer, N., Fernández, N., Marazuela, M.A., Diego-Feliu, M., Pool, M., **Goyetche, T.**, Palacios, A., Ledo, J., Pezard, F., Bour, O., Queralt, P., Marcuello, A., Garcia-Orellana, J., Saaltink, M.W., Vazquez-Suñé, E., & Carrera, J. Seawater intrusion dynamics monitoring with geophysical techniques combination. 25th Salt Water Intrusion Meeting (SWIM). Gdansk (Poland).

Martínez-Pérez, L., Marazuela, M.A., Luquot, L., Folch, A., del Val, L., **Goyetche, T**., Diego-Feliu, M., Ferrer, N., Rodellas, V., Bellmunt, F., Ledo, J., Pool, M., García-Orellana, J., Pezard P., Saaltink, M.W., Vázquez-Suñé, E. & Carrera, J. Integrated methodology to characterize hydro-geochemical properties in an alluvial coastal aquifer affected by seawater intrusion (SWI) and submarine groundwater discharge (SGD). 25th Salt Water Intrusion Meeting (SWIM). Gdansk (Poland).

Palacios, A., Ledo, J., Linde, N., Carrera, J., Luquot, L., Bellmunt, F., Folch, A., Bosch, D., Del Val, L., Martínez-Pérez, L., **Goyetche, T**., Diego-Feliu, García-Orellana, J. & Pool, M. Time-lapse Cross-Hole Electrical Resistivity Tomography (CHERT) for monitoring seawater intrusion dynamics in a Mediterranean aquifer. 25th Salt Water Intrusion Meeting (SWIM). Gdansk (Poland).

Pezard, P., Henry, G., Brun, L., **Goyetche, T.,** Luquot, L., Del Val, L., Martínez-Pérez, L., Folch, A., García-Orellana, J., Ledo, J., & Carrera, J. Innovate downhole geophysical methods for high-frequency seawater intrusion dynamics monitoring. 25th Salt Water Intrusion Meeting (SWIM). Gdansk (Poland).

Goyetche, T., Diego-Feliu, M., Luquot, L., Garcia-Orellana, J. & Carrera, J. Effects of a heavy rain event on the hydrodynamical and hydrogeochemical parameters in an alluvial coastal

aquifer. 4th Cargèse Summer School – Flow and Transport in Porous and Fractured Media. Cargèse (France).

2019

Goyetche, T., Pool, M. & Carrera, J. Hydraulic and mechanical characterisation of tide-induced head fluctuations in coastal aquifers. EGU General Assembly 2019. Vienna (Austria).

Del Val., L., Saaltink, M.W., Folch, A., **Goyetche, T.**, Pool, M., Carrera, J., Bour, O. & Selker, J.S. Distributed temperature sensing to monitor the fresh/salt groundwater interface. EGU General Assembly 2019. Vienna (Austria).

Martínez-Pérez, L., Marazuela, M.A., Luquot, L., Folch, A., del Val, L., **Goyetche, T**., Diego-Feliu, M., Saaltink, M.W., Rodellas, V., Pool, M., Bellmunt, F., García-Orellana, J., Pezard, P., Ledo, J., Vázquez-Suñé, E. & Carrera, J. Facing geological heterogeneity impact on reciprocal coastal systems. EGU General Assembly 2019. Vienna (Austria).

Folch. A, del Val, L., Luquot, L., Martínez-Pérez, L., Bellmunt, F., Le Lay, H., Rodellas, V., Ferrer, N., Fernández, S., Marazuela, M.A., Diego-Feliu, M., Pool, M. & **Goyetche, T**. Do groundwater data from piezometers correlate with FO-DTS and CHERT in costal aquifers?. EGU General Assembly 2019. Vienna (Austria).

2020

No international presentations during 2020, since congress was canceled or reported for COVID-19. The initial plan was to present at AGU general assembly and the 26th Salt Water Intrusion Meeting.

2021

Palacios, A., **Goyetche, T.**, Linde, N. & Carrera, J. Hydrogeophysical coupled inversion in coastal aquifers: the Argentona case. EGU General Assembly 2021. Virtual conference.

APPENDIX B

Tidal harmonics amplitude and time-shift, filtering error and calibrated amplitude

In the following table the amplitude and the time-shift is presented for each tidal harmonics at the observation points. The values presented in the first table correspond to the values obtained applying equation 3-1, 3-2 and 3-3.

In the second table, values are obtained from the calibration process by numerical modeling (presented in 3.3.4). A/A_0 and ωt_s are not presented for the "full" and the "harmonic sum" such that the A and t_s identification is not feasible.

Appendix B - Tidal harmonics amplitude and time-shift, filtering error and calibrated amplitude

MEASURED		O1		K1		N2		M2		K2		M4		RMSE	nRMSE		
Period (h)		25.82		23.9		12.66		12.41		11.95		6.2					
Parameter		A (m)	ϕ (Rad)	A (m)	ϕ (Rad)	A (m)	ϕ (Rad)	A (m)	ϕ (Rad)	A (m)	ϕ (Rad)	A (m)	ϕ (Rad)			hmax	hmin
Sea		0.0155	-1.6206	0.0381	-1.5943	0.0115	-1.7620	0.0504	-0.8799	0.0120	0.3387	0.0050	1.2903	0.0362	10.9%	0.180	-0.152
Observation point	Distance from the coast (m)	A0/A (-)	ωts (-)	A0/A (-)	ωts (-)	A0/A (-)	ωts (-)	A0/A (-)	ωts (-)	A0/A (-)	ωts (-)	A0/A (-)	ωts (-)	RMSE	nRMSE		
N1-15	62.93	0.5494	0.4762	0.4021	0.1431	0.4449	0.3151	0.3964	0.1206	0.5820	0.2272	0.3960	0.5494	0.0083	7.1%	0.063	-0.054
N2-15	97.98	0.3872	0.6525	0.2816	0.4803	0.2678	0.6052	0.2418	0.2942	0.5259	0.4871	0.2405	0.7845	0.0079	9.2%	0.049	-0.037
N3-15	80.15	0.4591	0.5679	0.3327	0.3074	0.3409	0.4363	0.3077	0.2160	0.5389	0.3587	0.3070	0.7020	0.0079	8.0%	0.053	-0.045
N4-15	82.04	0.4702	0.5069	0.3394	0.2517	0.3703	0.4342	0.3231	0.1941	0.5577	0.3022	0.3298	0.6549	0.0083	7.9%	0.056	-0.049
N1-20	60.27	0.5400	0.4859	0.4066	0.1418	0.4541	0.2703	0.4010	0.1181	0.6071	0.2168	0.4341	0.7172	0.0086	7.0%	0.062	-0.061
N2-20	99.89	0.4753	0.4625	0.3272	0.2101	0.3568	0.3489	0.3229	0.1553	0.5446	0.3328	0.3312	0.6217	0.0081	7.4%	0.059	-0.050
N3-20	79.77	0.5092	0.4856	0.3717	0.1919	0.3860	0.3219	0.3611	0.1427	0.5454	0.2485	0.3838	0.5924	0.0083	7.4%	0.057	-0.054
N4-20	81.19	0.5293	0.4663	0.3746	0.1818	0.4088	0.3264	0.3624	0.1459	0.5615	0.2287	0.3752	0.6955	0.0084	7.7%	0.057	-0.052
PP-18	39.63	0.5982	0.6862	0.4406	0.3690	0.4969	0.7972	0.4334	0.6304	0.6159	0.6818	0.4310	1.7095	0.0089	6.5%	0.066	-0.071
N1-25	62.37	0.5351	0.6222	0.3869	0.3884	0.4194	0.5985	0.3620	0.3620	0.6204	0.3854	0.2842	1.0486	0.0082	7.1%	0.063	-0.052
N2-25	98.37	0.5009	0.7417	0.3340	0.6484	0.3088	0.4568	0.2507	0.3373	0.6108	1.0461	0.2559	1.2100	0.0061	7.1%	0.049	-0.037
N3-25	78.11	0.6231	0.5050	0.3856	0.4060	0.4231	0.1288	0.3270	0.2252	0.6466	0.9594	0.3507	0.9494	0.0060	5.5%	0.059	-0.050
N4-25	82.62	0.5004	0.7249	0.3608	0.4570	0.3900	0.8585	0.3555	0.6480	0.5662	0.7778	0.3462	1.6654	0.0082	7.0%	0.061	-0.057
PS-25	83.31	0.4249	0.7159	0.3361	0.4764	0.3164	0.6784	0.2775	0.3923	0.5431	0.4610	0.2740	0.8739	0.0081	8.7%	0.052	-0.041

CALIBRATED		O1		K1		N2		M2		K2		M4	
Period (h)		25.82		23.9		12.66		12.41		11.95		6.2	
Observation point	Distance (m)	A0/A (-)	ωts (-)	A0/A (-)	ωts (-)	A0/A (-)	ωts (-)	A0/A (-)	ωts (-)	A0/A (-)	ωts (-)	A0/A (-)	ωts (-)
N1-15	62.93	0.5428	0.4522	0.4081	0.2702	0.4244	0.2893	0.3719	0.2829	0.6031	0.3025	0.3927	0.5707
N2-15	97.98	0.4505	0.5836	0.3032	0.4546	0.2913	0.5671	0.2812	0.4008	0.5119	0.4216	0.2873	0.7762
N3-15	80.15	0.4965	0.5162	0.3332	0.3960	0.3420	0.4840	0.3116	0.3340	0.5560	0.3642	0.3380	0.6625
N4-15	82.04	0.4915	0.5237	0.3298	0.4022	0.3362	0.4928	0.3083	0.3410	0.5512	0.3702	0.3322	0.6746
N1-20	60.27	0.5500	0.4422	0.4126	0.2637	0.4284	0.2828	0.3763	0.2740	0.6060	0.2984	0.4018	0.5569
N2-20	99.89	0.4455	0.5942	0.3493	0.3633	0.3715	0.3830	0.3140	0.4106	0.5638	0.3594	0.2801	0.8110
N3-20	79.77	0.4971	0.5180	0.3804	0.3120	0.3995	0.3314	0.3445	0.3403	0.5849	0.3283	0.3366	0.6816
N4-20	81.19	0.4934	0.5232	0.3782	0.3155	0.3975	0.3350	0.3423	0.3452	0.5834	0.3305	0.3325	0.6891
PP-18	39.63	0.5998	0.4095	0.4300	0.3268	0.4437	0.3176	0.4025	0.2808	0.5513	0.5360	0.4459	0.5526
N1-25	62.37	0.5264	0.6339	0.3662	0.4054	0.3740	0.5974	0.3422	0.4401	0.5814	0.3874	0.3065	1.0415
N2-25	98.37	0.4423	0.7078	0.3248	0.6423	0.3424	0.6410	0.2974	0.6182	0.4708	0.9378	0.2428	1.1807
N3-25	78.11	0.4971	0.5581	0.3679	0.4155	0.3865	0.4199	0.3378	0.4129	0.5200	0.5432	0.3171	0.8021
N4-25	82.62	0.4772	0.7212	0.3363	0.4951	0.3474	0.7107	0.3101	0.5545	0.5619	0.4268	0.2598	1.2481
PS-25	83.31	0.4755	0.7241	0.3353	0.4981	0.3465	0.7144	0.3091	0.5584	0.5612	0.4281	0.2584	1.2549

APPENDIX C

Hydrochemical data for EMMA analysis

n_s	1	2	3	4	5	6	7	8	9	10	11	12	13	14	15	16	17	18	19	20
Chemical species	**Alk**	**Al**	**Ca**	**SO4**	**Na**	**K**	**Mg**	**DO**	**NO3**	**Mn**	**Fe**	**F**	**Ba**	**Si**	**d18O**	**dD**	**EC**	**Br**	**Li**	**Cl**
Units	mmol/L	mmol/L	mmol/L	mmol/L	mmol/L	mmol/L	mmol/L	mmol/L	mmol/L	mmol/L	mmol/L	mmol/L	mmol/L	mmol/L	‰	‰	mS/cm	mmol/L	mmol/L	mmol/L
F1	5.279	0.005	3.668	1.072	4.703	0.064	1.943	0.035	1.516	0.001	0.004	0.010	0.000	0.329	-6.143	-37.527	0.980	0.011	0.000	1.881
SW	2.098	0.008	10.233	30.259	489.071	9.890	59.659	0.324	0.000	0.000	0.002	0.057	0.000	0.004	0.700	7.500	53.000	0.898	0.028	612.162
N1-25	1.901	0.030	42.429	16.037	265.893	3.916	48.146	0.025	0.037	0.004	0.011	0.004	0.001	0.354	-1.700	-8.100	39.900	0.621	0.016	427.055
SEWAGE	4.918	0.000	0.158	0.015	0.110	0.009	0.016	0.032	0.006	0.000	0.001	0.001	0.000	0.285	-6.185	-37.804	0.600	0.000	0.000	0.047
RIVER	4.918	0.000	0.818	0.068	0.482	0.345	0.582	0.032	0.105	0.000	0.018	0.004	0.003	0.285	-6.154	-37.599	0.880	0.000	0.000	0.241
PP15	4.902	0.006	10.882	1.837	11.733	0.146	4.616	0.036	1.102	0.000	0.001	0.009	0.001	0.336	-5.310	-33.522	4.140	0.061	0.001	32.558
PP20A	4.602	0.017	19.060	6.929	87.109	0.720	16.297	0.047	1.171	0.000	0.001	0.014	0.001	0.313	-4.500	-26.700	15.190	0.215	0.001	143.759
N1-15	5.502	0.003	8.067	1.714	9.757	0.134	3.120	0.022	1.154	0.000	0.000	0.017	0.001	0.330	-5.252	-32.992	2.990	0.043	0.001	22.537
N3-15	5.102	0.003	4.108	1.462	5.414	0.145	1.535	0.028	1.310	0.000	0.000	0.013	0.000	0.338	-5.475	-35.235	1.580	0.015	0.001	7.210
N4-15	5.502	0.001	3.317	1.561	4.125	0.049	1.121	0.007	1.379	0.000	0.000	0.010	0.000	0.332	-5.933	-37.330	1.290	0.013	0.001	4.042
N2-15	4.802	0.000	2.921	1.480	3.661	0.050	0.979	0.046	1.500	0.000	0.001	0.012	0.000	0.360	-5.890	-37.350	1.120	0.012	0.000	2.499
PP20B	3.101	0.019	31.176	20.956	338.865	2.950	48.337	0.016	0.219	0.000	0.000	0.009	0.001	0.272	-0.800	-3.300	45.000	0.680	0.009	466.107
N1-20	2.701	0.016	24.268	24.768	420.467	3.437	51.880	0.025	0.027	0.001	0.000	0.008	0.001	0.268	0.100	3.300	50.800	0.768	0.010	525.340
N3-20	4.602	0.016	27.094	4.783	57.205	0.431	15.226	0.053	0.663	0.000	0.001	0.009	0.002	0.311	-5.100	-30.000	13.090	0.184	0.001	122.992
N4-20	4.101	0.015	39.368	7.255	83.429	0.634	23.050	0.016	0.539	0.001	0.001	0.009	0.002	0.292	-4.600	-26.800	20.100	0.288	0.003	195.685
N2-20	4.802	0.018	26.207	3.607	35.699	0.336	12.883	0.053	0.734	0.000	0.000	0.011	0.001	0.299	-5.300	-30.900	11.080	0.158	0.001	103.385
N3-25	2.801	0.019	24.821	20.760	366.816	3.914	51.161	0.048	0.155	0.005	0.007	0.008	0.001	0.298	-0.500	-1.500	46.700	0.723	0.012	493.298
N4-25	2.401	0.016	29.363	21.385	356.742	3.636	52.437	0.014	0.010	0.002	0.001	0.007	0.001	0.287	-0.500	-1.500	47.300	0.734	0.013	502.001
N2-25	2.501	0.024	38.779	14.683	269.921	3.267	53.693	0.032	0.010	0.003	0.009	0.006	0.002	0.323	-1.500	-8.000	39.200	0.628	0.012	428.945
PS25	1.891	0.022	30.061	21.048	320.761	2.628	48.101	0.003	0.046	0.002	0.001	0.007	0.001	0.279	-0.900	-4.300	46.200	0.710	0.010	485.614

APPENDIX D

Stoichoimetric and component matrix for the iteration process

Here we detail the stoichiometric and component matrix used in each iteration during the iteration process (**Figure 4-3**).

1.1. Iteration 1: Stoichiometric and component matrix for cation exchange and gypsum precipitation

We start from a chemical system governed by four chemical reactions (n_r = 4), with cation exchange (Na-Ca, K-Ca and Mg-Ca) and gypsum precipitation. We defined SO_4, Na, K and Mg as secondary species. Such that the stoichiometric matrix can be writen as: $S = (S_1|-I)$. The secondary species have to coincides with the opposite of the identity matrix, I. For this first chemical system the stoichiometric matrix is:|

Stoichiometric matrix		1 Alk	2 Al	3 Ca	4 DO	5 NO3	6 Mn	7 Fe	8 F	9 Ba	10 Si	11 SO4	12 Na	13 K	14 Mg
R1 Ca - yeso = SO4	R1	0	0	-1	0	0	0	0	0	0	0	-1	0	0	0
R2 Na + 0.5X-Ca =X-Na + 0.5Ca	R2	0	0	0.5	0	0	0	0	0	0	0	0	-1	0	0
R3 K + 0.5X-Ca =X-K + 0.5Ca	R3	0	0	0.5	0	0	0	0	0	0	0	0	0	-1	0
R4 Mg + X-Ca = Ca - X-Mg	R4	0	0	1	0	0	0	0	0	0	0	0	0	0	-1
		Primary species										Secondary species			

The component matrix (U) is then obtained by transforming the stoichiometric matrix as follows $U = (I|S_u^t)$. The obtained component matrix for iteration 1 is:

	Components matrix		Alk	Al	Ca	DO	NO3	Mn	Fe	F	Ba	Si	SO4	Na	K	Mg
	Alk	1	1	0	0	0	0	0	0	0	0	0	0	0	0	0
	Al	2	0	1	0	0	0	0	0	0	0	0	0	0	0	0
u1	Ca - SO4 + 0.5Na + 0.5K + Mg	3	0	0	1	0	0	0	0	0	0	0	-1	0.5	0.5	1
	DO	4	0	0	0	1	0	0	0	0	0	0	0	0	0	0
	NO3	5	0	0	0	0	1	0	0	0	0	0	0	0	0	0
	Mn	6	0	0	0	0	0	1	0	0	0	0	0	0	0	0
	Fe	7	0	0	0	0	0	0	1	0	0	0	0	0	0	0
	F	8	0	0	0	0	0	0	0	1	0	0	0	0	0	0
	Ba	9	0	0	0	0	0	0	0	0	1	0	0	0	0	0
	Si	10	0	0	0	0	0	0	0	0	0	1	0	0	0	0

In this first iteration, one conservative component is obtained such that: $u_1 = Ca^{2+} - SO_4^{2-} + 0.5Na^{+} + 0.5K^{+} + Mg^{2+}$. Then the same process is repeated for each chemical system, where new chemical reactions are included in the stoichiometric matrix.

1.2. Iteration 2: Stoichiometric and component matrix for redox reactions

The stoichiometric matrix is:

		1	2	3	4	5	6	7	8	9	10	11	12	13	14
	Stoichiometric matrix	Alk	Al	Ca	F	Ba	Si	SO4	Na	K	Mg	DO	NO3	Mn	Fe
R1	Ca - yeso = SO4	R1	0	0	-1	0	0	0	-1	0	0	0	0	0	0	0
R2	Na + 0.5X-Ca =X-Na + 0.5Ca	R2	0	0	0.5	0	0	0	0	-1	0	0	0	0	0	0
R3	K + 0.5X-Ca =X-K + 0.5Ca	R3	0	0	0.5	0	0	0	0	0	-1	0	0	0	0	0
R4	Mg + X-Ca = Ca - X-Mg	R4	0	0	1	0	0	0	0	0	0	-1	0	0	0	0
R5	Redox O2	R5	1	0	0	0	0	0	0	0	0	0	-1	0	0	0
R6	Redox NO3	R6	1.25	0	0	0	0	0	0	0	0	0	0	-1	0	0
R7	Redox Mn	R7	0.5	0	0	0	0	0	0	0	0	0	0	0	-1	0
R8	Redox Fe	R8	0.25	0	0	0	0	0	0	0	0	0	0	0	0	-1

Primary species | Secondary species

The component matrix is:

	Components matrix		Alk	Al	Ca	F	Ba	Si	SO4	Na	K	Mg	DO	NO3	Mn	Fe
u2	Alk + DO + 1.25NO3 + 0.5Mn + 0.25Fe	1	1	0	0	0	0	0	0	0	0	0	1	1.25	0.5	0.25
	Al	2	0	1	0	0	0	0	0	0	0	0	0	0	0	0
u1	Ca - SO4 + 0.5Na + 0.5K + Mg	3	0	0	1	0	0	0	-1	0.5	0.5	1	0	0	0	0
	F	4	0	0	0	1	0	0	0	0	0	0	0	0	0	0
	Ba	5	0	0	0	0	1	0	0	0	0	0	0	0	0	0
	Si	6	0	0	0	0	0	1	0	0	0	0	0	0	0	0

A new conservative component is obtained : $u_2 = HCO_3^{-} + DO + 1.25NO_3^{-} + 0.5Mn^{2+} + 0.25Fe^{2+}$.

1.3. Iteration 3: Stoichiometric and component matrix for minerals dissolution-precipitation reactions

The stoichiometric matrix is:

	Stoichiometric matrix		1 Alk	2 Al	3 Ca	4 SO4	5 Na	6 K	7 Mg	8 DO	9 NO3	10 Mn	11 Fe	12 F	13 Ba	14 Si
R1	Ca - yeso = SO4	R1	0	0	-1	-1	0	0	0	0	0	0	0	0	0	0
R2	Na + 0.5X-Ca =X-Na + 0.5Ca	R2	0	0	0.5	0	-1	0	0	0	0	0	0	0	0	0
R3	K + 0.5X-Ca =X-K + 0.5Ca	R3	0	0	0.5	0	0	-1	0	0	0	0	0	0	0	0
R4	Mg + X-Ca = Ca - X-Mg	R4	0	0	1	0	0	0	-1	0	0	0	0	0	0	0
R5	Redox O2	R5	1	0	0	0	0	0	0	-1	0	0	0	0	0	0
R6	Redox NO3	R6	1.25	0	0	0	0	0	0	0	-1	0	0	0	0	0
R7	Redox Mn	R7	0.5	0	0	0	0	0	0	0	0	-1	0	0	0	0
R8	Redox Fe	R8	0.25	0	0	0	0	0	0	0	0	0	-1	0	0	0
R9	F + 1/2Ca = 1/2CaF3	R9	0	0	-0.5	0	0	0	0	0	0	0	0	-1	0	0
R10	Ba + SO4 = BaSO4	R10	0	0	1	0	0	0	0	0	0	0	0	0	-1	0
R11	Si = 1/3Feldspath Alteration - 1/3K - 1/3 Al	R11	0	0.33	0.17	0	0	0	0	0	0	0	0	0	0	-1

Primary species — Secondary species

The component matrix is:

			Alk	Al	Ca	SO4	Na	K	Mg	DO	NO3	Mn	Fe	F	Ba	Si
u2	**Alk** + DO +1.25NO3 + 0.5Mn + 0.25Fe	1	1	0	0	0	0	0	0	1	1.25	0.5	0.25	0	0	0
u3	**Al** + 0.33 Si	2	0	1	0	0	0	0	0	0	0	0	0	0	0	0.33
u1	**Ca** - SO4 + 0.5Na + 0.5K + Mg -0.5F + Ba + 1/6Si	3	0	0	1	-1	0.5	0.5	1	0	0	0	0	-0.5	1	0.17

A new conservative component is obtained : $u_3 = Al^{3+} + 1/3Si^{4+}$ and the conservatives components u_1 and u_2 now reads as follows: $u_1 = Ca^{2+} - SO_4^{2-} + 0.5Na^+ + 0.5K^+ + Mg^{2+} - 0.5F^- + Ba^{2+} + 1/6Si^{4+}$. u_2 is identical to the previous iteration: $u_2 = HCO_3^- + DO + 1.25NO_3^- + 0.5Mn^{2+} + 0.25Fe^{2+}$.

1.4. Iteration 4: Stoichiometric and component matrix for gibbsite precipitation

The stoichiometric matrix is:

Stoichiometric matrix		1 Alk	2 Ca	3 SO4	4 Na	5 K	6 Mg	7 DO	8 NO3	9 Mn	10 Fe	11 F	12 Ba	13 Si	14 Al
Ca - yeso = SO4	R1	0	-1	-1	0	0	0	0	0	0	0	0	0	0	0
Na + 0.5X-Ca =X-Na + 0.5Ca	R2	0	0.5	0	-1	0	0	0	0	0	0	0	0	0	0
K + 0.5X-Ca =X-K + 0.5Ca	R3	0	0.5	0	0	-1	0	0	0	0	0	0	0	0	0
Mg + X-Ca = Ca - X-Mg	R4	0	1	0	0	0	-1	0	0	0	0	0	0	0	0
Redox O2	R5	1	0	0	0	0	0	-1	0	0	0	0	0	0	0
Redox NO3	R6	1.25	0	0	0	0	0	0	-1	0	0	0	0	0	0
Redox Mn	R7	0.5	0	0	0	0	0	0	0	-1	0	0	0	0	0
Redox Fe	R8	0.25	0	0	0	0	0	0	0	0	-1	0	0	0	0
F + 1/2Ca = 1/2CaF3	R9	0	-0.5	0	0	0	0	0	0	0	0	-1	0	0	0
Ba + SO4 = BaSO4	R10	0	1	0	0	0	0	0	0	0	0	0	-1	0	0
Si = 1/3Feldspath Alteration - 1/3K - 1/3 Al	R11	0	0.17	0	0	0	0	0	0	0	0	0	0	-1	0
Al --> Gibbsite	R12	0	0	0	0	0	0	0	0	0	0	0	0	0	-1
		Primary species		Secondary species											

The component matrix is:

		Alk	Ca	SO4	Na	K	Mg	DO	NO3	Mn	Fe	F	Ba	Si	Al
u2	**Alk** + DO +1.25NO3 + 0.5Mn + 0.25Fe	1	0	0	0	0	0	1	1.25	0.5	0.25	0	0	0	0
u1	**Ca** - SO4 + 0.5Na + 0.5K + Mg -0.5F + Ba + 1/6Si	0	1	-1	0.5	0.5	1	0	0	0	0	-0.5	1	0.17	0

During this iteration, u_3 is removed and only and the conservatives components u_1 and u_2 remain unchanged.

APPENDIX E

Rainfall event chemical analysis

Appendix E - Rainfall event chemical analysis

n_s	1	2	3	4	5	6	7	8	9	10	11	12	13	14	15	16	17	18
Specie	**Alk**	**Al**	**Ca**	**SO4**	**Na**	**K**	**Mg**	**DO**	**NO3**	**Mn**	**Fe**	**F**	**Ba**	**Si**	**EC**	**Br**	**Li**	**Cl**
Units	mmol/L	mmol/L	mmol/L	mmol/L	mmol/L	mmol/L	mmol/L	mmol/L	mmol/L	mmol/L	mmol/L	mmol/L	mmol/L	mmol/L	mS/cm	mmol/L	mmol/L	mmol/L
F1	5.279	0.005	3.668	1.072	4.703	0.064	1.943	0.035	1.516	0.001	0.004	0.010	0.000	0.329	0.980	0.011	0.000	1.881
SW	2.301	0.001	10.484	34.792	477.283	10.156	59.659	0.324	0.000	0.000	0.002	0.078	0.000	0.004	53.000	0.981	0.028	673.052
RAIN	0.054	0.004	0.023	0.022	0.227	0.009	0.021	0.267	0.022	0.000	0.001	0.000	0.000	0.004	0.033	0.000	0.000	0.201
SEWAGE	4.391	0.000	0.158	0.015	0.110	0.009	0.016	0.258	0.006	0.000	0.001	0.001	0.000	0.004	0.600	0.010	0.000	0.047
RIVER OUT	4.341	0.000	0.818	0.068	0.483	0.345	0.582	0.278	0.105	0.000	0.018	0.004	0.003	0.285	0.881	0.015	0.000	0.241
RIVER UP	4.386	0.000	0.733	0.087	0.688	0.261	0.429	0.281	0.117	0.000	0.018	0.006	0.003	0.285	0.149	0.003	0.000	0.525
PP20A	4.401	0.005	13.698	8.807	115.982	1.436	17.727	0.052	0.850	0.000	0.000	0.020	0.000	0.284	16.390	0.247	0.001	178.189
PP18	3.301	0.012	20.732	6.953	82.980	0.979	15.985	0.053	1.153	0.000	0.001	0.016	0.001	0.297	15.120	0.221	0.001	160.236
N115	4.001	0.012	21.834	3.983	37.852	0.293	11.628	0.035	1.407	0.000	0.000	0.012	0.001	0.315	9.600	0.140	0.001	103.524
N120	3.601	0.008	19.322	31.064	432.046	5.991	53.135	0.042	0.001	0.002	0.000	0.020	0.000	0.245	49.530	0.912	0.014	617.200
N420	2.701	0.009	29.698	15.933	203.387	1.547	33.324	0.018	0.000	0.000	0.001	0.014	0.001	0.259	29.300	0.504	0.004	347.387
N125	2.601	0.013	33.615	22.818	294.288	5.135	47.172	0.025	0.002	0.002	0.019	0.001	0.001	0.301	40.990	0.769	0.014	519.508
N315	3.401	0.001	4.059	1.461	4.578	0.165	1.483	0.059	1.614	0.000	0.002	0.014	0.000	0.320	1.500	0.032	0.000	7.848
PP15	5.002	0.004	5.403	1.828	12.580	0.359	2.956	0.026	1.316	0.000	0.002	0.020	0.001	0.292	2.800	0.034	0.001	22.928
N320	3.501	0.021	42.807	16.821	197.227	1.276	38.145	0.029	0.312	0.002	0.002	0.014	0.001	0.264	31.500	0.554	0.014	383.402
N325	1.901	0.004	26.028	24.017	352.619	5.372	52.844	0.041	0.001	0.018	0.026	0.001	0.001	0.290	44.060	0.797	0.014	543.362
N215	3.901	0.004	2.668	1.290	3.473	0.113	0.912	0.072	1.578	0.000	0.002	0.014	0.000	0.333	0.973	0.006	0.000	2.576
N225	2.701	0.009	28.446	10.517	217.489	4.799	41.144	0.062	0.018	0.002	0.016	0.001	0.001	0.268	31.932	0.551	0.014	225.708
N220	2.801	0.028	56.739	15.215	168.301	1.357	40.457	0.025	0.310	0.002	0.002	0.014	0.001	0.277	31.350	0.564	0.014	388.574
PS25	1.901	0.009	21.823	28.892	392.924	5.014	51.821	0.065	0.000	0.002	0.002	0.001	0.001	0.262	46.780	0.873	0.014	597.863
N415	3.801	0.004	3.678	1.390	4.068	0.073	1.283	0.077	1.062	0.000	0.002	0.016	0.000	0.329	3.750	0.038	0.001	6.193
PP20B	4.301	0.009	16.767	13.490	179.132	2.182	25.502	0.215	0.560	0.000	0.004	0.021	0.001	0.276	25.200	0.394	0.003	276.710
PP20A	4.301	0.001	6.741	3.923	47.431	0.656	7.047	0.056	0.816	0.000	0.002	0.020	0.000	0.267	7.200	0.087	0.001	71.060
PP20B	5.202	0.003	7.495	4.500	55.596	0.765	8.210	0.038	0.807	0.000	0.001	0.020	0.000	0.272	8.150	0.104	0.001	83.909
PP18	3.801	0.013	20.690	7.593	93.076	1.121	17.292	0.108	1.111	0.001	0.002	0.010	0.001	0.290	14.380	0.235	0.001	173.418
N115	4.401	0.006	17.197	3.303	28.807	0.238	9.038	0.052	1.297	0.000	0.002	0.012	0.001	0.312	7.790	0.105	0.001	80.351
N120	3.001	0.007	19.142	30.706	423.816	5.898	52.671	0.044	0.002	0.002	0.002	0.001	0.000	0.243	49.500	0.882	0.014	608.110
N125	2.201	0.017	31.736	24.925	333.401	5.434	50.485	0.041	0.001	0.002	0.011	0.001	0.001	0.299	43.170	0.790	0.014	541.204
N315	4.401	0.004	4.064	1.449	4.460	0.164	1.473	0.237	1.445	0.000	0.000	0.013	0.000	0.323	1.490	0.026	0.000	7.486
PP20A	5.502	0.004	2.825	2.429	27.555	0.472	3.016	0.113	0.272	0.000	0.002	0.040	0.000	0.218	4.140	0.061	0.001	35.606
PP20B	5.802	0.023	3.014	2.403	29.481	0.527	3.228	0.081	0.297	0.000	0.012	0.040	0.000	0.285	4.120	0.096	0.001	35.238
PP18	2.801	0.000	16.673	6.021	71.340	0.813	12.888	0.033	0.330	0.000	0.002	0.008	0.001	0.300	12.430	0.168	0.001	128.431
N115	3.901	0.001	16.054	3.278	28.561	0.248	8.641	0.065	0.886	0.000	0.001	0.016	0.001	0.311	7.560	0.096	0.001	74.394
N120	2.101	0.007	19.073	31.076	426.391	5.855	52.225	0.023	0.013	0.002	0.000	0.001	0.000	0.245	49.417	0.881	0.014	615.057
N315	2.801	0.004	3.499	1.603	4.560	0.148	1.277	0.029	1.468	0.000	0.002	0.013	0.000	0.328	1.431	0.000	0.000	5.520
N125	1.500	0.011	26.435	27.448	372.793	5.544	51.002	0.029	0.004	0.002	0.004	0.001	0.001	0.282	45.520	0.822	0.014	573.918
N325	1.801	0.004	17.769	23.312	307.999	4.335	41.897	0.029	0.002	0.009	0.003	0.001	0.002	0.221	38.500	0.674	0.014	472.223
N320	1.901	0.019	40.383	18.409	214.244	1.426	39.628	0.041	0.270	0.002	0.001	0.001	0.001	0.254	33.690	0.578	0.014	410.597
N215	3.201	0.004	2.569	1.175	3.636	0.135	0.879	0.020	1.505	0.000	0.002	0.014	0.000	0.327	0.930	0.000	0.000	2.364
N225	2.301	0.012	22.014	27.376	367.382	4.669	48.828	0.015	0.039	0.002	0.037	0.001	0.002	0.245	44.539	0.807	0.014	561.371
N220	2.501	0.028	55.746	14.783	161.577	1.239	38.606	0.302	0.368	0.002	0.002	0.009	0.001	0.270	30.260	0.536	0.014	376.264
PP18	3.601	0.002	15.326	5.829	68.008	0.800	11.769	0.041	0.888	0.000	0.002	0.008	0.001	0.298	11.390	0.157	0.001	121.547
PP20A	4.902	0.006	2.503	2.313	28.125	0.525	2.799	0.091	0.410	0.000	0.020	0.049	0.000	0.325	3.800	0.080	0.001	32.518
PP20B	3.301	0.031	2.424	2.297	27.571	0.515	2.699	0.104	0.423	0.000	0.009	0.051	0.000	0.268	3.720	0.142	0.001	32.374
PP20A	5.602	0.004	3.192	3.262	44.426	0.736	4.668	0.120	0.328	0.000	0.002	0.061	0.000	0.225	5.750	0.059	0.001	54.136
PP20B	4.702	0.000	10.974	10.767	137.514	1.817	19.237	0.069	0.146	0.000	0.001	0.033	0.001	0.240	18.770	0.263	0.001	201.895
N125	2.601	0.009	21.516	28.403	399.788	5.674	51.805	0.021	0.004	0.002	0.003	0.001	0.001	0.263	47.200	0.832	0.014	578.704
PP18	3.401	0.004	12.335	5.660	69.603	0.847	10.938	0.048	0.996	0.000	0.002	0.008	0.001	0.291	11.170	0.148	0.001	115.603
N120	2.501	0.009	19.208	30.278	423.798	5.905	52.528	0.009	0.005	0.002	0.000	0.001	0.000	0.244	49.190	0.858	0.014	598.501
N115	4.902	0.001	15.511	2.950	25.856	0.236	8.180	0.027	1.252	0.000	0.002	0.012	0.001	0.318	6.900	0.087	0.001	68.587
N325	2.501	0.005	19.199	26.054	360.622	4.830	46.674	0.026	0.002	0.011	0.010	0.001	0.002	0.233	42.680	0.748	0.014	526.388
N315	4.602	0.004	3.336	1.728	4.356	0.156	1.205	0.031	1.209	0.000	0.001	0.014	0.000	0.336	1.240	0.022	0.000	4.605
N320	3.201	0.018	42.695	19.123	234.627	1.508	42.112	0.007	0.222	0.002	0.002	0.014	0.001	0.258	34.400	0.598	0.014	423.838
N215	3.501	0.004	2.364	1.120	3.324	0.140	0.820	0.022	1.398	0.000	0.002	0.014	0.000	0.327	0.890	0.016	0.000	2.298
N225	2.601	0.001	21.632	29.715	405.808	5.127	52.109	0.004	0.003	0.002	0.019	0.001	0.001	0.249	47.990	0.851	0.014	597.857
N220	3.301	0.021	54.344	15.204	175.052	1.381	40.236	0.009	0.256	0.002	0.002	0.008	0.001	0.275	31.330	0.545	0.014	383.863
PP20A	6.202	0.004	1.896	2.243	31.704	0.635	2.633	0.135	0.254	0.000	0.002	0.068	0.000	0.218	3.860	0.024	0.001	32.871
PP18	4.001	0.002	13.571	5.553	66.565	0.827	11.320	0.025	0.540	0.000	0.000	0.013	0.001	0.288	11.070	0.151	0.001	116.077
PP18	3.601	0.004	15.512	6.148	75.792	0.910	13.277	0.029	0.850	0.000	0.000	0.008	0.001	0.291	13.238	0.175	0.001	135.120
N125	2.401	0.010	20.590	28.445	393.063	5.440	50.242	0.011	0.002	0.002	0.006	0.001	0.001	0.258	46.889	0.842	0.014	583.819
N120	2.701	0.006	19.181	29.756	425.330	5.890	52.405	0.065	0.000	0.002	0.002	0.001	0.000	0.241	49.483	0.828	0.014	588.676
PP20B	4.902	0.013	18.052	19.734	258.029	3.171	35.566	0.023	0.294	0.002	0.002	0.028	0.002	0.228	35.400	0.539	0.014	390.895

N325	1.701	0.009	20.010	27.365	385.808	5.221	49.541	0.207	0.000	0.017	0.025	0.001	0.001	0.250	45.399	0.777	0.014	560.508
N320	3.601	0.022	42.389	18.258	219.533	1.444	40.365	0.005	0.378	0.002	0.002	0.014	0.001	0.263	33.076	0.581	0.014	408.782
N115	5.002	0.004	16.706	3.137	27.080	0.241	8.756	0.015	1.355	0.000	0.000	0.012	0.001	0.316	8.357	0.096	0.001	76.077
N225	2.901	0.008	21.361	30.178	407.330	5.198	52.190	0.026	0.000	0.002	0.022	0.001	0.001	0.246	48.232	0.840	0.014	604.834
N315	5.402	0.004	3.422	1.601	4.519	0.152	1.246	0.026	1.359	0.000	0.002	0.014	0.000	0.333	1.255	0.008	0.000	5.228
N220	3.501	0.026	56.250	15.328	173.921	1.468	41.730	0.007	0.369	0.002	0.002	0.014	0.001	0.274	31.740	0.557	0.014	394.215
N215	4.702	0.004	2.524	1.207	3.470	0.139	0.873	0.024	1.565	0.000	0.001	0.014	0.000	0.326	0.941	0.009	0.000	2.573
PP18	4.301	0.006	17.466	6.319	75.433	0.899	14.149	0.274	0.660	0.000	0.001	0.012	0.001	0.293	13.178	0.185	0.001	141.384
N125	2.501	0.009	24.172	26.503	368.704	5.559	51.239	0.017	0.002	0.002	0.008	0.001	0.001	0.282	45.192	0.786	0.014	559.275
N120	3.001	0.008	19.144	31.567	433.855	5.966	52.795	0.006	0.000	0.002	0.002	0.001	0.000	0.248	49.495	0.876	0.014	624.444
PP20A	4.802	0.004	10.373	8.071	105.830	1.370	15.370	0.026	0.738	0.000	0.002	0.023	0.001	0.280	15.275	0.206	0.001	158.335
PP20B	3.601	0.008	24.456	26.531	365.207	4.426	48.812	0.021	0.165	0.002	0.000	0.022	0.001	0.226	46.442	0.742	0.014	533.977
N115	3.801	0.011	17.314	3.154	27.590	0.256	9.094	0.016	1.319	0.000	0.002	0.016	0.001	0.316	7.633	0.100	0.001	78.370
N315	5.302	0.004	3.601	1.607	4.254	0.156	1.293	0.019	1.190	0.000	0.002	0.014	0.000	0.329	1.247	0.014	0.000	5.068
N325	3.101	0.003	21.801	27.076	381.519	5.697	51.754	0.031	0.002	0.016	0.026	0.001	0.001	0.274	46.090	0.813	0.014	580.851
N215	4.602	0.004	2.596	1.260	3.473	0.111	0.881	0.048	1.906	0.000	0.002	0.013	0.000	0.328	0.951	0.004	0.000	2.585
N320	3.601	0.019	44.747	19.299	232.930	1.527	42.707	0.019	0.199	0.002	0.002	0.009	0.001	0.270	34.770	0.601	0.014	432.857
N220	3.701	0.028	57.568	15.004	171.068	1.380	41.330	0.026	0.380	0.002	0.002	0.009	0.001	0.276	31.431	0.543	0.014	388.246
N225	2.801	0.010	26.929	24.960	354.306	4.999	53.233	0.012	0.001	0.002	0.012	0.001	0.001	0.276	43.298	0.771	0.014	552.337

APPENDIX F

Reaction extent during the rainfall event

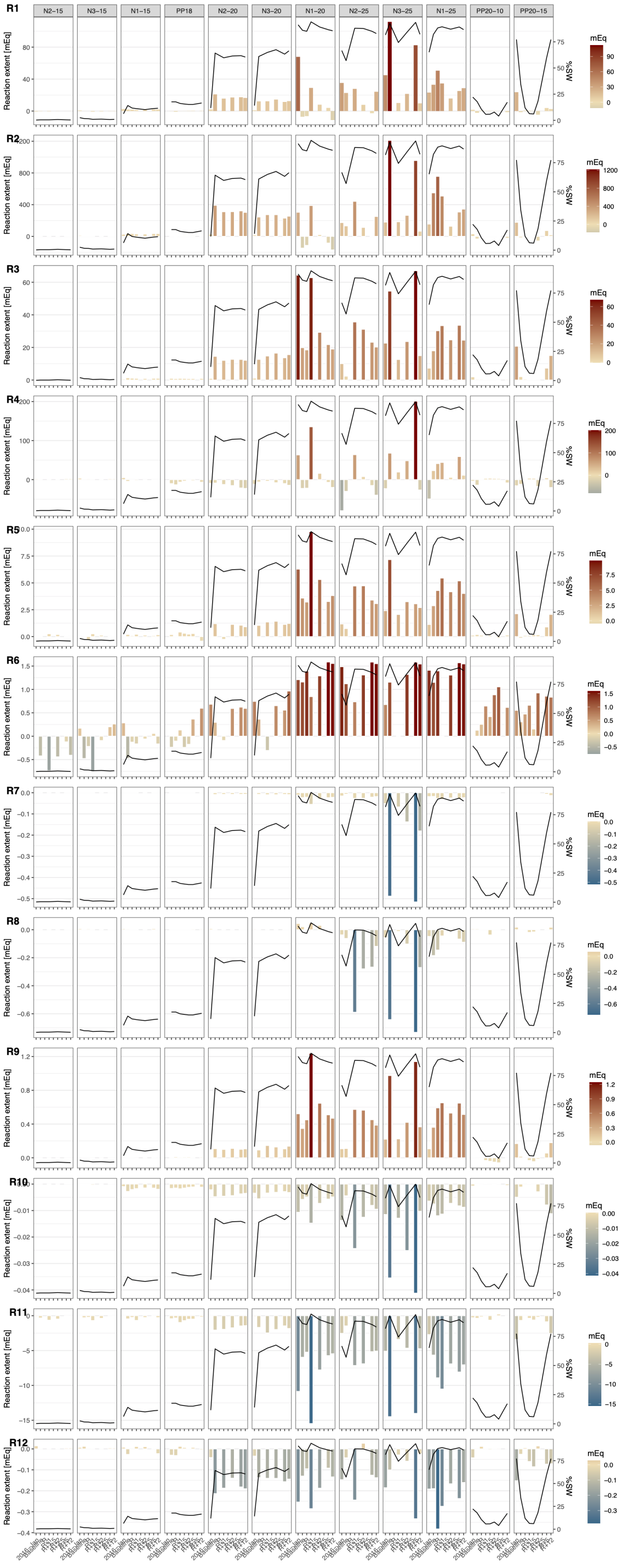
R1
R2
R3
R4
R5
R6
R7
R8
R9
R10
R11
R12
N2–15
N3–15
N1–15
PP18
N2–20
N3–20
N1–20
N2–25
N3–25
N1–25
PP20–10
PP20–15
Reaction extent [mEq]
%SW
mEq

Bibliography

Adger, N. W., Arnell, N. W., & Tompkins, E. L. (2005). Successful adaptation to climate change across scales. *Global Environmental Change, 15*(2), 77-86. doi:10.1016/j.gloenvcha.2004.12.005

Agència Catalana de l'Aigua. (2001). Delimitació de zones inundables per a la redacció de l'INUNCAT. *Departament de Medi Ambient, Generalitat de Catalunya.*

Alcaraz, M., Carrera, J., Cuello, J., Guarracino, L., & Vives, L. (2021). Determining hydraulic connectivity of the coastal aquifer system of La Plata river estuary (Argentina) to the ocean by analysis of aquifer response to low-frequency tidal components. *Hydrogeology Journal*, 1-13.

Alcolea, A., Castro, E., Barbieri, M., Carrera, J., & Bea, S. (2007). Inverse modeling of coastal aquifers using tidal response and hydraulic tests. *Groundwater, 45*(6), 711-722.

Alcolea, A., Renard, P., Mariethoz, G., & Bertone, F. (2009). Reducing the impact of a desalination plant using stochastic modeling and optimization techniques. *Journal of Hydrology, 365*(3-4), 275-288.

Alfarrah, N., & Walraevens, K. (2018). Groundwater overexploitation and seawater intrusion in coastal areas of arid and semi-arid regions. *Water, 10*(2), 143.

Andersen, M. S., Nyvang, V., Jakobsen, R., & Postma, D. (2005). Geochemical processes and solute transport at the seawater/freshwater interface of a sandy aquifer. *Geochimica et Cosmochimica Acta, 69*(16), 3979-3994. doi:https://doi.org/10.1016/j.gca.2005.03.017

Anderson, D. M., Glibert, P. M., & Burkholder, J. M. (2002). Harmful algal blooms and eutrophication: nutrient sources, composition, and consequences. *Estuaries, 25*(4), 704-726.

Androulidakis, Y. S., Kombiadou, K. D., Makris, C. V., Baltikas, V. N., & Krestenitis, Y. N. (2015). Storm surges in the Mediterranean Sea: Variability and trends under future climatic conditions. *Dynamics of Atmospheres and Oceans, 71*, 56-82. doi:10.1016/j.dynatmoce.2015.06.001

Appelo, C. A. J., & Postma, D. (2005). Geochemistry. *Groundwater and pollution, 536*.

Appelo, C. A. J., & Willemsen, A. (1987). Geochemical calculations and observations on salt water intrusions, I. A combined geochemical/minxing cell model. *Journal of Hydrology, 94*(3-4), 313-330.

Arabelos, D. N., Papazachariou, D. Z., Contadakis, M. E., & Spatalas, S. D. (2011). A new tide model for the Mediterranean Sea based on altimetry and tide gauge assimilation. *Ocean Science, 7*(3), 429-444. doi:10.5194/os-7-429-2011

Archie, G. E. (1942). The Electrical Resistivity Log as an Aid in Determining Some Reservoir Characteristics. *Transactions of the AIME, 146*(01), 54-62. doi:10.2118/942054-G

Armstrong, F. A. J. (1957). The iron content of sea water. *Journal of the Marine Biological Association of the United Kingdom, 36*(3), 509-517.
Ataie-Ashtiani, B., Werner, A. D., Simmons, C. T., Morgan, L. K., & Lu, C. (2013). How important is the impact of land-surface inundation on seawater intrusion caused by sea-level rise? *Hydrogeology Journal, 21*(7), 1673-1677. doi:10.1007/s10040-013-1021-0
Ataie-Ashtiani, B., Volker, R., & Lockington, D. (2001). Tidal effects on groundwater dynamics in unconfined aquifers. *Hydrological Processes, 15*(4), 655-669.
Back, W., Hanshaw, B. B., Herman, J. S., & Van Driel, J. N. (1986). Differential dissolution of a Pleistocene reef in the ground-water mixing zone of coastal Yucatan, Mexico. *Geology, 14*(2), 137-140.
Barker, A. P., Newton, R. J., Bottrell, S. H., & Tellam, J. H. (1998). Processes affecting groundwater chemistry in a zone of saline intrusion into an urban sandstone aquifer. *Applied Geochemistry, 13*(6), 735-749. doi:https://doi.org/10.1016/S0883-2927(98)00006-7
Barker, S., & Ridgwell, A. (2012). Ocean acidification. *Nature Education Knowledge, 3*(10), 21.
Batu, V. (1998). *Aquifer hydraulics: a comprehensive guide to hydrogeologic data analysis*: John Wiley & Sons.
Bear, J. (1972). *Dynamics of fluids in porous media*: Dover Publications.
Bear, J. (1999). *Seawater Intrusion in Coastal Aquifers — Concepts, Methods and Practices* (J. Bear, A. H. D. Cheng, S. Sorek, D. Ouazar, & I. Herrera Eds. Vol. 14). Dordrecht: Springer Netherlands.
Beaujean, J., Nguyen, F., Kemna, A., Antonsson, A., & Engesgaard, P. (2014). Calibration of seawater intrusion models: Inverse parameter estimation using surface electrical resistivity tomography and borehole data. *Water Resources Research, 50*(8), 6828-6849. doi:https://doi.org/10.1002/2013WR014020
Beekman, H. E. *Ion chromatography of fresh-and seawater intrusion*: Free University, Amsterdam.
Boulton, N. S. (1954). The drawdown of the water-table under non-steady conditions near a pumped well in an unconfined formation. *Proceedings of the Institution of Civil Engineers, 3*(4), 564-579.
Boulton, N. S. (1963). Analysis of data from non-equilibrium pumping tests allowing for delayed yield from storage. *Proceedings of the Institution of Civil Engineers, 26*(3), 469-482.
Bouwer, H., & Rice, R. C. (1978). Delayed aquifer yield as a phenomenon of delayed air entry. *Water Resources Research, 14*(6), 1068-1074.
Bristow, L. A., Mohr, W., Ahmerkamp, S., & Kuypers, M. M. M. (2017). Nutrients that limit growth in the ocean. *Current Biology, 27*(11), R474-R478.
Brown, C. J., Coates, J. D., & Schoonen, M. A. A. (1999). Localized Sulfate-Reducing Zones in a Coastal Plain Aquifer. *Groundwater, 37*(4), 505-516.
Burnett, B. (1999). Offshore springs and seeps are focus of working group. *Eos, Transactions American Geophysical Union, 80*(2), 13-15.
Burnett, W. C. (1996). Tracing groundwater flow into surface waters using natural super (222) RN. *LOICZ Reports Studies*(8), 22-36.
Burnett, W. C., Taniguchi, M., & Oberdorfer, J. (2001). Measurement and significance of the direct discharge of groundwater into the coastal zone. *Journal of Sea Research, 46*(2), 109-116.
Canfield, D. (2001). Biogeochemistry of sulfur isotopes. *Reviews in mineralogy and geochemistry, 43*(1), 607-636.

Cardenas, M. B., Bennett, P. C., Zamora, P. B., Befus, K. M., Rodolfo, R. S., Cabria, H. B., & Lapus, M. R. (2015). Devastation of aquifers from tsunami-like storm surge by Supertyphoon Haiyan. *Geophysical Research Letters, 42*(8), 2844-2851. doi:https://doi.org/10.1002/2015GL063418

Carr, P. A., & Van Der Kamp, G. S. (1969). Determining aquifer characteristics by the tidal method. *Water Resources Research, 5*(5), 1023-1031. doi:https://doi.org/10.1029/WR005i005p01023

Carrera, J., & Neuman, S. P. (1986). Estimation of aquifer parameters under transient and steady state conditions: 3. Application to synthetic and field data. *Water Resources Research, 22*(2), 228-242.

Carrera, J., Vázquez-Suñé, E., Castillo, O., & Sánchez-Vila, X. (2004). A methodology to compute mixing ratios with uncertain end-members. *Water Resources Research, 40*(12).

Cerdà-Domènech, M., Rodellas, V., Folch, A., & Garcia-Orellana, J. (2017). Constraining the temporal variations of Ra isotopes and Rn in the groundwater end-member: Implications for derived SGD estimates. *Science of The Total Environment, 595*, 849-857. doi:10.1016/j.scitotenv.2017.03.005

Cisteró, X. F., & Camarós, J. G. (2014). Les rierades al Maresme. *Atzavara, L'*(23), 61-79.

Comte, J. C., Wilson, C., Ofterdinger, U., & González-Quirós, A. (2017). Effect of volcanic dykes on coastal groundwater flow and saltwater intrusion: A field-scale multiphysics approach and parameter evaluation: VOLCANIC DYKES AND GROUNDWATER FLOW. *Water Resources Research, 53*(3), 2171-2198. doi:10.1002/2016WR019480

Custodio, E. (1992). Coastal aquifer salinization as a consequence of aridity: the case of Amurga phonolitic massif, Gran Canaria Island. *Study and Modelling of Salwater Intrusion, CIMNE-UPC, Barcelona*, 81-98.

Custodio, E. (2005). *Coastal aquifers as important natural hydrogeological structures. Groundwater and Human Development* (CRC Press ed.). London: 15-38.

Chapelle, F. H., & Lovley, D. R. (1992). Competitive exclusion of sulfate reduction by Fe (lll)-reducing bacteria: a mechanism for producing discrete zones of high-iron ground water. *Groundwater, 30*(1), 29-36.

Chatton, E., Aquilina, L., Pételet-Giraud, E., Cary, L., Bertrand, G., Labasque, T., . . . Pauwels. (2016). Glacial recharge, salinisation and anthropogenic contamination in the coastal aquifers of Recife (Brazil). *Science of The Total Environment, 569-570*, 1114-1125. doi:https://doi.org/10.1016/j.scitotenv.2016.06.180

Chen, X., Cukrov, N., Santos, I. R., Rodellas, V., Cukrov, N., & Du, J. (2020). Karstic submarine groundwater discharge into the Mediterranean: Radon-based nutrient fluxes in an anchialine cave and a basin-wide upscaling. *Geochimica et Cosmochimica Acta, 268*, 467-484.

Christophersen, N., Neal, C., Hooper, R. P., Vogt, R. D., & Andersen, S. (1990). Modelling streamwater chemistry as a mixture of soilwater end-members—a step towards second-generation acidification models. *Journal of Hydrology, 116*(1-4), 307-320.

Chuang, M.-H., & Yeh, H.-D. (2008). Analytical solution for tidal propagation in a leaky aquifer extending finite distance under the sea. *Journal of Hydraulic Engineering, 134*(4), 447-454.

Church, P. E., & Granato, G. E. (1996). Bias in ground-water data caused by well-bore flow in long-screen wells. *Groundwater, 34*(2), 262-273.

Davis, S. N., & DeWiest, R. J. M. (1966). Hydrogeology John Wiley Sons New York NY.

de Franco, R., Biella, G., Tosi, L., Teatini, P., Lozej, A., Chiozzotto, B., . . . Gasparetto-Stori, G. (2009). Monitoring the saltwater intrusion by time lapse electrical resistivity tomography: The Chioggia test site (Venice Lagoon, Italy). *Journal of Applied Geophysics, 69*(3), 117-130. doi:10.1016/j.jappgeo.2009.08.004

De Simoni, M., Carrera, J., Sanchez-Vila, X., & Guadagnini, A. (2005). A procedure for the solution of multicomponent reactive transport problems. *Water Resources Research, 41*(11).

de Toro, C., Vieira, R., & Sevilla, M. J. (1994). Tidal models of the Mediterranean sea. 17.

Del Val, L., Carrera, J., Martínez-Pérez, L., Pool, M., Saaltink, M. W., & Folch, A. (in press). A method to interpret coastal aquifer pumping tests: removing noise and natural groundwater head fluctuations.

Del Val, L., Carrera, J., Pool, M., Martínez, L., Casanovas, C., Bour, O., & Folch, A. (2021). Heat Dissipation Test With Fiber-Optic Distributed Temperature Sensing to Estimate Groundwater Flux. *Water Resources Research, 57*(3), e2020WR027228. doi:https://doi.org/10.1029/2020WR027228

Diego-Feliu, M., Rodellas, V., Saaltink, M. W., Alorda-Kleinglass, A., Goyetche, T., Martínez-Pérez, L., . . . Garcia-Orellana, J. (2021). New perspectives on the use of 224Ra/228Ra and 222Rn/226Ra activity ratios in groundwater studies. *Journal of Hydrology, 596*, 126043. doi:10.1016/j.jhydrol.2021.126043

Dietrich, S., Carrera, J., Weinzettel, P., & Sierra, L. (2018). Estimation of specific yield and its variability by electrical resistivity tomography. *Water Resources Research, 54*(11), 8653-8673.

Diez, J. J., Esteban, M. D., López-Gutiérrez, J. S., & Negro, V. (2013). Meteocean Influence on Inland and Coastal Floods in the East of Spain. *Journal of Coastal Research, 291*, 72-80. doi:10.2112/JCOASTRES-D-11-00226.1

Drogue, C., Razack, M., & Krivic, P. (1984). Survey of a coastal karstic aquifer by analysis of the effect of the sea-tide: Example of the Kras of Slovenia, Yugoslavia. *Environmental Geology and Water Sciences, 6*(2), 103-109. doi:10.1007/BF02509916

Duque, C., Russoniello, C. J., & Rosenberry, D. O. (2020). History and evolution of seepage meters for quantifying flow between groundwater and surface water: Part 2–Marine settings and submarine groundwater discharge. *Earth-Science Reviews, 204*, 103168.

Eissa, M. A. (2018). Application of multi-isotopes and geochemical modeling for delineating recharge and salinization sources in Dahab Basin aquifers (South Sinai, Egypt). *Hydrology, 5*(3), 41.

Emery, W. J., & Thomson, R. E. (2001). Time-series analysis methods. *Data Analysis Methods in Physical Oceanography, 371*.

Erskine, A. D. (1991). The effect of tidal fluctuation on a coastal aquifer in the UK. *Groundwater, 29*(4), 556-562.

Ferris, J. G. (1952). *Cyclic fluctuations of water level as a basis for determining aquifer transmissibility*. Retrieved from Washington, D.C.:

Field, M. S. (2021). Groundwater sampling in karst terranes: passive sampling in comparison to event-driven sampling strategy. *Hydrogeology Journal, 29*(1), 53-65. doi:10.1007/s10040-020-02240-9

Fleury, P., Bakalowicz, M., & de Marsily, G. (2007). Submarine springs and coastal karst aquifers: a review. *Journal of Hydrology, 339*(1-2), 79-92.

Folch, A., del Val, L., Luquot, L., Martínez-Pérez, L., Bellmunt, F., Le Lay, H., . . . Carrera, J. (2020). Combining fiber optic DTS, cross-hole ERT and time-lapse induction logging to characterize and monitor a coastal aquifer. *Journal of Hydrology, 588*, 125050. doi:10.1016/j.jhydrol.2020.125050

Fratesi, B. (2013). Hydrology and geochemistry of the freshwater lens in coastal karst *Coastal karst landforms* (pp. 59-75): Springer.

Gattuso, J. P., Frankignoulle, M., Bourge, I., Romaine, S., & Buddemeier, R. W. (1998). Effect of calcium carbonate saturation of seawater on coral calcification. *Global and Planetary Change, 18*(1-2), 37-46.

Gaume, E., Borga, M., Llassat, M. C., Maouche, S., Lang, M., & Diakakis, M. (2016). Mediterranean extreme floods and flash floods *The Mediterranean Region under Climate Change. A Scientific Update* (pp. 133-144): IRD Editions.

Geng, X., Li, H., Boufadel, M. C., & Liu, S. (2009). Tide-induced head fluctuations in a coastal aquifer: effects of the elastic storage and leakage of the submarine outlet-capping. *Hydrogeology Journal, 17*(5), 1289-1296.

Giménez-Forcada, E. (2014). Space/time development of seawater intrusion: A study case in Vinaroz coastal plain (Eastern Spain) using HFE-Diagram, and spatial distribution of hydrochemical facies. *Journal of Hydrology, 517*, 617-627. doi:10.1016/j.jhydrol.2014.05.056

Giménez-Forcada, E. (2010). Dynamic of sea water interface using hydrochemical facies evolution diagram. *Groundwater, 48*(2), 212-216.

Godin, G. (1972). *The analysis of tides*.

Gomis-Yagües, V., Boluda-Botella, N., & Ruiz-Beviá, F. (1997). Column displacement experiments to validate hydrogeochemical models of seawater intrusions. *Journal of Contaminant Hydrology, 29*(1), 81-91. doi:10.1016/S0169-7722(96)00088-5

Gomis-Yagües, V., Boluda-Botella, N., & Ruiz-Beviá, F. (2000). Gypsum precipitation/dissolution as an explanation of the decrease of sulphate concentration during seawater intrusion. *Journal of Hydrology, 228*(1-2), 48-55.

Grzelak, K., Tamborski, J., Kotwicki, L., & Bokuniewicz, H. (2018). Ecostructuring of marine nematode communities by submarine groundwater discharge. *Marine environmental research, 136*, 106-119.

Guarracino, L., Carrera, J., & Vázquez-Suñé, E. (2012). Analytical study of hydraulic and mechanical effects on tide-induced head fluctuation in a coastal aquifer system that extends under the sea. *Journal of Hydrology, 450-451*, 150-158. doi:10.1016/j.jhydrol.2012.05.015

Guo, H., Jiao, J. J., & Li, H. (2010). Groundwater response to tidal fluctuation in a two-zone aquifer. *Journal of Hydrology, 381*(3-4), 364-371. doi:10.1016/j.jhydrol.2009.12.009

Guomin, L., & Chongxi, C. (1991). Determining the length of confined aquifer roof extending under the sea by the tidal method. *Journal of Hydrology, 123*(1-2), 97-104.

Haan, C. T., Barfield, B. J., & Hayes, J. C. (1994). *Design Hydrology and Sedimentology for Small Catchments*: Elsevier.

Hanshaw, B. B., & Back, W. (1980). Chemical mass-wasting of the northern Yucatan Peninsula by groundwater dissolution. *Geology, 8*(5), 222-224.

Hassen, I., Hamzaoui-Azaza, F., & Bouhlila, R. (2018). Establishing complex compartments-aquifers connectivity via geochemical approaches towards hydrogeochemical conceptual model: Kasserine Aquifer System, Central Tunisia. *Journal of Geochemical Exploration, 188*, 257-269.

Hoegh-Guldberg, O., Jacob, D., Bindi, M., Brown, S., Camilloni, I., Diedhiou, A., . . . Guiot, J. (2018). Impacts of 1.5 C global warming on natural and human systems. *Global warming of 1.5 C. An IPCC Special Report*.

Hooper, R. P. (2003). Diagnostic tools for mixing models of stream water chemistry. *Water Resources Research, 39*(3).

Hooper, R. P., Christophersen, N., & Peters, N. E. (1990). Modelling streamwater chemistry as a mixture of soilwater end-members—An application to the Panola Mountain catchment, Georgia, USA. *Journal of Hydrology, 116*(1-4), 321-343.

Horowitz, A. J. (2008). Determining annual suspended sediment and sediment-associated trace element and nutrient fluxes. *Science of The Total Environment, 400*(1-3), 315-343.

Hu, C., Muller-Karger, F. E., & Swarzenski, P. W. (2006). Hurricanes, submarine groundwater discharge, and Florida's red tides. *Geophysical Research Letters, 33*(11).

Huizer, S., Karaoulis, M. C., Oude Essink, G. H. P., & Bierkens, M. F. P. (2017). Monitoring and simulation of salinity changes in response to tide and storm surges in a sandy coastal aquifer system. *Water Resources Research, 53*(8), 6487-6509.

Hurrell, J. W., Holland, M. M., Gent, P. R., Ghan, S., Kay, J. E., Kushner, P. J., . . . Lindsay, K. (2013). The community earth system model: a framework for collaborative research. *Bulletin of the American Meteorological Society, 94*(9), 1339-1360.

Hutchins, S. R., & Acree, S. D. (2000). Ground water sampling bias observed in shallow, conventional wells. *Groundwater Monitoring & Remediation, 20*(1), 86-93.

Jacob, C. E. (1950). Engineering hydraulics. *Flow of ground waterJohn Wiley and Sons, New York*, 321-386.

Jardani, A., Dupont, J. P., Revil, A., Massei, N., Fournier, M., & Laignel, B. (2012). Geostatistical inverse modeling of the transmissivity field of a heterogeneous alluvial aquifer under tidal influence. *Journal of Hydrology, 472-473*, 287-300. doi:10.1016/j.jhydrol.2012.09.031

Jeng, D.-S., Li, L., & Barry, D. A. (2002). Analytical solution for tidal propagation in a coupled semi-confined/phreatic coastal aquifer. *Advances in Water Resources, 25*(5), 577-584.

Jiao, J. J., & Li, H. (2004). Breathing of coastal vadose zone induced by sea level fluctuations. *Geophysical Research Letters, 31*(11).

Jiao, J. J., & Post, V. (2019). *Coastal Hydrogeology*. Cambridge: Cambridge University Press.

Jiao, J. J., & Tang, Z. (1999). An analytical solution of groundwater response to tidal fluctuation in a leaky confined aquifer. *Water Resources Research, 35*(3), 747-751.

Johnes, P. J. (2007). Uncertainties in annual riverine phosphorus load estimation: Impact of load estimation methodology, sampling frequency, baseflow index and catchment population density. *Journal of Hydrology, 332*(1-2), 241-258.

Jurado, A., Vázquez-Suñé, E., Carrera, J., Tubau, I., & Pujades, E. (2015). Quantifying chemical reactions by using mixing analysis. *Science of The Total Environment, 502*, 448-456. doi:https://doi.org/10.1016/j.scitotenv.2014.09.036

Kendall, C., & Caldwell, E. A. (1998). Chapter 2 - Fundamentals of Isotope Geochemistry. In C. Kendall & J. J. McDonnell (Eds.), *Isotope Tracers in Catchment Hydrology* (pp. 51-86). Amsterdam: Elsevier.

Kendall, M. G. (1946). The advanced theory of statistics. *The advanced theory of statistics.*(2nd Ed).

Ketabchi, H., Mahmoodzadeh, D., Ataie-Ashtiani, B., & Simmons, C. T. (2016). Sea-level rise impacts on seawater intrusion in coastal aquifers: Review and integration. *Journal of Hydrology, 535*, 235-255.

Kilroy, G., & Coxon, C. (2005). Temporal variability of phosphorus fractions in Irish karst springs. *Environmental Geology, 47*(3), 421-430.

Kim, J.-H., Kim, K.-H., Thao, N. T., Batsaikhan, B., & Yun, S.-T. (2017). Hydrochemical assessment of freshening saline groundwater using multiple end-members mixing modeling: A study of Red River delta aquifer, Vietnam. *Journal of Hydrology, 549*, 703-714. doi:https://doi.org/10.1016/j.jhydrol.2017.04.040

Kłostowska, Ż., Szymczycha, B., Lengier, M., Zarzeczańska, D., & Dzierzbicka-Głowacka, L. (2020). Hydrogeochemistry and magnitude of SGD in the Bay of Puck, southern Baltic Sea. *Oceanologia, 62*(1), 1-11. doi:10.1016/j.oceano.2019.09.001

Knudby, C., & Carrera, J. (2006). On the use of apparent hydraulic diffusivity as an indicator of connectivity. *Journal of Hydrology, 329*(3), 377-389. doi:https://doi.org/10.1016/j.jhydrol.2006.02.026

Kouzana, L., Mammou, A. B., & Felfoul, M. S. (2009). Seawater intrusion and associated processes: Case of the Korba aquifer (Cap-Bon, Tunisia). *Comptes Rendus Geoscience, 341*(1), 21-35. doi:10.1016/j.crte.2008.09.008

Langevin, C. D., Thorne Jr, D. T., Dausman, A. M., Sukop, M. C., & Guo, W. (2008). *SEAWAT version 4: a computer program for simulation of multi-species solute and heat transport* (2328-7055). Retrieved from

Lesmes, D. P., & Friedman, S. P. (2005). Relationships between the electrical and hydrogeological properties of rocks and soils *Hydrogeophysics* (pp. 87-128): Springer.

Li, G., Li, H., & Boufadel, M. C. (2008). The enhancing effect of the elastic storage of the seabed aquitard on the tide-induced groundwater head fluctuation in confined submarine aquifer systems. *Journal of Hydrology, 350*(1-2), 83-92. doi:10.1016/j.jhydrol.2007.11.037

Li, H., Boufadel, M. C., & Weaver, J. W. (2008). Tide-induced seawater–groundwater circulation in shallow beach aquifers. *Journal of Hydrology, 352*(1-2), 211-224.

Li, H., & Jiao, J. J. (2001a). Tide-induced groundwater fluctuation in a coastal leaky confined aquifer system extending under the sea. *Water Resources Research, 37*(5), 1165-1171. doi:10.1029/2000WR900296

Li, H., & Jiao, J. J. (2001b). Analytical studies of groundwater-head fluctuation in a coastal confined aquifer overlain by a semi-permeable layer with storage. *Advances in Water Resources, 24*(5), 565-573.

Li, H., & Jiao, J. J. (2002). Analytical solutions of tidal groundwater flow in coastal two-aquifer system. *Advances in Water Resources, 25*(4), 417-426. doi:10.1016/S0309-1708(02)00004-0

Li, H., & Jiao, J. J. (2003a). Influence of the tide on the mean watertable in an unconfined, anisotropic, inhomogeneous coastal aquifer. *Advances in Water Resources, 26*(1), 9-16. doi:10.1016/S0309-1708(02)00097-0

Li, H., & Jiao, J. J. (2003b). Tide-induced seawater–groundwater circulation in a multi-layered coastal leaky aquifer system. *Journal of Hydrology, 274*(1-4), 211-224. doi:10.1016/S002-1694(02)00413-4

Li, H., Li, G., Cheng, J., & Boufadel, M. C. (2007). Tide-induced head fluctuations in a confined aquifer with sediment covering its outlet at the sea floor. *Water Resources Research, 43*(3).

Li, P., Wu, J., & Qian, H. (2016). Preliminary assessment of hydraulic connectivity between river water and shallow groundwater and estimation of their transfer rate during dry season in the Shidi River, China. *Environmental Earth Sciences, 75*(2). doi:10.1007/s12665-015-4949-7

Liu, K.-F. (1996). Tide-induced ground-water flow in deep confined aquifer. *Journal of Hydraulic Engineering, 122*(2), 104-110.

Liu, Y., Jiao, J. J., Liang, W., & Kuang, X. (2017). Hydrogeochemical characteristics in coastal groundwater mixing zone. *Applied Geochemistry, 85*, 49-60. doi:10.1016/j.apgeochem.2017.09.002

Liu, Y., Jiao, J. J., Liang, W., Santos, I. R., Kuang, X., & Robinson, C. E. (2021). Inorganic carbon and alkalinity biogeochemistry and fluxes in an intertidal beach aquifer: Implications for ocean acidification. *Journal of Hydrology, 595*, 126036. doi:https://doi.org/10.1016/j.jhydrol.2021.126036

Long, A. J., & Valder, J. F. (2011). Multivariate analyses with end-member mixing to characterize groundwater flow: Wind Cave and associated aquifers. *Journal of Hydrology, 409*(1), 315-327. doi:10.1016/j.jhydrol.2011.08.028

Luijendijk, E., Gleeson, T., & Moosdorf, N. (2020). Fresh groundwater discharge insignificant for the world's oceans but important for coastal ecosystems. *Nature Communications, 11*(1). doi:10.1038/s41467-020-15064-8

Luo, X., & Jiao, J. J. (2016). Submarine groundwater discharge and nutrient loadings in Tolo Harbor, Hong Kong using multiple geotracer-based models, and their implications of red tide outbreaks. *Water research, 102*, 11-31.

Lv, M., Xu, Z., Yang, Z. L., Lu, H., & Lv, M. (2021). A comprehensive review of specific yield in land surface and groundwater studies. *Journal of Advances in Modeling Earth Systems, 13*(2), e2020MS002270.

Magaritz, M., Goldenberg, L., Kafri, U., & Arad, A. (1980). Dolomite formation in the seawater–freshwater interface. *Nature, 287*(5783), 622-624.

Mahlknecht, J., Merchán, D., Rosner, M., Meixner, A., & Ledesma-Ruiz, R. (2017). Assessing seawater intrusion in an arid coastal aquifer under high anthropogenic influence using major constituents, Sr and B isotopes in groundwater. *Science of The Total Environment, 587*, 282-295.

Mahmoodzadeh, D., & Karamouz, M. (2019). Seawater intrusion in heterogeneous coastal aquifers under flooding events. *Journal of Hydrology, 568*, 1118-1130.

Martínez-Pérez, L., Carrera, J., Palacios, A., Goyetche, T., Ledo, J., Pezard, P., . . . Luquot, L. (in press b). The role of salinity profiles in the traditionnal paradigm for seawater intrusion.

Martínez-Pérez, L., Luquot, L., Carrera, J., Marazuela, M. A., Goyetche, T., Pool, M., . . . Folch, A. (in press a). Multidisciplinary approach to characterize coastal alluvial aquifers affected by seawater intrusion and submarine groundwater discharge.

Martínez, D., & Bocanegra, E. (2002). Hydrogeochemistry and cation-exchange processes in the coastal aquifer of Mar Del Plata, Argentina. *Hydrogeology Journal, 10*(3), 393-408.

McMahon, P. B., Chapelle, F. H., & Bradley, P. M. (2011). Evolution of redox processes in groundwater *Aquatic Redox Chemistry* (pp. 581-597): ACS Publications.

Medina, A., Alcolea, A., Galarza, G., & Carrera, J. (2004). TRANSIN IV – Fortran code for solving the coupled non-linear flow and transport inverse problem. (Hydrogeology Group, School of Civil Engineering, Technical University of Catalonia (Spain)), 1-182.

Medina, A., & Carrera, J. (1996). Coupled estimation of flow and solute transport parameters. *Water Resources Research, 32*(10), 3063-3076.

Medina, A., & Carrera, J. (2003). Geostatistical inversion of coupled problems: dealing with computational burden and different types of data. *Journal of Hydrology, 281*(4), 251-264.

Meier, P. M., Carrera, J., & Sanchez-Vila, X. (1999). A numerical study on the relationship between transmissivity and specific capacity in heterogeneous aquifers. *Groundwater, 37*(4), 611-617.

Meinzer, O. E. (1932). *Outline of methods for estimating ground-water supplies*. Retrieved from

Merritt, M. L. (2004). *Estimating hydraulic properties of the Floridan aquifer system by analysis of earth-tide, ocean-tide, and barometric effects, Collier and Hendry Counties, Florida*: US Department of the Interior, US Geological Survey.

METEOCAT. (2017). Servei Meteorològic de Catalunya. Retrieved from https://www.meteo.cat/

Milliman, J. D. (1993). Production and accumulation of calcium carbonate in the ocean: Budget of a nonsteady state. *Global Biogeochemical Cycles, 7*(4), 927-957.

Molins, S., Carrera, J., Ayora, C., & Saaltink, M. W. (2004). A formulation for decoupling components in reactive transport problems. *Water Resources Research, 40*(10).

Monastersky, R. (1996). Seep and ye shall find: Hidden water flow. *Science News*, 245-245.

Moore, W. S. (1999). The subterranean estuary: a reaction zone of ground water and sea water. *Marine Chemistry, 65*(1-2), 111-125. doi:10.1016/S0304-4203(99)00014-6

Morse, J. W., & Berner, R. A. (1995). What determines sedimentary C/S ratios? *Geochimica et Cosmochimica Acta, 59*(6), 1073-1077.

Nakaya, S., Uesugi, K., Motodate, Y., Ohmiya, I., Komiya, H., Masuda, H., & Kusakabe, M. (2007). Spatial separation of groundwater flow paths from a multi-flow system by a simple mixing model using stable isotopes of oxygen and hydrogen as natural tracers. *Water Resources Research, 43*(9).

Neuman, S. P. (1972). Theory of flow in unconfined aquifers considering delayed response of the water table. *Water Resources Research, 8*(4), 1031-1045.

Nguyen, F., Kemna, A., Antonsson, A., Engesgaard, P., Kuras, O., Ogilvy, R., . . . Pulido-Bosch, A. (2009). Characterization of seawater intrusion using 2D electrical imaging. *Near Surface Geophysics, 7*(5-6), 377-390.

Nielsen, P. (1990). Tidal dynamics of the water table in beaches. *Water Resources Research, 26*(9), 2127-2134.

Nikolaidis, C., Mandalos, P., & Vantarakis, A. (2008). Impact of intensive agricultural practices on drinking water quality in the EVROS Region (NE GREECE) by GIS analysis. *Environmental Monitoring and Assessment, 143*(1), 43-50.

Ogilvy, R. D., Meldrum, P. I., Kuras, O., Wilkinson, P. B., Chambers, J. E., Sen, M., . . . Frances, I. (2009). Automated monitoring of coastal aquifers with electrical resistivity tomography. *Near Surface Geophysics, 7*(5-6), 367-376.

Palacios, A., Ledo, J. J., Linde, N., Luquot, L., Bellmunt, F., Folch, A., . . . Martínez, L. (2020). Time-lapse cross-hole electrical resistivity tomography (CHERT) for monitoring seawater intrusion dynamics in a Mediterranean aquifer. *Hydrology and Earth System Sciences, 24*(4), 2121-2139.

Paldor, A., & Michael, H. A. (2021). Storm Surges Cause Simultaneous Salinization and Freshening of Coastal Aquifers, Exacerbated by Climate Change. *Water Resources Research*, e2020WR029213.

Papapetridis, K., & Paleologos, E. K. (2011). Contaminant detection probability in heterogeneous aquifers and corrected risk analysis for remedial response delay. *Water Resources Research, 47*(10).

Pelizardi, F., Bea, S. A., Carrera, J., & Vives, L. (2017). Identifying geochemical processes using End Member Mixing Analysis to decouple chemical components for mixing ratio calculations. *Journal of Hydrology, 550*, 144-156.

Peng, T., Zhu, Z., Du, J., & Liu, J. (2021). Effects of nutrient-rich submarine groundwater discharge on marine aquaculture: A case in Lianjiang, East China Sea. *Science of The Total Environment*, 147388.

Poulsen, D. L., Cook, P. G., Simmons, C. T., McCallum, J. L., & Dogramaci, S. (2019). Effects of intraborehole flow on purging and sampling long-screened or open wells. *Groundwater, 57*(2), 269-278.

Puertos del estado, p. e. (2017). Retrieved from http://www.puertos.es/es-es/oceanografia/Paginas/portus.aspx

Pulido-Leboeuf, P. (2004). Seawater intrusion and associated processes in a small coastal complex aquifer (Castell de Ferro, Spain). *Applied Geochemistry, 19*(10), 1517-1527.

Purvance, D. T., & Andricevic, R. (2000). On the electrical-hydraulic conductivity correlation in aquifers. *Water Resources Research, 36*(10), 2905-2913.

Rabiet, M., Margoum, C., Gouy, V., Carluer, N., & Coquery, M. (2010). Assessing pesticide concentrations and fluxes in the stream of a small vineyard catchment–effect of sampling frequency. *Environmental pollution, 158*(3), 737-748.

Ratner-Narovlansky, Y., Weinstein, Y., & Yechieli, Y. (2020). Tidal fluctuations in a multi-unit coastal aquifer. *Journal of Hydrology, 580*, 124222. doi:10.1016/j.jhydrol.2019.124222

Rezaei, M., Sanz, E., Raeisi, E., Ayora, C., Vázquez-Suñé, E., & Carrera, J. (2005). Reactive transport modeling of calcite dissolution in the fresh-salt water mixing zone. *Journal of Hydrology, 311*(1-4), 282-298.

Richard, C. (2015). *The United Nations world water development report 2015: water for a sustainable world*: UNESCO Publishing.

Richey, A. S., Thomas, B. F., Lo, M.-H., Reager, J. T., Famiglietti, J. S., Voss, K., . . . Rodell, M. (2015). Quantifying renewable groundwater stress with GRACE. *Water Resources Research, 51*(7), 5217-5238. doi:https://doi.org/10.1002/2015WR017349

Rosecrans, C. Z., Nolan, B. T., & Gronberg, J. M. (2017). Prediction and visualization of redox conditions in the groundwater of Central Valley, California. *Journal of Hydrology, 546*, 341-356.

Rufí-Salís, M., Garcia-Orellana, J., Cantero, G., Castillo, J., Hierro, A., Rieradevall, J., & Bach, J. (2019). Influence of land use changes on submarine groundwater discharge. *Environmental Research Communications, 1*(3), 031005. doi:10.1088/2515-7620/ab1695

Russak, A., & Sivan, O. (2010). Hydrogeochemical Tool to Identify Salinization or Freshening of Coastal Aquifers Determined from Combined Field Work, Experiments, and Modeling. *Environmental Science & Technology, 44*(11), 4096-4102. doi:10.1021/es1003439

Russak, A., Sivan, O., & Yechieli, Y. (2016). Trace elements (Li, B, Mn and Ba) as sensitive indicators for salinization and freshening events in coastal aquifers. *Chemical Geology, 441*, 35-46.

Rusydi, A. F., Onodera, S.-I., Saito, M., Ioka, S., Maria, R., Ridwansyah, I., & Delinom, R. M. (2021). Vulnerability of groundwater to iron and manganese contamination

in the coastal alluvial plain of a developing Indonesian city. *SN Applied Sciences, 3*(4), 1-12.

Sanchez-Vila, X., Guadagnini, A., & Carrera, J. (2006). Representative hydraulic conductivities in saturated groundwater flow. *Reviews of Geophysics, 44*(3). doi:10.1029/2005RG000169

Santos, I. R. S., Burnett, W. C., Chanton, J., Mwashote, B., Suryaputra, I. G. N. A., & Dittmar, T. (2008). Nutrient biogeochemistry in a Gulf of Mexico subterranean estuary and groundwater-derived fluxes to the coastal ocean. *Limnology and Oceanography, 53*(2), 705-718. doi:https://doi.org/10.4319/lo.2008.53.2.0705

Sawyer, A. H., Michael, H. A., & Schroth, A. W. (2016). From soil to sea: the role of groundwater in coastal critical zone processes. *WIREs Water, 3*(5), 706-726. doi:https://doi.org/10.1002/wat2.1157

Scott, G., & Crunkilton, R. L. (2000). Acute and chronic toxicity of nitrate to fathead minnows (Pimephales promelas), ceriodaphnia dubia, and Daphnia magna. *Environmental Toxicology and Chemistry, 19*(12), 2918-2922. doi:https://doi.org/10.1002/etc.5620191211

Schleppi, P., Waldner, P. A., & Fritschi, B. (2006). Accuracy and precision of different sampling strategies and flux integration methods for runoff water: comparisons based on measurements of the electrical conductivity. *Hydrological Processes: An International Journal, 20*(2), 395-410.

Schuite, J., Longuevergne, L., Bour, O., Guihéneuf, N., Becker, M. W., Cole, M., . . . Boudin, F. (2017). Combining periodic hydraulic tests and surface tilt measurements to explore in situ fracture hydromechanics. *Journal of Geophysical Research: Solid Earth, 122*(8), 6046-6066.

Shalev, E., Lazar, A., Wollman, S., Kington, S., Yechieli, Y., & Gvirtzman, H. (2009). Biased Monitoring of Fresh Water-Salt Water Mixing Zone in Coastal Aquifers. *Groundwater, 47*(1), 49-56. doi:https://doi.org/10.1111/j.1745-6584.2008.00502.x

Sherif, M. M., El Mahmoudi, A., Garamoon, H., Kacimov, A., Akram, S., Ebraheem, A., & Shetty, A. (2006). Geoelectrical and hydrogeochemical studies for delineating seawater intrusion in the outlet of Wadi Ham, UAE. *Environmental Geology, 49*(4), 536-551.

Sherif, M. M., & Singh, V. P. (1999). Effect of climate change on sea water intrusion in coastal aquifers. *Hydrological Processes, 13*(8), 1277-1287.

Shin, K., Koh, D.-C., Jung, H., & Lee, J. (2020). The Hydrogeochemical Characteristics of Groundwater Subjected to Seawater Intrusion in the Archipelago, Korea. *Water, 12*(6), 1542.

Sivan, O., Yechieli, Y., Herut, B., & Lazar, B. (2005). Geochemical evolution and timescale of seawater intrusion into the coastal aquifer of Israel. *Geochimica et Cosmochimica Acta, 69*(3), 579-592. doi:https://doi.org/10.1016/j.gca.2004.07.023

Slomp, C. P., & Van Cappellen, P. (2004). Nutrient inputs to the coastal ocean through submarine groundwater discharge: controls and potential impact. *Journal of Hydrology, 295*(1), 64-86. doi:10.1016/j.jhydrol.2004.02.018

Slooten, L. J., Carrera, J., Castro, E., & Fernandez-Garcia, D. (2010). A sensitivity analysis of tide-induced head fluctuations in coastal aquifers. *Journal of Hydrology, 393*(3-4), 370-380. doi:10.1016/j.jhydrol.2010.08.032

Small, C., & Nicholls, R. J. (2003). A global analysis of human settlement in coastal zones. *Journal of Coastal Research*, 584-599.

Snyder, M., Taillefert, M., & Ruppel, C. (2004). Redox zonation at the saline-influenced boundaries of a permeable surficial aquifer: effects of physical forcing on the biogeochemical cycling of iron and manganese. *Journal of Hydrology, 296*(1), 164-178. doi:10.1016/j.jhydrol.2004.03.019

Spotte, S. (1979). Fish and invertebrate culture: water management in closed systems-2.

Sutcliffe Jr, W. H. (1972). Some relations of land drainage, nutrients, particulate material, and fish catch in two eastern Canadian bays. *Journal of the Fisheries Board of Canada, 29*(4), 357-362.

Taniguchi, M., Dulai, H., Burnett, K. M., Santos, I. R., Sugimoto, R., Stieglitz, T., . . . Burnett, W. C. (2019). Submarine groundwater discharge: updates on its measurement techniques, geophysical drivers, magnitudes, and effects. *Frontiers in Environmental Science, 7*, 141.

Teo, H. T., Jeng, D. S., Seymour, B. R., Barry, D. A., & Li, L. (2003). A new analytical solution for water table fluctuations in coastal aquifers with sloping beaches. *Advances in Water Resources, 26*(12), 1239-1247.

Terzaghi, K. (1954). Anchored bulkheads. *American Society of Civil Engineers Transactions*.

Todd, D. K. (1980). Groundwater Hydrology. *Hydrology, 2nd Edition, John Willey and Sons, 315p*, 235-247.

Trefry, M. G., & Bekele, E. (2004). Structural characterization of an island aquifer via tidal methods: STRUCTURAL CHARACTERIZATION OF AN ISLAND AQUIFER. *Water Resources Research, 40*(1). doi:10.1029/2003WR002003

Trefry, M. G., & Johnston, C. D. (1998). Pumping test analysis for a tidally forced aquifer. *Groundwater, 36*(3), 427-433.

Tubau, I., Vàzquez-Suñé, E., Jurado, A., & Carrera, J. (2014). Using EMMA and MIX analysis to assess mixing ratios and to identify hydrochemical reactions in groundwater. *Science of The Total Environment, 470-471*, 1120-1131. doi:10.1016/j.scitotenv.2013.10.121

U. S. Environmental Protection Agency. (1986). *Quality criteria for water* (EPA 440/5-86-0013). Retrieved from Washington, DC.:

Valiela, I., Costa, J., Foreman, K., Teal, J. M., Howes, B., & Aubrey, D. (1990). Transport of groundwater-borne nutrients from watersheds and their effects on coastal waters. *Biogeochemistry, 10*(3), 177-197. doi:10.1007/BF00003143

Van Der Kamp, G. S. (1972). Tidal fluctuations in a confined aquifer extending under the sea. *PROC. LNT. GEOL. CONGR., 24TH SECTION 11 HYDROGEOL*, 101-106.

Van der Kamp, G. S., & Gale, J. E. (1983). Theory of earth tide and barometric effects in porous formations with compressible grains. *Water Resources Research, 19*(2), 538-544.

Vázquez-Suñé, E., Carrera, J., Tubau, I., Sánchez-Vila, X., & Soler, A. (2010). An approach to identify urban groundwater recharge. *Hydrology and Earth System Sciences, 14*(10), 2085-2097. doi:10.5194/hess-14-2085-2010

Wang, C., Li, H., Wan, L., Wang, X., & Jiang, X. (2014). Closed-form analytical solutions incorporating pumping and tidal effects in various coastal aquifer systems. *Advances in Water Resources, 69*, 1-12. doi:10.1016/j.advwatres.2014.03.003

Waxman, M. H., & Smits, L. J. M. (1968). Electrical conductivities in oil-bearing shaly sands. *Society of Petroleum Engineers Journal, 8*(02), 107-122.

Werner, A. D., Bakker, M., Post, V. E. A., Vandenbohede, A., Lu, C., Ataie-Ashtiani, B., . . . Barry, D. A. (2013). Seawater intrusion processes, investigation and

management: Recent advances and future challenges. *Advances in Water Resources, 51*, 3-26. doi:10.1016/j.advwatres.2012.03.004

Westra, S., Fowler, H. J., Evans, J. P., Alexander, L. V., Berg, P., Johnson, F., . . . Roberts, N. M. (2014). Future changes to the intensity and frequency of short-duration extreme rainfall. *Reviews of Geophysics, 52*(3), 522-555.

Wicks, C. M., & Herman, J. S. (1996). Regional hydrogeochemistry of a modern coastal mixing zone. *Water Resources Research, 32*(2), 401-407.

Wigley, T. M. L., & Plummer, L. N. (1976). Mixing of carbonate waters. *Geochimica et Cosmochimica Acta, 40*(9), 989-995. doi:10.1016/0016-7037(76)90041-7

Wilkinson, B. H., & Algeo, T. J. (1989). Sedimentary carbonate record of calcium-magnesium cycling. *American Journal of Science, 289*(10), 1158-1194.

Wilson, A. M., Moore, W. S., Joye, S. B., Anderson, J. L., & Schutte, C. A. (2011). Storm-driven groundwater flow in a salt marsh. *Water Resources Research, 47*(2).

Windom, H. L., Moore, W. S., Niencheski, L. F. H., & Jahnke, R. A. (2006). Submarine groundwater discharge: A large, previously unrecognized source of dissolved iron to the South Atlantic Ocean. *Marine Chemistry, 102*(3), 252-266. doi:10.1016/j.marchem.2006.06.016

Yang, J.-A., Kim, S., Mori, N., & Mase, H. (2018). Assessment of long-term impact of storm surges around the Korean Peninsula based on a large ensemble of climate projections. *Coastal Engineering, 142*, 1-8.

Yang, J., Graf, T., Herold, M., & Ptak, T. (2013). Modelling the effects of tides and storm surges on coastal aquifers using a coupled surface–subsurface approach. *Journal of Contaminant Hydrology, 149*, 61-75.

Yang, J., Graf, T., & Ptak, T. (2015). Sea level rise and storm surge effects in a coastal heterogeneous aquifer: a 2D modelling study in northern Germany. *Grundwasser, 20*(1), 39-51.

Yin, J., Lin, N., & Yu, D. (2016). Coupled modeling of storm surge and coastal inundation: A case study in N ew Y ork C ity during H urricane S andy. *Water Resources Research, 52*(11), 8685-8699.

Yu, H., Shen, Y., Kelly, R. M., Qi, X., Wu, K., Li, S., . . . Bao, X. (2020). Trends in social vulnerability to storm surges in Shenzhen, China. *Natural Hazards and Earth System Sciences, 20*(9), 2447-2462.

Zhou, P., Li, G., & Lu, Y. (2016). Numerical modeling of tidal effects on groundwater dynamics in a multi-layered estuary aquifer system using equivalent tidal loading boundary condition: case study in Zhanjiang, China. *Environmental Earth Sciences, 75*(2). doi:10.1007/s12665-015-5034-y

Zhou, X. (2008). Determination of aquifer parameters based on measurements of tidal effects on a coastal aquifer near Beihai, China. *Hydrological Processes, 22*(16), 3176-3180. doi:10.1002/hyp.6906

Zhuang, C., Zhou, Z., & Illman, W. A. (2017). A joint analytic method for estimating aquitard hydraulic parameters. *Groundwater, 55*(4), 565-576. doi:10.1111/gwat.12494